SUBTASK 3.1 – BAKKEN RICH GAS ENHANCED OIL RECOVERY PROJECT

Topical Report

(for the period of September 1, 2017, through January 31, 2022)

Prepared for:

AAD Document Control

National Energy Technology Laboratory
U.S. Department of Energy
626 Cochrans Mill Road
PO Box 10940, MS 921-107
Pittsburgh, PA 15236-0940

Cooperative Agreement No.: DE-FE0024233
DOE Technical Monitor: Gary Covatch

Prepared by:

Steven A. Smith
James A. Sorensen
Bethany A. Kurz
Loreal V. Heebink
Nicholas A. Azzolina
Lu Jin
Lingyun Kong
Xue Yu
Xincheng Wan
Yang Yu
Jin Zhao
Christopher J. Beddoe
Blaise A.F. Mibeck
Shane K. Butler
Alexander Azenkeng
Marc D. Kurz
Chad A. Wocken
Alexander V. Chakhmakhchev
Todd Jiang
Nicholas W. Bosshart
Matthew E. Burton-Kelly
David V. Nakles
Charles D. Gorecki
John A. Harju
Edward N. Steadman

Energy & Environmental Research Center
University of North Dakota
15 North 23rd Street, Stop 9018
Grand Forks, ND 58202-9018

2022-EERC-01-09

January 2022

EERC DISCLAIMER

LEGAL NOTICE This research report was prepared by the Energy & Environmental Research Center (EERC), an agency of the University of North Dakota, as an account of work sponsored by the U.S. Department of Energy (DOE) National Energy Technology Laboratory (NETL) and the North Dakota Industrial Commission (NDIC). Because of the research nature of the work performed, neither the EERC nor any of its employees makes any warranty, express or implied, or assumes any legal liability or responsibility for the accuracy, completeness, or usefulness of any information, apparatus, product, or process disclosed or represents that its use would not infringe privately owned rights. Reference herein to any specific commercial product, process, or service by trade name, trademark, manufacturer, or otherwise does not necessarily constitute or imply its endorsement or recommendation by the EERC.

ACKNOWLEDGMENT

This material is based upon work supported by DOE NETL under Award No. DE-FE-0024233.

DOE DISCLAIMER

This report was prepared as an account of work sponsored by an agency of the United States Government. Neither the United States Government, nor any agency thereof, nor any of their employees, makes any warranty, express or implied, or assumes any legal liability or responsibility for the accuracy, completeness, or usefulness of any information, apparatus, product, or process disclosed, or represents that its use would not infringe privately owned rights. Reference herein to any specific commercial product, process, or service by trade name, trademark, manufacturer, or otherwise does not necessarily constitute or imply its endorsement, recommendation, or favoring by the United States Government or any agency thereof. The views and opinions of authors expressed herein do not necessarily state or reflect those of the United States Government or any agency thereof.

NDIC DISCLAIMER

This report was prepared by the Energy & Environmental Research Center (EERC) pursuant to an agreement partially funded by the Industrial Commission of North Dakota, and neither the EERC nor any of its subcontractors nor the North Dakota Industrial Commission nor any person acting on behalf of either:

(A) Makes any warranty or representation, express or implied, with respect to the accuracy, completeness, or usefulness of the information contained in this report or that the use of any information, apparatus, method, or process disclosed in this report may not infringe privately owned rights; or

TABLE OF CONTENTS

Continued . . .

Continued . . .

TABLE OF CONTENTS (continued)

LIST OF FIGURES

Continued . . .

LIST OF FIGURES (continued)

Continued . . .

LIST OF FIGURES (continued)

Continued . . .

LIST OF FIGURES (continued)

Continued . . .

LIST OF FIGURES (continued)

Continued . . .

LIST OF FIGURES (continued)

Continued . . .

LIST OF FIGURES (continued)

Continued . . .

LIST OF FIGURES (continued)

Continued . . .

LIST OF FIGURES (continued)

Continued . . .

LIST OF FIGURES (continued)

LIST OF TABLES

Continued . . .

LIST OF TABLES (continued)

NOMENCLATURE

2D	two-dimensional
3D	three-dimensional
A/A	aromatic/aliphatic
AHM	automatic history matching
AI	artificial intelligence
API	American Petroleum Institute
bbl	barrel
BDA	big data analytics
bfpd	barrels of fluid per day
BHP	bottomhole pressure
bhp	brake horsepower
BI	brittleness index
BIC	Bayesian information criterion
bpd	barrel per day
bpm	barrels per minute
BPS	Bakken petroleum system
CA	contact angle
CCE	constant composition expansion
CMG	Computer Modelling Group
CO_2	carbon dioxide
CT	computed tomography
DFN	discrete fracture network
DI	deionized
DOE	U.S. Department of Energy
DSU	drill spacing unit
ECDF	empirical cumulative distribution function
EDFM	embedded discrete fracture model
EDFN	embedded discrete fracture network
EDS	energy-dispersive spectroscopy
EERC	Energy & Environmental Research Center
EOR	enhanced oil recovery
EOS	equation of state
fc	fracture conductivity
FESEM	field emission scanning electron microscopy
FID	flame ionization detection
fsw	fracture initial water saturation
FVF	formation volume factor
GC	gas chromatography
GOF	global objective function
GOR	gas:oil ratio
HC	hydrocarbon
HnP	huff ‘n’ puff
IC	isoalkanes
IFT	interfacial tension
IP	initial production

LB	Lower Bakken
LBS	Lower Bakken Shale
LHS	Latin hypercube sampling
LP	Lodgepole
LR	Liberty Resources Management Company LLC
MAE	mean absolute error
MB	Middle Bakken
MCMC	Markov Chain Monte Carlo
MINC	multiple interacting continua
ML	machine learning
MM	million
MMP	minimum miscibility pressure
MMscf	million standard cubic feet
MMscfd	million standard cubic feet per day
MP(I)R	monthly production (and injection) rates
MW	molecular weight
NC	normal alkanes
NDGS	North Dakota Geological Survey
NDIC	North Dakota Industrial Commission
NETL	National Energy Technology Laboratory
NGL	natural gas liquid
NMR	nuclear magnetic resonance
NN	neural network
NNC	nonneighboring connection
Pa	pascal
PSD	particle-size distribution
PVT	pressure, volume, temperature
RF	random forest
RMSE	root mean square error
RRMSE	relative root mean square error
RTVFC	real-time visualization, forecasting, and control
SRV	stimulated reservoir volume
stb	stock tank barrel
stbd	stock tank barrel per day
STP	standard temperature and pressure
SVM	support vector machine
Sw	water saturation
TDS	total dissolved solids
TF	Three Forks
T_{max}	thermal maturity
TOC	total organic carbon
UB	Upper Bakken
UBS	Upper Bakken Shale
UI	user interface
VIT	vanishing interfacial tension
WHP	wellhead pressure
xf	fracture half-length
XGBoost	extreme gradient boosting

XRD	x-ray diffraction
XRF	x-ray fluorescence

SUBTASK 3.1 – BAKKEN RICH GAS ENHANCED OIL RECOVERY PROJECT

EXECUTIVE SUMMARY

Total in-place oil for the Bakken petroleum system (BPS) (which includes the Bakken and Three Forks Formations) has been estimated to be 600 billion barrels (bbl). However, BPS wells have decline rates as high as 85% over the first 3 years of their lives, and primary recovery factors typically range from 3% to 10% of original oil in place. Given the low initial recovery rates, even small incremental productivity improvements could dramatically increase technically recoverable oil in the BPS. One potential solution is enhanced oil recovery (EOR) using gas injection, such as carbon dioxide (CO_2) or hydrocarbon (HC) gases. While commonly used in conventional reservoirs, CO_2 EOR in unconventional tight oil reservoirs has been limited to pilot tests. EOR using rich gas (mixture of methane, ethane, and propane) has also been employed in numerous pilots in several unconventional plays and has recently been successfully applied in the Eagle Ford play. If successful, large-scale gas-based EOR in the BPS could dramatically increase oil productivity and recovery factors and extend the life of the play for decades.

While CO_2 may be a technically suitable working fluid for EOR in the BPS, supplies are limited and costs for using CO_2 in EOR pilots are prohibitively high. Meanwhile, produced gas flaring has presented challenges for BPS operators in North Dakota. Analysis conducted by the North Dakota Pipeline Authority indicates that the current gas-gathering infrastructure in North Dakota is insufficient to accommodate all of the associated gas that is produced from the BPS. The geographically isolated location of North Dakota relative to large natural gas markets, combined with suppressed natural gas prices, has made it economically challenging for industry to invest capital in expanding gas-gathering infrastructure in the state. These circumstances led to a research program conducted by the Energy & Environmental Research Center (EERC) in partnership with Liberty Resources Management Company LLC (LR) to examine the potential to use rich gas injection for EOR and mitigate flaring.

A rich gas EOR pilot test was designed and executed by LR at its Stomping Horse development area in Williams County, North Dakota. From July 2018 through May 2019, a total of 160 million standard cubic feet (MMscf) of rich produced gas was injected into the BPS using five different wells in a sequential injection strategy. LR's Leon–Gohrick drill spacing unit (DSU) was used as the test site. Regulatory oversight was provided by the North Dakota Industrial Commission (NDIC). Technical support was provided by the EERC through a series of laboratory, modeling, and field-based activities, and additional post-pilot research activities incorporated learnings from the test, developed new laboratory data, improved fracture modeling methods, and developed machine learning and big data analytics.

The results from the Stomping Horse rich gas EOR pilot activities indicate that developing an effective, economical EOR approach for the BPS will require more field tests. Another key lesson learned from the Stomping Horse tests is that detailed pre- and posttest data on reservoir conditions and fluids production are essential. Robust reservoir characterization provides information that is crucial to creating realistic geomodels and conducting valid dynamic simulations of potential EOR scenarios. A detailed understanding of the completions and production history of offset wells is also necessary for valid test result interpretations. This knowledge is essential to designing the operational parameters of injectivity tests and interpreting the results. A conformance control strategy is also essential to success.

Laboratory-based examinations of rich gas interactions with reservoir fluids and rocks were conducted, with an emphasis on determining the ability to mobilize oil in the tight reservoir rocks and shales of the BPS. Injection fluid composition was shown to have a positive impact on reducing reservoir oil minimum miscibility pressure (MMP), reducing interfacial tension (IFT), and altering wettability. IFT and contact angle measurements demonstrated that wettability can be altered in the presence of rich gas, suggesting the potential to improve oil recovery.

Iterative modeling of surface infrastructure and reservoir performance using data generated by the various project activities was conducted. A geologic model of the Stomping Horse area was built; history-matched oil, gas, and water production was used in simulations of various EOR scenarios. Early programmatic modeling results were used to support LR's design and operation of the EOR pilot and to provide insight regarding optimization of future commercial-scale BPS EOR design and operations. Post-pilot modeling focused on alternative methods of understanding complex fracture networks and accelerating simulation time. These led to improved simulation run times and provide excellent history-matching results. Several of these iterative models were used as the bases for developing algorithms into machine learning and big data analytics.

History matching in reservoir simulation is time-consuming and computer processing-intensive. Machine learning algorithms were created, and an automated history-matching tool was developed. A large set of synthetic reservoir simulations were created to generate well responses (oil, gas, and water production, well bottomhole pressure [BHP], and tracer or propane breakthrough) for a set of EOR operating parameters that included offset well status (open or closed), injectate (rich gas or propane), injection rate, and injection well BHP. A user interface was developed to provide real-time visualization. Machine learning-based models were developed to provide rapid forecasting of well performance given a set of user-defined EOR operating parameters. These predictive models allow the user to modify the offset well status, injection rate, and injection well BHP and rapidly forecast future production performance. The combination of real-time visualization tools with real-time forecasting tools provides a framework for real-time control—operational changes that the EOR site operator can enact (e.g., changing gas injection rates) to affect the observed performance and potentially improve the EOR outcome.

There is great reason to be optimistic about the future of EOR in the Bakken. The results of the laboratory studies suggest significant potential for high rates of oil mobilization using produced field gas injection under the right conditions. The results of the lab studies, combined with rigorous statistical analysis of well production data and associated modeling efforts, confirm the notion that fluid mobility within the reservoir is controlled by fractures. As more knowledge is gained about the nature and distribution of fracture networks in the Bakken, the industry will be in a better position to predict and, ultimately, influence fluid mobility. New field tests are necessary to develop a more complete understanding of those conditions. Thoughtful and creatively engineered field tests within a well-characterized geologic setting will yield the fundamental knowledge needed to take Bakken oil production to the next level.

This subtask was cofunded through the EERC–U.S. Department of Energy Joint Program on Research and Development for Fossil Energy-Related Resources Cooperative Agreement No. DE-FE0024233. Nonfederal funding was provided by the North Dakota Industrial Commission's Oil and Gas Research Program and Computer Modelling Group.

SUBTASK 3.1 – BAKKEN RICH GAS EOR RESEARCH EFFORTS: OVERALL OBSERVATIONS AND CONCLUSIONS

OBSERVATIONS

The laboratory, modeling, and field-based activities conducted by the Energy & Environmental Research Center (EERC) over the course of Subtask 3.1 yielded valuable insight regarding the potential for using rich gas injection as a means of enhanced oil recovery (EOR) in the Bakken petroleum system (BPS). Key observations from the project include the following:

- Minimum miscibility pressure (MMP) was not achieved in the reservoir during the pilot test. Achieving MMP in a reservoir at an advanced state of depletion requires considerable quantities of injection gas or, perhaps, the use of water injection as a means of pressurization prior to gas injection.

- Reservoir surveillance and monitoring data demonstrate the injected gas can be controlled and contained within the DSU (drill spacing unit).

- Injection fluid composition has a large impact on reservoir oil MMP, and enriching produced gas with additional ethane and/or propane before injection will favorably alter reservoir response. The lower MMP achievable with enriched gas would also allow for using less injection gas for initial repressuring of the reservoir and continuation of injection operations at lower pressure.

- Injection of rich gas (ca. 70/20/10 methane/ethane/propane) produced from the BPS can achieve MMP at pressures that are similar to the pressures required by CO_2, approximately 2420 psi. Methane requires very high pressures to achieve MMP: 4200 psi. Ethane requires approximately 1350 psi to reach MMP and propane about 550 psi to achieve MMP.

- Adding NGLs (natural gas liquids) like ethane and propane to produced gas is an efficient way to lower MMP if excess NGLs are available.

- At pressures above MMP, phase partitioning occurs between the thousands of complex HC (hydrocarbon) components in crude oil and the injected gas. The HC composition of both the injectant-dominated phase and the bulk crude oil phase continually changes with pressure and temperature. The oil-rich phase has higher molecular weights, viscosities, and densities (lower API [American Petroleum Institute] gravities) after exposure to all tested injection fluids, but propane shows the least negative changes, since it vaporizes the broadest spectrum of liquid HC components.

- Results of HC extraction experiments from core specimens are consistent with the miscible-phase sampling experiments, as would be expected based on the concentration gradient/diffusion extraction mechanism that appears to be a major factor controlling rock extractions.

- At 5000 psi, produced gas does nearly as well as propane at extracting the bulk of HCs from core samples. However, even at 5000 psi, methane can only slowly extract heavier HCs.

- The traditional fracture system model used for simulation can replicate the depletion and evaluate the EOR mechanisms using a small-scale model, but it encounters numerical challenges in the gas injection simulation at larger scale and has difficulties handling strong interference effects between wells.

CONCLUSIONS

The results and lessons learned from the Stomping Horse rich gas EOR pilot activities indicate that developing an effective, economical EOR approach for the Bakken will require more field tests. Robust reservoir characterization and understanding of the behavior of the injected fluid in the reservoir are necessary to create realistic geomodels and conduct valid dynamic simulations of potential EOR scenarios. This knowledge is essential to designing the operational parameters of injectivity tests and interpreting the results.

There is great reason to be optimistic about the future of EOR in tight oil formations such as the Bakken. The results of EERC laboratory studies suggest significant potential for high rates of oil mobilization using both CO_2 and produced field gas injection under the right conditions. The results of the lab studies, combined with rigorous statistical analysis of well production data and associated modeling efforts, confirm the notion that fluid mobility within the reservoir is controlled by fractures. As more knowledge is gained about the nature and distribution of fracture networks in the Bakken, the industry will be in a better position to predict and, ultimately, influence fluid mobility. New field tests are necessary to develop a more complete understanding of those conditions. Improvements in modeling software specifically designed to address challenges inherent in unconventional tight reservoirs, combined with the application of machine learning and artificial intelligence to reservoir surveillance data processing and interpretation, will streamline the design and execution of future EOR pilots. Thoughtful and creatively engineered field tests within a well-characterized geologic setting will yield the fundamental knowledge needed to take Bakken oil production to the next level.

ACKNOWLEDGMENTS

The authors acknowledge the tremendous personal commitments and contributions to this work made by Mark Pearson, Gordon Pospisil, Duane Fadness, Ken Tompkins, Paul Weddle, Jeremy McChesney, and Stacy Strickland of Liberty Resources, as well as Bryan Bugg and Tammy Kaier formerly of Liberty Resources. The authors also acknowledge and thank Jared Ciferno, Gary Covatch, and Olayinka Ogunsola of the U.S. Department of Energy (DOE) for their support of this program. The modeling work conducted under this program was made possible by contributions of software licenses from Computer Modelling Group (CMG) and Schlumberger Oilfield Services.

BACKGROUND

DOE has taken a leading role in developing programs aimed at advancing energy options to fuel the American economy, strengthen security, and improve the environment. With respect to oil and gas, enhanced resource production and environmentally prudent development of resources are priorities for the National Energy Technology Laboratory's (NETL's) Natural Gas and Oil Program. To support NETL in its goals, the EERC is currently conducting a project as part of the EERC–DOE Joint Cooperative Agreement Subtask 3.1 entitled "Bakken Rich Gas Enhanced Oil Recovery Project." The overall goal of the project is to determine the feasibility of reinjecting captured rich gas into a Bakken reservoir for EOR. Laboratory, modeling, and field-based activities conducted by the EERC since July 2017 have focused on supporting a pilot-scale rich gas EOR field test being conducted by Liberty Resources Management Company (LR) at the Stomping Horse complex in western North Dakota. Early observations from the site-specific work, combined with the results of recently completed DOE-funded efforts at the EERC to examine the use of CO_2 for EOR in the Bakken, have led to a recognition that broad application of rich gas for EOR throughout the Bakken play will require data beyond what can be generated by the current activities at Stomping Horse.

To expand the applicability of the results of Subtask 3.1, the EERC added additional activities to address three technical areas. The additional efforts will support the goal of developing cost-effective EOR schemes that can be deployed across the Bakken and other tight oil plays. The additional activities will 1) improve understanding of wettability, relative permeability, and fracture network distribution across the Bakken in support of EOR optimization; 2) use advanced reservoir models to evaluate alternative injection strategies to minimize early breakthrough and develop optimized EOR strategies at scales beyond the Stomping Horse pilot test; and 3) use science-informed machine learning (ML) and big data analytics (BDA) to perform iterative modeling of surface and subsurface EOR components to streamline pilot performance assessments. This work has resulted in knowledge that is being applied in the near-term within the Bakken play. At the time of reporting, the scientific understanding gained from these research activities is supporting pilot-scale deployment of rich gas EOR in the Bakken.

ACTIVITY 2.0 – RICH GAS INTERACTIONS WITH RESERVOIR FLUID AND ROCKS

INTRODUCTION

Laboratory-based examinations of rich gas interactions with reservoir fluids and tight rocks (including oil-rich shales) have been conducted. These studies focused on determining 1) the MMP of Bakken petroleum system crude oil with different candidate gas injectant mixtures, 2) the HC composition in the "miscible" phase generated by crude oil/injectant exposures, and 3) the mixed fluids' ability to recover oil from rock samples collected from tight reservoir rocks of the BPS (Three Forks Formation and the Middle Member of the Bakken Formation) and the Upper and Lower Bakken Shales. All experiments were performed at relevant reservoir temperatures and pressures. The following provides a summary of Activity 2.0.

Subactivity 2.1 – Rich Gas–Oil Fluid Behavior and Rock Extraction Studies

MMP Studies

Selection of injection fluids and required pressures for EOR will depend both on their relative abilities to mobilize crude oil as well as their availability and costs. A fundamental parameter used to select and compare potential injectant fluids and operational pressures required for EOR is their MMP, which is the pressure required for significant mobilization of reservoir crude oil by the injected fluid. Therefore, to support LR's design of an EOR scheme, the EERC conducted work to present a "baseline" of laboratory data to aid in the initial design of the Stomping Horse Field project by measuring the MMPs obtained with individual pure component HCs (methane, ethane, and propane), and mixtures of those HC gases that commonly occur in Bakken produced gas (i.e., rich gas) for crude oils from the BPS. Data generated from previous EERC studies on MMPs for CO_2 in Bakken crude oil are presented for comparison purposes. MMPs were determined using a capillary-rise vanishing interfacial tension (VIT) method originally developed by Rao and Lee (2003), modified as described in detail (Hawthorne and others, 2016; Hawthorne and Miller, 2018), and validated by comparison to the traditional slim-tube technique (Hawthorne and others, 2016; Rao and Lee, 2003; Ayirala and Rao, 2011; Ghorbani and others, 2014; Ahmad and others, 2016; Thomas and others, 1994).

To broaden the applicability of the study, two produced crude oil samples were collected from test separators in a developed area of the Bakken in North Dakota: one from a non-LR-operated well producing from the Middle Bakken Formation and one from a LR well producing from the Three Forks Formation in the Stomping Horse complex. All samples were refrigerated, shipped, and stored in sealed glass vessels until use. Crude oil viscosities and densities are given in Table 1.

Table 1. Reservoir Temperatures and Crude Oil Densities and Viscosities

Crude Oil	Reservoir Temp., °C	Viscosity, µPa·s	Density, g/mL	API, Gravity
Middle Bakken	110	2220	0.817	41.7
Three Forks	127	2040	0.824	40.2

Similar data sets were obtained for both crude oils, with five injection test fluids, methane, ethane, propane, a representative produced gas mixture, and CO_2. The MMPs determined with duplicate experiments for each test fluid with each crude oil are shown in Figure 1. MMP values varied dramatically with the different pure fluids for both oil samples. As expected, for both oils, methane has much higher MMP, about 30 MPa (4350 psi). The pressure required to achieve MMP with CO_2 was about 17 MPa (2470 psi). Ethane required about 9.3 MPa (1350 psi), and propane's MMP was even lower, approximately 3.8 MPa (550 psi) (Figure 1). Produced gas yielded intermediate results, about 17 MPa (2470 psi), similar to CO_2.

Although the MMP data presented show that the rich gas produced from the Bakken is potentially useful for EOR, the excess of produced NGLs in North Dakota suggests that enriching produced gas with additional ethane and/or propane could be a practical way to lower MMPs and further enhance oil recoveries at lower pressures. Therefore, the EERC determined the effect of adding additional ethane and propane to produced gas on MMP values. MMP values were obtained with the initial HC mixtures, then ethane (or propane) was added to the mixing chamber and mixed overnight before the MMP with the enriched fluid was measured. This process was continued until propane was added to 25 mol% and ethane added to 68 mol%.

The results of added ethane and propane on MMPs are shown in Figure 2. MMPs with added propane decreased from 17.9 MPa (2600 psi) (with the original 70.7/22.6/6.7 mole ratio mix) to 12.7 MPa (1840 psi) when the propane was increased to 25 mol%. Adding ethane was also effective in lowering MMP, with the MMP decreasing from 18.6 MPa (2700 psi) (with the original 76/13.5/10.5 mole ratio mix) to 12.7 MPa (1840 psi) as the ethane concentration was increased to 68 mol%. Figure 2 also shows the MMPs that might be expected if only a linear combination of the MMP values for the pure methane, ethane, and propane were considered (i.e., multiplying the MMP for each pure fluid times its mole fraction and summing those values). For example, estimating the MMP of the initial 70.7/22.6/6.7 HC mixture based only on the pure fluid MMPs and their mole ratios would yield an MMP of 24.4 MPa (3540 psi), a value about double the experimental MMP for the same mixture. Similar results were found for all of the mixtures enriched with added ethane or propane (Figure 2), showing that enriching produced gas is more effective at lowering MMPs than might be expected based on only the pure fluids' MMP values and that estimates of produced or mixed gas MMPs based on pure component calculations may be too pessimistic.

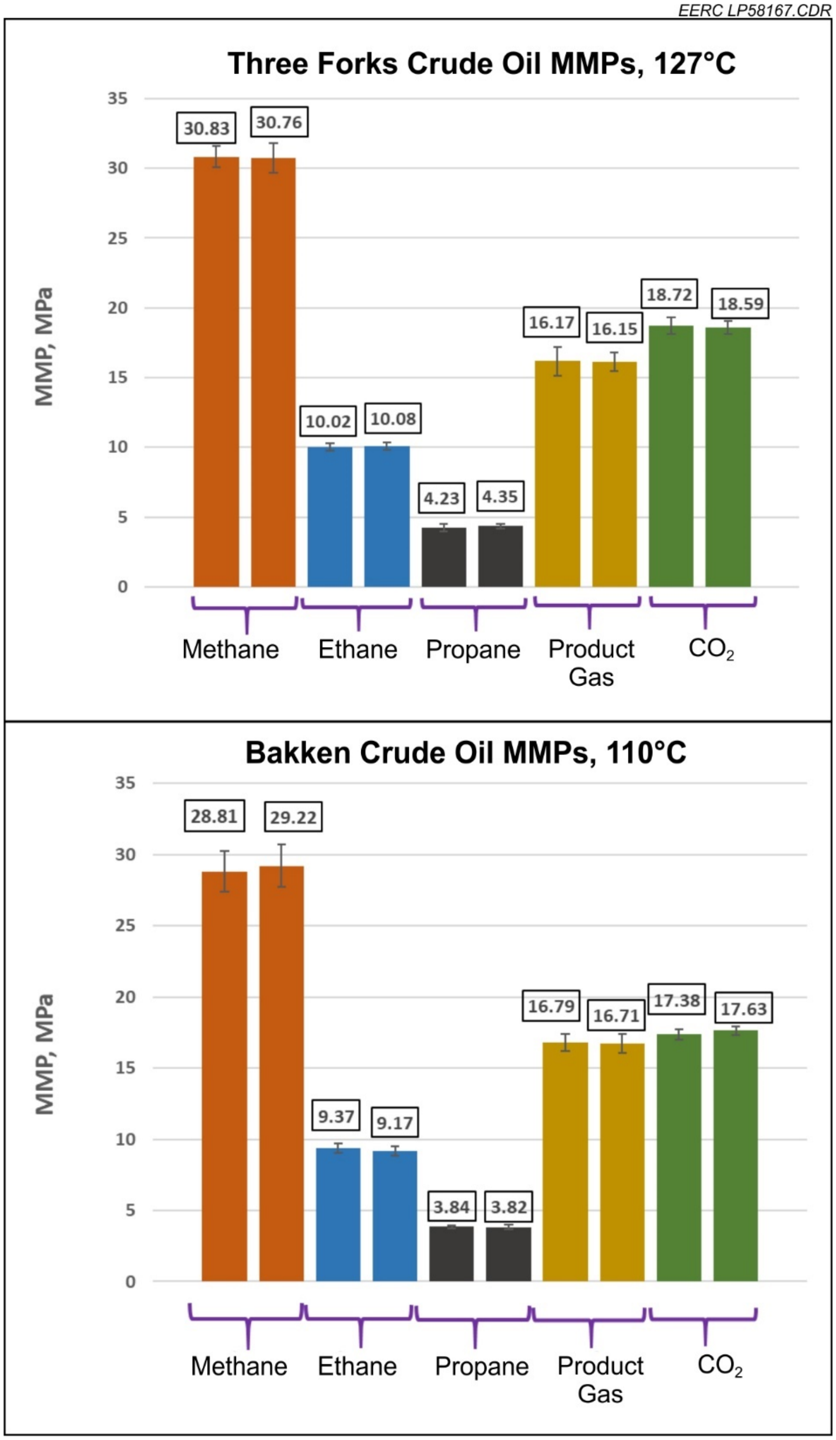

Figure 1. Experimental MMP values for crude oils from Bakken and Three Forks petroleum reservoirs. The MMPs with each injection fluid for each oil were determined with duplicate experiments using the capillary-rise VIT technique. Error bars are based on the standard deviation in MMP values from the three different-sized capillaries used to perform each experiment. Produced gas molar ratios for methane/ethane/propane were 69.5/21/9.5.

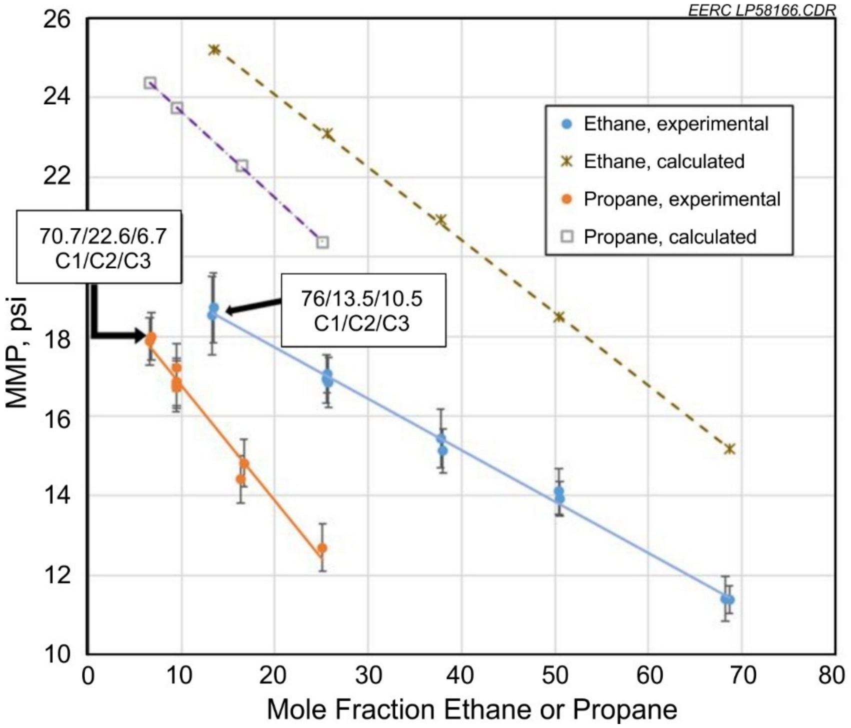

Figure 2. Effect of adding ethane or propane to produced gas on MMP values for Bakken crude oil at 110°C. The initial methane/ethane/propane molar fractions for the propane additions (orange) and ethane additions (blue) are shown in the figure.

In summary the results of the MMP determinations for Bakken and Three Forks crude oils yield several key observations that can be applied to the design and operation of an EOR project:

- Rich gas mixtures (ca. 70/20/10 methane/ethane/propane) produced from the BPS can achieve MMP at pressures similar to the pressures required by CO_2.
- Methane requires very high pressures, 2 to 3 times those required by CO_2 or produced gas, to achieve MMP.
- Both ethane and propane are superior to CO_2 (and produced gas), with ethane requiring about one-half of the pressure and propane about one-sixth of the pressure needed by CO_2 to achieve MMP.
- Adding NGLs like ethane and propane to produced gas is an efficient way to lower MMP if excess NGLs are available.

Miscible-Phase Compositional Studies

In addition to the measurement of MMP for several EOR fluids, additional experiments were performed to measure the variation of HC concentration in the different injection gases at different pressures. This information provides insight into the effects of pressure on mobilizing different molecular weight species of HCs within the target reservoir. More detail can be found in Hawthorne and Miller (2019). The experiments were performed because conventional VIT experiments to measure MMP showed the continued existence of two fluid phases in the cell, even at pressure considerably above MMP. The upper, gas-dominated phase contained mostly injection fluid plus dissolved HCs, while the lower, liquid-dominated phase contained mostly bulk crude oil plus dissolved injection gas. The VIT test cell was modified to be able to draw samples of fluid from the gas-dominated phase within the cell that could then be analyzed using gas chromatography/flame ionization detection (GC/FID) methods (Figure 3).

Figure 3. Test cell (left image) and cell with two fluid phases present (right image). The gas is percolated through a 10-mL (8-gram) oil column and equilibrated at reservoir temperature (23°F) and pressure (1500–5000 psi). The upper "miscible" phase is sampled while maintaining reservoir temperature and pressure. Dissolved HCs are collected and analyzed by GC/FID**.**

The experimental results show considerable variation in the ability of different injection gases to vaporize different amounts of oil components and, significantly, that all the tested injection gases continue to vaporize more and more HCs as pressure continues to increase above MMP. This is illustrated by the three plots shown in Figure 4. Each plot shows the same experiments but performed at different constant pressure conditions: 1500, 3000, and 5000 psi. All tests were performed at 230°F. The HC concentration, in mg/mL, is shown on the y-axis, while the x-axis shows the sequential samplings of the gas-dominated phase. Propane is effective at all pressures, ethane requires higher pressures, and methane is the least effective at all pressures. Produced gas is moderately effective at 5000 psi but not at lower pressures. Methane, ethane, and propane mass (g/mL) and molar (moles/L) densities correlate with their general abilities

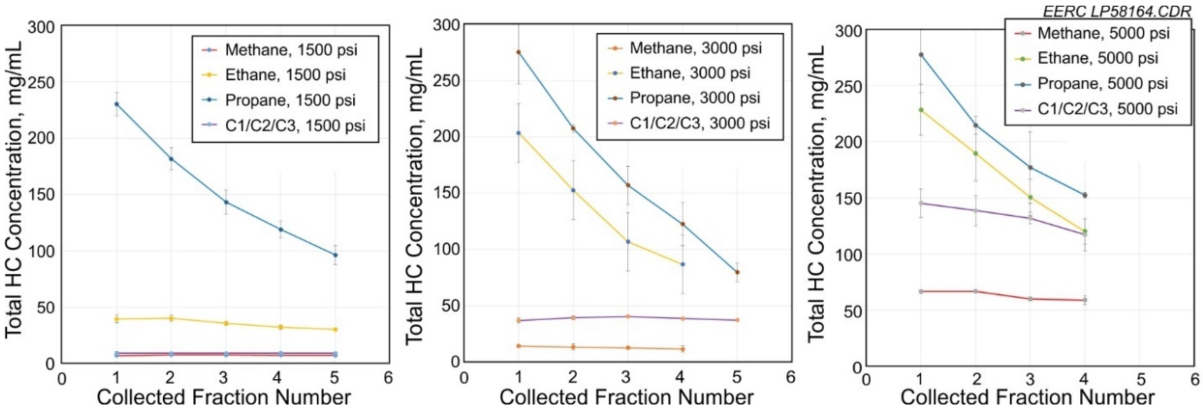

Figure 4. 10 mL of crude oil equilibrated with 10 mL of injected C1, C2, C3, or produced gas in headspace at reservoir conditions before taking five sequential aliquots at 1-hour intervals. The error bars represent the standard deviation in HC concentrations for triplicate experiments at each condition.

to mobilize crude oil HCs into the gas-dominated phase. Higher pressure does not affect propane's capability nearly as much as methane and ethane since propane's density does not change much above 1000 psi. Figure 5 compares the performance of methane and produced gas at different pressures. At 1500 psi, both methane and produced gas are poor with respect to vaporizing HC components; 1500 psi is below the MMP for both gases. At 3000 psi, produced gas is somewhat better than pure methane since the MMP for produced gas is below 3000 psi. At 5000 psi, both improve their vaporization performance, but both remain less effective than either ethane or propane.

Properties of the residual liquid or oil-dominated phase were also measured. All fluid exposures favor the mobilization and removal of lower-molecular-weight (MW) HCs and leave HC residues with higher MW, viscosity, and density. Propane is the best for dissolving higher-MW HCs and leaves behind the least viscous and lightest-residue oil. Methane and 70/20/10 (C1/C2/C3) do not dissolve enough HCs to significantly change the residue crude, except at 5000 psi.

The results of miscible-phase sampling experiments yield valuable insight regarding the effects of the key EOR operational parameters of injected gas composition and pressure on mobilizing different HC species. Potentially useful observations include:

- All injection fluids prefer vaporized lower-MW HCs, regardless of whether pressures are below or above MMP. Propane does the best with higher-MW HCs; ethane is next best followed by CO_2. Methane can only mobilize the lightest HCs, except at very high pressures.

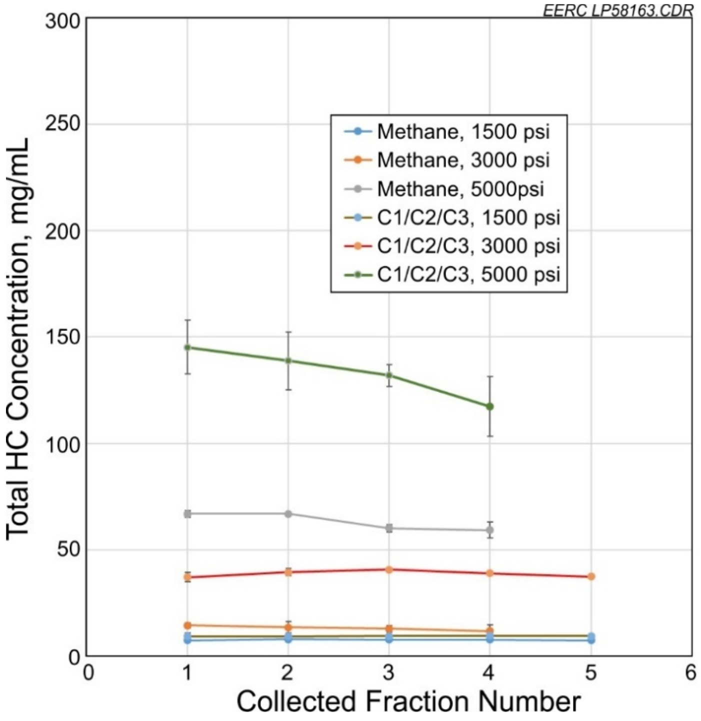

Figure 5. Concentration of vaporized HCs in methane-rich injection phase versus produced gas-dominated injection phase. Produced gas does not become more effective until pressure exceeds 1500 psi.

- Phase partitioning occurs between thousands of HC components and the injected gas. The HC composition of both the injectant-dominated phase and bulk crude oil phase is continually changing with pressure and temperature.

- Residual oils have higher MWs, viscosities, and densities (lower API gravities) after exposure to all fluids, but propane shows the least negative changes.

Rock Extraction Experiments

HC extraction experiments using a series of rich gas EOR fluids were performed using a set of Middle Bakken and Bakken Lower Shale core samples. Core was obtained from the North Dakota Geological Survey (NDGS) Wilson M. Laird Core and Sample Library on the campus of the University of North Dakota (Grand Forks, North Dakota), where the cores had been stored at room temperature since collection. Rods were drilled from the original collected 10.2-cm (4-in.) cores with a 12.7-mm (½-in.) core bit yielding rods with a measurement of 11.2-mm diameter and 4−5-cm length. The selected core well location was approximately 20 miles south of and in a similar structural position as the LR pilot test site. It is important to note that the rock core samples were used as-received and that there was no pretreatment (other than drilling the core rods). Thus all oil HCs recovered from the rock samples were "native" (not added) HCs that were present in the rock samples when they were collected from the reservoir. Figure 6 shows an example

Figure 6. Example core specimen (left) and core holder (right).

of the test specimens. Samples were placed in a test vessel, also shown in Figure 6, where the EOR test fluids were introduced around the sample at elevated temperature and pressure. It is important to note that the core samples were bathed or soaked in the EOR fluid and were not subjected to differential pressure displacement or flow-through testing. Recovered HCs were collected periodically and analyzed by GC/FID (kerogen not determined); 100% HC recovery was based on final-crushing the sample and solvent extracted after EOR fluid exposure. The experimental methodology is discussed in more detail in Hawthorne and others (2019). Exposures were performed at pressures of 1500–5000 psi and 230°F. EOR fluids used for the tests were methane, ethane, propane, and a 70/20/10 molar ratio mixture of C1/C2/C3 to represent produced gas.

Results from the experiments are shown in Figure 7. Each of the plots within the figure represents a different injection gas. Each plot contains three experiments using Middle Bakken samples and three experiments using Lower Bakken Shale samples. Ethane and propane are more effective solvents, particularly for the Middle Bakken samples. Results are more mixed for the methane and produced gas experiments. Higher pressure, 5000 psi, is needed for both methane and produced gas to approach 100% extraction of in situ HCs.

As with the miscible-phase studies, the results of the Bakken HC extraction experiments yield information regarding the effects of injected gas composition and pressure on the mobilization of oil. Key observations include the following:

- The HC gas mixture that is representative of the wellhead rich gas stream produced from wells in the Stomping Horse complex was found to be effective at mobilizing oil from Middle Bakken and Bakken Shale rock samples.

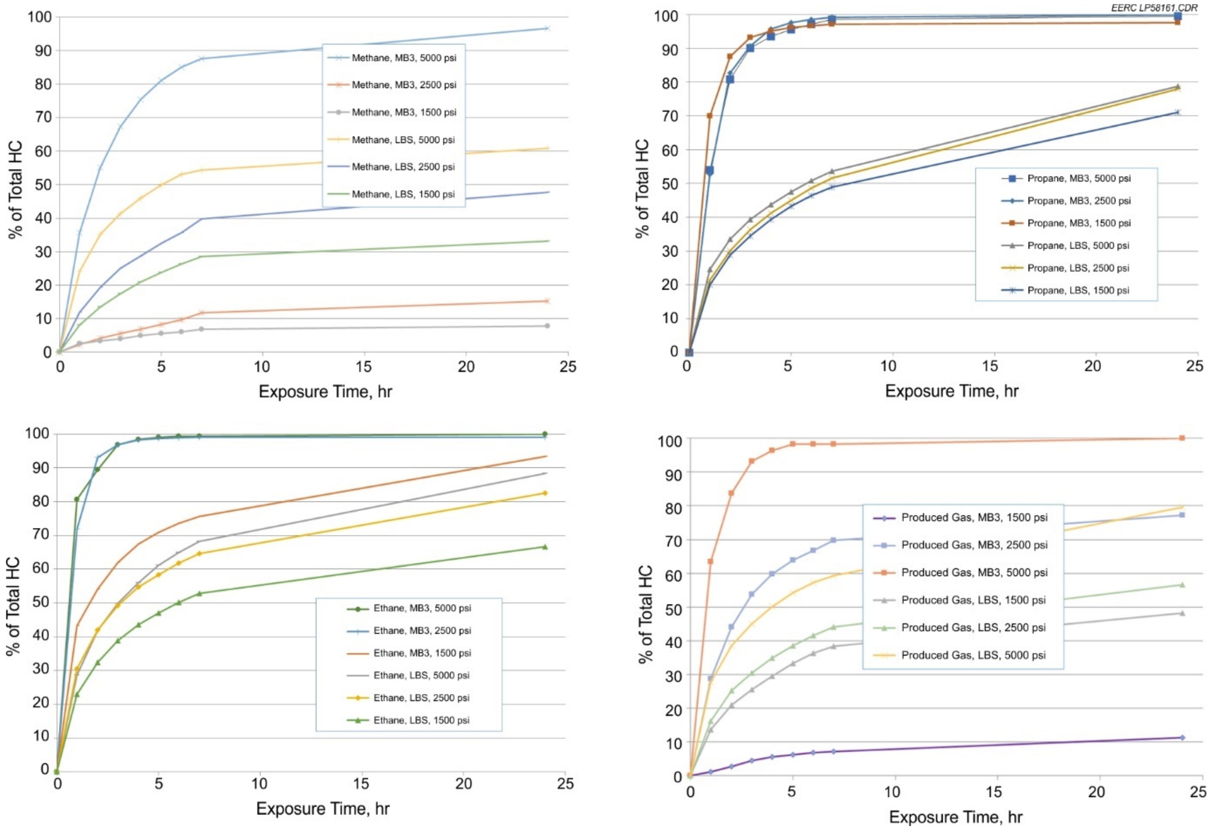

Figure 7. Recoveries with methane and produced gas are highly dependent on pressure; ethane is moderately controlled by pressure; and pressure has little effect on propane.

- Results are consistent with miscible-phase sampling experiments, as would be expected based on the concentration gradient/diffusion extraction mechanism that appears to be a major factor controlling the rock extractions.

- At 5000 psi, produced gas does nearly as well as propane at extracting the bulk of the oil HCs.

- Even at 5000 psi, methane can only slowly extract heavier HCs.

Subactivity 2.2 – Rich Gas in Shale Permeability and Sorption Studies

Background

The Bakken Formation is an unconventional tight oil formation that holds hundreds of billions of barrels of oil (Nordeng and Helms, 2010). However, the extremely low permeability limits primary recovery to around 10% or less. Tight oil formations like the Bakken are attractive candidates for EOR as they present a significant opportunity for additional oil recovery. Previous laboratory-based rock extraction experiments by the EERC indicate that carbon dioxide, ethane, and methane/ethane mixtures can mobilize oil from Bakken shales (Jin and others, 2016;

Hawthorne and others, 2017). Other experiments suggest that Bakken shales are capable of sorbing CO_2 (Psarras and others, 2017; Weniger and others, 2010; Hu, 2014).

Based on these earlier studies, it was hypothesized that during a rich gas EOR pilot where the gas could contact organic-rich shale there could be preferential sorption of one gas species over another. Preferential sorption would imply that the composition of gas produced during an EOR operation may change and affect both surface operations and reservoir performance.

To address these issues, a flow-through experiment was designed to evaluate the potential migration and/or sorption of mixed gas blends in the Bakken Shales. A rich gas flow-through apparatus was built based on previous experience with multiphase permeability experiments involving brine, sCO_2 (supercritical CO_2), and oil.

Two samples of Upper Bakken Shale from different wells were used in the rich gas flow-through experiments. Each test began by measuring the breakthrough of methane, ethane, and propane followed by a pressure drawdown to observe desorption. During testing, gas samples were collected and analyzed using GC. The composition of the gas blend was measured before and after exposure to the shale samples to evaluate preferential sorption of specific hydrocarbon gas species. Most of the analytic work focused on the characterization of the samples pre- and postexperiment at micrometer to nanometer scales.

Sample Selection

Two samples were selected for testing. One sample (126950) was from North Dakota Industrial Commission (NDIC) well 24123, and one sample (118939) was from NDIC well 29097. The EERC assigns unique sample numbers as part of the EERC's laboratory sample management system. Those numbers are used as identifiers for the two shale samples in this report. The respective well locations from which the core samples were collected are shown in Figure 8, which also shows the estimated thermal maturity (T_{max}). There is an approximate 30-mile well separation, and the T_{max} of 118939 is higher than that of 126950, while the estimated total organic content (TOC) of 126950 appears to be higher than 118939. However, as shale formations are highly heterogeneous, the TOC present in individual samples can fluctuate significantly, even in very close proximity. Sample properties are listed in Table 2.

EERC CB58080.CDR

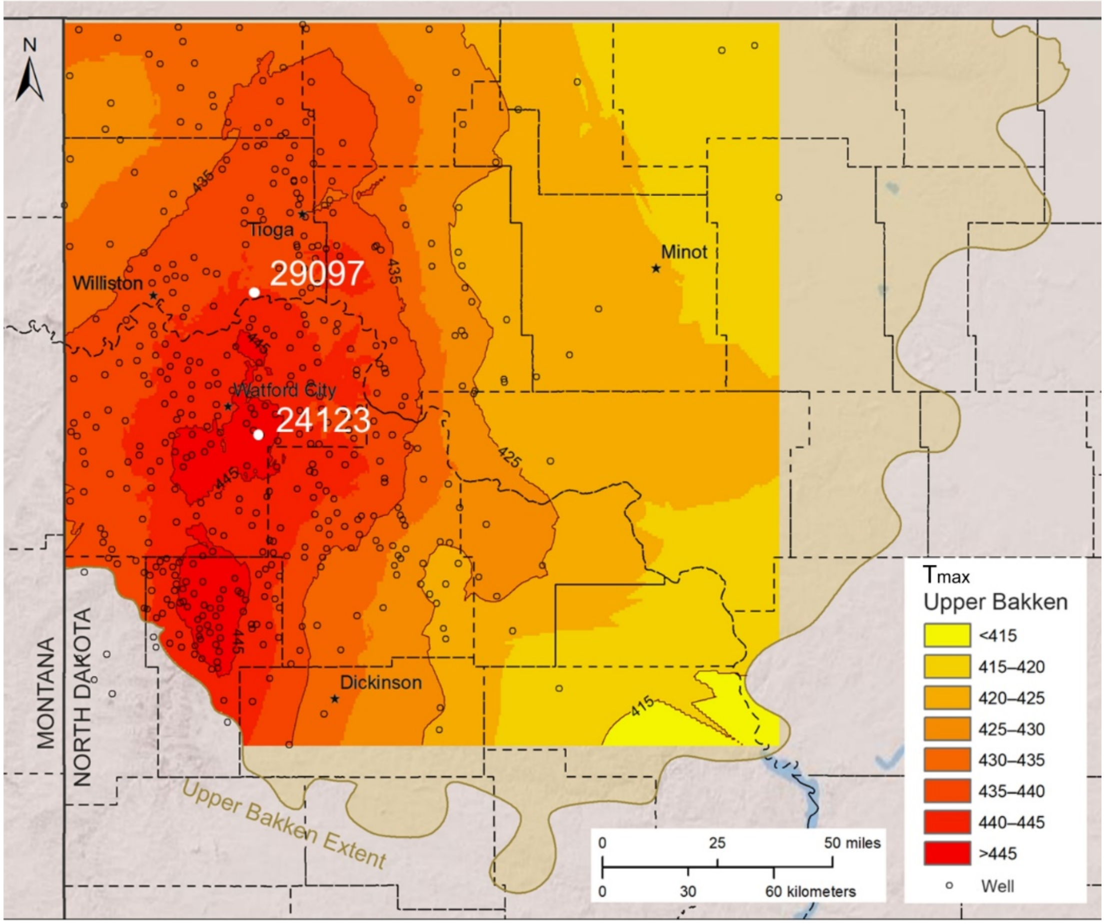

Figure 8. NDGS core analysis map of T_{max} for Upper Bakken Shale (2020).

Table 2. Sample Dimensions and Properties Determined by Helium Porosimeter and NMR[a]

Sample:		**118939**	**126950**
NDIC Well Number		24123	29097
Depth, ft		11,056.9	10,798
Lithofacies		Upper Bakken Shale	Upper Bakken Shale
Diameter, cm		3.02	2.39
Length, cm		3.77	2.88
Mass, g		59.9	29.1
Bulk Volume, mL		26.9	12.4
Bulk Density, g/mL		2.23	2.25
Grain Density, g/mL		2.41	2.33
Pore Volume, mL		2.01	0.448
Stressed Permeability, µD:	2400 psi	0.296	102.6
	4800 psi	0.117	38.59
	7200 psi	0.0543	18.90
Porosity Helium (unconfined), vol%		7.47	3.46
Stressed Porosity, vol%:	2400 psi	4.64	0.41
	4800 psi	3.83	0.24
	7200 psi	0.98	0.11
Porosity NMR, vol%		2.56 (pre)	1.50 (pre) 1.69 (post)
Total Organic Carbon, %mass		10.51	13.0–16.0[b]
Hydrogen Index, mg/g TOC		137.6	100–200[b]
T_{max}, °C		455	440–445[b]

[a] Nuclear magnetic resonance.

[b] Indicates data from NDGS (2020).

Test Methods

MicroCT

MicroCT uses a series of x-ray images to reconstruct the 3D distribution of mass in a sample. The GE v|tome|x s MicroCT 240-kV microfocus x-ray CT (computed tomography) system was used to scan samples both before testing and after rich gas flow-through experiments. Prior to testing, samples were screened for sample integrity to eliminate samples with large inclusions, such as shell fossils, voids, or large fractures, that would negatively impact flow-through testing. The resulting 3D images have a voxel size around 35 µm and a 16-bit gray-scale format. MicroCT volume data were aligned and comparisons made before and after flow-through testing to identify structural changes in the sample.

Nuclear Magnetic Resonance

NMR is a method in which nuclei in a strong constant magnetic field are perturbed by a weak oscillating magnetic field and respond by producing an electromagnetic signal with a frequency characteristic of the magnetic field at the nucleus. This signal can then be processed in such a way to allow for the determination of pore-size distributions, effective porosity, and fluid typing (i.e., water vs. hydrocarbon) within a rock sample. An Oxford Geospec2 Core NMR was used to determine pore-size distributions and effective porosity of the two Bakken shale samples and to perform 2D T1–T2 mapping (fluid typing). Samples were submitted for NMR before and after rich gas flow-through experiments to identify changes in pore saturations and hydrocarbon mobilization. Unfortunately, the NMR instrument used for this project suffered a data acquisition system failure in the latter stages of the study which required service. The instrument was unavailable for the final posttest analysis; therefore, no data exist for 118939 posttest.

Unstressed Porosity Measurements

A modified MetaRock PDP-300 gas porosimeter was used to measure grain volume of each core plug. The grain volume (V_G) of a sample was determined by applying Boyle's gas law equations as referenced in API RP 40 (American Petroleum Institute, 1998). Sample preparation involved machining of the inlet and outlet face to be perpendicular to the plug axis, and bulk volume (V_B) was determined using a micrometer. Porosity (fraction) was calculated as $\emptyset = \frac{V_B - V_G}{V_B}$. Low-porosity, low-permeability samples such as Bakken Shale are challenging and require that the vacuum and fill steps in the porosimeter are of significantly longer duration than those required for conventional samples.

FESEM

Electron microscopy works by impacting a surface with a beam of electrons. The resulting interaction provides spatial and composition information in the form of images and spectra for element analysis. The Hitachi SU5000 field emission scanning electron microscope (FESEM) has a large magnification range and nanometer resolution and allows for variable-pressure operation. Point and area elemental composition was measured with the included Bruker Quantax energy-dispersive spectroscopy (EDS) system. Samples were submitted for FESEM imaging before and after flow-through experiments with rich gas to identify structural and chemical changes to the sample.

Gas Chromatography

GC involves separation of sample constituents with a column followed by their measurement on one or more detectors. The EERC operates a Hewlett-Packard GC refinery gas-analyzing system (HP-5972) employing three capillary columns and five packed columns and operates with three detectors (two thermal conductivity and one flame ionization). This instrument requires at least 50 mL of sample gas at standard temperature and pressure (STP). The limit of detection for methane, ethane, and propane is on the order of 10–20 ppm. Repeated tests on samples of certified gas mixtures resulted in deviations below ±5%. GC was used to monitor changes in gas composition during testing. Injection and production gas compositions were compared to identify preferential sorption of gas species.

Pulse Decay Permeameter

A pulse decay permeameter provides measurement of permeability by monitoring the pressure response of the sample to a pulse of gas passed through the sample. This method provides accurate measurement of porosity and permeability in the 0.1 millidarcy to 1 nanodarcy ranges. Tests were operated using nitrogen gas at ambient temperature over a range of pore pressures and confining pressures to evaluate the stress sensitivity of the samples. As confining pressures are increased, fractures and pores are squeezed closed.

Rich Gas Flow-Through Test

The rich gas flow-through apparatus shown in Figure 9 was constructed to allow for the measurement of injected and produced gas samples during flow-through testing. Comparing the injected and produced gas concentrations allows for observations of gas sorption and sorption, which contribute to preferential gas storage and flow-through shale reservoirs.

The injection pump supplies water to the gas transfer vessel to pressurize the 70% methane, 20% ethane, and 10% propane mixture for core injection. After the system was filled with rich gas, the system was heated to 230°F (110°C) and pressurized to 5000 psi (345 bar). Initially, the injection side of the system was pressurized with rich gas, and the production side and sample were pressurized with argon up to the core injection valve (V3). Injection and production samples were collected for GC analysis before the start of the test to serve as a baseline.

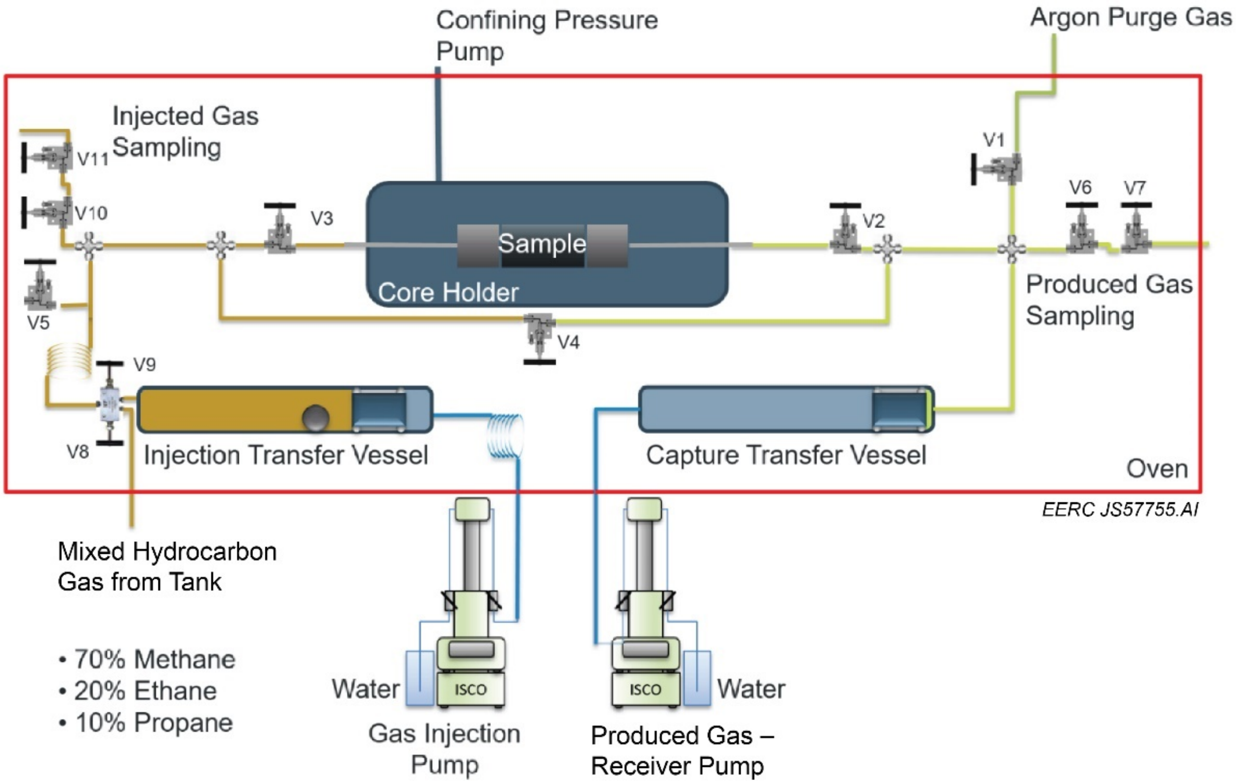

Figure 9. Apparatus designed for rich gas flow-through tests.

The sorption test was started by setting the injection flow rate to 0.0016 mL/min and opening V3. The production gas pump was set to maintain a constant system back pressure. Production gas was sampled at approximately 2- to 4-hour increments as gas was produced out of the sample. The back-end volume was maintained at approximately 4 mL after each sampling event. Sampling continued until the produced gas composition matched the injected gas composition. At this point, the flow was assumed to be steady state. When testing was completed, the injection flow rate was stopped, and V3 was closed.

The desorption test was started after the adsorption test was completed. The purpose of this test was to help determine if the sample was adsorbing gas or if it was being restricted by a physical flow mechanism. If the sample were preferentially adsorbing a specific type of gas, then that gas should be released in larger concentrations as the sample was depressurized with V3 closed and the production valve open (V2). This depressurization was accomplished by taking gas samples from the production side of the core every 1 to 2 hours through the production gas-sampling valves. The gas samples are analyzed using GC to determine the compositional changes throughout the depressurization process.

Results

MicroCT

MicroCT data for each sample before and after flow-through testing were processed and compared to each other. The voxel size is approximately 35 µm for each scan. At this level of detail, both samples show a laminated fine grain matrix containing fractures (red arrows) along bedding planes and similar fossil and pyrite content. After flow-through tests, most fractures in both samples "healed," which experience shows results from applying confining pressure at temperature and pressure. One exception to this is the appearance of a fracture perpendicular to the plug axis for Sample 118939 posttest (yellow arrow) (Figure 10). This fracture may have occurred during the test or was the result of damage during posttest handling. It is not expected to be significant.

Sample 126950 appears to be more heavily fractured than 118939 before flow-through experiments. After the flow-through experiment, most fractures disappear, meaning that they are smaller than 35 µm (Figures 10 and 11).

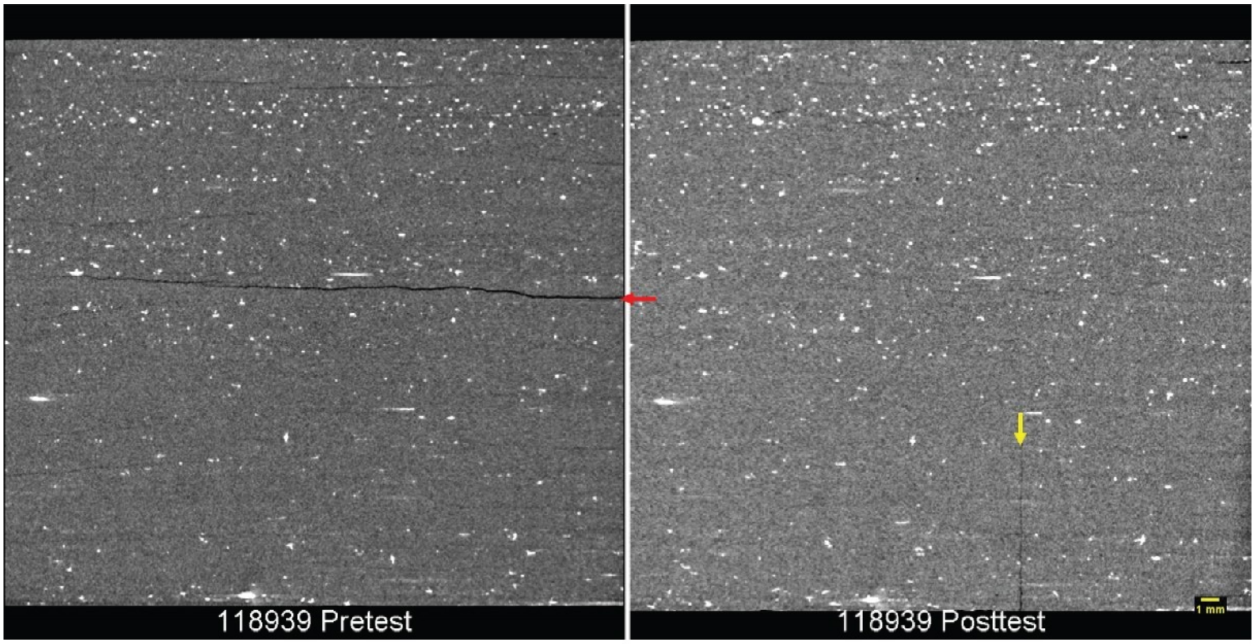

EERC JS57756.AI

Figure 10. Sample 118939 MicroCT cross sections showing pretest fracture (red arrow), posttest fracture “healing,” and handling damage (yellow arrow).

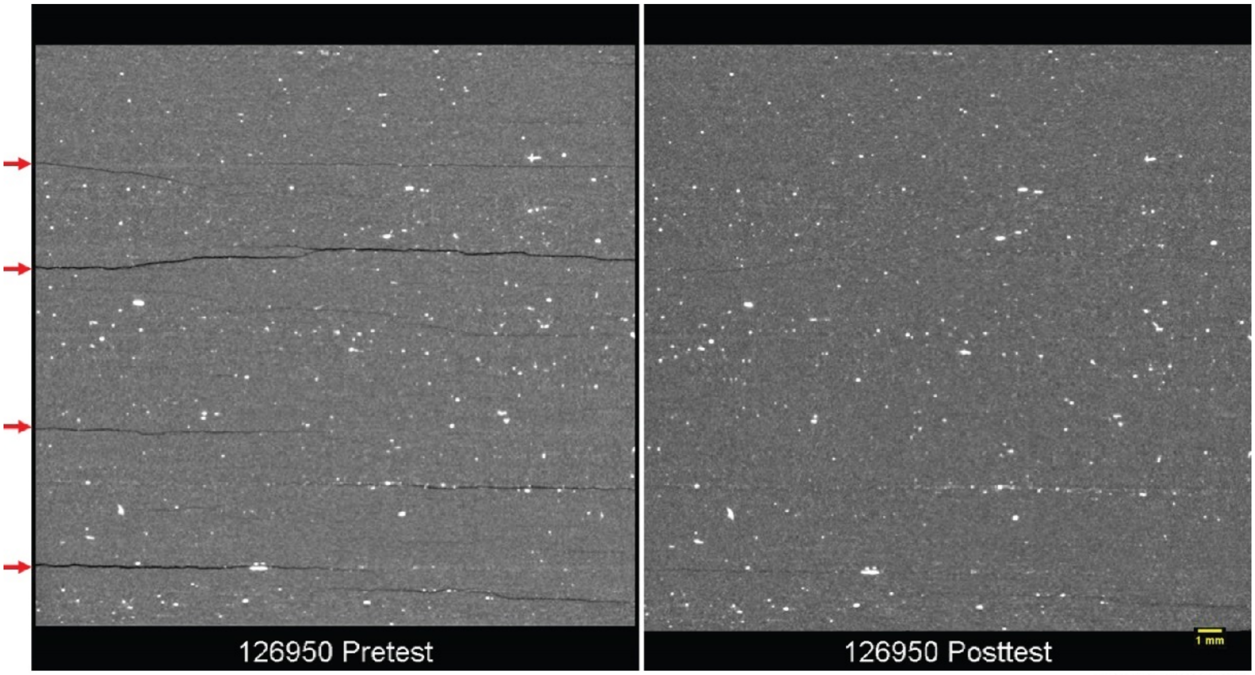

EERC JS57757.AI

Figure 11. Sample 126950 MicroCT cross sections showing pretest fracture (red arrows) and posttest fracture “healing.”

FESEM

The outlet face of Sample 118939 was imaged using FESEM before and after testing with an emphasis on imaging the same scenes during each session, as shown in Figure 12. The surface was not coated or polished before posttest imaging which allowed for direct comparison of structures. Observations include the collapse of some fractures, the creation of small fractures, and the formation of faceted halite associated with fractures. Fracture structures show compression and closing as was also observed in the MicroCT scans. Figure 12 shows the removal of calcite crystals that are dispersed within a grain of organic matter. The dissolution appears to be concentrated near the center of the organic grain. The mobilization of some of these structures may be attributable to a small amount of water or moisture moving through the core.

No pretest imaging was performed on Sample 126950. After the test, the outlet face was hand-polished to 2000 grit and imaged. The most significant observation was the formation of halite/sylvite associated with organic solids, shown in Figure 13 (inset). These salt crystals appear to be dendrites, indicating they formed by diffusion-limited aggregation (Choudhury and others, 2015). Element maps of the same area confirm that these halite/sylvite crystals are indeed suspended inside the organic matter particle. At lower magnification, many organic grains showed similar dendritic salt. The yellow circles of Figure 13 represent other instances of dendritic salts, showing that this occurrence was not unique in the frame.

Sample 118939 was prepared again after the critical structures were imaged to investigate the possible presence of diffusion-limited dendrite structures inside the internal organic-filled pores. The pores were surveyed, but no such structures were found. Qualitatively, it appears that 126950 contains a higher number and/or larger-sized organic matter particles compared to 118939 and regional NDGS data (Figure 8) shows that 126950 is located in a region with lower thermal maturity.

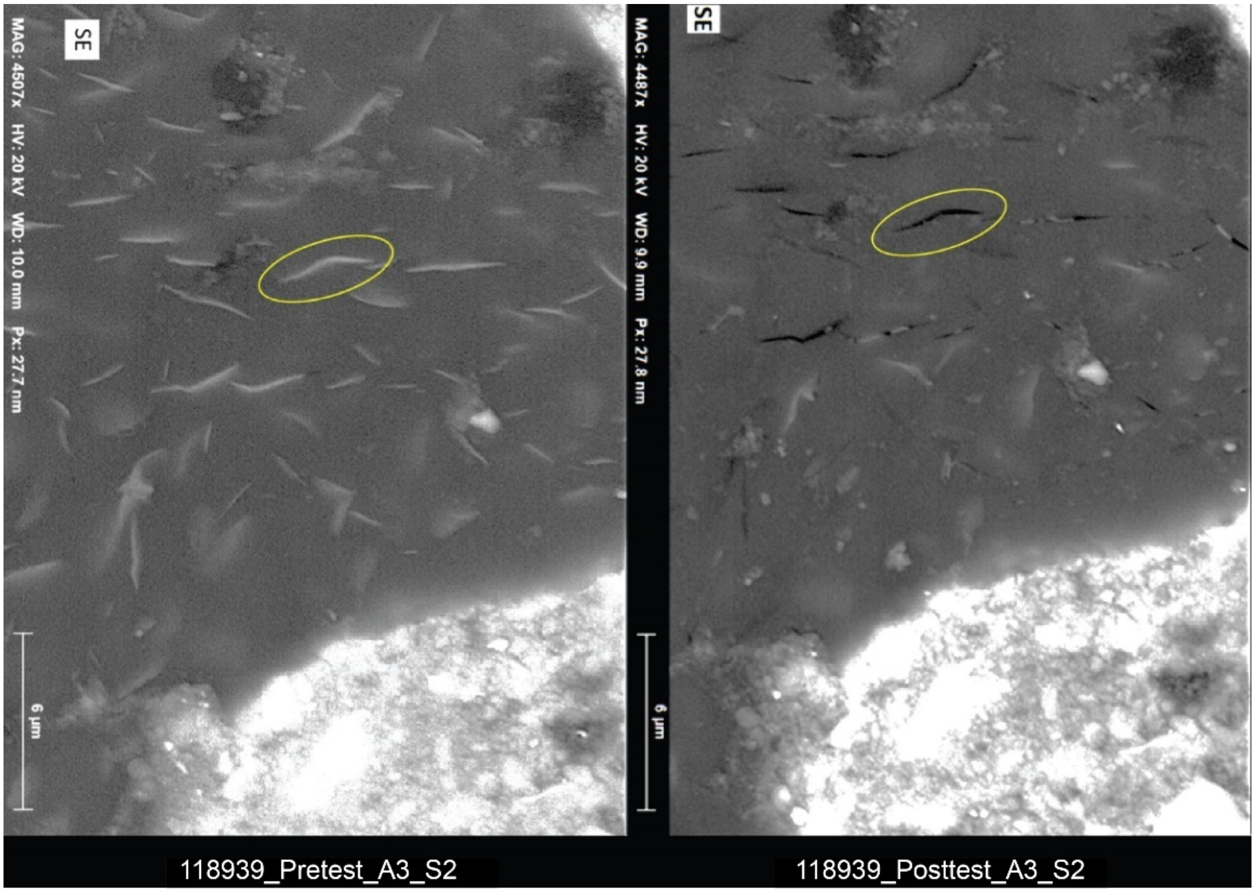

EERC JS57758.AI

Figure 12. Sample 118939 organic matter pre-/posttest showing loss of calcite leaving behind empty cracks (yellow oval). The dissolution of this calcite could be because of the presence of water in this sample.

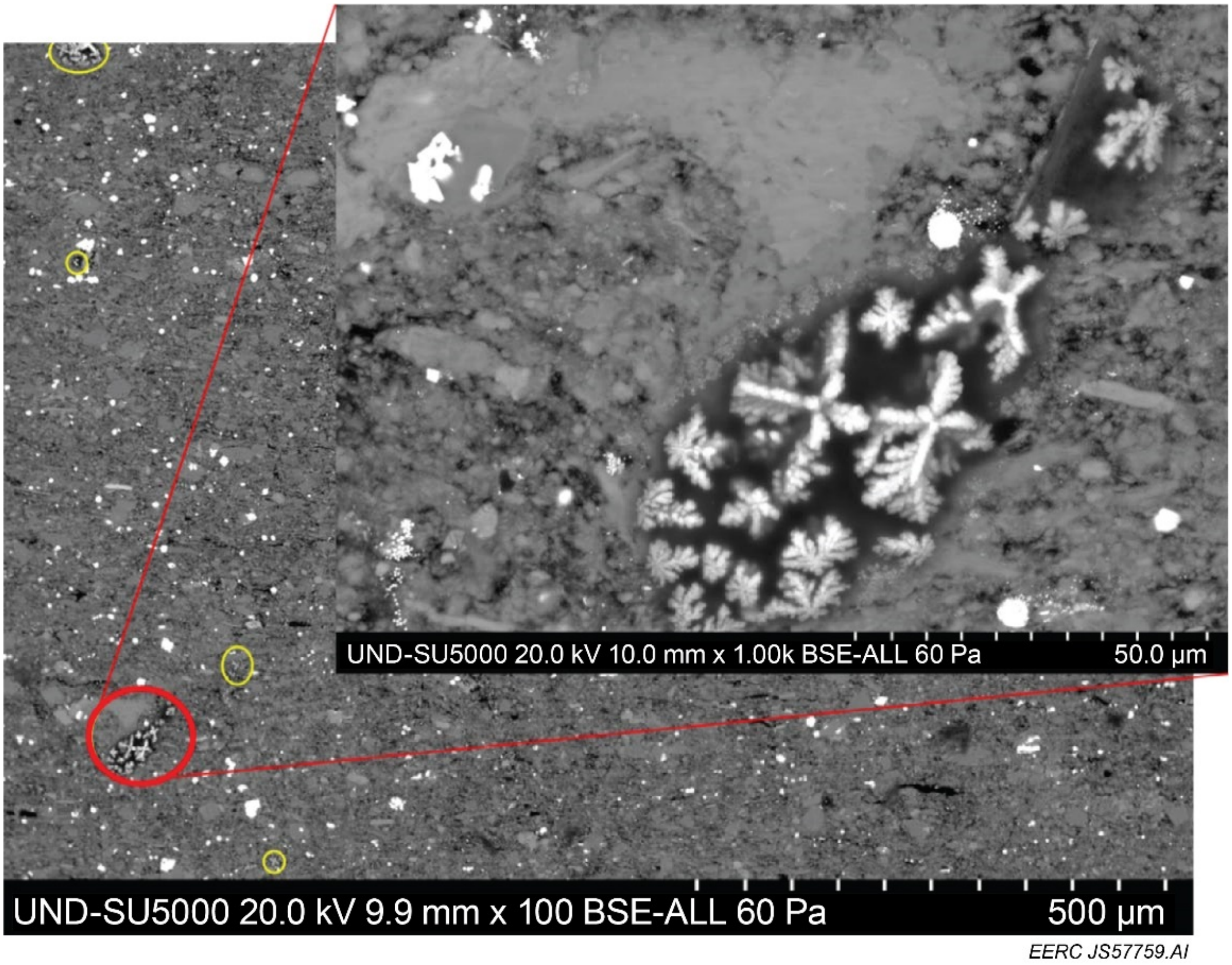

Figure 13. Sample 126950 (posttest) showing the presence of salt that formed dendrites inside of organic matter particles (yellow ovals). Inset (close-up of red oval) shows detail of this crystal habit also known as diffusion-limited aggregation.

NMR

NMR is sensitive to the concentration and decay behavior of protons in the sample. These protons are present as hydrogen from water, hydroxyls within clay and hydrogen in organic fluids, and gases present in pore space. The decay behavior is governed by the fluid properties (density, viscosity), the wettability of pore walls and, finally, the size distribution of the pore space. The results reported by NMR take two forms: the two-dimensional T1–T2 map (2D NMR) and the one-dimensional T2 relaxation, which gives the pore-size distribution (PSD). The pore sizes in the PSD are in terms of T2 relaxation time which is related to pore size; as pore size increases, so does the T2 relaxation time.

2D NMR plots correlate T2 relaxation time with the T1 relaxation time. T1–T2 maps are interpreted by recognizing the regions that signals occupy. Figure 14 (adapted from Fleury and Romero-Sarmiento, 2016) depicts the approximate locations of typical fluids present in shales. The ratio T1/T2 equals one for water and at low T2 times is associated with clay or organic-bound water. Signals with T1/T2 ≥ 2 and low T2 times are because of solid organics, bound gas, and oil. Signals from T1/T2 ≥2 and high T2 times represent organic fluids and gas occupying pore space.

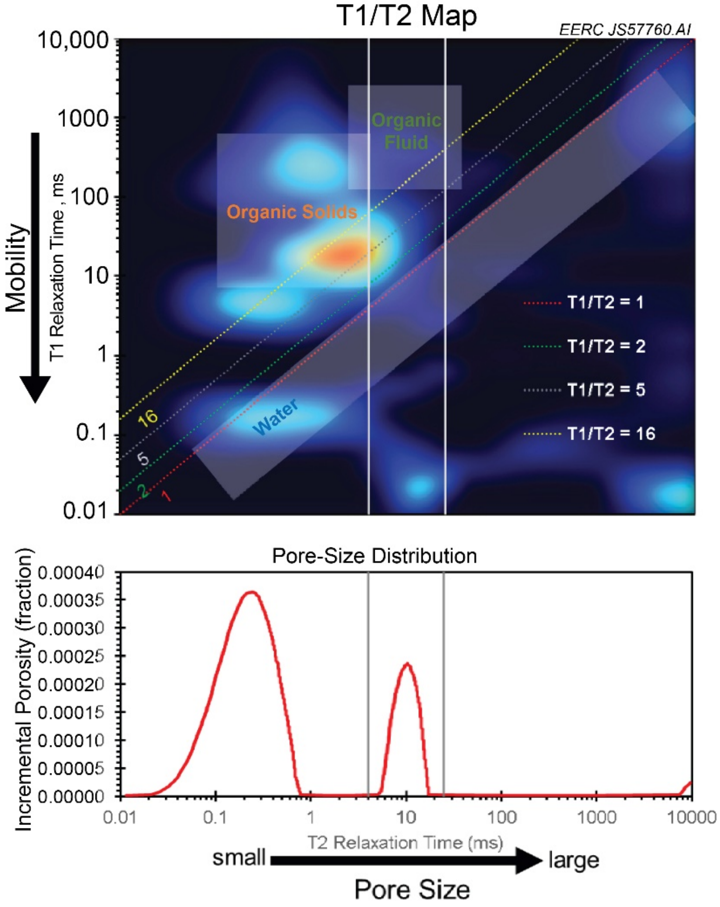

Figure 14. A simplified diagram of a T1/T2 map adapted from Fleury and Romero-Sarmiento (2016).

There is no NMR data for the posttest Sample 118939 because of a lack of instrument availability. NMR indicates that Samples 118939 and 126950 are different (Figure 15). Data from NDGS and Rock Eval suggest that Sample 118939 is more thermally mature (Table 2). Both samples contain organic solids and a mobile organic liquid. In 126950, the organic liquid phase occupies a smaller-sized pore space compared to the same phase in Sample 118939. This can be seen in the T2 values: for 118939, the mobile phase is between 4.6 and 23 ms, while the mobile phase in 126950 is between 1.8 and 11.8 ms.

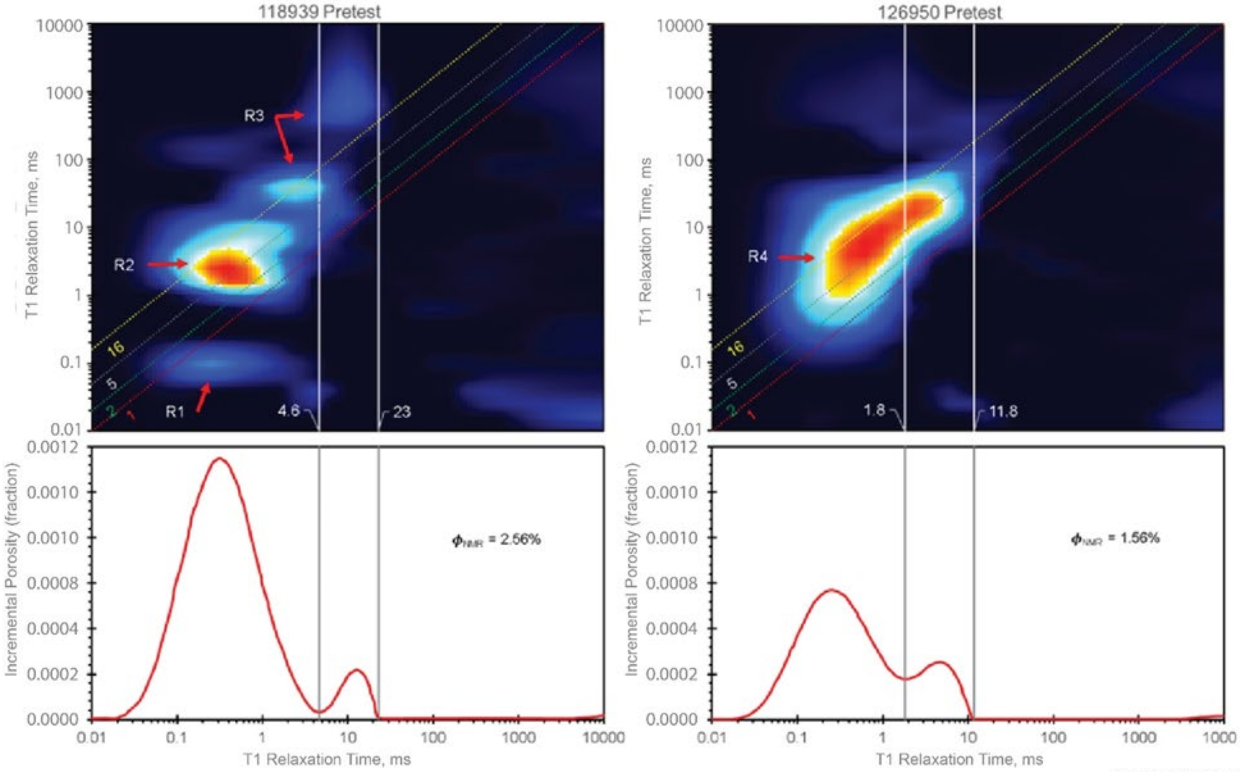

EERC CB57955.AI

Figure 15. Pretest NMR pore-size distributions comparing Samples 118939 and 126950.

In Figure 15 (118939), there are three distinct fluid types: bound water phase (R1), organic solids (R2), and a mobile oil phase (R3). In stark contrast, 126950 shows one contiguous region (R4), containing possibly more organic solids, and has no significant bound water. Directly measured Rock Eval is required for identifying the types of organic matter in this sample.

Comparing pre- and postexperiment NMR data for Sample 126950 (Figure 16), clear evidence shows that mobile organic fluid has been moved to larger pore spaces. It appears the contiguous region (R4) evolved into a solid organic (R6) and mobile organic phase (R7). A signal from water also appears more defined from the pretest NMR and occupies R5. The water in the posttest sample appears to be bound to organic matter because of the low T2 relaxation time.

Figure 16 PSD plots indicate a slight increase in porosity after flow-through testing for Sample 126950. The pretest NMR porosity was measured at 1.56%, and the posttest porosity was measured at 1.69%. The shift represents a slight increase in porosity. This shift is because of both an increase in low T2 signal (because of water seen in R5) and the movement of fluid to large pores.

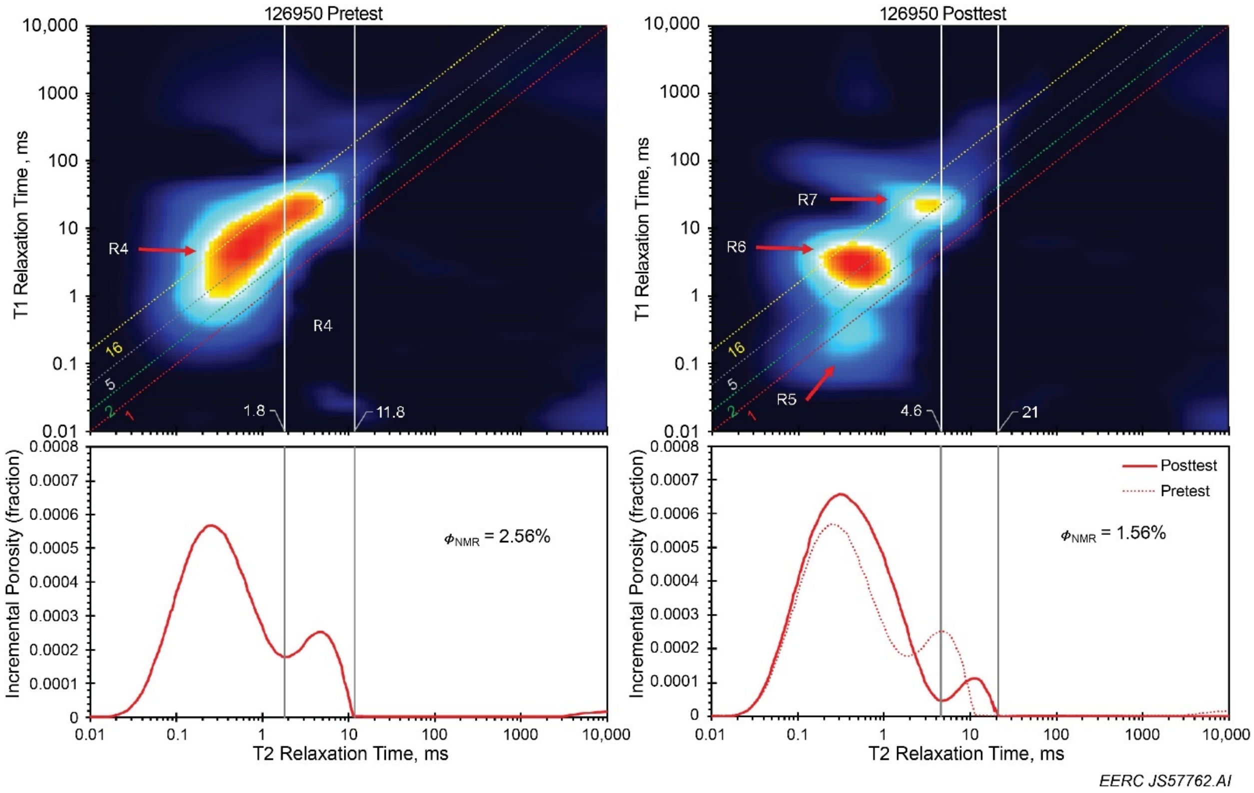

EERC JS57762.AI

Figure 16. Comparing the pre- and post-flow-through test NMR data for Sample 126950.

Rich Gas Flow-Through Tests

Figure 17 shows the normalized GC results for the preferential flow tests for Samples 126950 and 118939. The relative concentrations of methane, ethane, and propane are plotted against the injected pore volumes of gas at the time of production gas sampling. Table 3 lists the flow conditions of the tests for each sample.

Plotting gas injection as unconfined pore volume allows for direct comparison of the two samples where the sample geometry and porosity are otherwise significantly different. The behavior of the two samples was distinctly different. The NMR results and helium porosity suggest Sample 126950 should have significantly more restrictive flow characteristics. In contrast, the fractures observed in MicroCT and the permeability data suggest that the fracture networks play a significant role in the flow distribution and contact within this sample. FESEM analysis suggested that 126950 contains more organic matter. If a higher organic matter content is present, this would increase the sorption capacity of the shale matrix (Hu, 2014). In testing, Sample 126950 does show a significant delay in the expected breakthrough of the rich gas. Ethane and propane break through at approximately 2 pore volumes injected, and methane does not break through until after 4 pore volumes, indicating some significant interactions between the injected gas and the rock matrix. Conversely, Sample 118939 shows breakthrough before 1 pore volume of fluid is injected at approximately 0.7 pore volumes. This along with the lower permeability measurement suggests

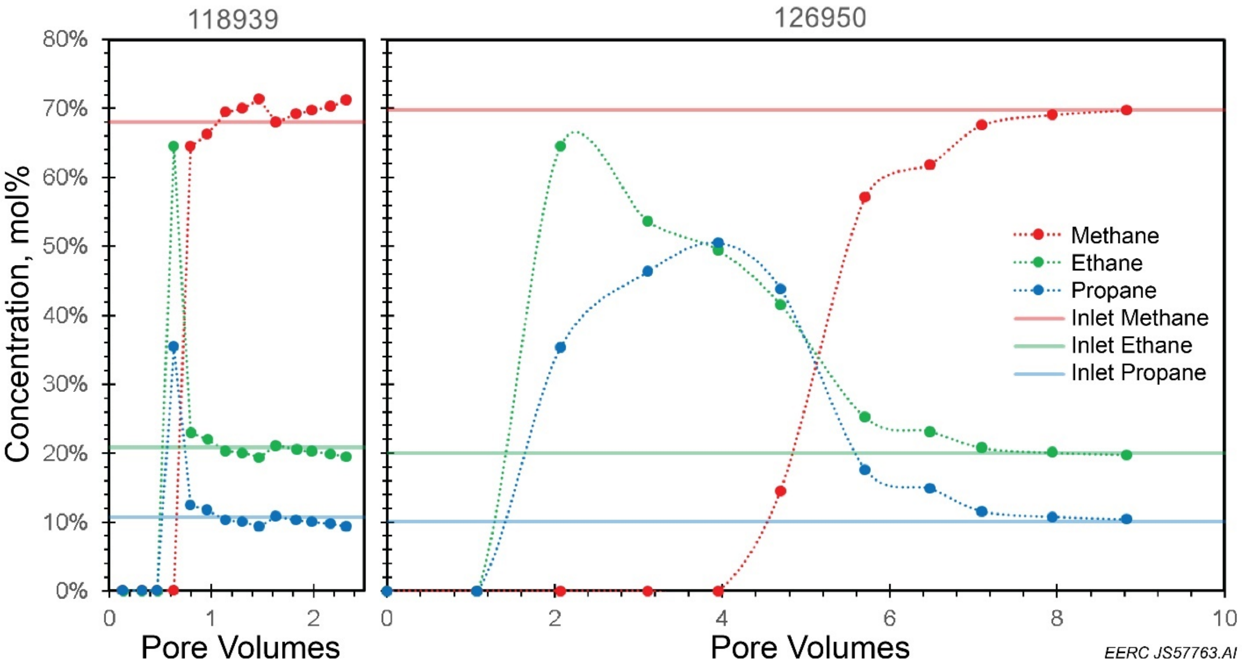

Figure 17. Preferential flow test results showing concentrations of methane, ethane, and propane from the produced gas compared to the baseline injected methane concentrations for Samples 126950 and 118939.

Table 3. Comparison of Rich Gas Flow-Through Test Parameters

Sample	118939	126950
Volumetric Flow Rate, mL/min	0.0016	0.0016
Pore Volume Exchange, 1/hour	0.048	0.214
Apparent Cross Section, cm^2	0.534	0.156
Superficial Velocity, cm/min	0.0030	0.0103
Residence Time, hours, assuming no interaction	20.97	4.67

that the sample pore volume is not being completely accessed on this sample and flow may be concentrated through, or in proximity to, the single dominant fracture as observed in the CT data within Figure 10. Sample 118939 also shows a slightly delayed methane response of approximately 0.1 pore volumes, but it is less pronounced. The slight methane delay could be attributable to the presence of organic matter in Sample 118939 but in lower levels to that in 126950, reducing gas retention. There also could be reduced retention because of a physical mechanism such as flow dominated by a single major fracture as shown in Figure 10. In comparison, it takes 6 pore volumes of production for Sample 126950 to reach the same mixed gas concentrations observed after 1 pore volume of Sample 118939 production. Sample 126950 shows a capacity to sorb approximately 200% more rich gas than the calculated pore volume, and the sorption capacity of methane alone may be much higher at 400%–600%. Sample 118939 shows almost no capacity to sorb the injected gas mixture in comparison. It is possible that with extended contact times the injected rich gas will make contact with additional pore space.

Figure 18 shows the changes in relative gas concentrations from the desorption test performed on both samples. If methane is preferentially sorbed, it is expected that as the pore pressure decreases, trapped methane should be released. There appears to be a slight trend for increasing methane concentrations throughout the desorption test above the baseline injection concentrations shown by the horizontal lines.

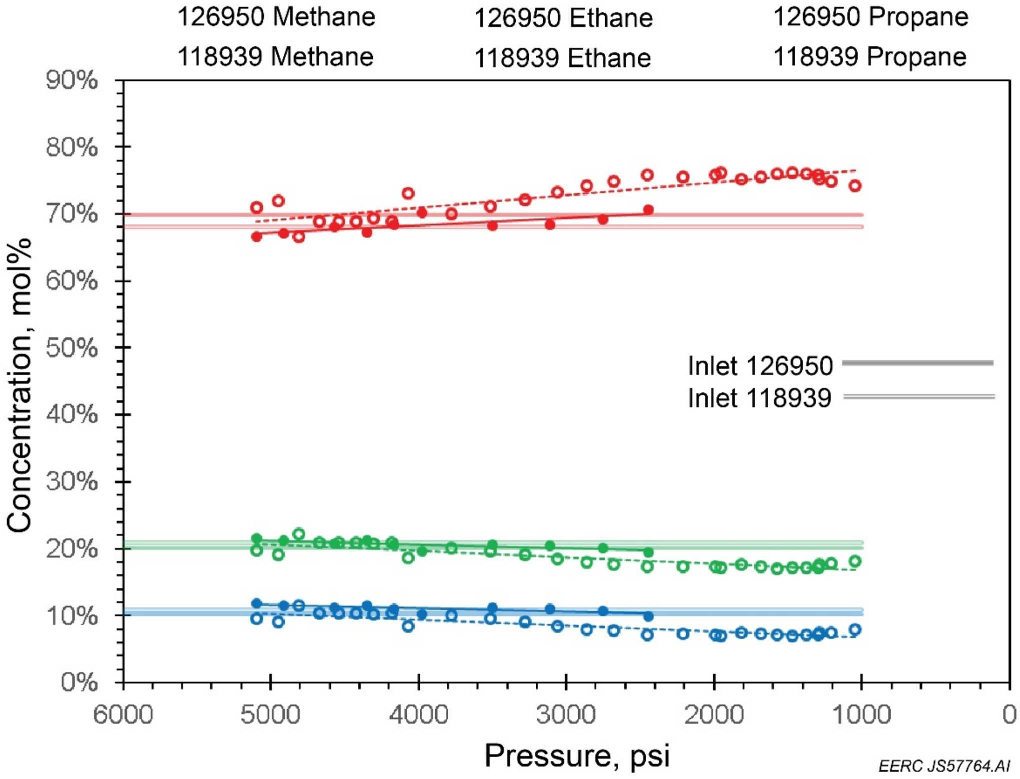

Figure 18. Desorption test results for Samples 126950 and 118939 compared to injected gas compositions.

The ethane and propane concentrations seem to trend together at decreasing concentrations while the methane increases slightly above baseline. This supports observations from the preferential flow test that the methane is being held inside the sample. However, further investigation is required to determine the mechanism. Sampling directly into a GC instrument in an automated fashion is recommended for future testing to reduce air intrusion, increase the sample quality, and reduce noise in the data.

Interpretation and Conclusions

The long delay of methane breakthrough for Sample 126950 indicates that significant interactions between rich gas and rock matrix are occurring. The data suggest methane is being preferentially sorbed over both ethane and propane. Sample 118939 was initially selected to accentuate the duration of this observed hydrocarbon breakthrough delay, but instead breakthrough was near immediate. Sample 118939 did show the same trend of the methane gas breakthrough delay compared to 126950; however, the magnitude of the delay was significantly reduced. The overall observation indicated that there is a significant difference between the two samples that allows 126950 to retain a significant portion of the injected hydrocarbons while some similarities that still impact methane flow in 118939 but to a much lesser degree. Stress sensitivity in the permeability results suggests that both samples are significantly affected by fracture flow. The highly fractured nature of 126950 increases the gas contact with the sample as opposed to Sample 118939, which appears to have only one major fracture visible in MicroCT data.

The NMR results show differences between the organic content between the two samples, with Sample 126950 having a higher organic content. This higher organic content combined with better gas contact within the sample appears to be responsible for the higher observed gas retention. NDGS data also suggest that Sample 126950 has a lower T_{max}.

The presence of diffusion-limited dendrite halite/sylvite salt structures in 126950 and lack of similar structures in 118939 may provide some evidence that diffusion-dominated flow through organics plays a role in the retention of these hydrocarbons. This diffusion flow is also supported by the much lower unstressed porosity of only 3.46% for Sample 126950. This porosity is reduced to 1% or less depending on the stress regime that will have been further reduced through closure of the numerous fractures shown by x-ray CT (Figure 11). More investigation is required to determine which mechanisms dominate flow and retention of HCs in Bakken shales.

Research by Hu (2014) suggests that organic matter content plays a significant role in the sorptive capacity of shales. Additional testing is required to prove organic matter gas sorption is responsible for the observed gas retention.

One significant consequence of the observed difference in gas retention is that field operators could see wildly variable injection performances and storage capacities depending on the mechanisms controlling this gas retention and their presence in the reservoir rock matrix. This testing suggests that some organic-rich shales in the Bakken Formation may retain greater than 200% more injected gas than would otherwise be calculated based on available pore space. Volumes may be as high as 400%–600% for high concentrations of methane injection, as shown in Figure 18. There is evidence to suggest that organic content and compositions of the Bakken shales play a major role in these observations. The retention of these gases is likely because of a combination of physical flow restriction and trapping within the nanoscale pores and organic structures. Further investigations to identify the specific driving mechanisms and the magnitude of their contributions will be critical for the design and application for rich gas storage and EOR activities in the Bakken.

ACTIVITY 3.0 – RICH GAS CHARACTERIZATION FOR EOR OPERATIONS

Subactivity 3.1 – Rich Gas Recovery, Processing, and Reinjections

Rich gas produced in association with oil recovery is the preferred EOR fluid for the Stomping Horse pilot EOR operations. The project team has evaluated the quality and quantity of rich gas available from the appropriate Stomping Horse production separator(s) at various points in the complex. Modeling work has been conducted to determine compression requirements to achieve the desired EOR design conditions (flow, temperature, pressure, and composition). These activities were done iteratively in close collaboration with LR and were critical to the assessment of different design scenarios with respect to potential configurations of the rich gas EOR pilot. Specifications for gas treatment equipment and compression were developed through the process-modeling effort. These data, combined with operational data and design parameters from the components of the Stomping Horse complex, have been used to develop a process model to assess gas treatment requirements (NGL recovery, sulfur treatment) to support injection. Results of this activity are integrated into modeling and simulation work reported in Activity 4.

Subactivity 3.2 – Examinations of Temporal Change in Gas and Fluid Compositions

Rich gas at the wellhead commonly exists as a mixture of methane (C1) with other HCs, including ethane (C2), propane (C3), butane (C4), pentane (C5), hexane, and higher (C6+) (Wocken and others, 2012). These gas compositions, as well as the produced fluid compositions, may change over time in both the tight oil reservoir and surface infrastructure environments. Those changes may affect reservoir and process facility performance. For instance, laboratory studies by Hawthorne and others (2017) indicate that changes in the ratio of methane to ethane in a rich gas mixture can significantly alter the MMP of the gas being used for EOR which, in turn, can affect the efficiency of the EOR operation. Very little data are currently available in the public domain regarding temporal changes in gas and fluid compositions on a reservoir- or gas plant-specific basis.

To address this data gap, produced fluids sampling and characterization have been conducted throughout the demonstration project to provide data necessary for project planning, development of the EOR scheme, establishing baseline conditions, and assessing EOR performance. Produced fluids, including crude oil, produced water, and associated gas, have been collected as a mixed fluid or discrete fluids from a separator periodically over the course of the project.

Temporal Evaluation of Bakken Fluids

Three newly completed wells, two Middle Bakken (MB) and one Three Forks (TF) Formation, were monitored for a period of 26 months beginning at initial production (IP). Two of the wells, MB1 and TF1, originated from the same well pad and were completed independently in the Middle Bakken and Three Forks Formations, respectively. The third well, MB2, was completed in the Middle Bakken Formation and is located approximately 15 miles away. Samples from each well were collected weekly for the first month, then monthly for 6 months, and then approximately quarterly thereafter. Samples were collected from the separator/treater, and analyses included gas composition, water chemistry, and compositional comparisons of the crude oil (HC fingerprinting). Results were evaluated for temporal trends and differences between the two completed formations. Cumulative and daily production statistics for each well were also evaluated.

Gas compositional trends for the first 26 months of production for all three wells show an increasing methane concentration and decreasing concentrations of the remaining constituents (i.e., ethane, propane, butanes, and pentanes). These trends illustrated in Figures 19a and 19b were similar regardless of the completed formation. Nitrogen and CO_2 concentrations (not shown) also show a slight increasing trend, and sporadic helium occurrences were detected (approximately 200–300 ppm). Gas composition from these wells will continue to be monitored for an additional 1 to 2 years, and results are being used as preliminary data to support modeling produced gas compositional changes over time throughout the basin to better understand economic recovery potential.

Cumulative and daily oil production rates were very similar for both wells that originate from the same well pad (MB1 and TF1), as shown in Figure 20. The third well, MB2, had a slightly less steep production decline curve and, ultimately, an approximately 30% higher cumulative production total after 26 months. Produced water production rates and totals were also very similar for the two wells on the same pad, as shown in Figure 21, while a steeper decline curve and approximate 30% less cumulative total is observed for the MB2 well. The difference in production statistics for wells in the two locations is likely a result of geographic location and/or possibly completion practices used. It is not unusual for production rates and water cuts of wells to vary significantly across the Bakken play.

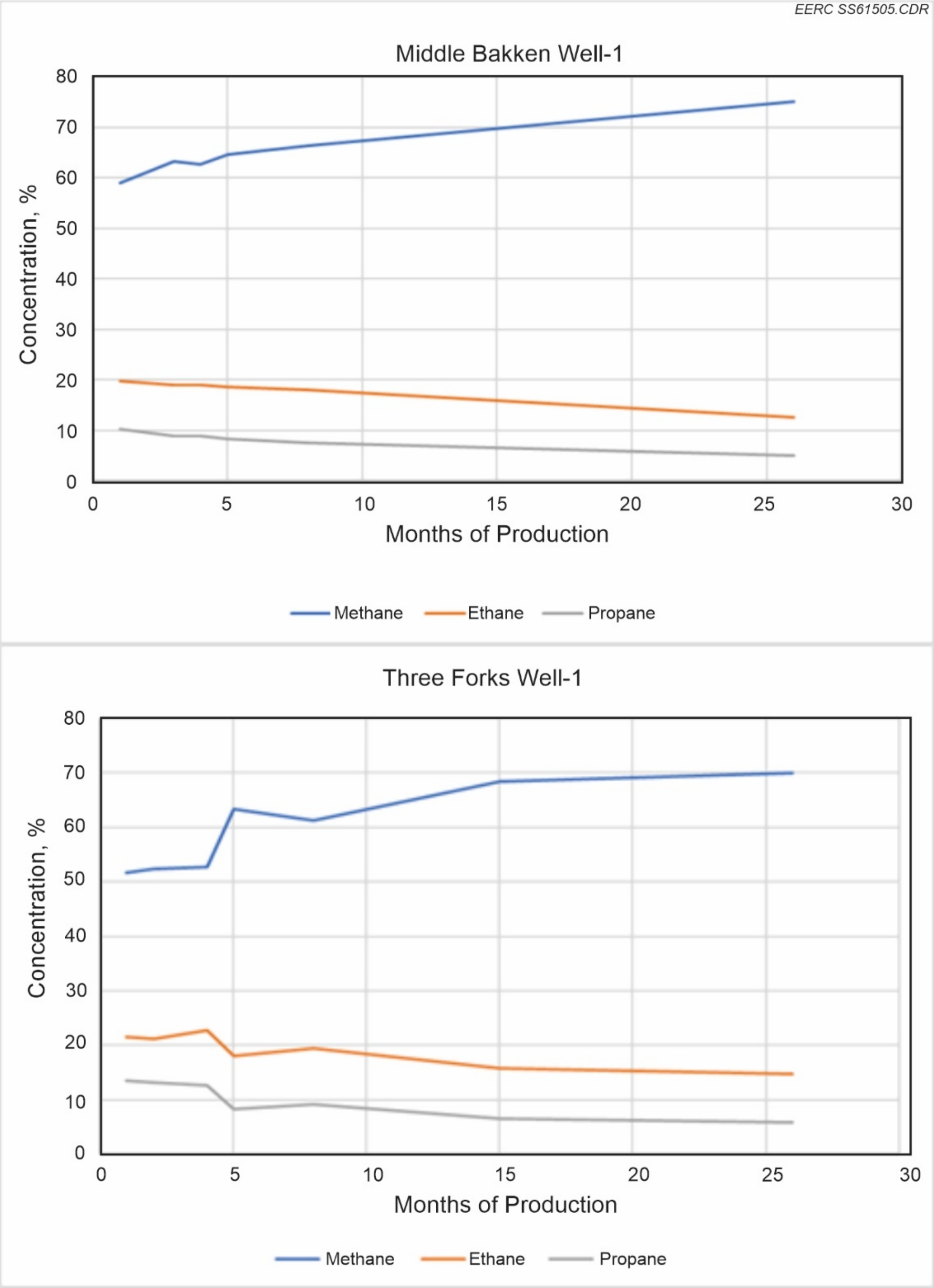

Figure 19a (top) and 19b (bottom). Gas compositional trends for both a Middle Bakken and Three Forks well.

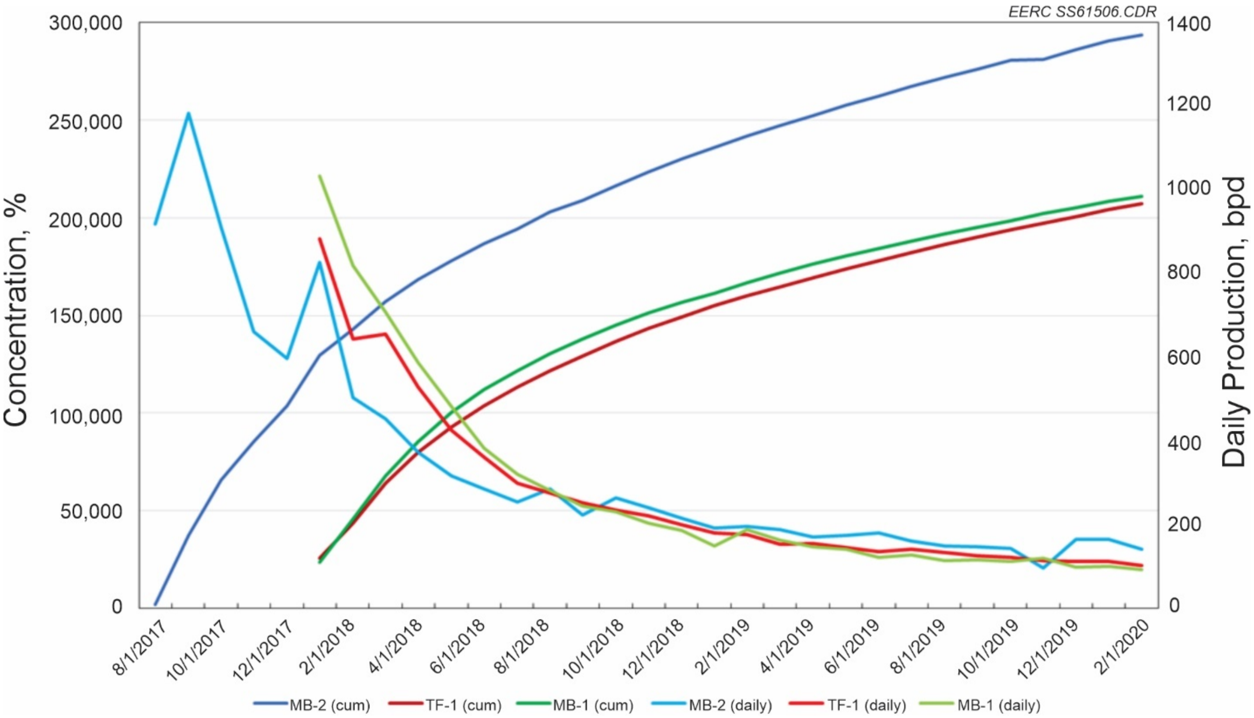

Figure 20. Daily and cumulative oil production for all three wells.

Produced water compositions were analyzed for total dissolved solids (TDS), major and minor cations and anions, and various other elements, including lithium. The results from all three wells are fairly similar over 26 months of monitoring. The two wells on the same pad, MB1 and TF1, exhibit an increasing concentration of TDS from approximately 260,000–270,000 mg/L up to slightly over 300,000 mg/L over the first 2–3 months, possibly indicating the gradual recovery of flowback fluid and a return to more representative formation waters. TDS concentrations then moderately fluctuate, as illustrated in Figures 22a and 22b, for the next 10–12 months before MB1 has a modest decrease in TDS and TF1 has a slight increase. No drastic fluctuations in production rates or volumes seem to be a contributing factor; however, field personnel have indicated that freshwater additions were adjusted in this time period and may be responsible for the fluctuations. Minor constituents for each well, as shown in Figures 23a and 23b, remain relatively stable over the life of the well, except lithium and iron. Lithium exhibits a slight increase over the first 9 months and then begins a slight decline in both wells. Iron also increases over the first several months in each well and then begins to increase significantly during the last 9 months. The iron in MB1 eventually begins to decrease as observed over the last couple months; however, the same decreasing trend is not yet seen in TF1. Although well maintenance may have influenced the produced water composition; these wells will be monitored for several more months to determine if trends continue.

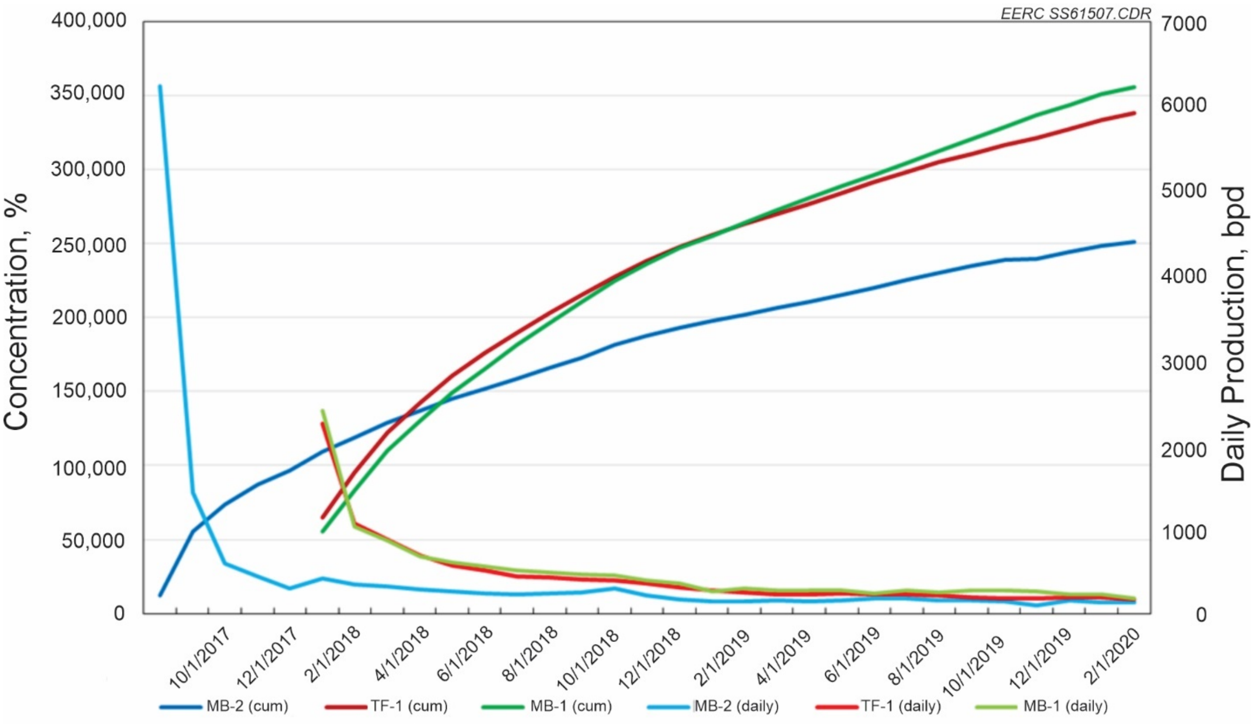

Figure 21. Daily and cumulative water production for all three wells.

Crude oil compositional comparisons were conducted using a newly developed HC fingerprinting method, with results shown in Figure 24. Star plots for samples from MB1 and TF1 wells were very similar, while the results from the MB2 well exhibited slight differences in a few areas of the plot. These differences between wells from two different areas in the Bakken are likely dependent on facies changes across the basin. These subtle differences in key areas of sample chromatograms indicate that additional modifications to analytical techniques may enable the method to distinguish crudes from the same formation in different geographical settings and also distinguish between oils from different facies of the formation.

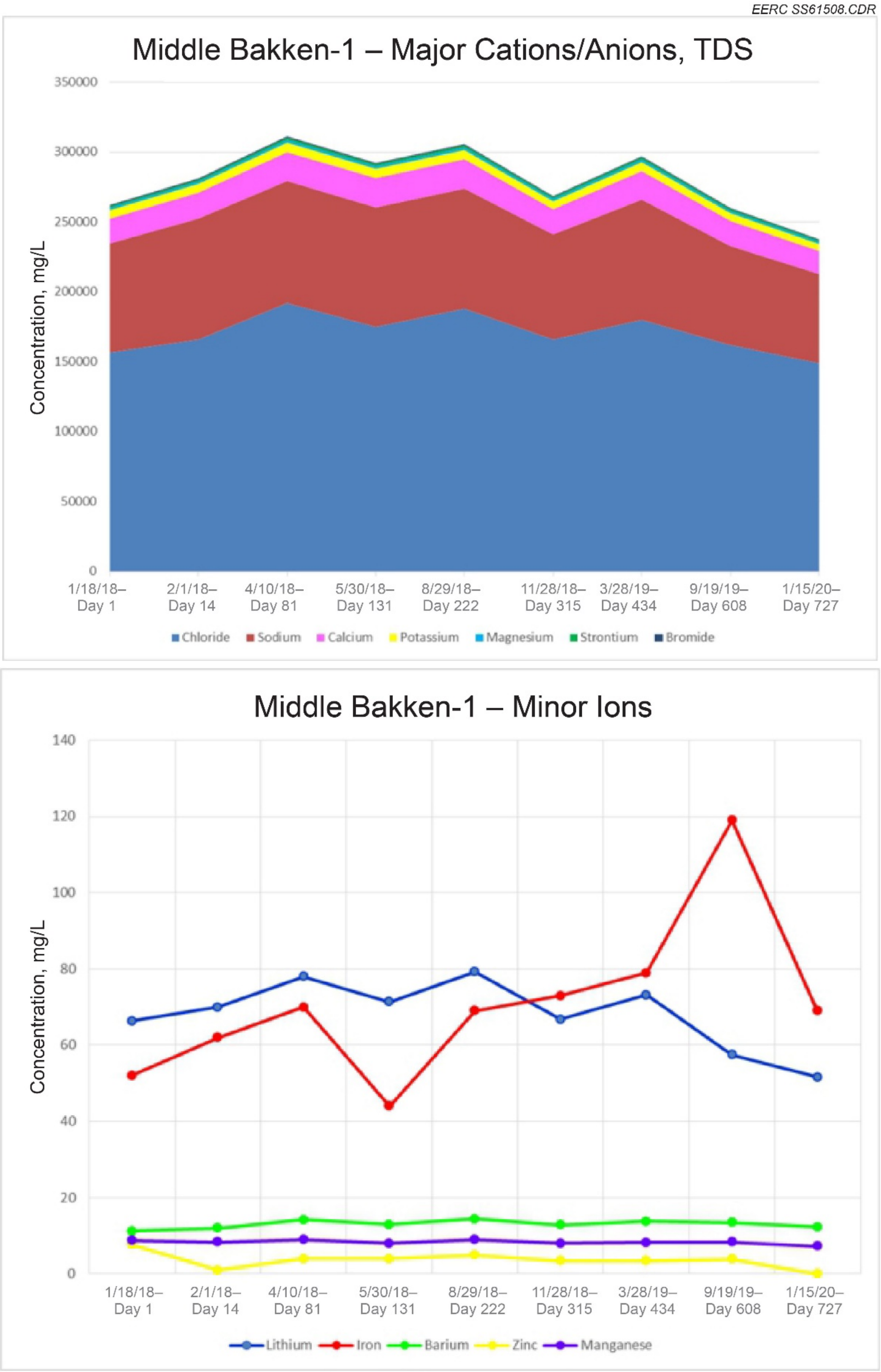

Figure 22a (top) and 24b (bottom). Produced water compositional trends for the MB1 well.

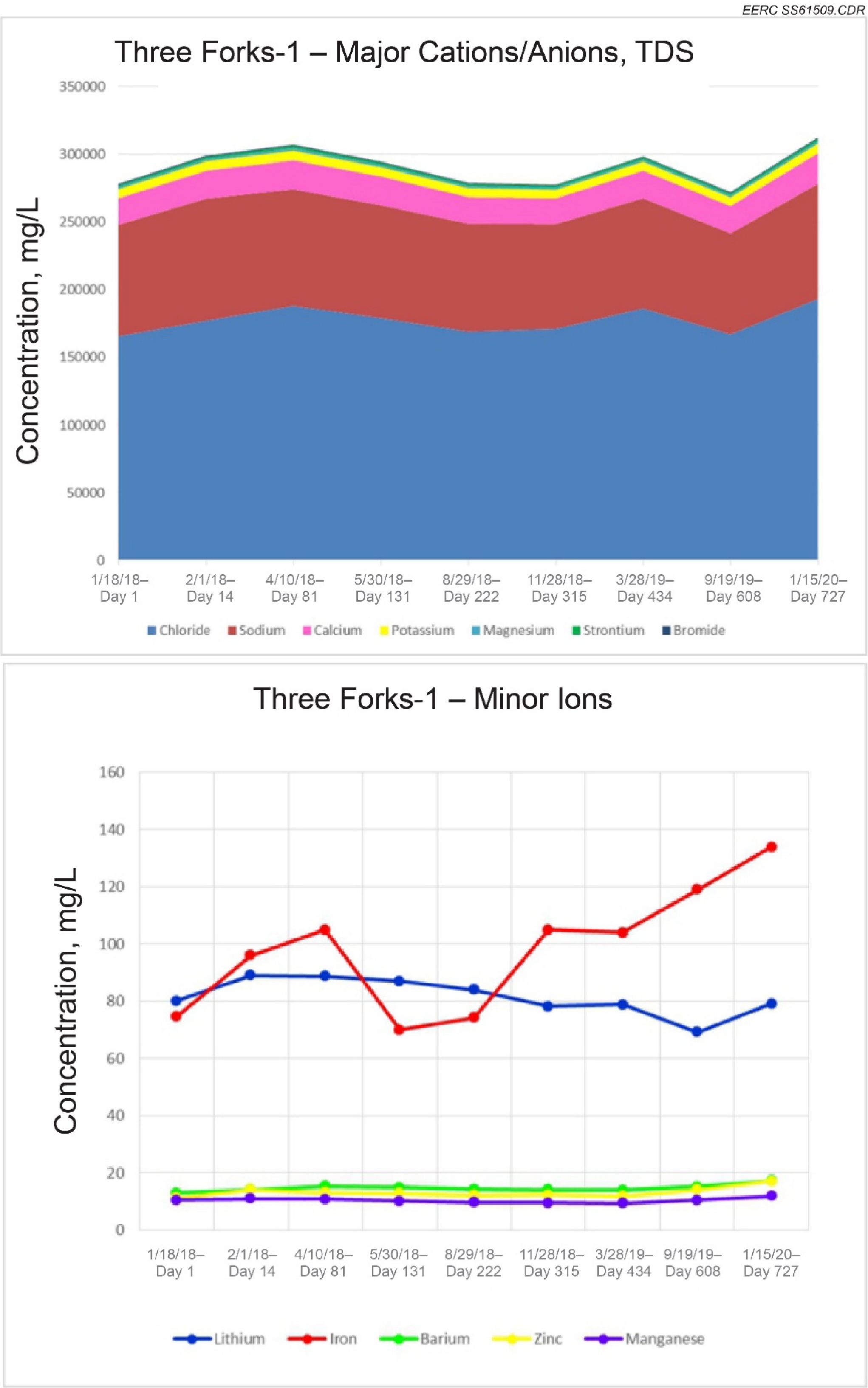

Figure 23a (top) and 25b (bottom). Produced water compositional trends for TF1 well.

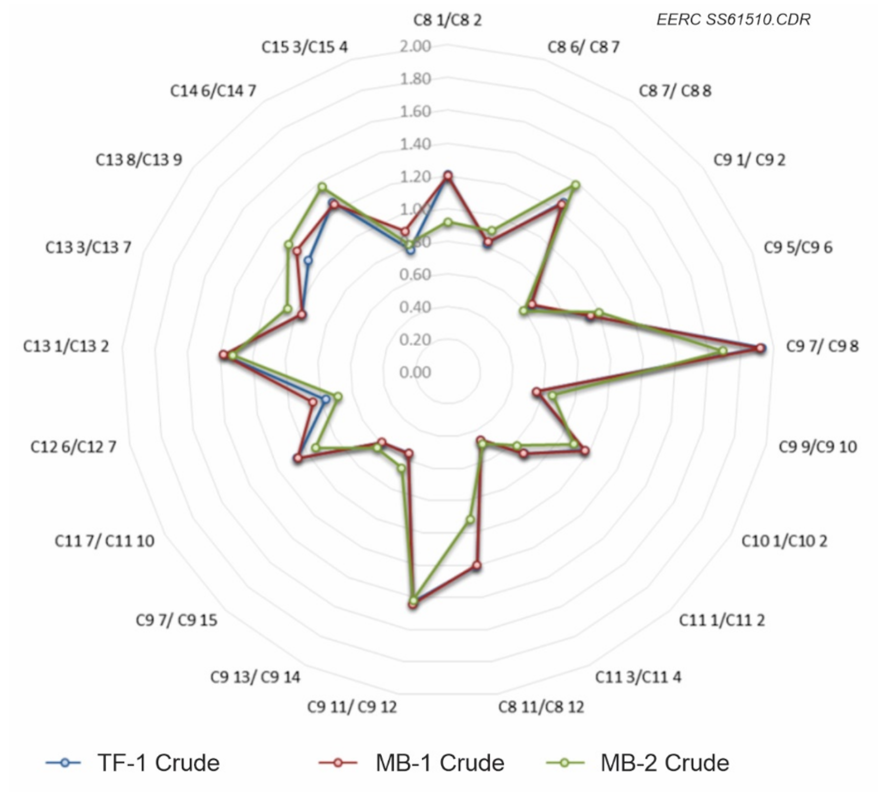

Figure 24. Star plot derived from HC fingerprinting data for all three wells.

Crude samples from each well were also analyzed by an aromatic/aliphatic (A/A) ratio analysis GC method to determine if any differences in composition between the wells existed. The results were also compared to previous A/A work performed on HCs extracted from the Middle Bakken member and the Upper and Lower Bakken Shales (UBS and LBS) to see if temporal changes in crude oil contributions from the various lithofacies could be determined. Crude oil HCs recovered from the UBS and LBS rocks consistently have higher proportions of aromatic HCs compared to aliphatic HCs than are present in the adjacent Middle Bakken and Three Forks Formations. Therefore, an upward or downward trend can indicate either more or less contribution from the UBS or LBS. However, the overall relative difference in ratios varies significantly from well to well and area to area, so determining the actual contributing lithofacies of the produced oils from a well can only be accurately determined on wells with available core extraction data. The A/A determinations for each well were plotted against overall production of each well independently. Figure 25 shows the A/A ratios in relation to the gas-to-oil ratio (left set) and water cut (right set) as production proxies. The results indicate that the A/A ratios are very similar between the two wells on the same pad (MB1 and TF1), with ratios averaging just slightly less than 2.0. These ratios do not change or fluctuate over the entire monitoring period, indicating that the contributing lithofacies are likely not changing during the first 26 months that monitoring occurred. The MB2 well also shows a relatively stable ratio of just slightly over 3.0. This ratio is distinctly different than the other two wells and may represent a different contributing lithofacies (i.e., more contribution from the shales); however, this well is approximately 15 miles away and

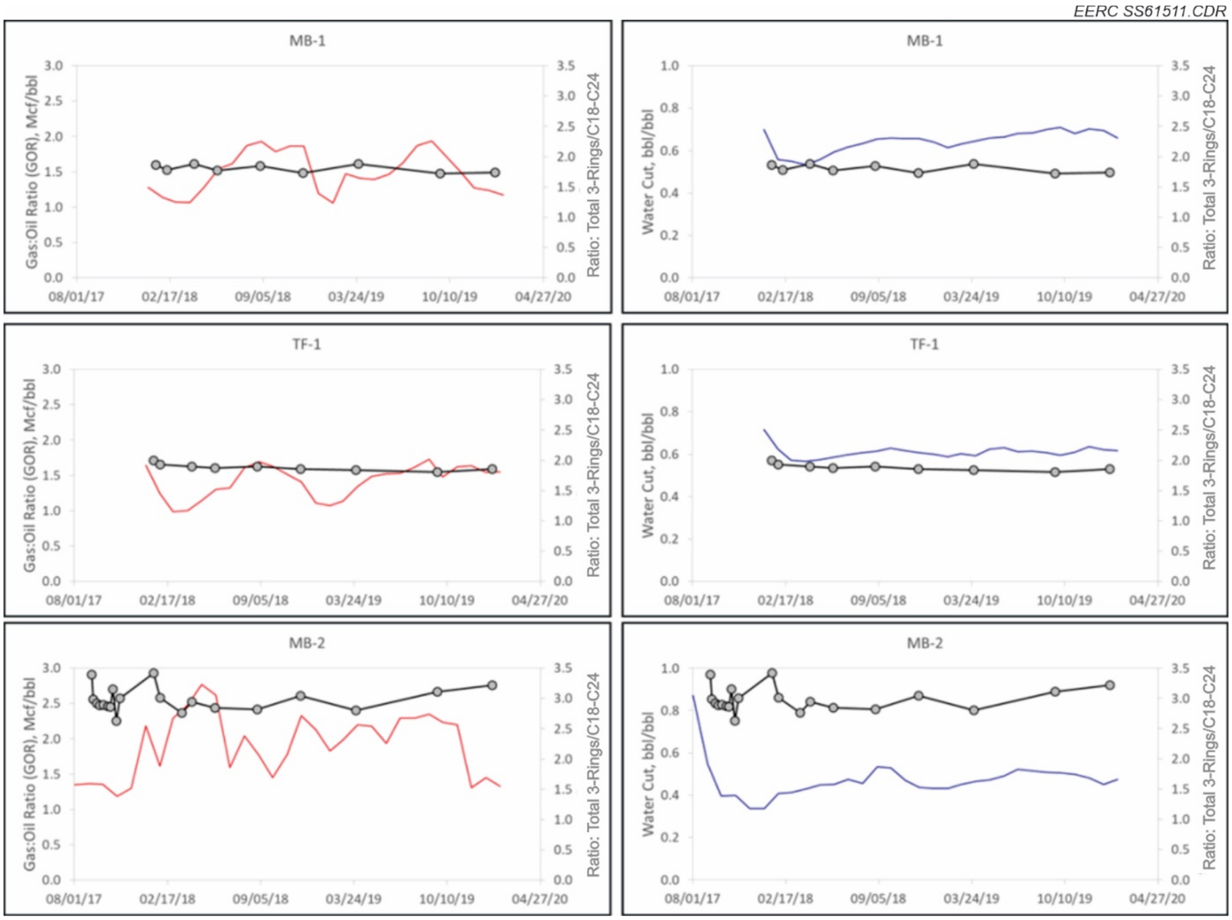

Figure 25. Scatterplots showing GOR (red, left) and water cut (blue, right) as surrogates for production over time and the A/A ratio, total 3-rings/C18–C24, for the temporal oil samples collected up to April 2020 for the temporally evaluated wells.

represents a different geographical area that may have a different relative A/A ratio. These wells will continue to be monitored to see if the A/A ratio indeed begins to deviate from the first 26 months, suggesting a change in contributing lithofacies.

Temporal monitoring of three wells, two of which were paired on a single well pad in different formations and starting at initial production, offered a unique opportunity to evaluate Bakken and Three Forks fluid characteristics and trends from several wells. A summary of the key findings from this effort follows.

Activity 3.0 – Summary of Key Findings

- Gas compositional trends for the first 26 months of production for all three wells show an increasing methane concentration and decreasing concentrations of the remaining constituents (i.e., ethane, propane, butanes, and pentanes). These findings are similar to those observed in an emerging EERC research project to understand produced gas composition trends across the Bakken.

- Evaluation of produced water and crude oil production statistics and compositional analyses are very similar overall between all wells, with slight geographical differences indicating possible lithofacies change and/or well stimulation approach influences. Water chemistry analysis was successful in illustrating an increasing trend in the first several months, indicating a return to native formation fluids with only moderate fluctuations thereafter.

- HC fingerprinting method results for samples from MB1 and TF1 wells were very similar, indicating a likely similar oil source. However, results from the MB2 well exhibited slight differences in a few areas of the plot. These differences between wells from two different areas in the Bakken are likely dependent on facies changes across the basin.

- The results of A/A ratio analyses indicate that the A/A ratios are very similar between the two wells on the same pad (MB1 and TF1), with ratios averaging just slightly less than 2.0. These ratios do not change or fluctuate over the entire monitoring period, indicating that the contributing lithofacies are likely not changing during the first 26 months that monitoring occurred. The MB2 well also shows a relatively stable ratio of just slightly over 3.0. This ratio is distinctly different than the other two wells and may represent a different contributing lithofacies (i.e., more contribution from the shales); however, this well is approximately 15 miles away and represents a different geographical area that may have a different relative A/A ratio. These results support the findings of similarities discovered using the HC fingerprinting method.

ACTIVITY 4.0 – ITERATIVE MODELING OF SURFACE AND SUBSURFACE EOR COMPONENTS

INTRODUCTION

Geologic modeling and simulation are integral parts of EOR pilot planning, operation, reservoir surveillance, and interpretation of results. As part of the research program, the EERC worked closely with LR to develop geologic models and conduct simulations to support the Stomping Horse EOR pilot. Horizontal wells in the Stomping Horse Complex are intensely hydraulically fractured, creating complex flow paths dominated by the fractures created in these wells, which also connect to each other either directly or indirectly through natural fractures. Because of the strong permeability contrast between these fractures and the matrix, as well as the pressure interference and fluid communication between wells, accurate simulation of dynamic multiphase fluid flow in the DSU becomes a very challenging task. A series of modeling and simulation activities were conducted in this study, aimed at effectively modeling and simulating the production/EOR processes to understand recovery mechanisms and potential performance.

Subactivity 4.1 – Modeling of Surface EOR Components

The rich gas EOR demonstration is a dynamic process with interactive feedback between the injected EOR fluid and the resulting produced fluids. The complexity of these processes warrants a dynamic, compositional process simulator, allowing researchers to predict the behavior of produced fluids in response to EOR injections and the impact these produced fluids will have on EOR fluid availability and production equipment, such as artificial lift, separators, pumps, pipelines, and tanks.

The EERC built a computational process model of LR's production equipment to simulate the effect EOR operations and associated changes in produced fluid rates and properties would have on equipment design and operations. An iterative approach between process modeling and reservoir simulation is anticipated, allowing output from reservoir simulation to provide input to production equipment performance models and vice versa.

The Leon and Gohrick surface facilities were modeled to assess whether production conditions altered by rich gas EOR injection activities might negatively affect or exceed design specifications of production equipment. The surface facilities modeled comprised primarily piping, phase separators, and associated process equipment, as shown in Figure 26.

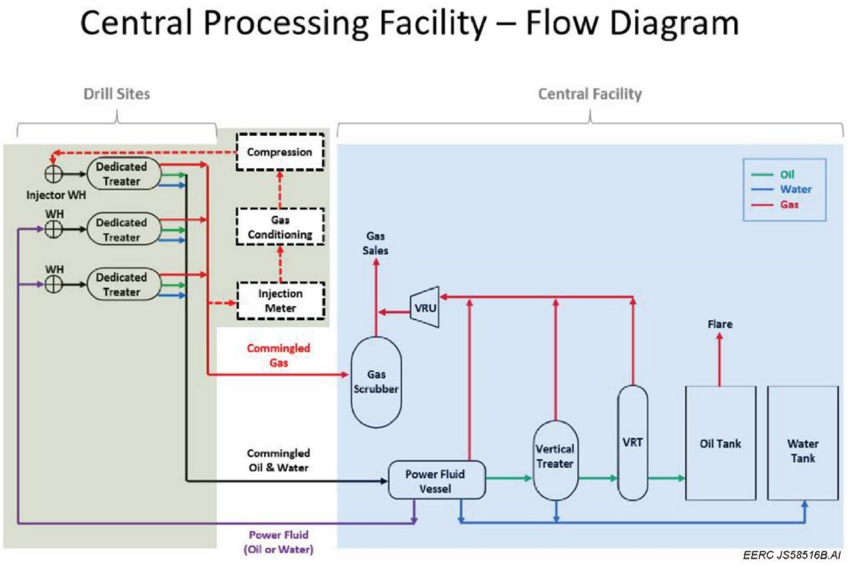

Figure 26. Leon–Gohrick DSU surface facility process flow.

Based on piping and instrumentation diagrams, simplified models of Leon and Gohrick surface facilities were developed that included major equipment and pipe runs. These simplified models, along with related operating conditions and produced fluid (oil, gas, and water) property data, were input to a steady-state process simulator to generate predictions of equipment performance.

Overall, the facility process simulation work indicated that existing facility capacity would be adequate to accommodate any realistic production rate resulting from the planned rich gas EOR project design conditions. Historical peak conditions and potential production limitations are shown in Figure 27. Field tests of rich gas EOR in the Leon–Gohrick DSU showed that the reservoir-to-surface simulation procedure developed in the EERC met the requirements of EOR tests in the field.

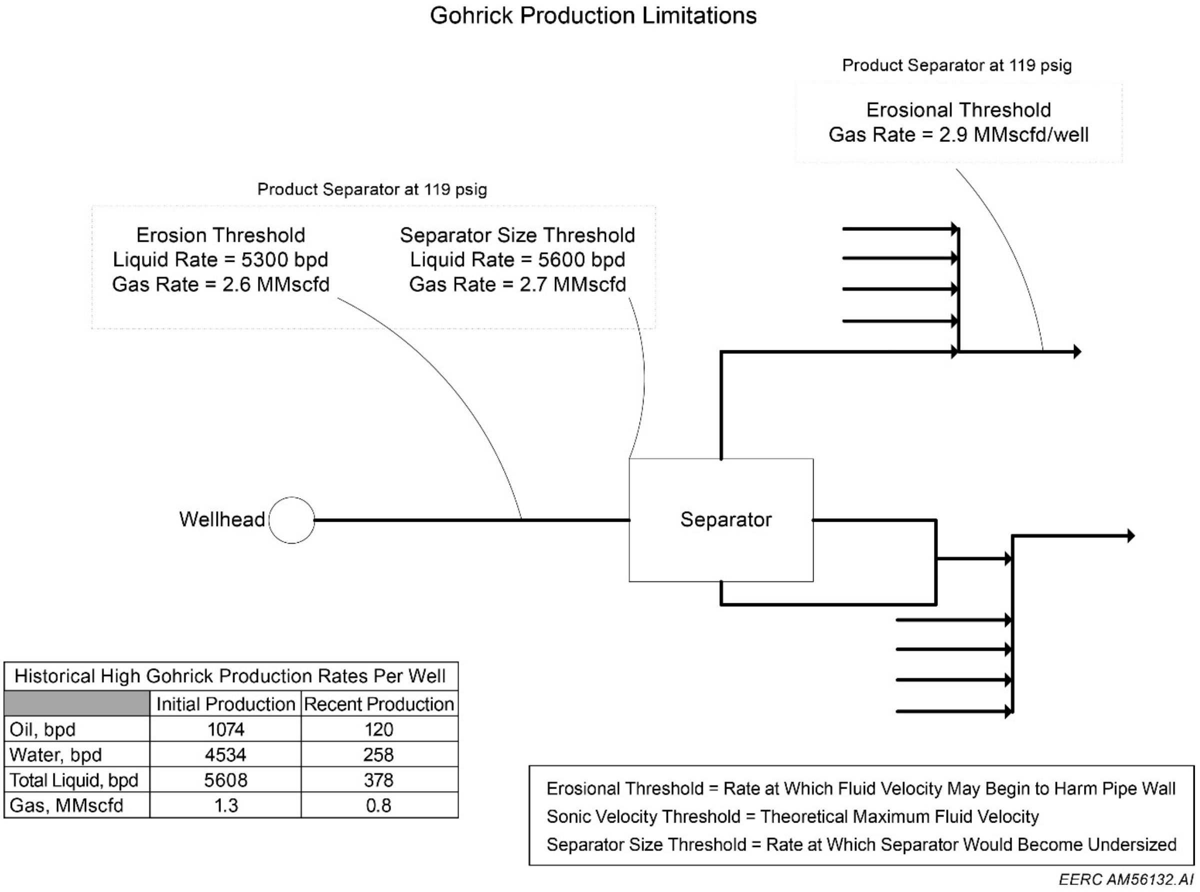

Historical High Gohrick Production Rates Per Well		
	Initial Production	Recent Production
Oil, bpd	1074	120
Water, bpd	4534	258
Total Liquid, bpd	5608	378
Gas, MMscfd	1.3	0.8

Erosional Threshold = Rate at Which Fluid Velocity May Begin to Harm Pipe Wall
Sonic Velocity Threshold = Theoretical Maximum Fluid Velocity
Separator Size Threshold = Rate at Which Separator Would Become Undersized

Figure 27. Gohrick facility constraints and historical peak conditions.

Subactivity 4.2 – Modeling of Subsurface EOR Components

Methodology for Reservoir Modeling

The methodology presented in this study mainly focuses on developing geologic and simulation models at different scales for the Leon and Gohrick wells. These models include a geologic model and two simulation models: a multiwell single-fracture-stage model and a DSU model with embedded discrete fractures. The goal was to investigate flow behavior in tight reservoirs to predict gas injection EOR performance by simulating different gas injection scenarios. A variety of well logs and rock–fluid data sets were used to characterize the formation in the study area. A database with fundamental reservoir properties, including porosity, permeability, pore throat size, and mineral composition, etc., for the Bakken and Three Forks Formations was also used to support the modeling activities. Two gridding approaches, a gridding-based planar fracture model and an embedded discrete fracture model (EDFM), were used to construct the fracture matrix grid blocks in the models.

Geologic Model Development

A Bakken/Three Forks model was created for a DSU-sized area (approx. 2 mi × 1 mi) in northwestern North Dakota on the western flank of the Nesson Anticline. Well tops and seismic data were used to correlate formation structure throughout the model area. The Lodgepole, Bakken, Three Forks, and Birdbear Formations were divided into several zones within the model. Targets of interest, the Bakken and Three Forks Formations (Figure 28), were further divided according to nomenclature used by NDGS (LeFever, 2007). Interpreted well logs were upscaled into the gridded 3D volume and distributed. Each modeled zone, as shown in Figure 29, was populated with geophysical properties (porosity, permeability, etc.) representative of each lithofacies, estimated from core measurements and geophysical logs originating within the DSU and the surrounding region.

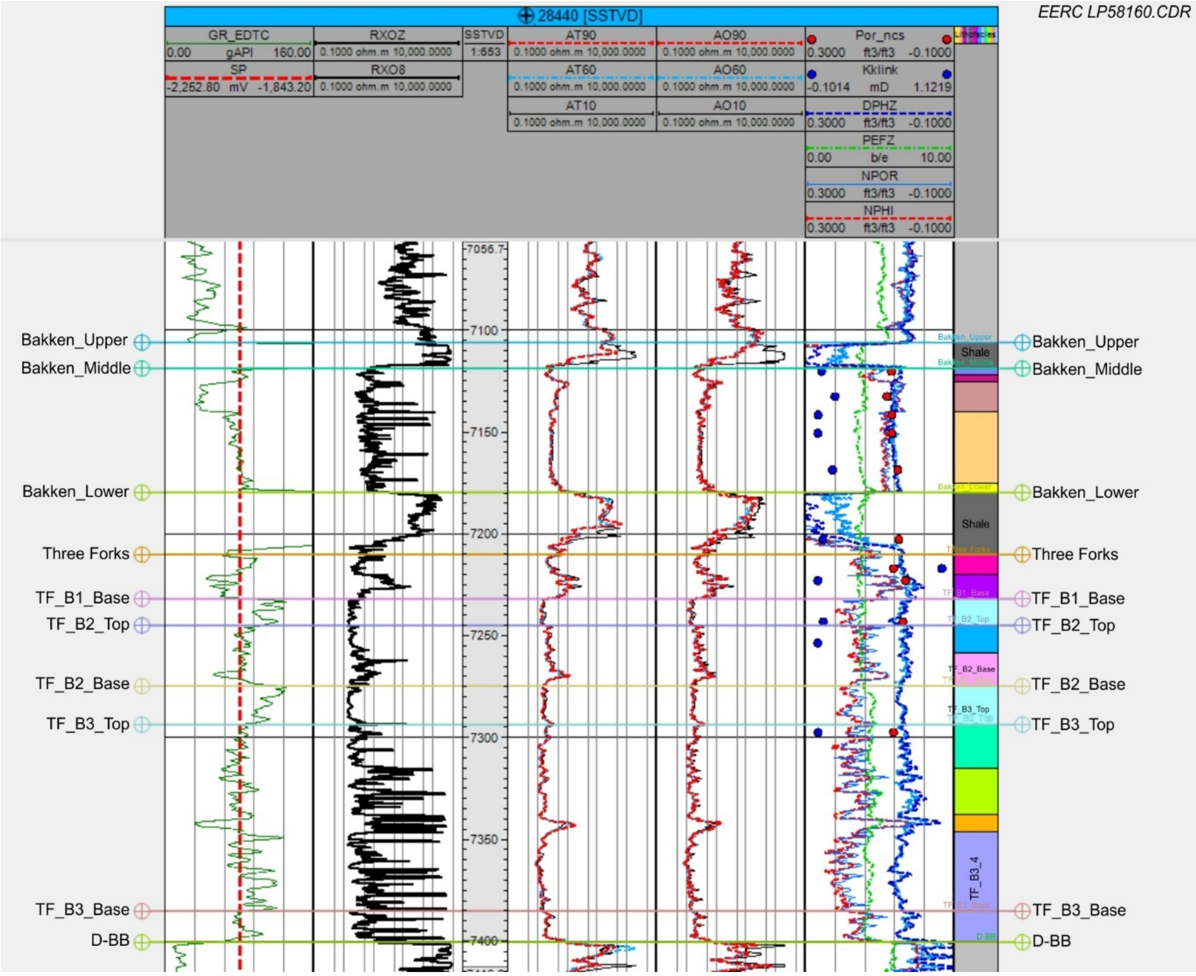

Figure 28. Well logs showing Bakken and Three Forks Formations.

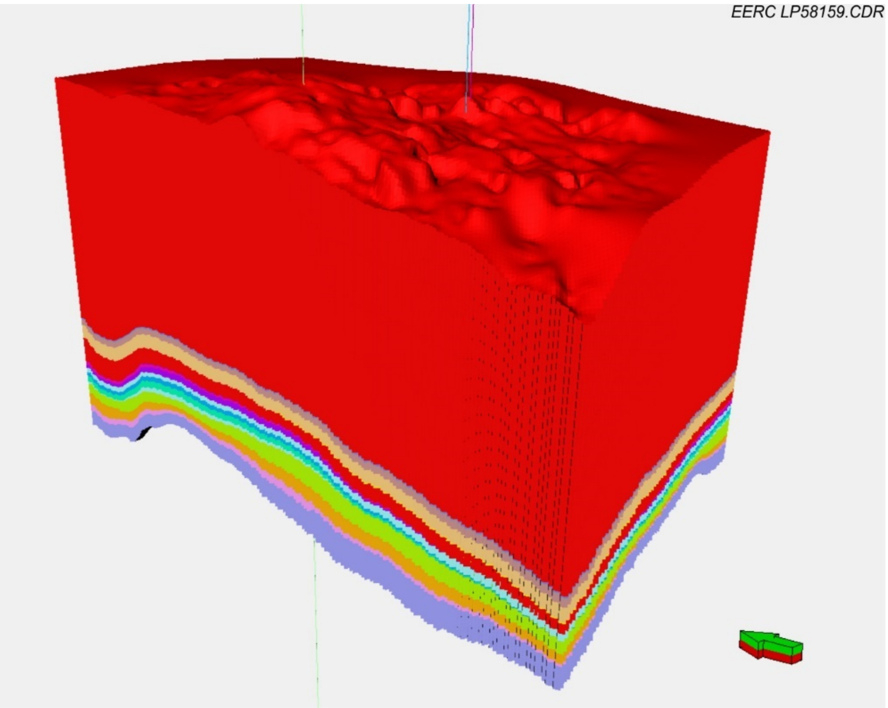

Figure 29. Southwestern view of modeled volume. Each color represents a modeled zone, 25× vertical exaggeration.

Additionally, a discrete fracture network (DFN) was created for the modeled area. A previously collected and processed seismic volume was used for the generation of the DFN. After the seismic volume was converted from time-depth to elevation-depth, a volume encapsulating the desired target space (Lodgepole to Birdbear) was clipped to help save computing time as well as to help the employed algorithm focus on local fractures. The clipped volume then was submitted to a preconditioning workflow to help limit non-fault-related noise on fault attributes within the data. Structural smoothing, dip deviation, variance (edge), and chaos attributes were all considered when the clipped seismic volume was preconditioned. Schlumberger's "ant tracking" algorithm from its Petrel modeling software was used to detect fractures from the preconditioned seismic volume. Filtering out any unwanted fault dip angles and outliers was necessary during this step because of noise that preconditioning could not mitigate. Multiple iterations of the algorithm were employed to further accentuate suspected fractures in the modeled volume, culminating in a new seismic attribute which essentially contains detected fractures. Aperture and permeability attributes were then edited manually before upscaling the detected fractures into the gridded 3D volume. These values are typically gathered from measured core, image logs, or thin sections but were not readily available from collected core; instead, values collected within the region were used.

Equation of State (EOS) Model

Compositional reservoir simulation requires an EOS model, which was created to replicate the data from pressure, volume, temperature (PVT) tests in order to represent the fluid properties during the simulation. PVT data parameters that were matched included bubble point pressure, differential liberation, constant composition expansion (CCE), separator GOR, and formation volume factor (FVF). To match those PVT data, the reservoir fluid sample from Gohrick 5TFH was characterized using a model with a total of nine fluid components. Individual lighter gas components were separated, and the heavier oil components were lumped into four pseudocomponents in order to improve simulation efficiency. Defining the gas components as individual components allows evaluation of different combinations of injection gas composition. The simulated injection gas composition was based on the project's proposed injection plan and is shown in Table 4.

Table 4. Proposed Injection Composition

CO_2	N_2	C_1	C_2	C_3	IC_4–NC_5	C_6–C_{10}	C_{11}–C_{20}	C_{21}–C_{36}
1%	3%	62%	19%	9%	6%	0%	0%	0%

Development of Simulation Models

Oil production from the low-permeability Bakken and Three Forks Formations mainly relies on fractures for fluid flow from the tight but oil-rich matrix to production wells. The key factors in unconventional oil and gas reservoir simulation include fracture–matrix flow and fracture–matrix interactions (Jin and others, 2017b, c; Xu and others, 2017). Depending on the well and fracture settings, the complexity level of simulation models can be described as shown in Figure 30. The simple model is shown on the left. In this case, the fracture is perpendicular to the wellbore that was widely used in earlier simulation of unconventional reservoirs. This setting is convenient to set up in the model but is not representative for the case in this study. The nonorthogonal hydraulic fracture setting, shown in the middle, is more representative of the actual fracture profile in Leon and Gohrick wells; however, it increases the simulation time and numerical difficulties and is less convenient to set up in the model. When adding the natural fracture networks in the system, as shown on the right, it makes the simulation model very difficult to run with a multiple-well pattern.

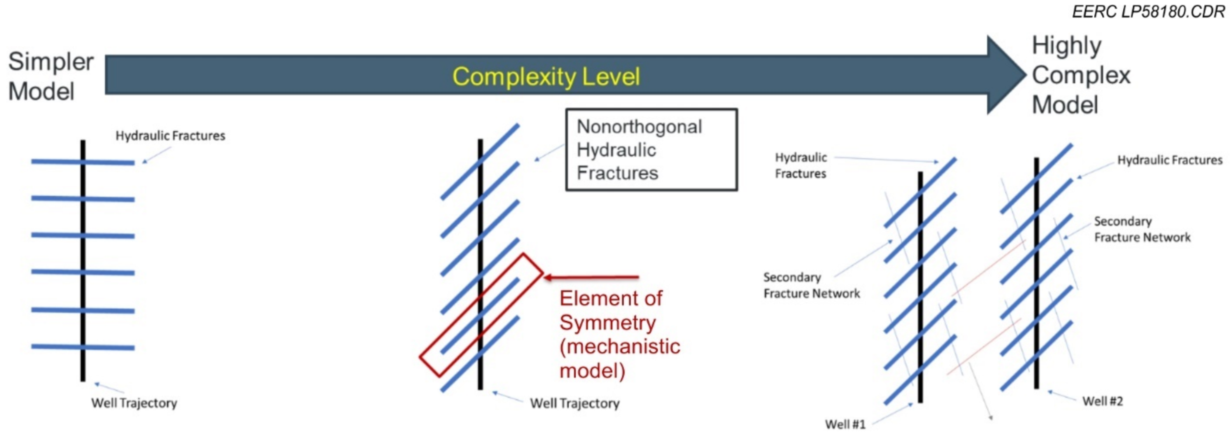

Figure 30. Complexity level of simulation models.

Multiwell Single-Fracture-Stage Modeling

To address the challenges for multiple-well-pattern simulation models of the Bakken, a single-stage simulation model consisting of multiple wells but only one hydraulic fracture stage from each well was developed based on the geologic model to consider the interference effects between wells (Figure 31). This approach was chosen in close consultation with LR reservoir engineers. The purpose of this modeling effort was to provide LR engineers with an order-of-magnitude understanding of expected injectivity and fluid behavior in the reservoir that would support the design and operation of the pilot (e.g., proper sizing of surface infrastructure, including compression). The dual-porosity (Warren and Root, 1963) and multiple interacting continua (MINC) (Cai and others, 2015; Pruess and Narasimhan, 1985; Pruess, 1992) methods were tested. Both methods allow each simulation block to have up to two porosity systems in an attempt to solve the interblock flows between fracture–matrix systems. However, the models with those systems would not be able to execute properly in the compositional simulator because of the complexity, the extremely low matrix permeability in shale, and interblock matrix-to-fracture flow challenges in those systems. Therefore, a grid-based approach for multiple hydraulic fractures was created. Using this approach requires generating a reasonably fine grid representation of the fracture using a planar hydraulic fracture model to represent the corresponding number of clusters in each fracture stage. In this approach, it is possible to accurately model the non-Darcy response if it is present in the fracture. The hydraulic fracture orientation is nonorthogonal to the wellbore direction, based on the measured geomechanical properties of the reservoir. Utilizing this single-stage model would mimic the fluid flow in every fracture at each single stage and the fracture connections/interferences of each well in the same producing unit. This design also allows a reasonable simulation time, assuming each single stage of fractures has the same properties and performs uniformly along the wellbore. Hydraulic fracture half-length was set at the length that would result in the fracture connections from offset wells, as this is one of the impactful parameters that were under investigation. These results could then be upscaled accordingly based on the total number of fracture stages in the well.

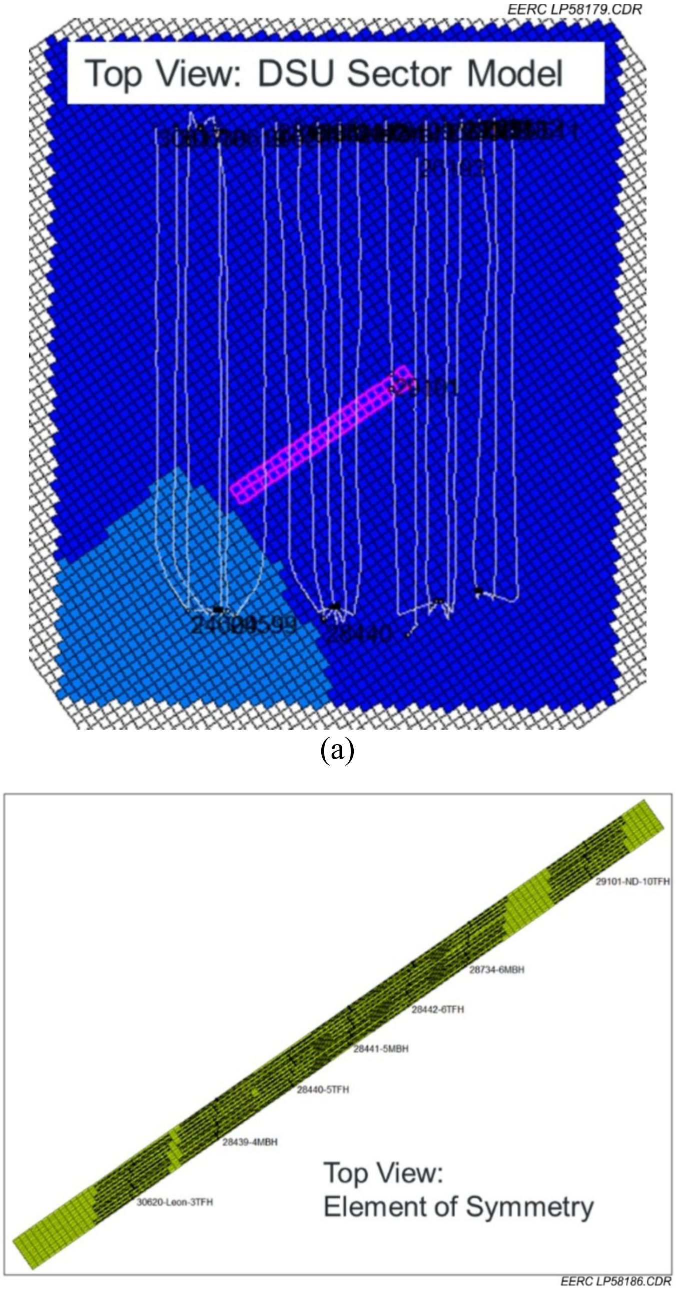

(a)

(b)

Figure 31. Illustrations of single-stage simulation model: a) top view of DSU sector model showing area of single-stage model, highlighted in pink; b) top view of single-stage model; and c) cross-sectional view of single-stage model (continued).

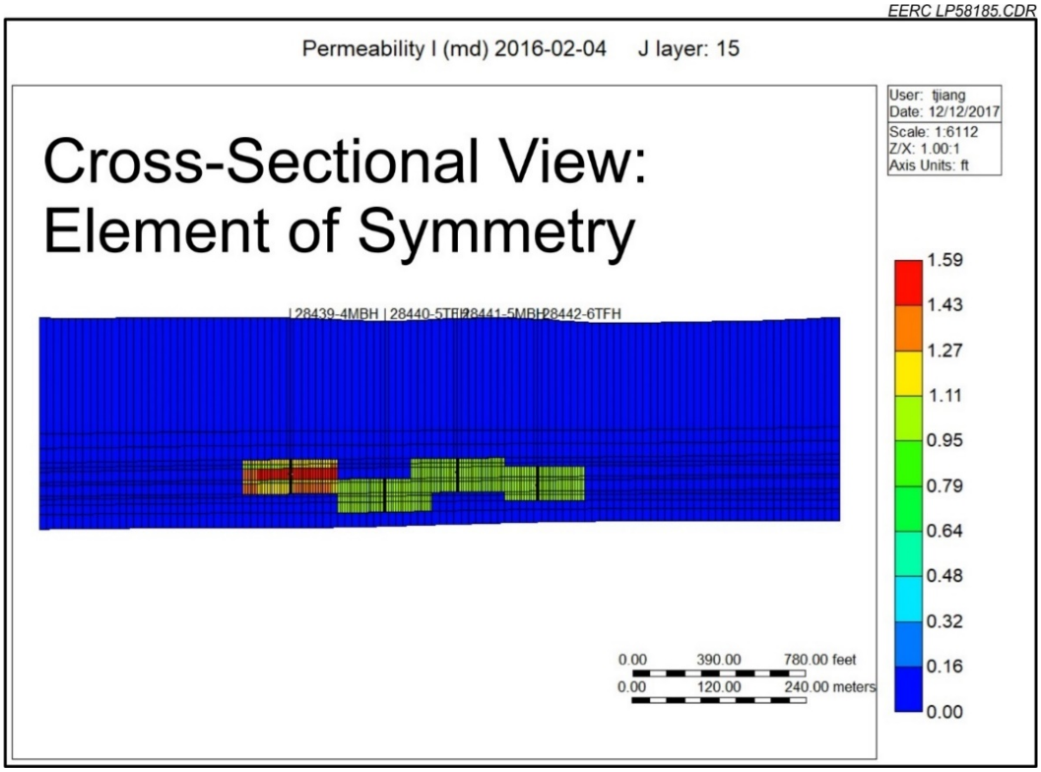

(c)

Figure 31 (continued). Illustrations of single-stage simulation model: a) top view of DSU sector model showing area of single-stage model, highlighted in pink; b) top view of single-stage model; and c) cross-sectional view of single-stage model.

History Match

The single-stage model consists of seven wells in total: five Gohrick wells and two offset wells—one from the Leon well pad on the west and another one from North Dakota State well pad located immediately to the east of the Gohrick wellpad. The history match attempt was made based on daily operational data provided by LR and using averaged fluids production based on the number of stages for each well. History match efforts suggested that simulated water production in the first few months could not get a good match, an issue likely related to the hydraulic fracture cleanup period. Nevertheless, the overall fluid rate match was good for selected wells prior to the pilot test, e.g., Well 28441, Gohrick 5MBH (Figure 32, solid line). Although there was no measured and recorded bottomhole pressure (BHP) for that producing period, it was believed that the bottomhole flowing pressure would be below 1000 psi, based on operator insight. It was found that to reduce the simulated BHP response to below 1000 psi by using matrix permeability reduction, the gas rate match was compromised (Figure 32, dotted line), although oil and water rate matches were intact. BHP reduction became a continuing challenge while honoring fluid production rates. A possible reason for this limitation is that the model averages production for each stage and neglects the geologic heterogeneity along the wellbore. It also neglects the fact that practical fracture performance can be different for each stage from heel to toe. Although limitations

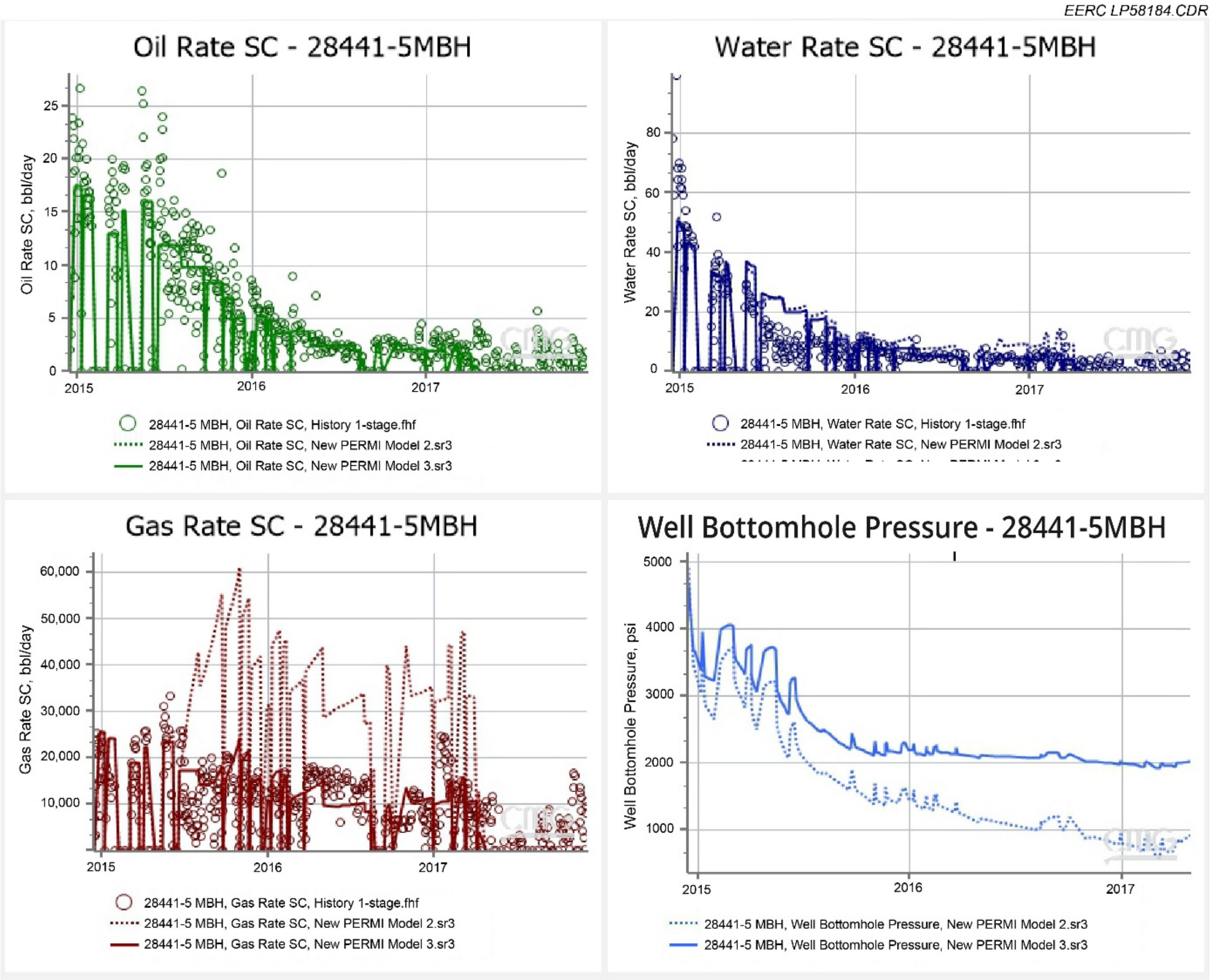

Figure 32. History match of Gohrick 5MBH fluid rates and BHP. Dotted lines show model results from lower permeability scenario, resulting in lower pressure response.

exist, the model served its purpose in guiding the design of the Stomping Horse pilot infrastructure and providing insight into how gas injection EOR operations could improve existing well performance.

EOR Forecasting

During the EOR evaluation, a wide variety of different injection cycles, injection volumes, pressures, and injection fluid compositions were evaluated. A detailed discussion of the simulation parameters, assumptions, and approaches is beyond the scope of this report. The EOR scenarios described and discussed below were selected to serve as illustrative examples that predict how different operational parameters may affect EOR operations in a Bakken reservoir.

Injection/production scenario tests of 1 and 3 months suggest that to inject gas at 1 MMscfd for 1 month would not result in significant oil recovery improvement compared to the case that continues using primary depletion production. Injection rate constraints were evaluated by testing

1 and 3 MMscfd for each well for 3 months before returning the wells to production. It was found that, with the 1-MMscfd injection rate, there is no significant improvement in production compared to depletion. If injection at 3 MMscfd is used for 30 years, an incremental recovery of 4% (Figure 33) to 26% (Figure 34) is calculated. The difference between these two outcomes is dictated by the well producing BHP constraint assumption. If the initial BHP is low, around 500 psi, injection of 3 MMscfd for 3 months would not be able to pressurize the formation enough to observe a significant EOR effect. In the other case, when the simulated BHPs for each well range from 1200 to 1400 psi, injecting 3 MMscfd is able to better pressurize the reservoir and create a 26% incremental recovery. It is noteworthy that the 1200- to 1400-psi BHP case does not consider the potential for reservoir blowdown to 500 psi near the end of project life, which would further improve recovery.

Injecting gas using a WHP (wellhead pressure) constraint of 1500 psi was also evaluated. Simulations showed that a 59%–63% oil recovery increment can be observed after 30 years of operation, and the estimated daily gas injection rate ranges between 19 and 30 MMscfd. Again, the difference in the result is due to the assumed producing BHP. The 500-psi BHP constraint results in a higher injection rate (Table 5). However, the higher injection rate results in less recovery. Again, the 1200–1400-psi BHP case does not consider the potential for reservoir blowdown to 500 psi near the end of project life, which would further improve recovery.

Different injection gas compositions were simulated to evaluate the potential effect of ethane and propane enrichment on incremental oil production performance. During those tests, the wells were constrained by an injection rate of 3 MMscfd for 3 months at each injection period and the

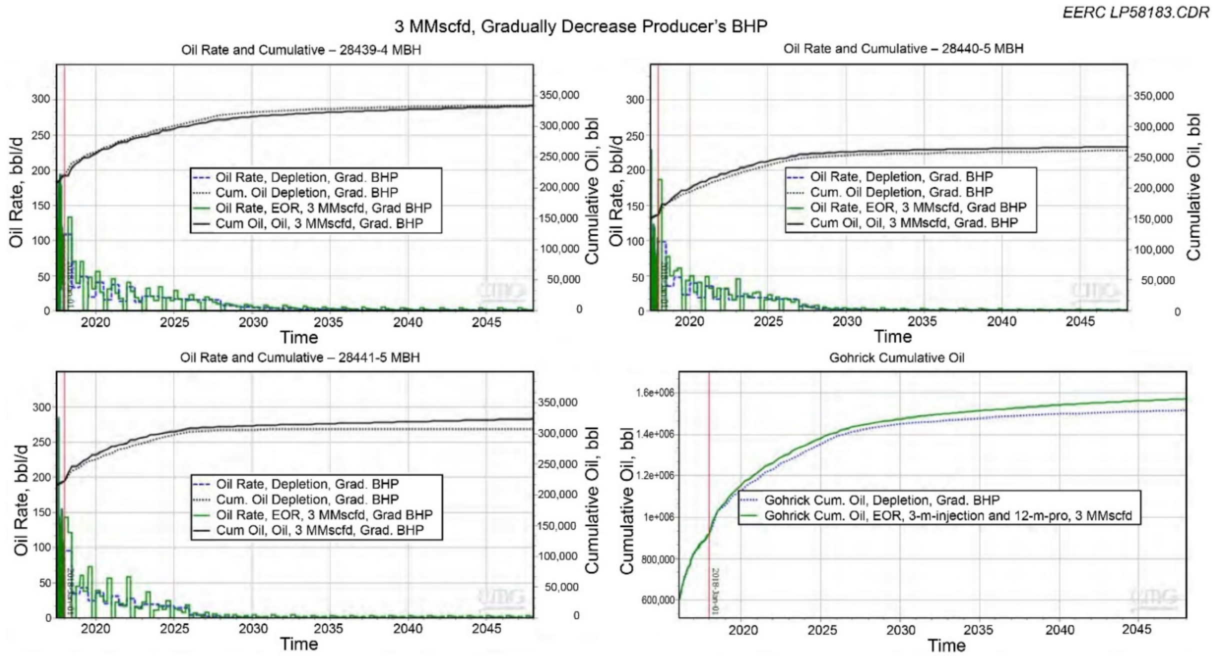

Figure 33. Gohrick pad oil recovery increment with 3-month injection cycle for each well at constant 3-MMscfd injection rate and BHP constraint of 500 psi. Modeling predicts EOR operations under these conditions yield 4% incremental recovery.

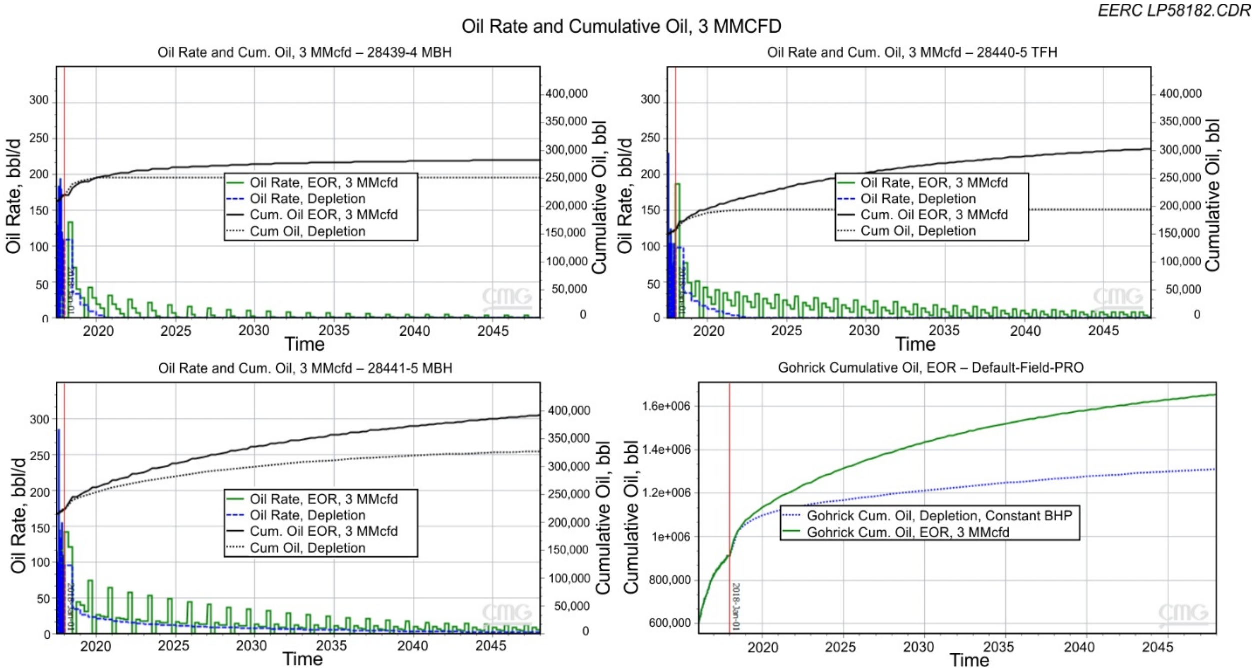

Figure 34. Gohrick pad oil recovery increment with 3-month injection cycle for each well at constant 3-MMscfd injection rate, using simulation estimated BHP of 1200–1400 psi. Modeling predicts EOR operations under these conditions yield 26% incremental recovery.

Table 5. Summary of Simulation Results with Different Injection Conditions

Injection Condition ➔	**WHP 1500 psi**	**WHP 1500 psi**	**Surface Rate 3 MMscfd**	**Surface Rate 3 MMscfd**
Producing BHP Constraint	1200–1400 psi	500 psi	1200–1400 psi	500 psi
Expected Injection Rate	Up to 19 MMscfd	Up to 30 MMscfd	3 MMscfd	3 MMscfd
Incremental Recovery above Depletion	63%	59%	26%	4%

producing BHP constraint was kept constant for each well. Gas was injected into one well at a time while other wells continued producing. The MMP for each composition was calculated through the tuned EOS model, and it was found that enriching the ethane and propane composition in the injected gas would result in lower MMPs. Simulations suggested that increasing propane 20% while reducing methane 20% could boost the production increment from ~4% to ~10%. Eliminating the 3% nitrogen from the gas stream would also improve performance, but the improvement was small.

Conclusions of the Stomping Horse Modeling Activities

The BPS in the Stomping Horse area was carefully characterized, and a geologic model, a tuned EOS model, and simulation models were developed to investigate different scenarios involved in the rich gas injection EOR process at the Stomping Horse Complex. Through the single-stage mechanistic model, simulation runs showed that gas can be injected into the tight, fractured Bakken Formation and gas injection has an incremental oil recovery in a 30-year production period when enough gas is injected. In addition, enriching the injection gas with ethane or propane would also improve the recovery factor. The gridding-based simplified hydraulic fracture description was convenient to set up, and the single-stage model could effectively simulate the primary depletion process and EOR process without numerical difficulties. However, this approach cannot be applied to the full DSU model because it will significantly increase the total number of grid blocks and require substantial local grid refinement for the fracture descriptions. Those critical challenges to the simulation process will cause slow running speed and numerical convergence failure because of pressure interference and fluid communication between fractures and wells.

ACTIVITY 5.0 – PILOT PERFORMANCE ASSESSMENT

Location and Well Pattern

LR's test site within the Stomping Horse complex, informally known as the Leon–Gohrick DSU, comprises Sections 8 and 17 of T.158N., R.95W. It has been fully developed with 11 wells, each with a nominal horizontal section of 10,000 ft, as shown in Figure 35. Six wells are completed in the Middle Bakken, and five are completed in the first bench, or upper part, of the Three Forks Formation. The first two wells, one into the Bakken and one into the Three Forks, were drilled and completed from the Leon-North well pad at the northern edge of the DSU prior to acquisition of the property by LR. Nine wells were drilled and completed by LR from two well pads constructed at the southern edge of the DSU. The Leon-South pad hosts two Bakken and two Three Forks wells, and the Gohrick pad supports three Bakken and two Three Forks wells. Figures 36 and 37 further illustrate the well pattern in cross-sectional and 3D views. LR presented its Case No. 26035 before NDIC on September 21, 2017, requesting approval to use the wells of the Leon–Gohrick DSU for injection in execution of the EOR pilot test. The project was approved as Order 28449 by NDIC on October 24, 2017. Equipment for the pilot injection test was installed with the intent of being able to direct gas to any well on either of the two southerly well pads. A stipulation of the permit was that only gas produced from wells within the Leon–Gohrick DSU could be used for the injection tests. Injection operations commenced on July 17, 2018.

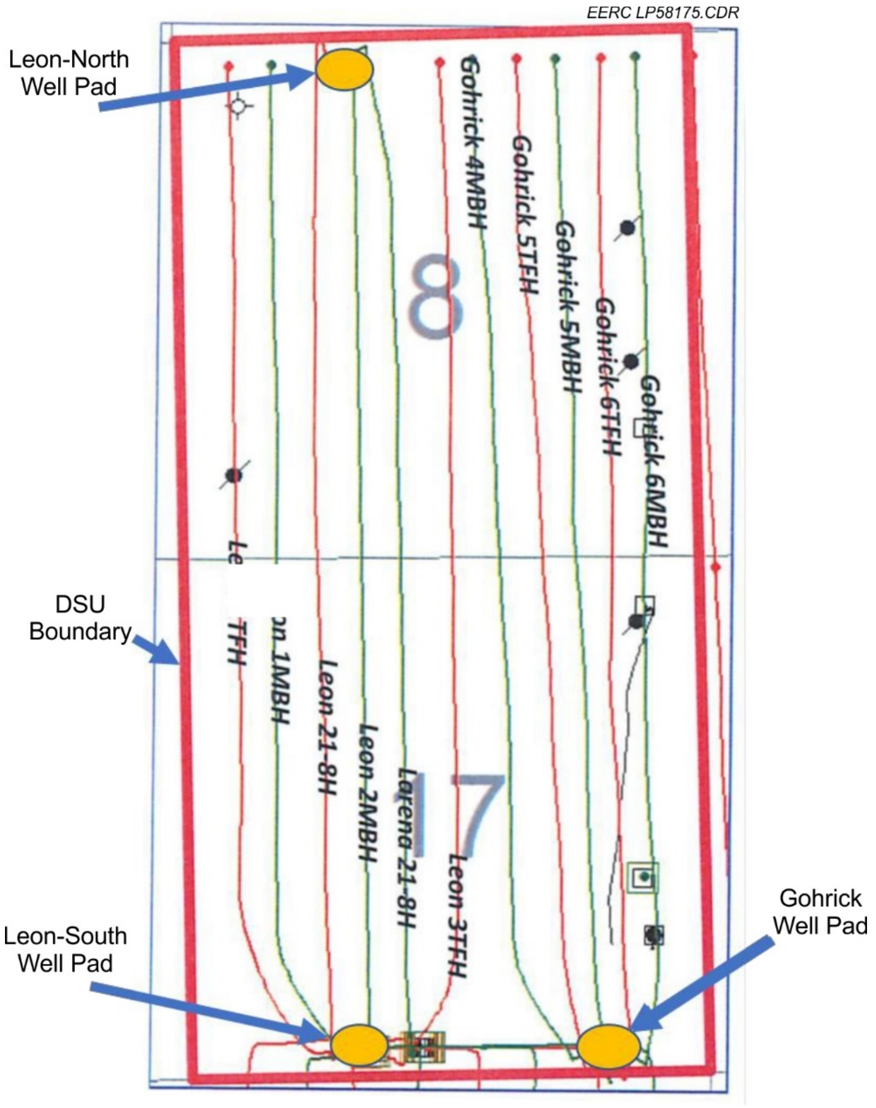

Figure 35. Leon–Gohrick DSU well pattern.

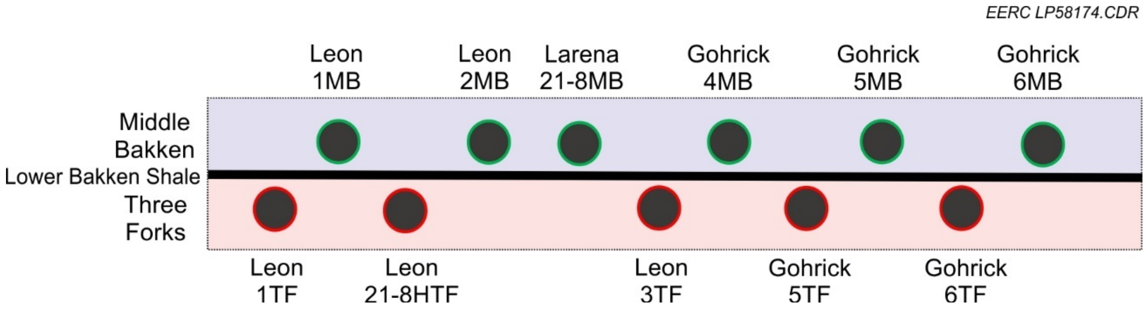

Figure 36. Leon–Gohrick DSU east–west cross section (not to scale). Average distance between two adjacent wells is ~400 ft. Average distance between two wells in the same formation is ~800 ft.

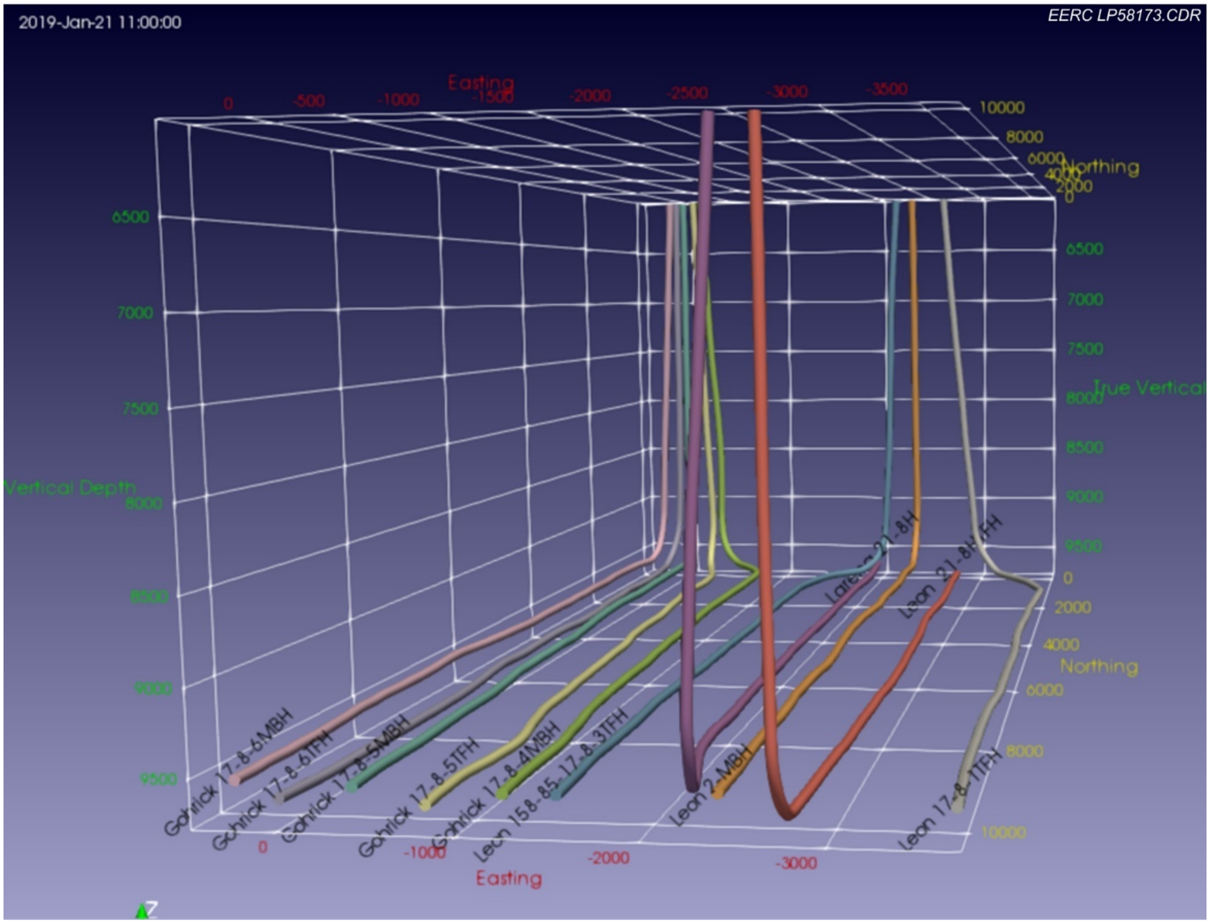

Figure 37. 3D illustration of well lateral layout of DSU (looking south). Note: The Leon 1MBH is absent from this image.

Hydraulic Fracturing

Wells drilled in the DSU by LR have benefitted from LR's advanced approach to hydraulic fracturing (Pearson and others, 2013, DW Energy, 2016; Lolon and others, 2016; Weddle and others, 2017; Bommer and others, 2017), which ensures the wells are effectively stimulated. LR has used real-time offset data collection methods during fracturing operations to demonstrate fracture network connectivity between wells completed in the Bakken and between wells completed in the Bakken and Three Forks. The wells have been completed using cemented liners, then plug and perf hydraulic fracturing methodology, with the number of stages ranging from 27 to 50 and eight to 15 perforation clusters per stage. Slickwater fracture treatments were typically performed at rates of 80 barrels per minute (bpm), with placement of 4 million to 6 million lb of proppant.

The effectiveness of the fracture treatments ensured good production performance. However, in the context of injecting rich gas as an EOR fluid, the apparent high degree of connectivity between wells was an early cause for concern with respect to building reservoir pressure, maintaining injection conformance, and minimizing fluid breakthrough.

Jet Pumps

After completion, wells were turned to natural flow for cleanup and an initial production period. After the period of natural flow, the wells were put on artificial lift using a jet pump system. Jet pumps make use of a downhole venturi nozzle arrangement to provide additional liquid lifting capability. A power transmission fluid (lease crude) is pumped from the surface, down the tubing, and through the venturi. Well production enters on the downstream, low-pressure side of the venturi and mixes with the power fluid before rising to the surface up the tubing/casing annulus. All fluids are run through the surface separation system, with a fraction of the oil recirculated as the power fluid.

For the Leon–Gohrick DSU, the jet pump system was designed for well production rates of 350–2000 barrels of fluid per day (bfpd). The jet pump system offers the benefits of using a minimum of moving parts, minimizes well workovers and downhole costs, and is tolerant of produced solids. However, larger fluid volumes must be processed through the separation system, and metering of fluid volumes is more complex. The accurate metering of fluid volumes becomes more important during execution of the pilot test. Over the course of a well's operational lifetime, and as a well's total fluid production rate falls below the jet pump operating range, the system is replaced by conventional rod pumping equipment.

Compression

Compression arrangements was one of the more challenging aspects for the pilot test. An ambitious project development schedule and the relatively short lifetime of the pilot test led LR to first arrange a short-term rental of two moderate-capability compressors while higher-pressure options continued to be investigated. Low- to medium-pressure compressors of this type are relatively available and are commonly used for gas lift operations. They can be procured from existing inventory with relative ease in a timely manner. LR's rental compressors, pictured in Figure 38, each had a maximum discharge pressure of 1400 psi and a rate of 1.4 MMscfd.

High-pressure, large-capacity compressors tend to be custom-built to specific requirements. Compressors operating above 4000 bhp (brake horsepower) or requiring pressure ratings of 5000 psi or above require 12–24-month lead time. LR was able to avoid such a long lead time by procuring a refurbished compressor with a maximum discharge pressure of 4200 psi at a rate of 3 MMscfd, pictured in Figure 39. Operating conditions for both compression solutions are summarized in Table 6.

Compression of rich gas will always require special attention to avoid condensation of NGLs and compressor damage. The combination of gas composition, pressure, and temperature must be evaluated to maintain gas phase throughout the compressor. Liquid recovery was not intended with either compressor package. The compressors were operated slightly warmer than usual in an attempt to keep as much of the richer gas components in the injection stream as possible. Also, actual compression pressure was not very high (<1500 psig), so NGL knockout was low, based on numerical modeling efforts. During operation, there was likely some liquid accumulation in the compressor knockout pots, but there are no available data.

EERC LP58172.CDR

Figure 38. Rental compression units.

EERC LP58171.CDR

Figure 39. Refurbished high-pressure compressor.

Table 6. Maximum Operating Conditions During Compressor Operations

File No.	Well Name	Max. Rate, Mscfd	Max. Inj. WHP, psi	Max. Inj. BHP, psi	Days of Injection	Cumulative Mscf	
30620	Leon 3TF	1143	1267	1916	20	10,822	Rental compressor
30619	Leon 2MB	874	1248	NA	19	13,775	Rental compressor
28441	Gohrick 5MB	2221	607	802	36	41,724	Refurbished compressor
28439	Gohrick 4MB	1961	1117	1885	65	74,561	Refurbished compressor
28442	Gohrick 6TF	2008	996	1431	15	17,410	Refurbished compressor

Field Pilot Execution

The Stomping Horse pilot testing began on July 2, 2018, with the initiation of field data collection. An extensive data collection and reservoir surveillance program at the site was carried out over the course of the pilot testing activities, including monitoring of oil, gas, and water rates; daily gas sampling from four nearby wellbores to be used for GC to identify changes in composition; BHP monitoring in six wellbores; and a tracer study.

Injection operations commenced on July 17, 2018. Injection proceeded sequentially through five wells, using six injection periods, until injection operations ended on May 30, 2019. A total of 160 MMscf was injected during that time, with periods of operational shutdown between injection periods. Figure 40 shows the progress of injection over time. Figure 41 indicates the relative well positions and sequence of injection, with the quantity of gas injected at each well.

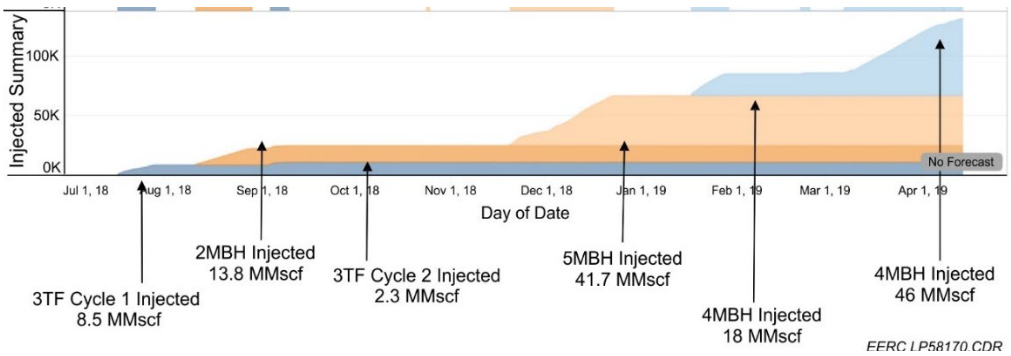

Figure 40. Leon–Gohrick injection pilot test profile. Smaller compressors were used for injection during summer 2018. Use of the larger compressor started in fall 2018. Total of 160 MMcf of gas was injected in five wells during six different injection periods.

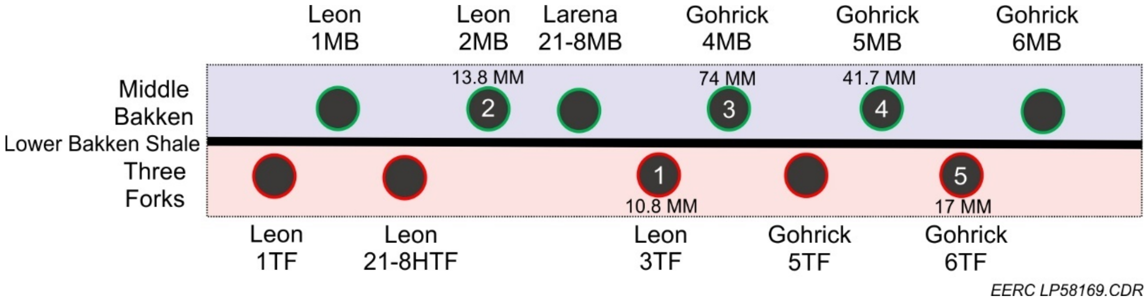

Figure 41. Cross section of well pattern with injection well sequence numbered 1 through 5 and quantities of injected gas (not to scale).

Injection Rates and Pressures; Production Well Responses

Daily production or injection data were collected for all 11 wells in the DSU. The specific data generated by these tests are considered to be proprietary and confidential by LR, and those data sets are not included in this report. However, trends and relationships observed in those data can be discussed in general terms. Some selected data on BHP relative to cumulative gas injection for the five injection wells are provided in Figure 42. Generally, BHP increase was modest for wells during their injection periods and none achieved sustained pressure above MMP. The Leon wells were found to be easier to pressure up than the Gohrick wells, and pressure buildup was easier to attain in the Three Forks wells than in the Bakken wells. The data also indicated two stages of pressure lifting: fracture filling and produced volume filling, with each type of filling displaying different slopes. Pressure rapidly fell back to preinjection level after injection stopped. Offset wells frequently saw a very rapid response; gas tracer breakthrough was observed within 48 hours, often followed by an increase in GOR. Offset producing wells were typically shut in after observed gas breakthrough. After injection, wells returned to production experienced a brief transient period of production increase (flush production).

Detailed analysis of the tracer data to estimate fluid flow rates and volumes between wells within the Leon–Gohrick DSU were complicated by the fact that the jet pumps use oil from the Leon–Gohrick DSU as power transmission fluid. However, the tracers yielded information about injection containment within the target reservoir by serving as a unique means of monitoring for any migration of injected gas outside of the Leon–Gohrick DSU. Analyses for the tracers in wells outside of the Leon–Gohrick DSU showed only a minor concentration of tracer in one gas sample from the westernmost well of the North Dakota State DSU, which is located immediately to the east of the Leon–Gohrick DSU. In this sense, the tracer study provided evidence that the injected rich gas was effectively contained within the target reservoir.

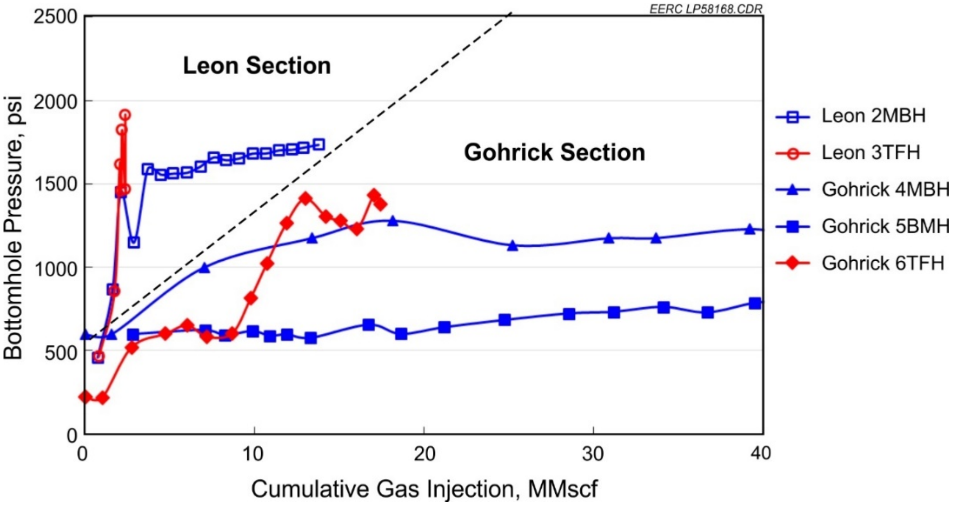

Figure 42. Relationships between BHP and cumulative gas injection for the five injection wells.

Interpretations from the Pilot Testing

The intent of the pilot test was to inject produced gas to locally increase reservoir pressure to miscible conditions which, in turn, would swell the oil and reduce viscosity so that larger quantities of oil could be produced when the well was returned to production and injection rotates to the next well. Although some degree of pressure buildup in the reservoir was achieved, with some wells gaining and maintaining over 1000 psi of BHP buildup, miscibility pressure between injection gas and oil in the fracture or matrix systems was not reached. At the start of pilot operations, BHP for producing wells, measured near the base of the well's vertical section, was variable but in the vicinity of 500 psi. Flowing pressure at the perforations along the horizontal section is not known, but the average distance from the pressure gauge to the wellbore–reservoir interface is approximately 5000 ft. Therefore, average sandface pressure along the horizontal wellbore would be higher than 500 psi. Similarly, pressure in the induced fracture network will be higher than the sandface pressure. The pressure drop across the fracture–matrix block interface is substantial but cannot be precisely measured. Measured BHP data collected during the test are invaluable as they provide new knowledge of the subsurface, but caution is advised when projecting those data to make estimates of average reservoir pressure. These differences may be at the heart of the observed simulation challenge to model the producing well/fracture system with a flowing BHP of ~500 psi and still maintain a gas production history match.

Data collected in 2015 as part of an LR proprietary study of fracture stage pressure communication at the Leon–Gohrick DSU and provided to EERC by LR showed clear pressure communication between individual hydraulic fracture stages in a new well and existing offset wells. Those data show that a variable degree of pressure communication was observed for nearly all fracture stages. During depletion, this implies that each fracture stage has a pathway to contribute, more or less, to the well's production. However, this also means that during injection, after significant depletion, the injection gas is more or less diverted by only a few fracture stages with the best communication and lowest pressure path to the offset producers. It is unknown how many fracture stages dominate reservoir flow in this way, their location along the horizontal well path, or how much variation to this behavior exists from one well to the next. The response of the Leon–Gohrick pilot test with frequent and fast gas breakthrough between wells is consistent with this description.

Therefore, to create a different outcome in future EOR attempts in the Bakken, it is imperative that pressure is maximized and pressure gradients are minimized in the fracture system to allow injected gas to more evenly penetrate as much of the fracture network as possible and, under favorable operations, to penetrate as much of the reservoir matrix as possible. Consideration should be given to choke back or temporarily shut in offset producers to minimize gas breakthrough and allow reservoir pressure to rise above MMP.

Although a high degree of communication between wells in the pilot DSU area was demonstrated, there was only minimal indication of communication between the pilot DSU and neighboring drilling units. Only minor amounts of gas tracer were observed in Well ND-State-10TFH immediately east of the pilot area. Wells in the DSU to the north of the pilot area were monitored for interference effects, but no effects were reported from that operator. On the west side of the pilot, three DSU wells were operating outside of the most westerly injector, Leon 2MBH. There was no observed interference in the next DSU to the west, which is operated by LR. Thus containment of the test to the pilot area was very good. Loss of containment was a concern during the design and regulatory approval phases of the project. Several reasons likely contributed to this outcome. No wells along the DSU boundary were used for injection, the quantity of injected gas was small compared to the size of the test area and limited general pressure buildup was observed, the test DSU was at an advanced state of depletion, and reservoir pressure may have been lower than that of surrounding drilling units, ensuring net fluid flow into the pilot area rather than out from it. Successful containment of the test within the designated DSU was an important achievement of the pilot test.

Lessons Learned for Future EOR Pilots in the Bakken

While it was difficult to definitively discern an increase in oil production at the Leon–Gohrick DSU as a result of the rich gas injection activities, a suite of valuable knowledge and insight was gained from the rich gas pilot injection activities at Stomping Horse. Lessons learned from the tests that may be readily applied to future EOR pilots in the Bakken include the following:

- The ability to inject gas into Bakken and Three Forks reservoirs and build pressure has been demonstrated, and injectivity is not a constraint on operations.

- Gas supply is a key factor in the successful outcome of pilot scale demonstrations in the BPS. Stomping Horse activities were impacted by limited natural gas supply.

- Gas breakthrough, inconsistent offset well production, and limited gas supply hinder rapid pressure buildup. An adequate supply of working fluid is essential.

- With respect to compression, considerable time and care are needed in the design and procurement of compressor solutions for rich gas injection, especially for discharge pressure above 4000 psi. The lead time to acquire larger compression systems needs to be considered when planning for an EOR pilot.

- Detailed pre- and posttest data on reservoir conditions and fluids production are essential for test and offset wells. A detailed understanding of the completions of the wells is also necessary for valid test result interpretations.

- EOR operations should be started before reservoir pressure becomes too depleted, ideally when reservoir pressure is still relatively close to MMP.

- Laboratory-based data on the effectiveness of potential working fluid compositions on MMP and the ability of working fluid compositions to mobilize oil from Bakken rocks over a range of expected reservoir conditions provided insight on designing operational parameters for the pilot tests.

- Primarily because of fracture connectivity and complex PVT behavior, numerical simulation is computationally heavy and places challenges on the modeling of large-scale DSUs to determine optimal strategies. These challenges need to be considered and accounted for when conducting the design phase of an EOR pilot test. The use of emerging modeling techniques, such as embedded discrete fracture network (EDFN) modeling, may be a means of improving simulation models for unconventional tight reservoirs.

- Multiple data sets and data types complicate rapid analysis and formation of insights about main mechanistic drivers occurring in the subsurface during a pilot. Real-time data would enable a framework to better monitor and enhance pilot analysis.

- Real-time data coupled with BDA and ML would enable a framework to better monitor reservoir response and enhance pilot analysis.

- Learnings from the Stomping Horse pilot were incorporated into a joint industry-/state-funded field pilot initiated in 2021 at the East Nesson Field located in Williams County, North Dakota. A fundamental focus of the pilot was to ensure adequate gas supply. The East Nesson pilot is separate from the activities that are the focus of this report.

ACTIVITY 6.0 – ADVANCED RESERVOIR CHARACTERIZATION FOR RICH GAS EOR

One of the objectives of Subtask 3.1 is to improve rich gas injection conformance and sweep efficiency, thereby maximizing the contact time of the injected fluid with the unswept matrix and improving the effectiveness of EOR. Understanding the mechanism for fluid flow in tight unconventional, hydraulically fractured reservoirs like the Bakken requires knowledge of petrographic and petrophysical rock characteristics, including wettability, relative permeability, and fracture distribution. Literature suggests that thermal maturity of shale may affect reservoir characteristics such as wettability, relative permeability, and natural fracture distribution (Li and others, 2016; Ojha and others, 2017; Sorensen and others, 2014). Literature also suggests that rock mineralogy strongly influences geomechanical properties such as brittleness which, in turn, can theoretically be used to predict the occurrence of fractures along a horizontal wellbore; however, detailed studies of this potential correlation in the Bakken are lacking (Kias and others, 2015; Nicksiar and Martin, 2013). All of these types of reservoir characterization data are elusive and generally site-specific, leading to uncertainty in estimates of wettability, relative permeability, and fracture network distribution used for modeling and simulation work. Results of Subactivties 6.1, Wettability and Relative Permeability Studies, and 6.2, Cuttings Characterization for Geomechanical Properties, are summarized below.

Subactivity 6.1 – Wettability and Relative Permeability Studies

Introduction

Efforts conducted under Subactivity 6.1 have applied advanced laboratory-based characterization techniques to determine wettability and relative permeability of Bakken rocks from areas of different thermal maturity in the North Dakota portion of the Williston Basin. Understanding the mechanism for fluid flow in tight unconventional reservoirs, which is essential for predicting rich gas EOR in the Bakken, requires knowledge of petrographic and petrophysical rock characteristics, including wettability and relative permeability. Petrographic characteristics include mineralogy, grain-to-grain relationships, and pore space within the bulk volume of a reservoir interval. The wettability of reservoir rocks is a controlling factor in the effective mobilization of in-place fluids. These parameters are important in tight unconventional resource development in that incremental recovery will be achieved through drainage of incrementally smaller fluid-saturated pores. Because matrix permeability is low in unconventional reservoirs, high capillary pressure is necessary to mobilize incremental oil. To understand the potential capillary pressure constraints, specifically in the presence of rich gas blends, direct measurements of interfacial tension (IFT), or the adhesion ability of one fluid in the presence of another, and contact angle are necessary to understand how the rich gas components can affect wettability which, in turn, will affect oil mobilization. To broaden the applicability of the results, determination of the relative permeability of oil to CO_2 and rich gas blends in Middle Bakken rocks have been conducted on samples representing different areas of Bakken productivity. These data are currently unavailable for site-specific reservoir parameters and will allow for improvements to predictive simulations of rich gas EOR performance across the Bakken play.

Method on the Measurement of IFT and Contact Angle

In this study, the pendant drop method was applied to measure the IFT of a liquid–liquid or liquid–gas system. In the pendant drop method, the drop is created from a needle (capillary tube) in a bulk phase (liquid or gas) inside a PVT cell. For the wettablity measurement, the contact angle method was employed to determine the angle between the surface of the liquid of the outline of the contact surface.

The commercially available system used in this study is designed to measure both IFT between two phases and contact angle between liquid and solid phase under high temperature and high pressure. The key components of the machine include IFT cell (viewable environmental chamber), metering pump (apply to work with accumulator to generate droplet), transfer vessel (storage of test fluids, such as gas and liquid), camera system with light source, PC, and software (capture the drop image, data collection, and processing).

Figure 43 illustrates the schematic of the experimental setup of the system. The IFT between two immiscible fluids is measured by introducing a droplet of the fluid with heavier density into a volume filled with the other phase (surrounding phase) with lower density; once the desired conditions of pressure and temperature are achieved, the camera captures the droplet shape image to determine the IFT using Equation 1, where ΔP is the density difference between the phases (g/mL), g is the local gravitational contant (cm/s^2), d is the maximum horizontal diameter of the unmagnified pendant drop (cm), and B is a shape parameter calculated from drop dimensions. The drop shape parameters are illustrated in Figure 44.

$$\sigma = \frac{\Delta \rho g d_e^2}{B} \qquad \text{[Eq. 1]}$$

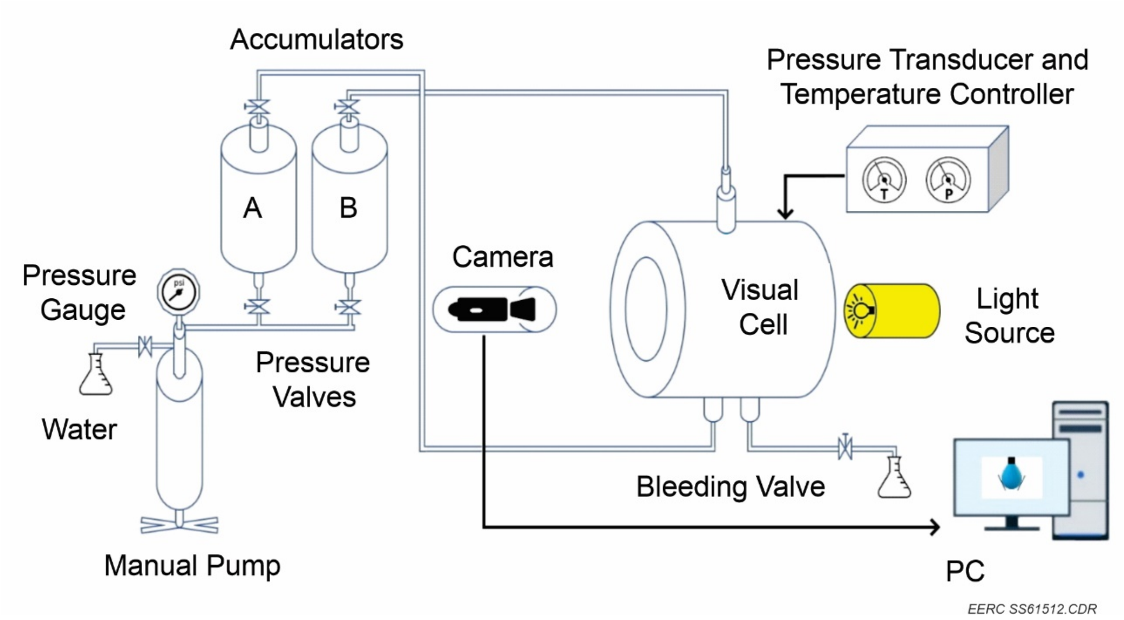

Figure 43. Schematic of the experimental setup.

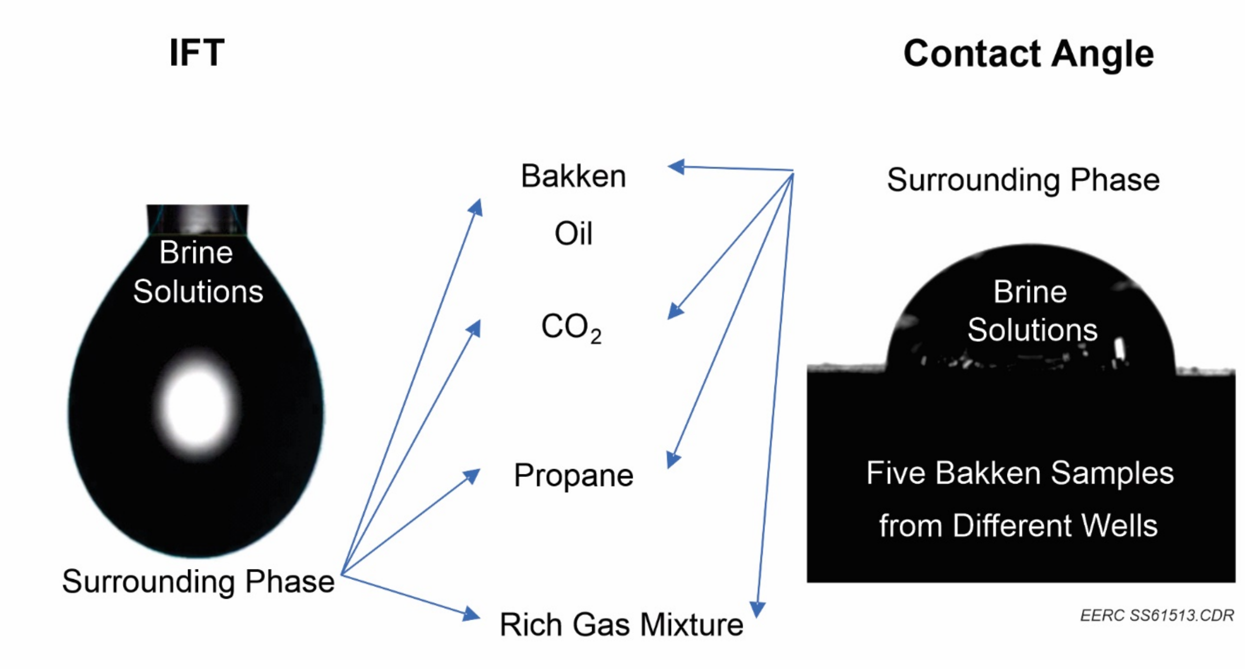

Figure 44. Experimental workflow for IFT and contact angle measurements.

For contact angle (wettability) evaluation, the rock sample is loaded into the view cell, the chamber is filled with the lower density surrounding phase, and then a droplet of the fluid with higher density is introduced onto the surface of the rock. When the test pressure and temperature come to equilibrium, the camera captures an image of the shape of the bubble, and the angle that forms between the droplet edge and the rock surface is measured to determine the wettability state of the system.

Determination of Relative Permeability

Relative permeability is a measurement of flow rates and differential pressure of specific fluids undergoing two-phase flow. While single-phase permeability is a relatively simple measurement of flow under operational conditions, two-phase flow presents a complex relationship dependent on saturation, wettability, surface tension, and force. Results of tests describe the ratio of flow of two fluids relative to the permeability of the sample at 100% saturated flow. The resulting curve of relative permeability against saturation is required for flow simulations but is also indicative of injectivity, identifies reducible fluid saturations, and estimates changes in wettability in the presence of differing fluids.

For this study, capillary pressure data were used to calculate a theoretical set of CO_2, rich gas mixtures, and rich gas components relative permeability curves. The Brooks–Corey method based on capillary pressure, contact angle, interfacial tension, and the pore-size distribution of each sample was used as the theoretical model for calculation. The curves were developed as a means of comparing the ability for different fluid pairs to affect wettability for the differing lithologies of the Middle Bakken.

Results – IFT and Contact Angle

Figure 44 presents the experimental workflow and the different fluid combinations used in the determination of interfactial tension and contact angle. All experiments were performed at a temperature of 250°F, considered "near reservoir" condition. The IFT of three brine solutions with different salinities and DI (deionized) water was measured in the presence of Bakken oil, CO_2, propane, and rich gas mixture (methane:ethane:propane – 7:2:1) under four pressures of 1000, 3000, 5000, and 7000 psi, respectively (Table 7). Figure 45 shows the results of the study. As shown, the IFT for each fluid pair is influenced by both water quality and pressure. In general, the results show that as TDS increases, the interfacial tension of each fluid pair increases. The effect of pressure shows that the oil/brine and propane/brine systems have increasing IFT with increasing pressure. The CO_2/brine and rich gas/brine systems each decrease with increasing pressure. This is an indicator of the potential for influencing wettability within reservoir systems.

Contact angle (CA) was determined for a total of five rock samples selected from different wells to represent the Middle Bakken siltstone member (Table 8). Rock samples were chosen from areas of the North Dakota portion of the Williston Basin representing varying production potential, likely attributed to thermal maturation of the overlying and underlying organic-rich shales. In general, the maturity and expulsion of HCs decreases to the north. Figure 46 shows the distribution of sampling throughout North Dakota. Samples chosen are from a siltstone interval of the Bakken because it is commonly targeted as the placement for horizontal lateral wells and commonly contains the largest grain sizes within the formation. Similar to IFT experiments, the CA of a brine droplet was measured while submersed in different surrounding phases which include Bakken oil, CO_2, propane, and rich gas, respectively. For each fluid combination, the CA was measured under 2000, 4000, and 6000 psi, respectively. Table 9 presents the CA experimental test matrix. Figure 47 shows the expected changes in wettability based on the drop shape developed on a solid surface. Reservoir systems with strong oil wettability typically have a strong bond between the grain surface and the oil present in the reservoir. In situ water will reside in the interior of the pore space. The opposite is true for strongly water-wet systems. Production from oil-wet systems suffers from higher water production for this reason and typically requires the injection of fluids to alter this wettabililty and release the bonding. Figure 48 shows the results of the CA studies in the context of the mineraology for each sample. The trends observed for CA consistently show that the oil/brine system has the highest oil wetting characteristics and CO_2 is always the lowest, or most water-wet. There is a common trend observed with the contact angle and mineralogy in that each of the four samples shows a strong oil-wetting characteristic with oil/brine and propane/brine systems and the sample with a dominant calcite mineralogy shows propane deviating toward a water-wetting character. In each of the tests, pressure is shown to decrease the observed contact angle. Both rich gas and propane show strong water wetting characteristics, implying that, if injected for EOR, the wettability of the HC/reservoir rock system may be altered and lead to enhanced production over time.

Table 7. Test Matrix for Determination of IFT

Gas Phase	Surrounding Liquid Phase	Test Conditions
Rich Gas (C1:C2:C3 = 7:2:1)	DI water and three brine samples	Constant temperature of 250°F Pressure: 1000, 3000, 5000, 7000 psi
Propane	DI water and three brine samples	Constant temperature of 250°F Pressure: 1000, 3000, 5000, 7000 psi
CO_2	DI water and three brine samples	Constant temperature of 250°F Pressure: 1000, 3000, 5000, 7000 psi

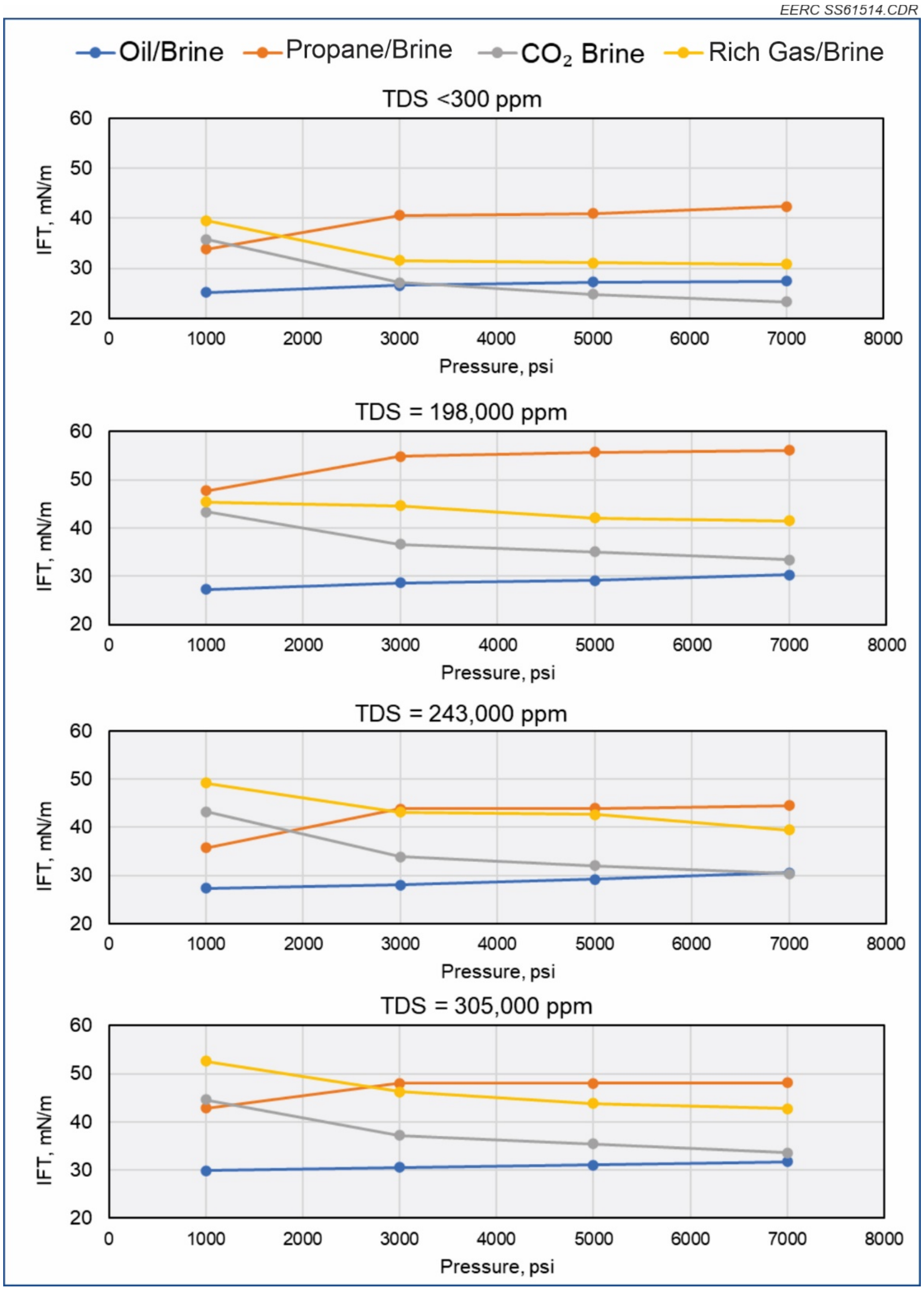

Figure 45. Results of IFT testing using multiple fluid pairs in the presence of different brine salinities.

Table 8. Samples Selected for Use in Contact Angle Studies

Sample ID	NDIC Well No.	Depth, ft	Lithofacies
118943	24123	11,072.7	MB3
120829	27366	10,685.1	MB3
122814	22388	10,656.2	MB3
122838	18829	6794.6	MB3
127240	34086	10,815	MB3

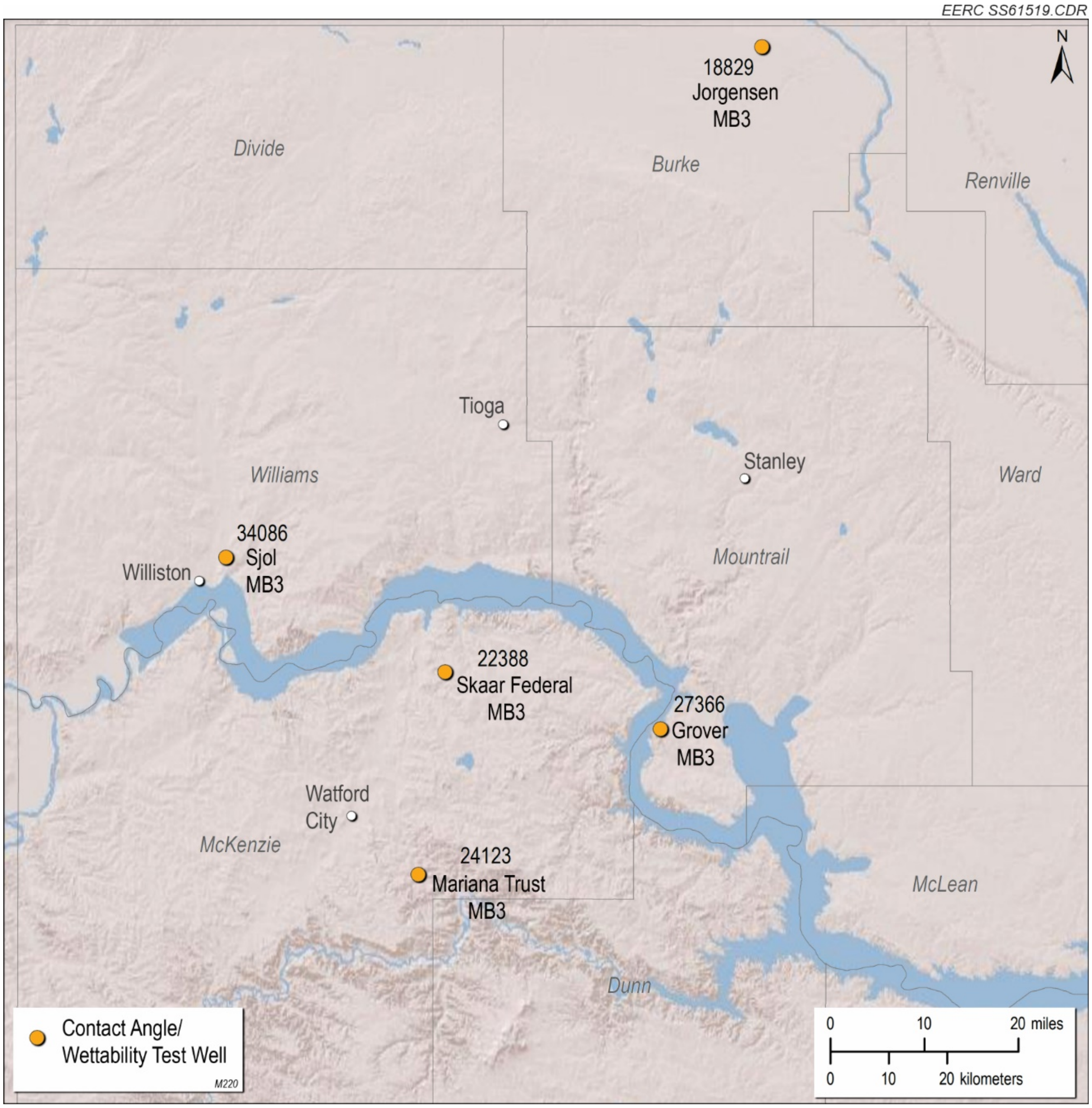

Figure 46. Distribution of Bakken samples evaluated for changes in wettability.

Table 9. Design of Contact Angle Measurement

Solid Phase	Drop Phase	Surrounding Phase	Test Conditions
Five Bakken Rock Samples from Different Wells	DI water and three brine samples	Bakken oil	Constant temperature of 250°F Pressures: 2000, 4000, 6000 psi
		Rich gas	
		Propane	
		CO_2	

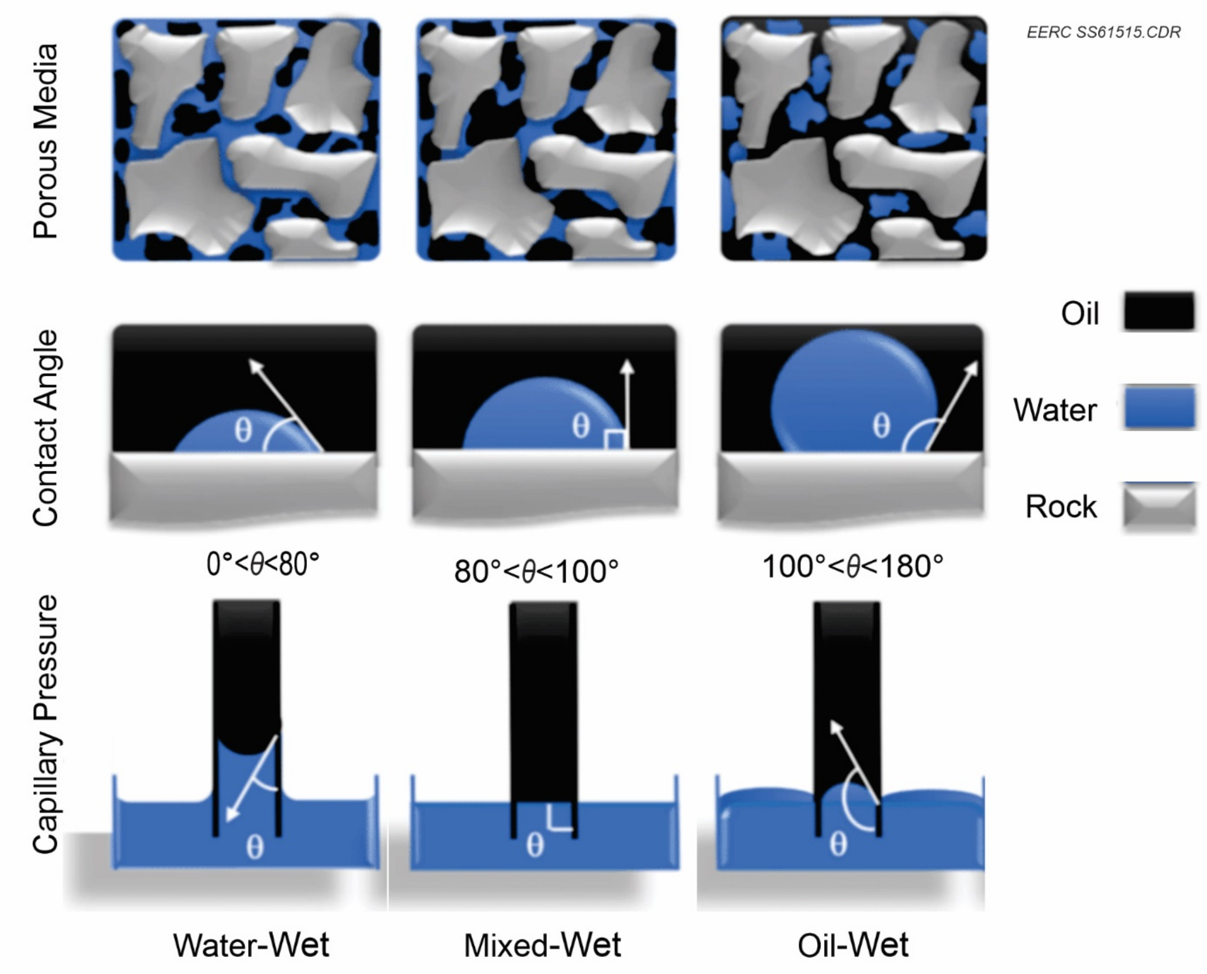

Figure 47. Changes in CA and their impact on surface wettability (modified based on Moghadam and Salehi, 2019).

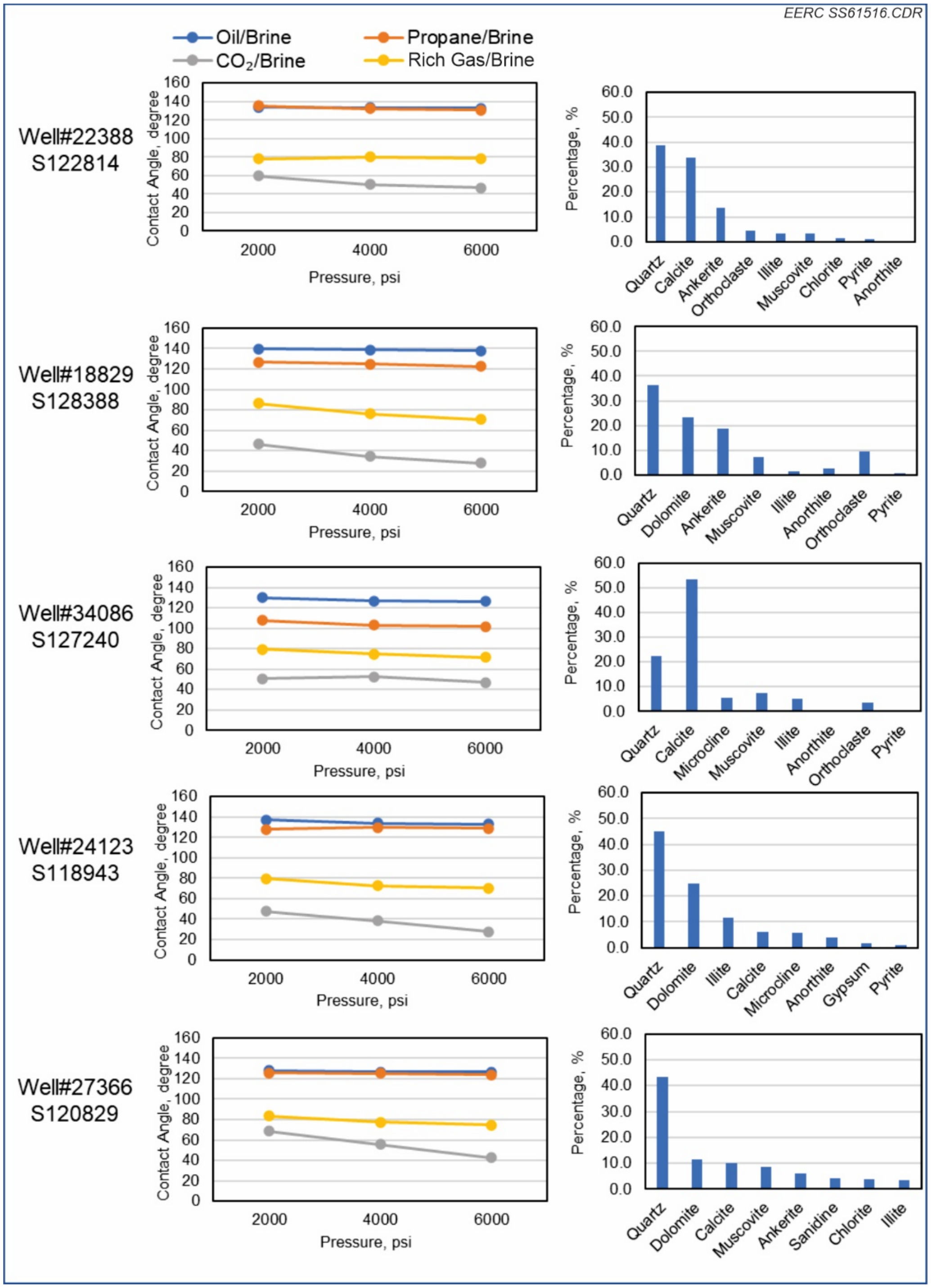

Figure 48. Results of CA testing in the presence of multiple fluid pairs. These tests were performed at 250°C and 243,000-ppm TDS. Mineralogy is shown on the right.

Results – Relative Permeability

As noted previously, capillary pressure data sets were used to calculate a series of relative permeability curves. The Brooks–Corey correlation relies on CA and IFT for converting the data from the laboratory-based mercury/air system to one specific to the fluid pairs of interest. When relative permeability curves are interpreted, the migration of the crossover point indicates the potential for changes in wettability (Figure 49). If the crossover is observed to move from the 50% mark toward the 100% mark, the system is expected to become increasingly water-wet. If the curve moves in the opposite direction, toward the 0% saturation, the system is believed to become more oil-wet. (Mahmud and others, 2019). The alteration of wettability has implications for oil mobility in that the force required to keep the oil tightly bound to the surface of the pore linings (IFT) is being relieved. Table 10 shows the data that informed the curves shown in Figure 50. As shown in the curves, the oil/brine relative permeability crossover is the furthest left and the rich gas/brine to the right. This suggests that, within the Bakken, the potential exists for improving wettability through the injection of the alternative fluids, namely, CO_2, propane, or rich gas blends.

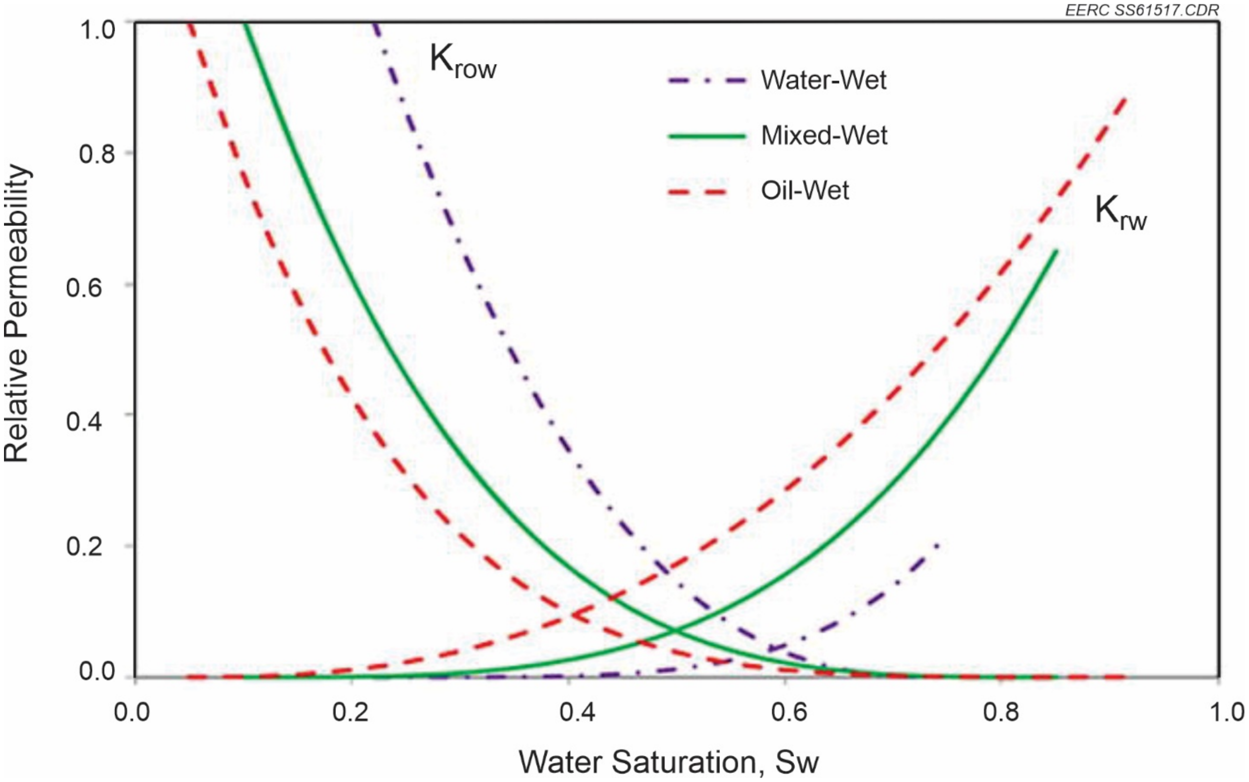

Figure 49. Example of the change in wettability observed in the relative permeability curve (Mahmud and others, 2019).

Table 10. IFT and CAs Used in the Determination of Relative Permeability

System	IFT	CA
CO_2/Brine	33	38.5
Oil/Brine	28.7	134
Propane/Brine	43.9	129.9
Rich Gas/Brine	42.9	72.8
CO_2/Brine	33	55.6
Oil/Brine	28.7	126.8
Propane/Brine	43.9	125.2
Rich Gas/Brine	42.9	77.3
CO_2/Brine	32.96	50.24
Oil/Brine	28.65	133.43
Propane/Brine	43.89	132.47
Rich Gas/Brine	42.89	79.9
CO_2/Brine	32.96	34.46
Oil/Brine	28.65	138.78
Propane/Brine	43.89	124.88
Rich Gas/Brine	42.89	76.18
CO_2/Brine	32.96	52.38
Oil/Brine	28.65	126.9
Propane/Brine	43.89	102.99
Rich Gas/Brine	42.89	74.68

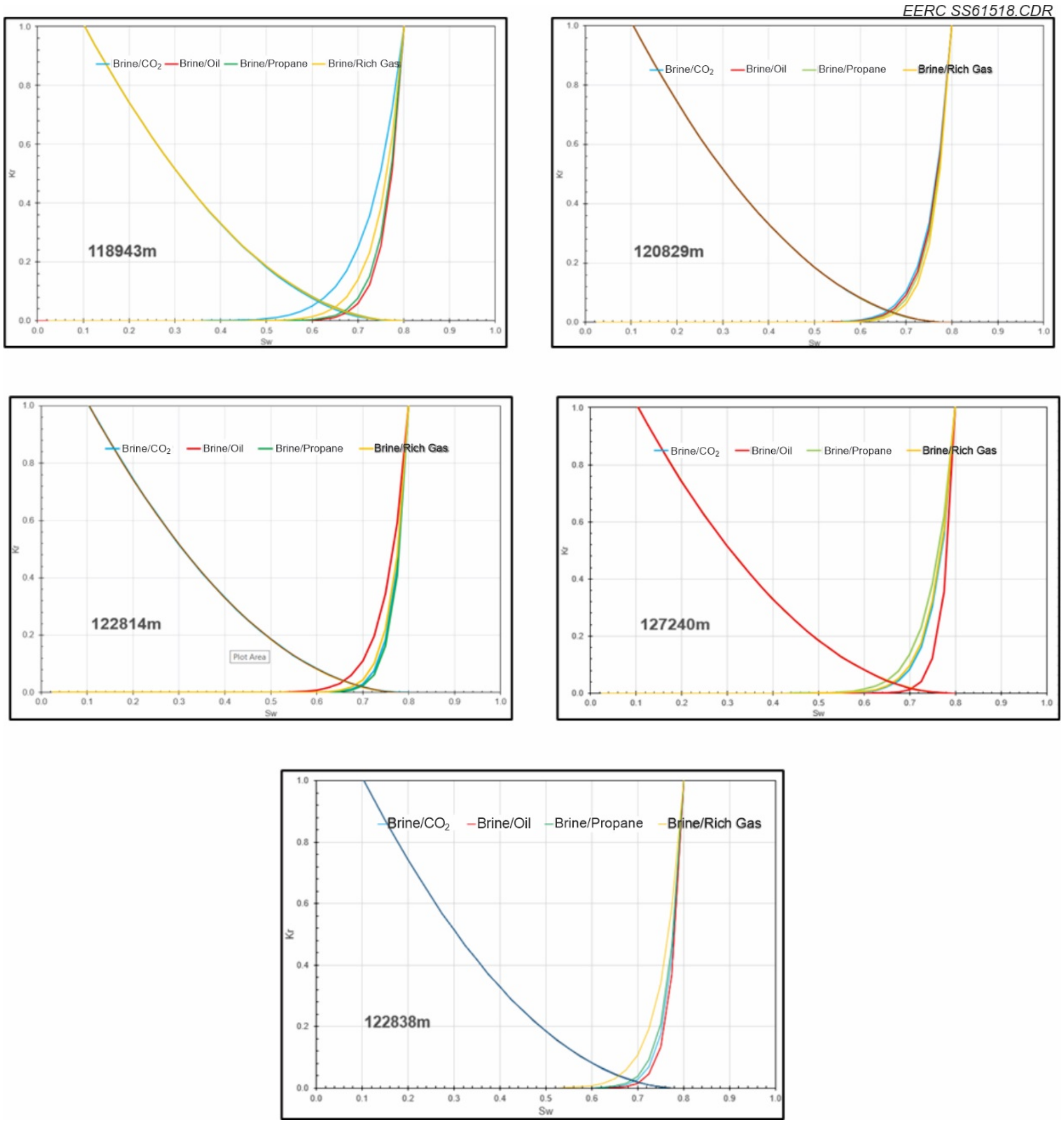

Figure 50. Relative permeability curves based on capillary pressure for four Bakken samples representing varying thermal maturity areas of the Bakken.

Conclusions

Work performed in this activity developed multiple elusive data sets pertaining to IFT and CA for fluids that have the potential to alter wettability in unconventional reservoir rocks. Data sets were created at reservoir conditions at multiple pressures and using multiple brine salinities. Oil/brine and propane/brine pairs showed the highest IFT compared to CO_2/brine and rich gas/brine systems. CO_2 was observed to have the lowest IFT of the pairs tested. A similar trend was observed for the newly generated CA data. Oil/brine and propane/brine showed the strongest oil wettability characteristics, with values consistently over 120°, with one exception. The sample containing calcite as the dominant mineral was determined to have very close to a mixed wettability character. This demonstrates that mineralogy can be taken into account when considering specific fluids for alteration of wettability through EOR. In other words, there may be multiple solutions for unconventional oil systems containing a complex clastic/carbonate lithology such as the Bakken. Additional observations for contact angle were that the effect of pressure were most notable in the CO_2/brine and rich gas/brine systems with wettability moving more toward the strongly water-wet system. This is consistent with the observations in MMP studies and rock extractions performed as part of Subtask 3.1 and reported in Section 2 of this report. Finally, relative permeability curves were created using capillary pressure data sets and the newly generated IFT and contact angle data. Interpretation of the crossover point on the curves demonstrated that wettability can be altered with the fluids tested. Further work will need to be performed to quantify the magnitude of this change.

Subactivity 6.2 – Cuttings Characterization for Geomechanical Properties

Introduction

Booming in late 2010s, the shale oil development in the Bakken Formation in the Williston Basin, one of the largest unconventional resources for both the United States and the world, benefited from innovative technologies, e.g., horizontal drilling and multiphase hydraulic fracturing (Hughes, 2013; Donnelly, 2014; Gold, 2014). Although a wide and relatively thin formation, the broad area of 158,000 square kilometers crossing parts of North Dakota, Montana, Saskatchewan, and Manitoba demonstrates a promising fossil energy production future (LeFever and Helms, 2006; Tran and others, 2011). The Middle Bakken Formation is the target member to implement successful hydraulic fracturing, rather than the Upper or Lower Bakken Formations (Zeng and Jiang, 2009). In this context, the term brittleness index (BI) is commonly used to describe the inclination of the formation rock subjected to hydraulic fluid injection and fracture propagation (Herwanger and others, 2015; Zhang and others, 2016; Feng and others, 2020). Some previous studies investigated a BI-relevant calculation and application in HC-rich basins. Harris and others (2011) studied the geomechanical properties of Woodford Shale in the Permian Basin and identified the brittle end member, by which the associated stratigraphic variation was displayed. Yang and others (2013) conducted triaxial experiments on core plug samples from shale reservoirs of Barnett, Haynesville, Fort St. John, and Eagle Ford to compare the BI results among them. Pei and others (2014) measured the geomechanical properties of the Middle Bakken Formation and determined a brittle/ductile region based on correlation plotting between Young's modulus and Poisson's ratio. Mustafa and others (2019) performed thin-section petrography, powder x-ray diffraction (XRD), logging data, and BI analysis whereby three lithofacies were identified in the lower Silurian Qusaiba Shale in Saudi Arabia.

Consisting of gray interbed and carbonate-rich siltstones and sandstones, the Middle Bakken Member is generally more brittle; however, results from evaluating and quantifying the BI within the member, specifically along the horizontal wellbore, are inconsistent and ambiguous (Novak and Egenhoff, 2019; Paris and Stewart, 2020). This is because of two reasons. First is the versatile range of BI definitions proposed and used in academia and industry, where no recognized well standard exists. More details will be explained in the Method section. Second is that different subsurface data sources, including core measurement in the laboratory, well logging, and seismic, caused the different BI ranges, which cannot be compared effectively. The most reliable BI determination method is geomechanical testing on core plugs; however, it typically requires intact core plugs and a long analysis time. Other data types, logging and seismic, cover a large area in the formation but lack the high resolution. Therefore, this study proposed the emerging technique for estimating BI based on drill cutting sample mineralogy. The mineralogy of a sample can be determined directly through XRD or indirectly using x-ray fluorescence (XRF) to measure the elemental composition of a sample from which mineralogy can be inferred. Both of these techniques require only drill cuttings (versus core plugs) for analysis, which is highly advantageous because core is very rarely available for the horizontal portion of a well, whereas drill cuttings are prevalent throughout the entire lateral length. Geomechanical testing can be conducted on multiple Bakken samples followed by mineralogical analysis using XRD and XRF. This will allow for comparison of the mineralogically predicted BI with that determined by geomechanical testing. Wherever possible, existing geomechanical and XRD data for Bakken samples will be used to supplement the data set. This comparison will allow for statistical evaluation and uncertainty determination of the different approaches to calculate the BI using mineralogy for Bakken reservoir samples.

This project developed a workflow (Figure 51) to calculate the BI from the elemental composition of well cutting samples. XRF, XRD, and geomechanical tests of cuttings and core plug samples were performed to generate a data set for the modeling. The modeling and calculation consisted of two major steps: predicting mineral composition from elemental composition and calculating BI from mineral composition. Two methods, a normative calculation method and a ML method (neural network [NN] algorithm), are compared in the first step. Both methods compared the accuracy and discrepancy in the XRD data. The second step employed the mineralogy-based brittleness calculation method to directly estimate the BI. Geomechanical tests were applied on four new samples to validate the results.

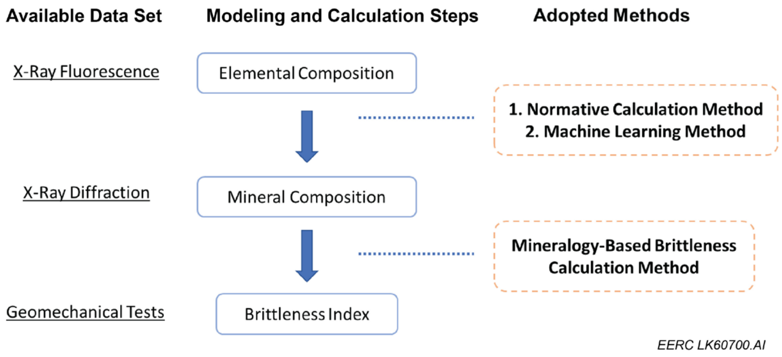

Figure 51. Workflow of BI calculation from well cuttings.

Methods

Normative Calculation Method

Unlike igneous rocks that follow a reasonably predictable pattern attributed to magma chemistry, sedimentary rocks are subjected to various depositional paleoenvironments, where diagenesis caused mineralogical alteration, resulting in substantial uncertainty when mineral composition is predicted from bulk geochemical data (Morad and others, 2000; Johnson and others, 2016). Specifically, sedimentary rocks contain minerals that have different origins but possess similar elemental components, which increases prediction difficulty (Tucker, 2001). Application of the normative calculation method to fine-grained, clay-bearing rocks provided a reasonable solution of calculating the mineralogy phases based on the elemental composition (Kackstaetter, 2014). Incorporating the model analytical procedures and statistical evaluation of empirical relationships is the core algorithm of this method, although essentially a mathematical approach. To achieve legitimate estimation, it demands tallying the balance of carbon dioxide distributed in multiple mineral phases.

In this study, the normative calculation method was revised and customized for the lithofacies and mineralogy of Middle Bakken samples (Kurtoglu and others, 2013; Jin and others, 2016). Some mineral phases, including kaolinite, gypsum, apatite, and hematite, were eliminated because of their absence in the target formation, whereas the clay classification remains in the pattern database of the algorithm because of the variation and uncertainty of the clay minerals. Therefore, the determinative minerals recognized in the XRD are quartz, potassium feldspar, plagioclase feldspar, rutile, pyrite, calcite, dolomite, ferrodolomite or ankerite, and clay minerals that include illite, chlorite, sericite, etc. The assumption of this method lies in the idealized chemical composition of each of the individual minerals, which is the premise of calculating the minerals made up of complex oxides, especially clays (Table 11). The determination of the idealized oxide formulas of minerals was also supported by the previous studies on Middle Bakken formations (Yarbrough and others, 2019; Sonnenberg, 2020; Milliken and others, 2021). Among all minerals, major phases have more precise and straightforward chemical formulas, while the clays appear more complicated, with clay minerals sharing many of the same elements in their chemical formulas. Using the empirical chemical formula as the basis, the clay minerals are regarded as the combination of multiple oxides, where the summative molecular weight of allotted mole fractions of these respective oxides agrees with the accepted average molecular weight of the mineral (Kackstaetter, 2014). Stepwise procedures of the calculation were implemented in the spreadsheet program from the normative calculation method. Thus it is suggested that the algorithm should be examined and customized for each study field where the paleoenvironment and its associated mineralogy vary.

Table 11. Idealized Chemical Compositions of Minerals in This Study

Mineral Name	Chemical Compositions
Quartz	SiO_2
K-Feldspar	$3SiO_2 – 0.5Al_2O_3 – 0.5K_2O$
Plagioclase Feldspar (albite)	$Na_2O – Al_2O_3 – 0.5K_2O$
Pyrite	FeS_2
Rutle	TiO_2
Calcite	$CaO – CO_2$
Dolomite	$CaO – MgO – 2CO_2$
Ferrodolomite/Ankerite	$CaO – 0.5Fe_2O_3 – 2CO_2$
Illite	$3.7SiO_2 – 0.7Al_2O_3 – 0.1Fe_2O_3 – 0.3MgO – 0.3K_2O – 2.7H_2O$

Neural Network Algorithm

NN algorithms were developed to comprehend the underlying relationship between the input and output of data sets as a way to mimic human brain operations (Mohaghegh, 1995; Li and others, 2018; Mlella and others, 2020). Consisting of layers of interconnected nodes, NNs are essentially the lineup of mathematical functions in a particular architecture that solves the modeling of predicting output from input (Rahmanifard and Plaksina, 2019; Wood, 2020; Yoon, 2020) (Figure 51). In this study, a NN algorithm was utilized as an alternative approach to predict the mineral composition from the elemental composition (Figure 52). These results are then compared to those from a normative calculation approach. The data are split into two groups: 80% for training and 20% for testing. Five hidden layers were configured in this study's NN, and the input and output dimensions were 15 and 7, which represent 15 elements and 7 mineral groups. Note the mineral types are grouped in the NN calculation after trial and error and optimization of the prediction performance. Specifically, the calcite, dolomite, and ferrodolomite are grouped into carbonate minerals, and all clay minerals including illite, muscovite, chlorite, kaolinite, and smectite are grouped into a single clay mineral type. Therefore, the seven output dimensions become quartz, carbonate, K-feldspar, Na/Ca-feldspar (plagioclase feldspar), pyrite, rutile, and clay.

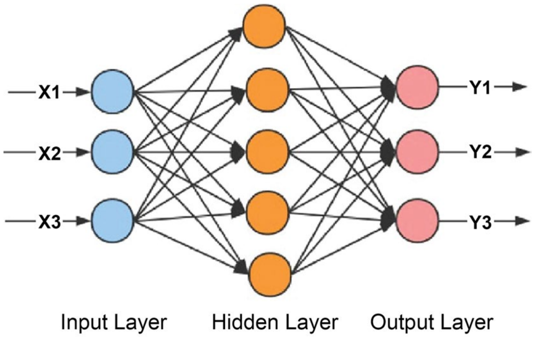

EERC LK60701.AI

Figure 52. Schematic diagram of basic NN architecture. X means the elemental composition in this study, and Y represents mineral composition.

BI Definition and Calculation

A number of the definitions of the BI were proposed and have been controversial regarding different application areas and situations (Rickman and others, 2008; Jin and others, 2014; Liu and Sun, 2015; Xu and Sonnenberg, 2016; Zhang and others, 2016; Feng and others, 2020; Kang and others, 2020). These BI definitions can be derived from different data sources, ranging from XRF and XRD on chip samples, core measurement, and wireline logs (Xu and Sonnenberg, 2016). Generally, the calculations of the BI can be divided into two types: mineralogy-based and elastic properties-based (Perez Altamar and Marfurt, 2014).

For a mineralogy-based BI, the concept assumes brittle minerals, which typically refer to quartz, feldspar, mica, calcite, and dolomite, contribute to the brittleness of rocks, while ductile materials, clay minerals, and organic matter reduce the brittleness. Below is the most commonly used equation (Xu and Sonnenberg, 2016), which was employed in this study:

$$B1 = \frac{Qz+Ca+Dol+Fel+Py}{Qz+Ca+Dol+Fel+Py+Cly+TOC} \qquad \text{[Eq. 2]}$$

However, the limitation of using minerology is that brittleness is not solely determined by mineral composition. Thus this approach neglects the effect of density, microstructure, and porosity. Other parameters, for instance, grain-size distribution, cementation, and confining pressure, are not considered either. The other calculation approach to BI is based on two important elastic properties: Young's modulus and Poisson's ratio, which can be acquired from laboratory geomechanical tests or well logging. The most commonly used approach in evaluating shale formation fracturing ability is the following (Grieser and Bray, 2007):

$$E_n = \frac{E-E_{min}}{E_{max}-E_{min}} \times 10 \qquad \text{[Eq. 3]}$$

$$\nu_n = \frac{\nu-\nu_{min}}{\nu_{max}-\nu_{min}} \times 100 \qquad \text{[Eq. 4]}$$

$$BI = \frac{E_n+\nu_n}{2} \qquad \text{[Eq. 5]}$$

The adoption of lab-tested data is believed to be the most reliable way to obtain the geomechanical properties; however, neither core plug mechanical tests nor loggings are efficient or generally available prior to hydraulic fracturing (Zoback, 2010). Therefore, investigating the BI based on the mineralogy approach still provides an alternative method that is rapid and feasible.

Results and Validation

Inferred Mineral Composition by Normative Calculation Method

Inferred mineral composition calculated by the normative method was compared with the measured mineral composition from XRD results (Figure 53). The absolute difference of each mineral with measured values was averaged in each sample. The result shows that 37 out of

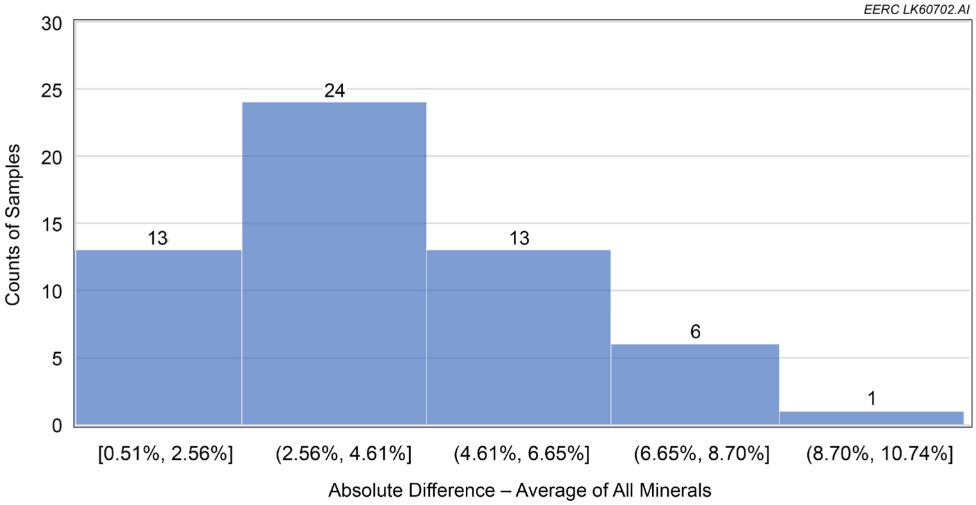

Figure 53. Absolute difference between inferred mineral composition and XRD results. The value of every sample is the average of all minerals.

58 samples (about 64% samples) had the absolute difference of less than 4.61% and 57 samples (98% samples) had the absolute difference of less than 8.7%. These data provide acceptable evidence that the predictions agree well with the measured mineral composition. Further, the absolute differences in every mineral type were calculated by averaging all the sample data sets, with results plotted in Figure 54. The illite, chlorite, kaolinite, smectite, and mica were grouped into a clay category. This grouping does not impact the brittleness evaluation because all clay minerals have a very similar low elastic modulus compared to other brittle minerals, i.e., quartz, dolomite, and calcite. Figure 54 shows that by averaging all sample results, quartz and feldspar have less than 5% difference between the mineral prediction and XRD results. The carbonate minerals, dolomite, calcite, and ankerite, present a higher difference between the mineral prediction and XRD results ranging from 6% to 9%. Pyrite and rutile demonstrate the least absolute difference at less than 1%. The prediction error of the clay mineral group is slightly above 4%. Since XRD provides a semiquantitative mineral composition, less than 10% of the absolute difference is admissible for reporting (Moore and Reynolds, 1997). Therefore, validated by XRD results, it is acceptable of the prediction performance to use the normative calculation method on the Middle Bakken samples.

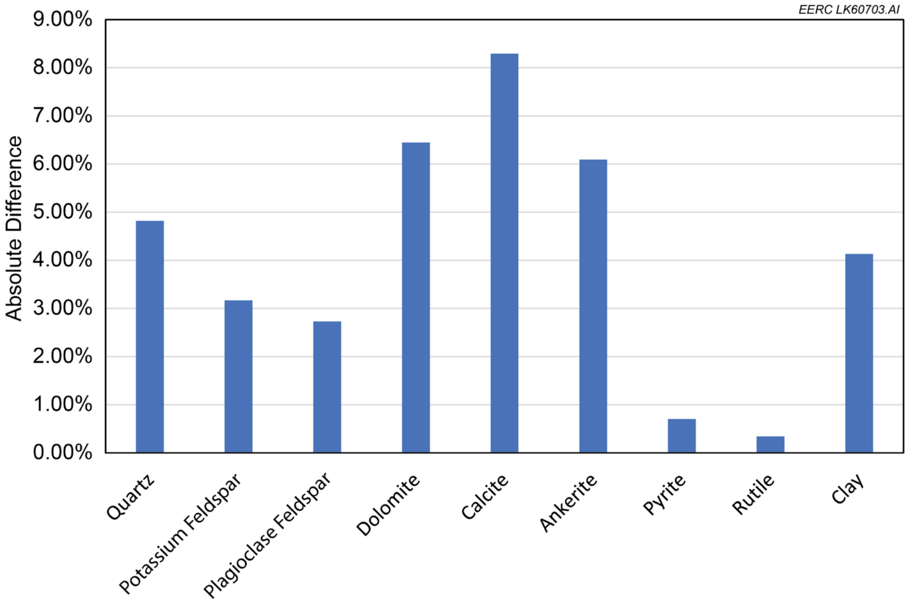

Figure 54. Absolute difference between inferred mineral composition and XRD results in terms of each mineral type. The value of each mineral is the average of all samples.

Inferred Mineral Composition by Neural Network Algorithm

The accuracy of predicted mineral composition by the ML method (NN algorithm specifically) is 83.33%. The mean absolute error (MAE) of seven mineral groups by ML method is plotted in Figure 55, which includes two data sets, all data, and testing data. It shows that quartz has the largest MAE compared with other mineral groups, up to 8%. The carbonate mineral group has around 3% uncertainty in both all data and testing data, while potassium feldspar and plagioclase feldspar present a large discrepancy, up to 3%, of the discrepancies between all data and testing data. Pyrite and rutile have about 4% and 0.3% of MAE, respectively, regardless of the data set difference. A great discrepancy occurs in the clay mineral group between the all-data set and the testing data set, which is about 5.5% on all data and 0.3% on testing data. This indicates the ML method did not capture the perfect relationship between element composition with clay minerals, and the testing data set just happens to be the simplest correlation. ML results on all data and testing data demonstrate a relatively consistent performance on other minerals, which are brittle components. The uncertainty is because of the elemental commonalities in different minerals (Si, Al, K, Ca).

In addition to the modeling on previously available data sets, four new samples from the Middle Bakken Formation were cored and tested by XRF, XRD, and geomechanical experiments to provide validation data points. Figure 56 shows validation of the ML prediction from XRF with the XRD results. The ML model established by the training and testing is used to infer the mineral composition from elemental composition. The validation showed the discrepancy varied in different samples and in different mineral groups. The ML-predicted quartz fractions of four samples were all less than those from XRD measurements. The MB3 lithofacies had the largest

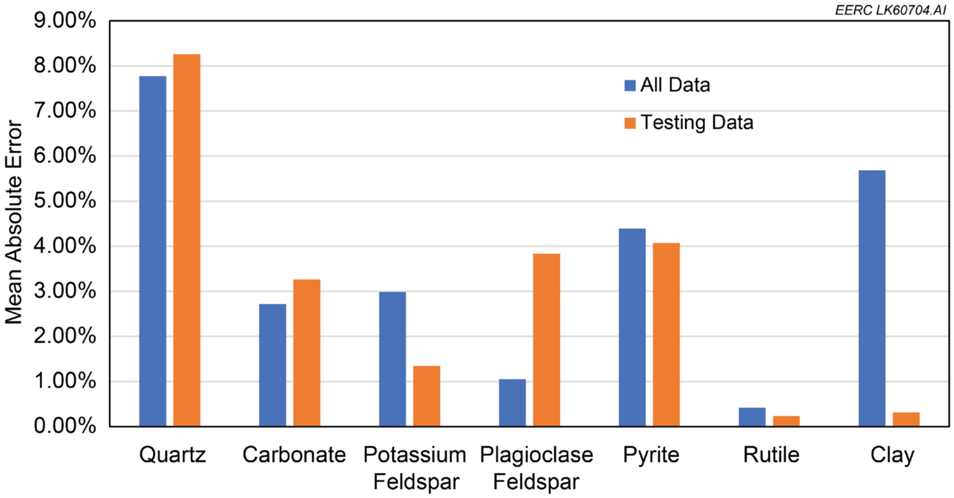

Figure 55. MAE of ML prediction performance.

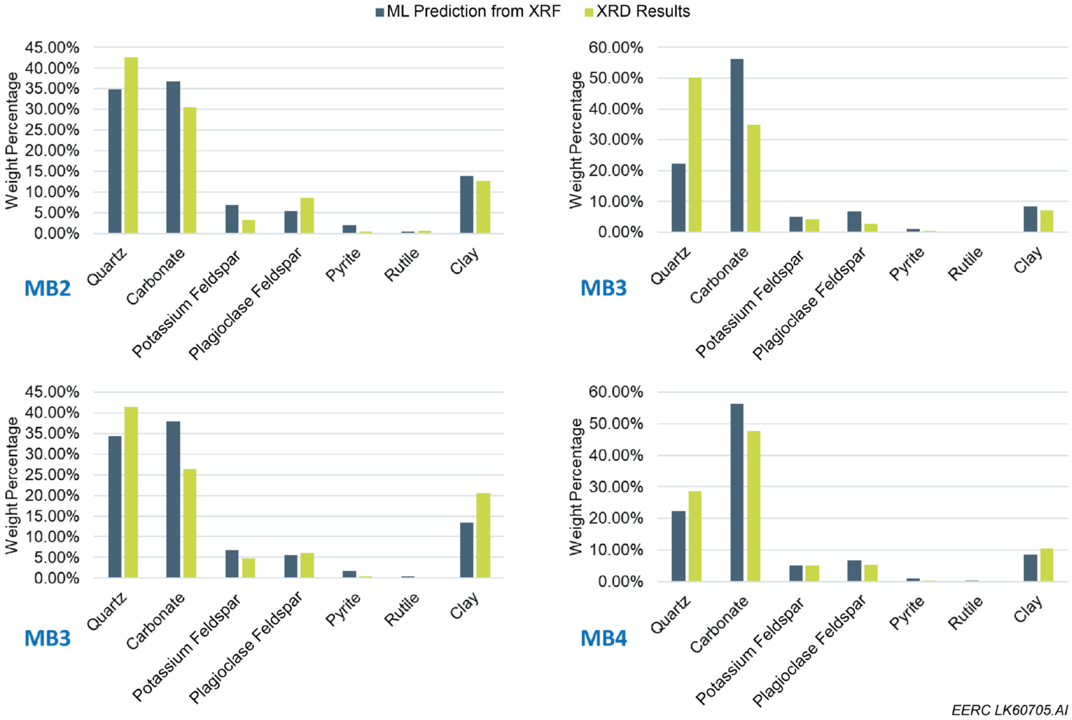

Figure 56. Validation on ML prediction using XRD results of four new Middle Bakken samples.

gap of nearly 30%, and others demonstrated a difference around 10%. The carbonate mineral group showed a higher predicted fraction than XRD results did. The prediction of feldspar and heavy minerals coincided well with XRD data. The disagreement on the clay mineral group was mostly less than 5%, which is acceptable to using semiquantitative mineral identification with XRD. Overall, the validation proved the ML model was reliable and can provide an acceptable prediction with rapid data acquisition. It is also notable that the ML model is dynamic and can keep evolving as it gains more data sets in the training process.

BI Estimation

Based on the minerology-based BI calculation method, the BI was calculated on the 58 samples. The left box chart of Figure 57 shows the BI statistics of all samples, where the cross depicts the mean value of the data range and the box lines represent the quartile range, 25%–75%. The average BI is 0.65, and the quartile range is 0.55–0.76. The right plot of Figure 57 shows four BI data curves based on the mineralogy BI method from previous studies of the Middle Bakken Formation. The light blue box that overlaps the curves is the current study result, which is generally higher than three studies (Jarvie and others, 2007; Wang and Gale, 2009; Jin and others, 2014) and lower than the result by Xu and Sonnenberg (2016). This comparison suggests the BI estimation method in this study is reasonable and reliable as it falls between the results of previous studies. Note that the unit of BI in this study is dimensionless because of its percentage. Previous studies also gave the BI without unit, but in the range of 0%–100%. The current study did not plot the BI data set correlated with depths because of the random permutation by the ML training process.

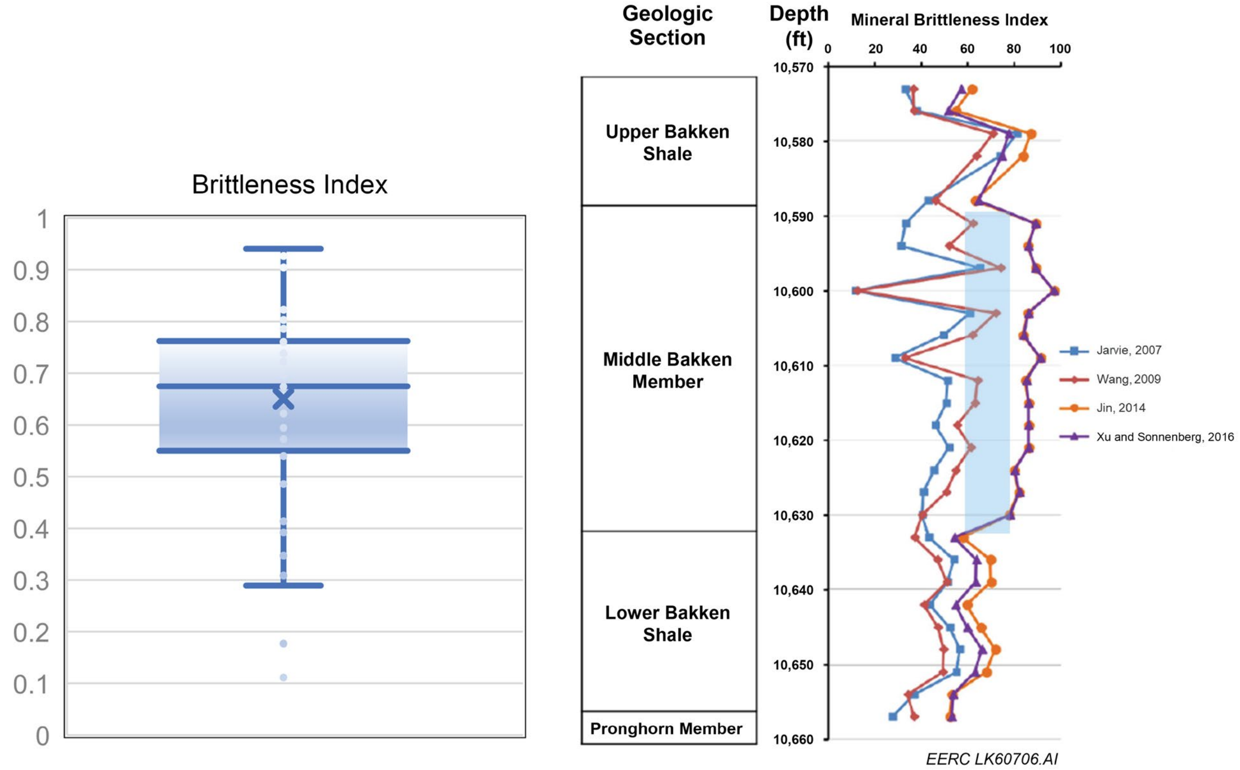

Figure 57. Box chart of predicted BI and well log interpreted BI from previous studies. All studies are based on the Middle Bakken Formation.

The aforementioned four samples were also tested in a triaxial stress condition and measured for static and dynamic elastic properties: Young's modulus and Poisson's ratio. Table 12 shows the basic information of the four Middle Bakken samples, including depths, test confining pressure, axial pressure, and bulk density. Dynamic Young's modulus and Poisson's ratio were calculated from acoustic measurement. The maximum and minimum elastic properties and porosity of Middle Bakken samples can be obtained from a previous EERC project (Hawthorne and others, 2013). The elastic property-based BI calculation method was applied to generate the BI range of 0.6–0.75 for these samples, which was consistent with the minerology-based BI quartile range, 0.55–0.76.

Table 12. Dynamic Elastic Parameters of Four Middle Bakken Samples and Corresponding BI

Sample Number	Depth, ft	Confining Pressure, psi	Axial Pressure, psi	Bulk Density, g/cm^3	Young's Modulus, $\times 10^6$ ps)	Poisson's Ratio	Brittleness Index
130123-3A	10810.61 – 10811.06	3900	3900	2.548	6.73	0.151	0.715
			16,000	2.548	7.33	0.189	0.658
130124-4A	10814.53 – 10815.03	3900	3900	2.636	8.80	0.214	0.656
			21,000	2.636	10.25	0.262	0.605
130125-5A	10826.04 – 10826.60	3900	3900	2.514	7.03	0.162	0.703
			18,000	2.514	7.37	0.197	0.643
130126-6A	10839.53 – 10840.03	3900	3900	2.512	6.94	0.142	0.740
			18,000	2.512	7.47	0.182	0.677

Discussion and Conclusion

This activity developed an efficient and effective geomechanical evaluation method that estimated the BI directly from elemental composition of well cutting samples acquired from the Middle Bakken Formation. Two steps were involved, from elemental composition to mineralogy composition and from mineralogy composition to BI. The first step used and compared two different methods. The results by the normative calculation method showed 98% of samples have less than 8.7% absolute difference when compared with XRD mineral composition. The ML method presented an accuracy of 83.33%, and the MAE of ML prediction performance was less than 10% on average with all mineral groups. Besides, the normative calculation method requires repetitive spreadsheet semiauto computation, while the ML method saves time by batch-processing on a trained model. Therefore, the ML method was much more efficient and preferred because of the fast prediction and potential to evolve owing to increasingly large data sets. The BI calculation also compared two methods: mineralogy-based and elastic properties-based. With the predicted mineral composition in the last step, the mineralogy-based BI method was applied and calculated on all 58 samples, which generated the quartile range as 0.55–0.76. When compared with four previous studies on the Middle Bakken, the range was reasonable and reliable. To validate the prediction, four new core plug samples from the MB2, MB3, and MB4 facies were acquired. Using the acoustic measurement results, dynamic elastic properties, Young's modulus and Poisson's ratio, were obtained and calculated to the BI by the elastic properties-based BI method. The BI range of 0.6–0.75 was consistent with the mineralogy-based BI approach. The method proposed in this study can be widely used to establish the BI of unconventional formations by utilizing XRF tests on drill cutting samples and forgoing multiple other test methods with core plugs. This approach only requires the XRF measurements of drill cuttings, which is highly advantageous as XRF is a low-cost, reliable, and fast method, and cuttings are widely available through a whole lateral interval. A timely and efficient evaluation of geomechanical information significantly contributes to the design of effective well stimulation and the prediction of a fracture network induced by hydraulic fracturing and is especially useful if conventional geomechanical tests that require core samples cannot be conducted.

ACTIVITY 7.0 – MODELING CONFORMANCE TREATMENTS AND EOR STRATEGIES

INTRODUCTION: BACKGROUND AND OBJECTIVES

Evaluation of previous pilot tests in the Bakken and the injection tests conducted at Stomping Horse between July 2018 and June 2019 has shown that oil recovery improvement was minimal when the reservoir pressure could not be boosted quickly by gas injection (Sorensen and Hamling, 2016; Pospisil and others, 2020). Very early breakthrough time and poor well conformance have been identified as plausible causes contributing to a lack of incremental oil production from the first generation of the Bakken injection pilot tests (Hoffman and Evans, 2016; Thakur, 2019). Because hydraulically induced and natural fracture networks heavily influence primary recovery, fractures are thought to be the main contributors for rapid injector–producer well communication. Strong well communication is expected to be more striking for multistage completions, which have been observed in the major U.S. unconventional basins, including Bakken, Eagle Ford, Haynesville, and Wolfcamp, etc. (Marongiu-Porcu and others, 2015; Sharma and Manchanda, 2015; Sani and others, 2015; Cao and others, 2017; Lindsay and others, 2018; Krishnamurthy and others, 2019; Scherz and others, 2019; Liu and others, 2020a). Field studies of infill drilling in the Bakken suggested that fracture geometry control technologies need to be applied to prevent direct well interference in order to improve the production performance (Vidma and others, 2019). Fiallos and others (2019) extended the investigation of well interference from primary depletion to gas EOR operations in the Eagle Ford. They found that interference (i.e., conformance issues) between wells should be carefully controlled to improve the EOR performance. Therefore, if EOR technologies are going to be successful to recover a fraction of the billions of barrels of HCs left behind with primary production recovery, diagnosis of premature gas breakthrough and application of conformance treatments specifically designed for hydraulically fractured wells need to be mastered. Systematic modeling and simulation efforts were performed by the EERC to develop effective conformance control and EOR strategies in the Bakken with the following two subactivities.

Subactivity 7.1 – Conformance Treatment

Lindsay and others (2016, 2018) evaluated the impact of well interference on production performance in the major unconventional plays, and they concluded that interferences between wells should be avoided in many locations, even in the primary depletion operations. The existence of well interference has become a critical issue for EOR operations in unconventional reservoirs, especially for EOR utilizing gas injection (Thakur, 2019). Since gas flows faster than oil and water in the reservoir because of its higher mobility, gas could not sweep the desired reservoir volume, and pressure could not be built up to the required level. Therefore, the lack of gas containment needs to be thoroughly understood, and conformance control strategies need to be developed to solve this critical challenge for effective gas EOR in fractured unconventional reservoirs (Fiallos and others, 2019; Haghshenas and Qanbari, 2020; Katiyar and others, 2021). The following tasks were performed in this subactivity:

1. Select two representative sites with single and multiple DSUs from the core oil-producing counties in the Bakken. Demonstrate well interference effects between wells.

2. Develop multiple-well, multiple-fracture simulation models using the EDFM approach, and tune the models with actual field data.

3. Test the models by mimicking the well interference behavior as observed in the field. This ensures the models can capture the fluid communication between wells so that the models can be used to develop conformance control and EOR strategies.

Site Selection and Well Interference Identification

Single DSU Site in Dunn County

Two sites in the core oil-producing areas were selected to study the well interference, EOR performance with different gas injection operations, and conformance control strategies. The first site is a single DSU located in Dunn County, North Dakota. This DSU has seven wells, including three wells completed in the Middle Bakken and four wells completed in the Three Forks, as shown in Figure 58. Wells TF2, MB2, TF3, and MB3 are parent wells, which were stimulated and brought to production in/before 2015. Wells TF1, MB1, and TF4 are child wells, which were stimulated and brought to production in/after 2018. The essential well data for the DSU can be found in Table 13.

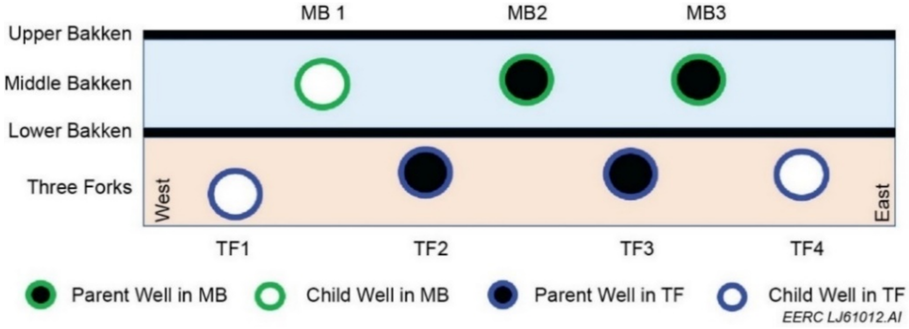

Figure 58. Distribution of wells in the DSU located in Dunn County, North Dakota.

Table 13. Essential Parameters for Wells in the DSU Located in Dunn County, North Dakota

No.	Well Name	Completed Formation/Unit	Well Type	Well Lateral Length, ft	Well Depth, ft	Fracture Stages	Production Start Time
1	TF1	Three Forks	Child	10,011	11,084	40	2018
2	MB1	Middle Bakken	Child	9784	10,541	40	2018
3	TF2	Three Forks	Parent	9977	11,064	45	2015
4	MB2	Middle Bakken	Parent	8879	11,006	30	2015
5	TF3	Three Forks	Parent	9074	11,045	19	2009
6	MB3	Middle Bakken	Parent	9684	11,007	40	2015
7	TF4	Three Forks	Child	15,391	11,092	60	2019

Well TF2 has been put on production from the Three Forks Formation since the middle of 2015. Adjacent neighboring well, MB1, was drilled, stimulated, and brought to production from the MB Unit in early 2018. Oil production in Well TF2 was positively impacted when Well MB1 was stimulated, as shown in Figure 59a, indicating communication between the MB Unit and TF Formation. Well MB3 has also been put on production since the middle of 2015. Adjacent neighboring well, TF4, was drilled, stimulated, and brought online from Three Forks in early 2019. Oil production in Well MB3 was positively impacted when Well TF4 was stimulated, as shown in Figure 59b. Since all wells were hydraulically fractured with a large volume of water in this DSU, the water cut in Wells TF2 and MB3 was also increased significantly, as shown in Figure 60a and b, respectively, when the neighboring wells were stimulated. The spikes of oil production rate and water cut indicated that the MB Unit and TF Formation are in hydraulic communication at this site. The well interference effect was also observed in other nearby DSUs, indicating that this effect is common in the area of interest. The significant increase of water cut observed in these DSUs indicates that conformance (e.g., gas crossflow between wells) would be a critical problem when gas EOR is applied to these sites.

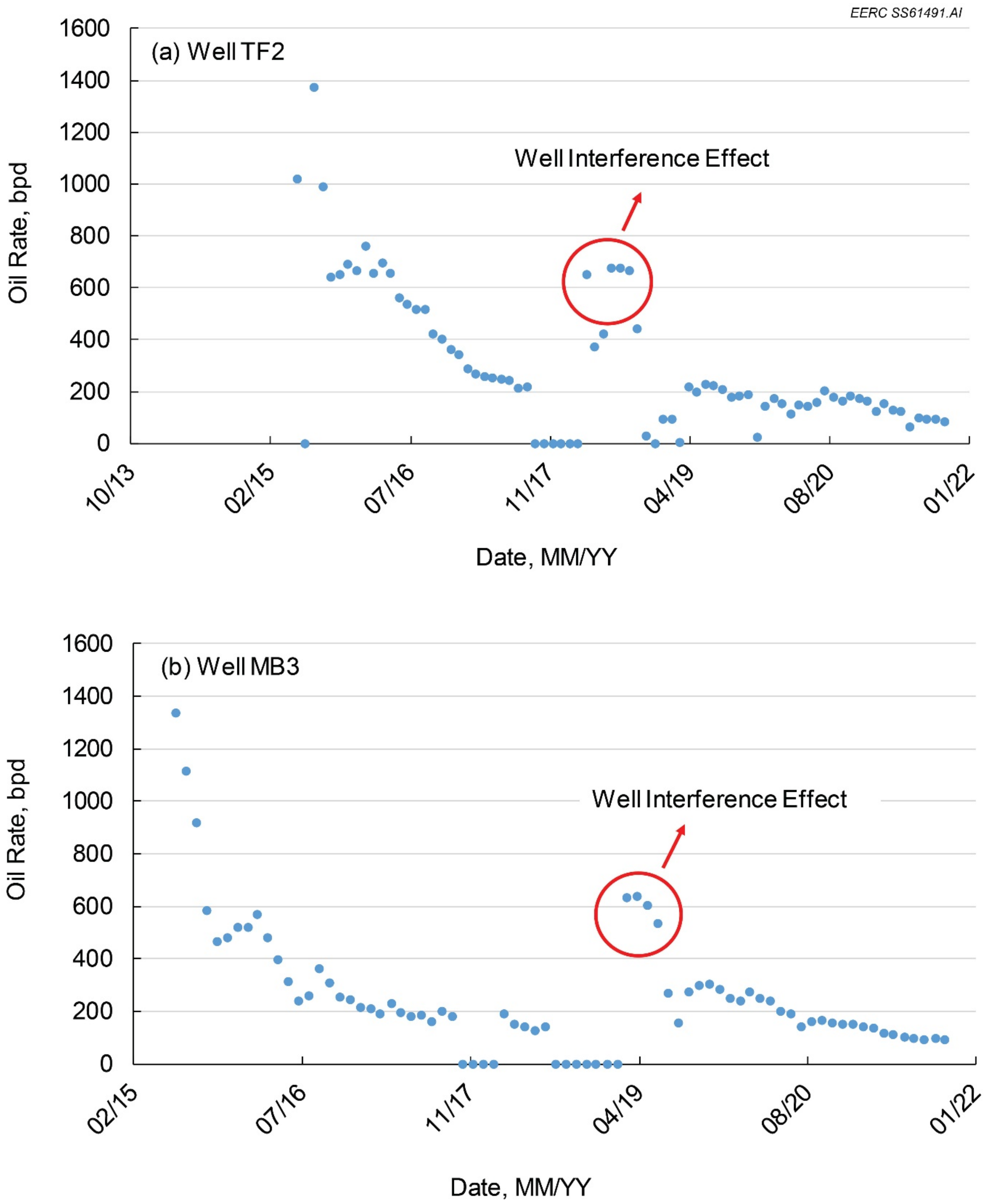

Figure 59. Illustration of well interference effect observed in wells completed in the MB Unit and the TF Formation based on analysis of oil production rate. The oil production spikes in the red circles are caused by interference from neighboring MB or TF wells, indicating hydraulic communication between MB and TF. The zero points mean the wells were shut in, and there was no production on these dates.

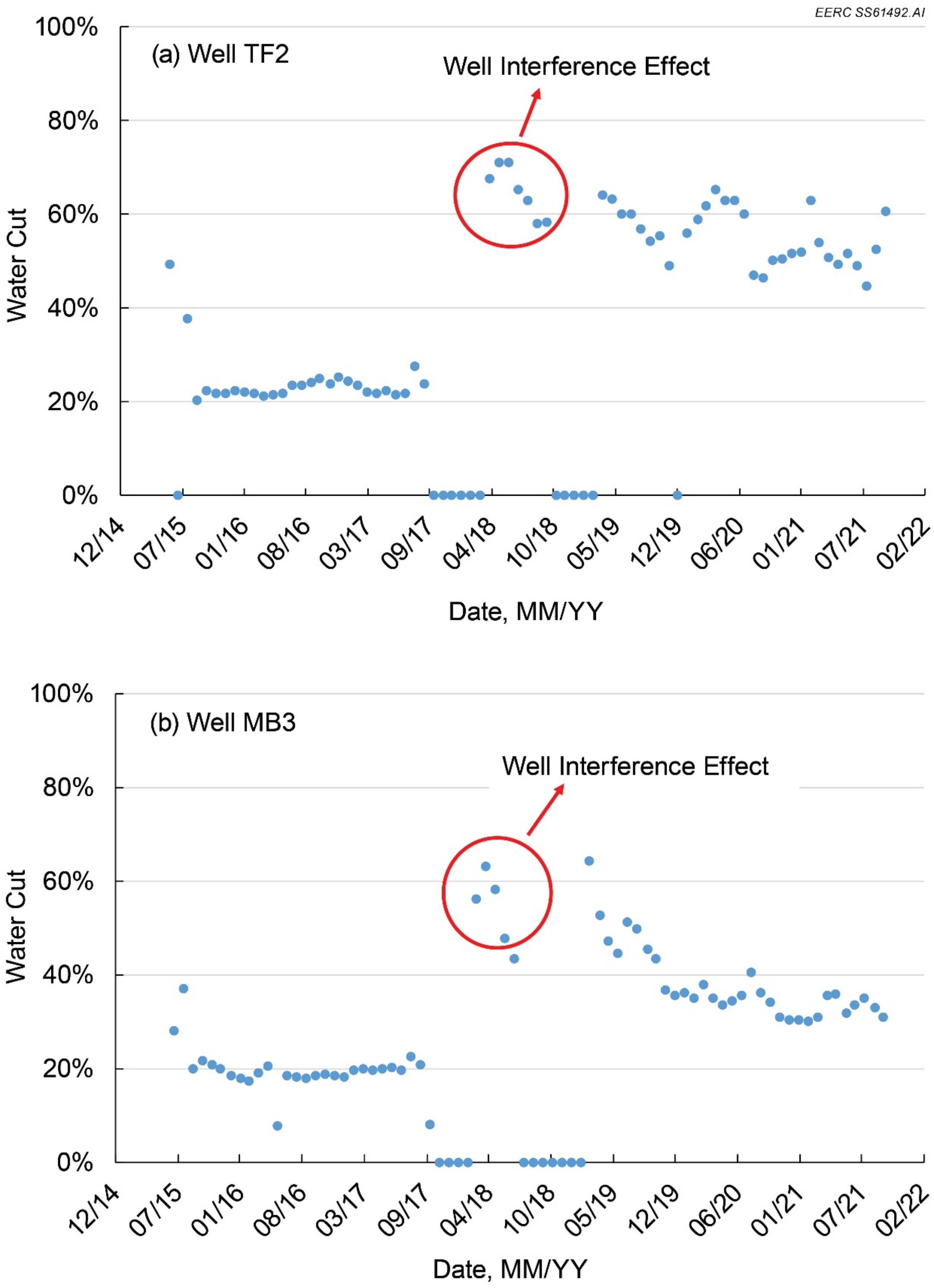

Figure 60. Illustration of well interference effect observed in wells completed in the MB Unit and the TF Formation based on analysis of water cut. The water cut spikes in the red circles are caused by interference from neighboring MB or TF wells, indicating hydraulic communication between MB and TF. The zero points mean the wells were shut in and there was no production on these dates. The data showed that the water cut could not return to the 20% level it was at before the new wells were stimulated.

Multiple DSU Site in Williams County

The second site with multiple DSUs is located in Williams County, North Dakota. This site has 16 wells, including eight wells completed in the MB and eight wells completed in the TF, as shown in Figure 61. The fundamental well and completion data for this site can be found in Table 14. Wells 2TFH, 3MBH, and 11MBH were stimulated and brought to production in 2013. Wells 4MBH, 5TFH, and 5MBH were stimulated and brought to production in 2014. Wells 6TFH, 6MBH, 10TFH, 11TFH, 12MBH, and 12TFH were stimulated and brought to production in 2015. Wells 1TFH, 1MBH, 2MBH, and 3TFH were stimulated and brought to production in 2016. Analysis of the water cut behavior in parent wells clearly showed that well interference exists in these DSUs, as shown in Figure 62. Similar to the DSU in Dunn County, the MB Unit and TF Formation are also hydraulically connected in these DSUs. Therefore, these two sites were used to develop conformance control and EOR strategies in the Bakken.

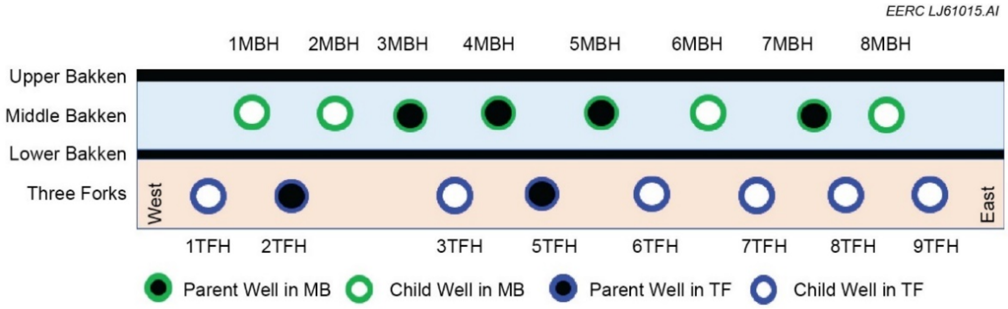

Figure 61. Distribution of wells in the DSUs located in Williams County, North Dakota.

Table 14. Essential Parameters for Wells in the DSUs Located in Williams County, North Dakota

No.	Well Name	Completed Formation/Unit	Well Type	Well Length, ft	Well Depth, ft	Fracture Stages	Production Start Time
1	1TFH	Three Forks	Child	9729	9684	35	2016
2	1MBH	Middle Bakken	Child	9564	9591	35	2016
3	2TFH	Three Forks	Parent	9741	9676	33	2013
4	2MBH	Middle Bakken	Child	9792	9589	35	2016
5	3MBH	Middle Bakken	Parent	9538	9585	33	2013
6	3TFH	Three Forks	Child	9763	9679	35	2016
7	4MBH	Middle Bakken	Parent	9566	9599	50	2014
8	5TFH	Three Forks	Parent	9529	9701	50	2014
9	5MBH	Middle Bakken	Parent	9617	9587	50	2014
10	6TFH	Three Forks	Child	9773	9674	50	2015
11	6MBH	Middle Bakken	Child	9719	9575	50	2015
12	10TFH	Three Forks	Child	9501	9664	35	2015
13	11MBH	Middle Bakken	Parent	9922	9547	35	2013
14	11TFH	Three Forks	Child	9573	9658	35	2015
15	12MBH	Middle Bakken	Child	9547	9561	35	2015
16	12TFH	Three Forks	Child	9469	9647	35	2015

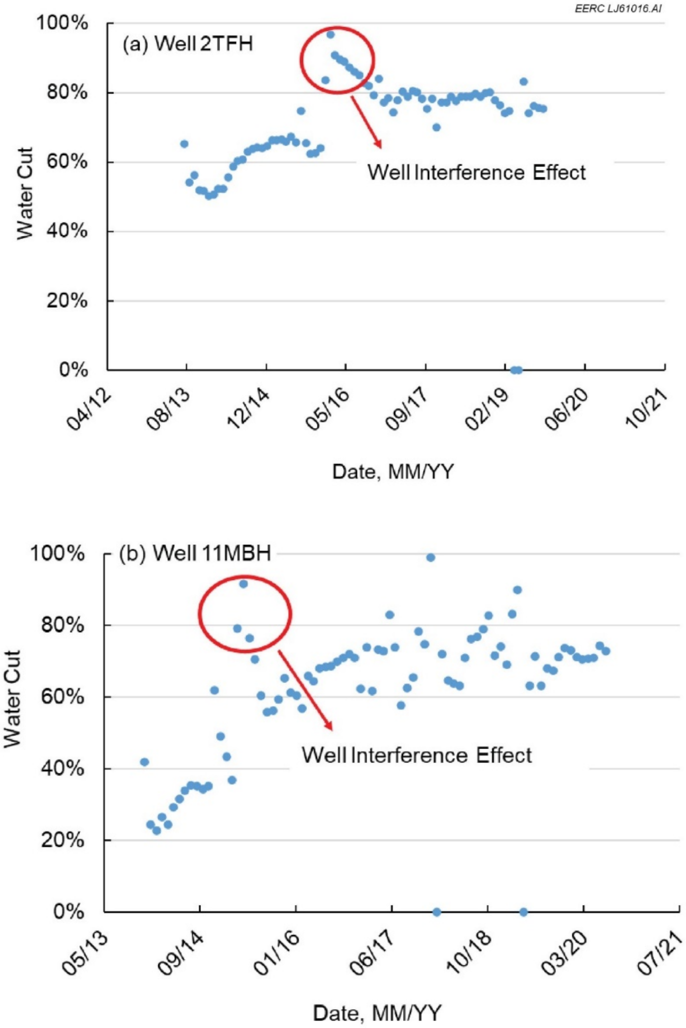

Figure 62. Illustration of well interference effect observed in the DSUs located in Williams County based on analysis of water cut. The water cut spikes in the red circles are caused by interference from neighboring MB or TF wells, indicating hydraulic communication between MB and TF.

Development of Reservoir Simulation Models

Because well interference was observed in both sites, two multiple-well, multiple-fracture reservoir simulation models were developed to investigate the conformance issues and EOR performance in this study. The models were designed to be able to evaluate the response of oil production to gas injection in single wells, as well as to simulate hydraulic communication between formations and production/injection interference between wells in the EOR process. The multiple-well setting enabled the simulation models to represent the actual reservoir situation more reasonably than a single-well model. Systematic modeling and simulation activities, including data collection, reservoir modeling, EOS regression, fracture modeling, history matching, conformance treatment, EOR strategy development, and sensitivity analysis, were conducted in this study to investigate the feasibility of conformance control and EOR improvement in the target sites.

Data from over 100 wells in Dunn and Williams Counties were collected from the NDIC database to characterize the reservoirs in the two selected sites. A database with fundamental reservoir properties, including porosity, permeability, pore throat size, and mineral composition, etc., for the Bakken and Three Forks Formations, was also used to support the modeling activities (Sorensen and others, 2014, 2018; Jin and others, 2017b, c; Pospisil and others, 2020).

Formation structures throughout the modeling areas were correlated with well logs and core measurements collected from the wells (and their neighboring wells) from the two sites. The overall geologic structures of the two sites are identical; both include the Lodgepole, Bakken, and Three Forks Formations. These formations were divided into several zones in the models according to the nomenclature used by NDGS (Nesheim, 2019). Based on the geologic modeling method described by Pospisil and others (2020), two fit-for-purpose reservoir models were developed for the sites.

EOS Regression

An EOS regressed from PVT data is an essential component needed to characterize the fluid properties in the reservoir. PVT parameters measured from a variety of tests, including saturation pressure, separator test, constant composition expansion, and differential liberation, were matched to mimic the fluid behavior. The EOS enables the simulation model to reproduce and predict the fluid dynamics in the production process since both pressure and volume of the oil and gas change constantly after production starts. Rich gas used for EOR usually has different components such as methane (C_1), ethane (C_2), and propane (C_3), etc., in the gas stream. When the gas is injected into the reservoir, these components will interact with oil based on their physical and chemical properties; i.e., the gas components perform differently from each other in the reservoir. A site-specific EOS is usually required to capture the gas–oil interaction in a particular reservoir.

Two EOSs with a different number of components were regressed from PVT data collected from the Dunn and Williams sites (Table 15). The first one was developed for the Dunn site with eight components, and the second one was developed for the Williams site with ten components. The number of components in each EOS was optimized to maximize the simulation efficiency based on site-specific PVT data. Both EOS models defined the gas components (N_2, C_1, C_2, and C_3) individually, allowing the evaluation of different combinations of injection gas composition in the EOR process. Results showed that both EOSs matched the experimental data satisfactorily in Table 15. Figure 63 shows an example of a good match for the GOR and relative oil volume in the two sites.

Table 15. Components in the EOS Models for the Dunn and Williams Sites

	EOS	
Component	**Dunn Site**	**Williams Site**
1	N_2	CO_2
2	CH_4	N_2
3	C_2H_6	CH_4
4	C_3H_8	C_2H_6
5	IC_4 to NC_4	C_3H_8
6	IC_5 to C_{12}	IC_4 to NC_4
7	C_{13} to C_{19}	IC_5 to C_7
8	C_{20} to C_{30}	C_8 to C_{12}
9		C_{13} to C_{19}
10		C_{20} to C_{30}

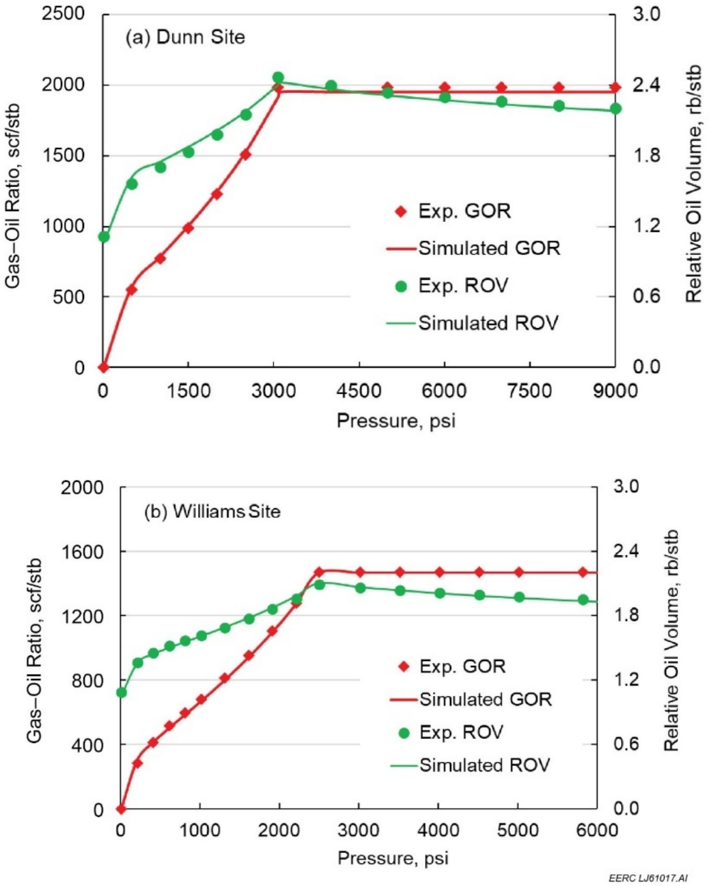

Figure 63. Example of EOS regression results for the PVT data from the two sites: a) Dunn site and b) Williams site.

Fracture Modeling with EDFM

Being able to predict the fluid distribution in the subsurface is paramount for advancing EOR strategies. Particularly, appropriate modeling of fracture geometries and uncertainties plays a critical role in the estimation of sweep efficiency and incremental oil recovery. However, the presence of fracture networks poses many challenges to traditional simulation methods. Conventional dual porosity and dual permeability methods lack accuracy because of the simple assumption of orthogonal fracture networks with cubic matrix blocks (Warren and Root, 1963; Yu and others, 2014; Xu and others, 2017). Local grid refinement and unstructured grid methods are also used frequently to simulate complex fracture geometries; however, their computation can be time-consuming because of the large number of grids and complicated gridding structure involved in the models (Conlin and others, 1990; Choi and others, 1997; Mirzaei and Cipolla, 2012; Jin and others, 2017a, 2019).

More recently, the EDFM technique has been developed to solve the challenges in fracture simulation. EDFM allows modeling complex fractures while keeping the computational efficiency of the dual-continuum models (Moinfar and others, 2014; Yan and others, 2016). The method integrates fracture cells with a nonneighboring connection (NNC) approach and three-dimensional (3D) modeling of slanted and nonplanar fractures into a regular grid system, as shown in Figure 64. The NNC settings enable structure grids to describe fractures in the model so that a traditional reservoir simulator like CMG's software package can be used to run a simulation model with complex fracture settings efficiently (Xu, 2015; Xu and others, 2017). High flexibility is another unique advantage of the EDFM approach: if a new fracture segment is added to the physical domain, a nonneighboring new fracture cell will be added to the computational domain accordingly to calculate fluid flow inside fractures or between fractures and the rock matrix. This feature makes it convenient to simulate complex fractures and fluid flow in the EOR process. A few cases have been reported to simulate both pressure depletion and gas EOR operations in unconventional reservoirs employing the EDFM approach (Moinfar and others, 2014; Yu and others, 2014, 2020; Yan and others, 2016; Fiallos and others, 2019). Therefore, the EDFM approach was selected to simulate the complex fracture geometries in the Bakken.

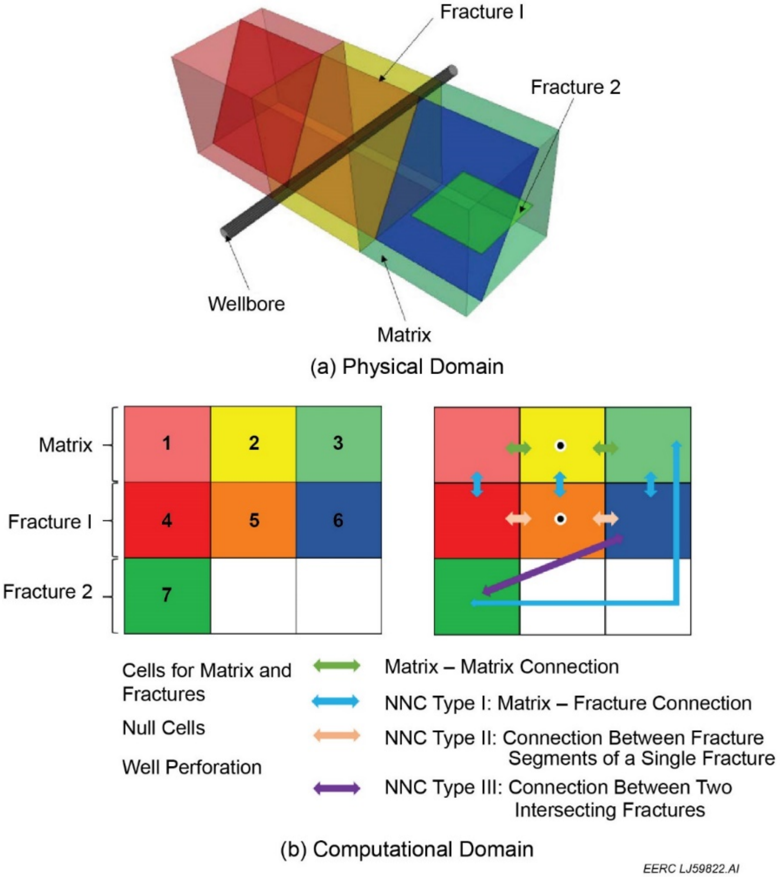

Figure 64. Explanation of physical and computational domains of EDFM and connections between wellbore, fractures, and matrix (Xu and others, 2017).

Reservoir Simulation Model for the Single DSU Site

Using the geologic/reservoir properties, EOS, and EDFM method, a compositional reservoir simulation model with main hydraulic fractures was developed for the Dunn site employing CMG's GEM. Seven wells were included in the simulation model. Because of the large number of fracture stages along the wellbore of each well, 25% of the fracture stages for each well were included in the models for an efficient simulation, as illustrated in Figure 65. For example, Well TF1 has 40 fracture stages and a lateral length of 10,011 ft in the actual field, so the model cut 2503 ft and ten fracture stages out of the well for simulation. The basic well and fracturing settings for the wells are shown in Table 16.

The length (in the X direction), width (in the Y direction), and height (in the Z direction) of the simulation model are 4000, 3250, and 206 ft, respectively. The model was divided into five formations with a total of 17 layers, including the Lodgepole (LP), Upper Bakken (UB), MB, Lower Bakken (LB), and TF Formations. The thickness of the LP, UB, MB, LB, and TF are 40, 18, 40, 18, and 90 ft, respectively. An additional 16 grids in the X direction were added to the EDFM for fracture calculation based on the algorithm described above. The additional grids were

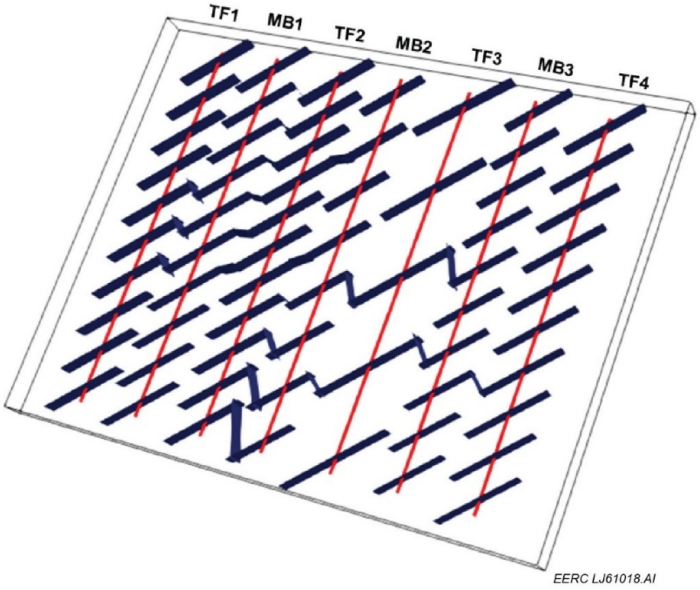

Figure 65. Schematic of fracture distribution in the simulation model for the Dunn site.

used for flow calculation only, and they did not change the material balance in the model. History match was conducted to reproduce the production data in the field. Figure 66 shows the matching results for Well MB2; other wells have similar matches. The results indicate that the model was able to capture the production behavior of the wells to a reasonable degree.

Table 16. Basic Well and Fracturing Data for the Simulated Wells in the Dunn Site

Site	Well Name	Well Length, ft	Fracture Stages
Dunn	TF1	2503	10
	MB1	2446	10
	TF2	2494	11
	MB2	2220	8
	TF3	2269	5
	MB3	2421	10
	TF4	3848	15

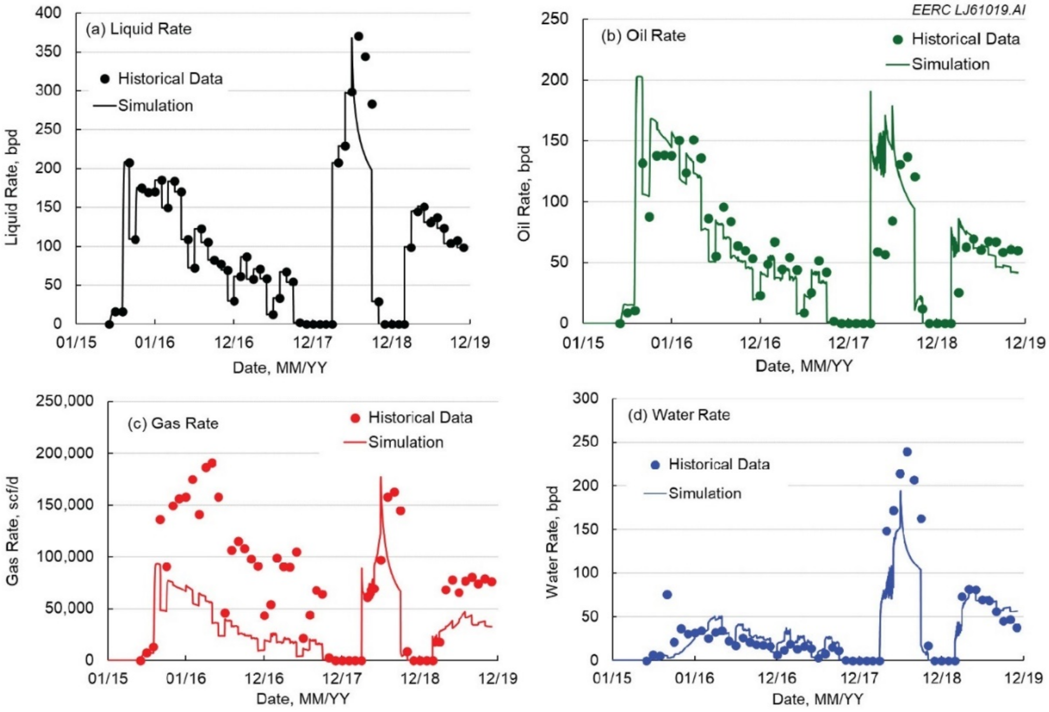

Figure 66. History match results for Well MB2: a) liquid rate, b) oil rate, c) gas rate, and d) water rate.

Reservoir Simulation Model for the Multiple DSU Site

Following the same methodology used for the Dunn site, a reservoir model with both hydraulic and natural fractures was built for the Williams site, where 16 wells were included in multiple DSUs. Since the simulation of 16 wells with over 630 hydraulic fracture stages requires high computational efforts, ca. 10% of the fracture stages for each well were included in the model. For example, Well 1TFH has 35 fracture stages and a lateral length of 9729 ft in the actual field; the model included four fracture stages and 973 ft of the wellbore length for this well. Figure 67 shows the well and fracture distribution in the simulation model for the Williams site. The basic well and fracturing data for the simulated wells are shown in Table 17. The properties of natural fractures such as permeability and aperture, etc., were adjusted in the history-matching process.

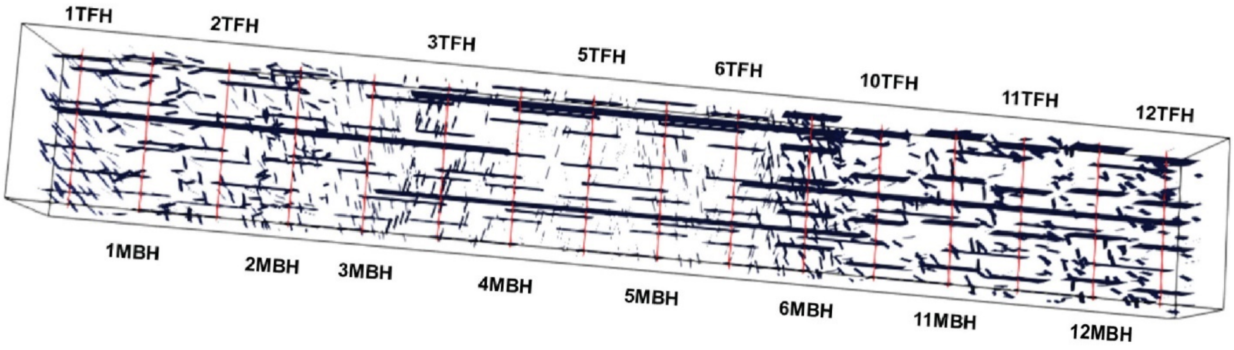

EERC LJ61020.AI

Figure 67. Schematic of fracture distribution in the simulation model for the Williams site.

Table 17. Basic Well and Fracturing Data for the Simulated Wells in the Williams Site

Site	Well Name	Well Length, ft	Fracture Stages
Williams	1TFH	973	4
	1MBH	956	4
	2TFH	974	4
	2MBH	979	4
	3MBH	954	4
	3TFH	976	4
	4MBH	957	5
	5TFH	953	5
	5MBH	962	5
	6TFH	977	5
	6MBH	972	5
	10TFH	950	4
	11MBH	992	4
	11TFH	957	4
	12MBH	955	4
	12TFH	947	4

The width (in the X direction), length (in the Y direction), and height (in the Z direction) of the model are 8000, 1000, and 840 ft, respectively. The model contains five geologic units with 22 layers, including LP, UB, MB, LB, and TF Formations. The thickness of the LP, UB, MB, LB, and TF are 350, 10, 60, 30, 40, 350 ft, respectively. An additional four grids in the X direction were added via EDFM to calculate fluid flow for fracture–fracture and fracture–matrix connections. The calculation did not affect the material balance of the model. History matching was performed to match the field production data.

Figures 68 and 69 illustrate example history-matching results for Wells 2TFH and 3MBH, respectively; other wells have similar matches. The results demonstrate that the simulation model can capture the flow dynamics for this site satisfactorily.

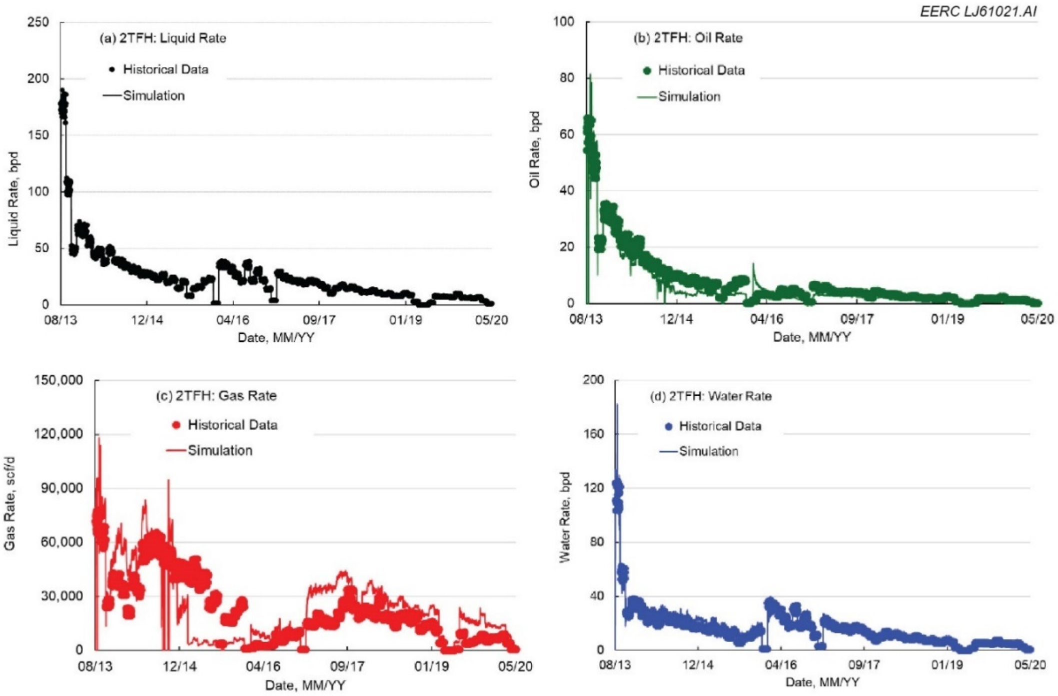
EERC LJ61021.AI

Figure 68. History match results for Well 2TFH: a) liquid rate, b) oil rate, c) gas rate, and d) water rate.

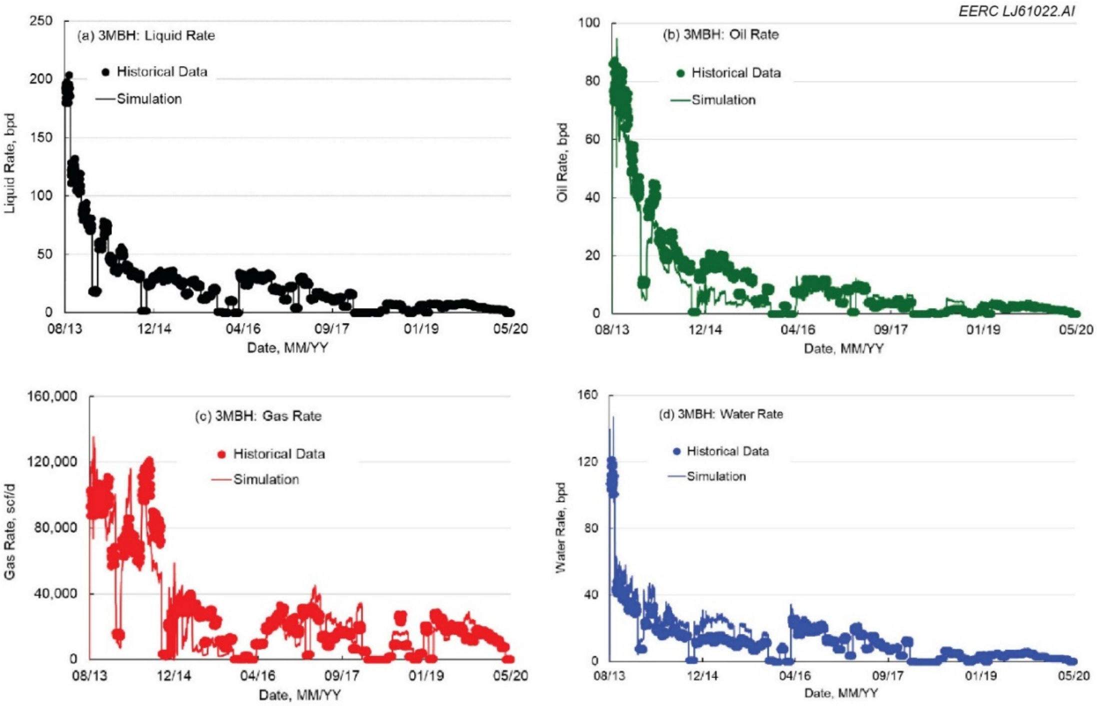

Figure 69. History match results for Well 3MBH: a) liquid rate, b) oil rate, c) gas rate, and d) water rate.

Simulation of Conformance Challenges

Usually, a large volume (20 thousand – 120 thousand bbl) of water is required in the hydraulic fracturing process to stimulate a well by creating multiple fracture stages in the Bakken. Such a large volume of injected water will cause a water cut increase or spike in one or more neighboring wells if the wells are connected, because the high injection pressure will force the injection water flowing from the injector to its neighboring well(s). Figures 60 and 62 clearly showed that water cut in parent wells was increased when a neighboring child well was stimulated. Therefore, water injection was used in this study to test the fluid communication between wells in both sites.

Parent wells are more likely to be used for EOR operations because of their longer production time and lower production rates, so four parent wells were selected in the two sites to test whether they have well interference with their adjacent offset wells and also whether the models can capture the fluid communication between the main oil-producing units, i.e., MB and TF. Table 18 shows the well interference design for the two sites. Wells MB2 and TF2 were selected in the Dunn site. Water was injected in these two wells separately, and water cut in the adjacent offset wells was monitored to observe the interference effects. For instance, water cut in Well TF2 was monitored when water was injected in Well MB2, and water cut in Well MB1 was monitored when water was injected in Well TF2, respectively, as shown in Figure 70a. The same method was applied to the Williams site: Wells 5TFH and 11MBH were selected as testing wells for water injection, and water cut in Wells 4MBH and 10TFH was closely monitored, as shown in Figure 70b.

Table 18. Well Interference Test Design in the Dunn and Williams Sites

Site	Test No.	Injection Well	Injection Fluid	Monitoring Well	Monitoring Parameter
Dunn	1	MB2	Water	TF2	Water cut
	2	TF2	Water	MB1	Water cut
Williams	3	5TFH	Water	4MBH	Water cut
	4	11MBH	Water	10TFH	Water cut

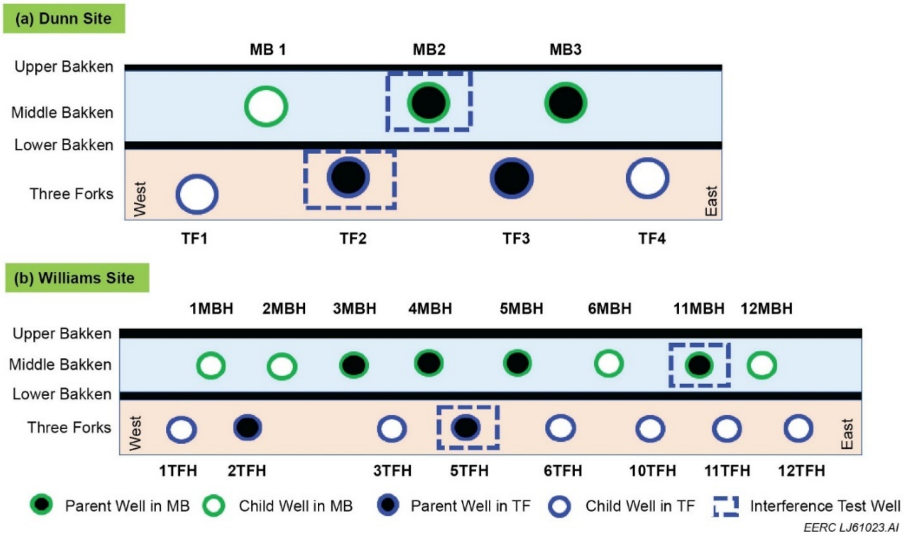

Figure 70. Location of wells used for interference test in a) Dunn site and b) Williams site.

In the first test, water was injected through well MB2 at a rate of 4000 bpd until reaching the maximum BHP of 7500 psi at the Dunn site, as shown in Figure 71, which illustrates that water injection can effectively lift the well BHP in the injection well. All other wells remained open for production in the injection process. Therefore, water cut in adjacent offset wells should increase if the model can capture the well interference effect as well as the hydraulic communication between the MB Unit and the TF Formation. Figure 72 shows the water cut behavior in Well TF2 when water was injected in Well MB2; a water cut curve for pressure depletion scenario was also added to the figure for comparison. Results clearly demonstrated the interference between the wells and the oil-producing zones because the injected water can easily flow from Well MB2 to Well TF2. In the second test, water was injected through Well TF2 using the same injection constraints as in the first test. Figure 73 shows that Wells MB1 and TF2 were also very well connected based on the smooth water cut increase in Well MB1 after water was injected in Well TF2.

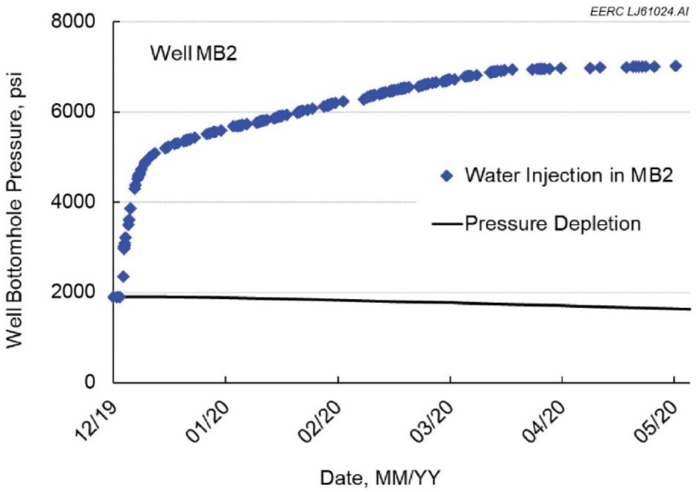

Figure 71. Comparison of BHP during normal pressure depletion and water injection processes in Well MB2 at the Dunn site.

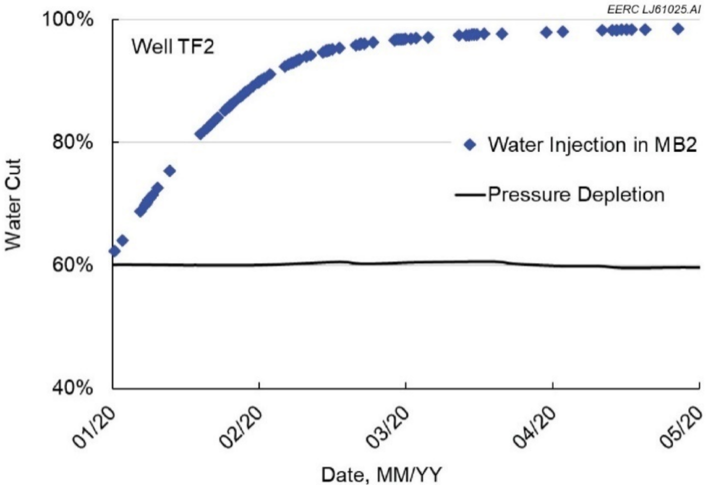

Figure 72. Water cut behavior in Well TF2 when water was injected in Well MB2 at the Dunn site. The black curve was the water cut under a pressure depletion scenario; it was added for comparison.

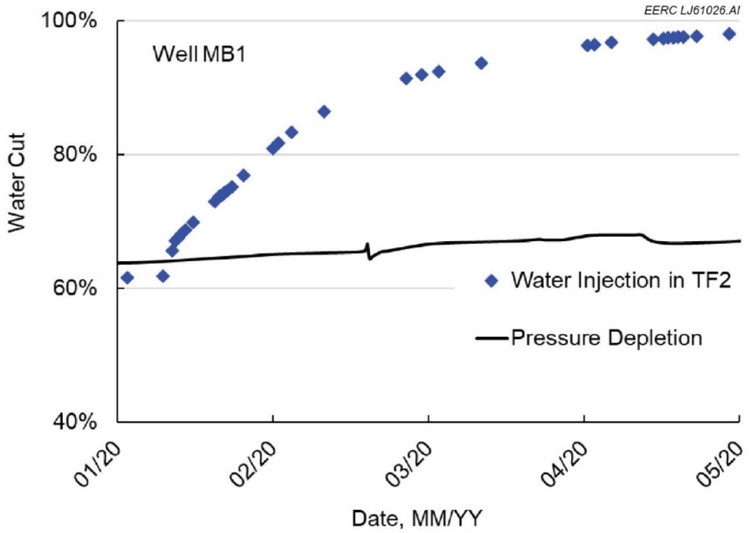

Figure 73. Water cut behavior in Well MB1 when water was injected in Well TF2 in the Dunn site. The black curve was the water cut under a pressure depletion scenario; it was added for comparison.

The same methodology was applied to the third and fourth tests to identify whether the model can capture the well interference effect and fluid communication between the MB Unit and the TF Formation in the Williams site. Water was injected through Well 5TFH at a rate of 4000 bpd until reaching the maximum bottomhole pressure of 6000 psi at the Williams site, as shown in Figure 74.

Compared to the pressure response in Well MB2 (Figure 71) at the Dunn site, the pressure increases slower in Well 5TFH because of the longer production history and lower initial reservoir pressure at the Williams site. The water cut response in the adjacent offset Well 4MBH is shown in Figure 75, which illustrates a strong fluid communication between these wells. The injected water may completely fill Well 4MBH in 2 months, with continuous injection in 5TFH. The well interference effect was demonstrated similarly in the fourth test, which employed Well 11MBH to inject water. Water will soon fill up the entire monitoring well after breakthrough because of the high fracture conductivity between wells. Once water breaks through to a producer, a pathway is established for the injected water to flow from the injector to the producer. Since the injected water is much easier to flow through the fractures than oil flows from the tight matrix to the fractures, the flow paths between the neighboring injector and producer will be soon filled with the injected water and make oil production difficult if water injection continues. Figures 75 and 76 demonstrate this observation clearly; i.e., water cut in the monitored producers reaches 100% within 2 months of water injection. Since gas has much higher mobility than water in the reservoir, the gas breakthrough will be earlier than that of water when the same injection pressure is applied in the EOR process; in other words, the well interference effect will be stronger when gas injection is used for EOR.

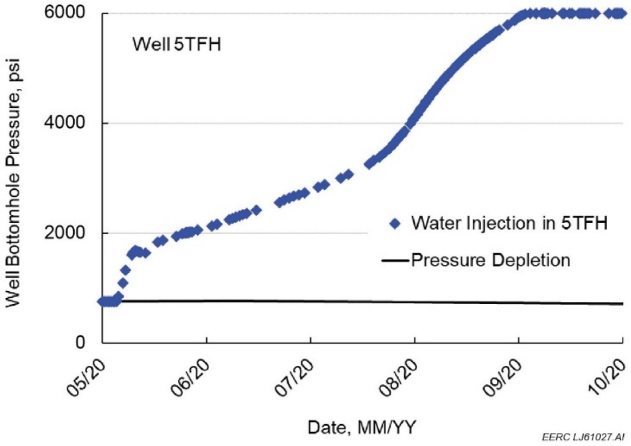

Figure 74. Comparison of BHP during normal pressure depletion and water injection processes in Well 5TFH at the Williams site.

These tests showed that both models can capture the well interference effects in the Bakken. Although there is a shale formation (LB) between the MB and TF, these two pay zones may be connected for fluid flow when two or more neighboring wells are drilled and hydraulically fractured in these two zones: the LB shale may no longer act as a barrier between them. Therefore, conformance control needs to be considered for wells in both MB and TF in the gas injection process no matter whether the gas injector is located in the MB or TF.

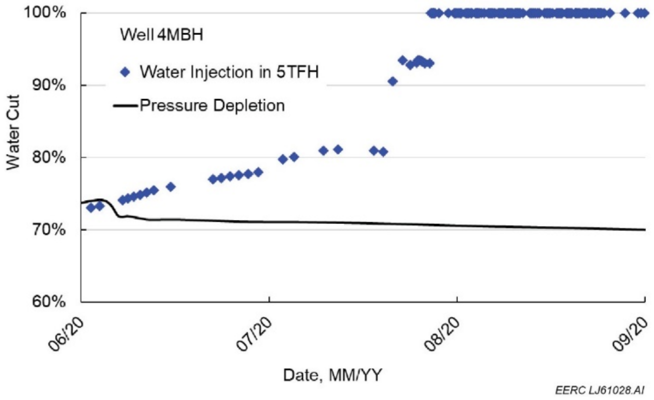

Figure 75. Water cut increases in Well 4MBH when water was injected in Well 5TFH at the Williams site.

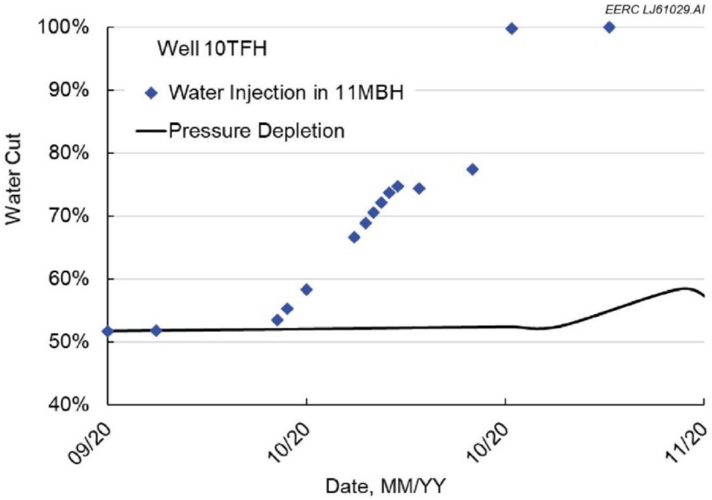

Figure 76. Water cut increases in Well 10TFH when water was injected in Well 11MBH at the Williams site.

Subactivity 7.2 – Alternative EOR Strategies Integrated with Conformance Control

An evaluation of the Bakken rich gas EOR test at the Stomping Horse complex, combined with an examination of results from previous rich gas injection tests in the Bakken and Eagle Ford, suggests that including water injection as a component of a Bakken EOR scheme may be beneficial to managing conformance. Water injection was also used to prevent strong well interference effects (frac hits) during hydraulic fracturing operations in unconventional reservoirs (Esquivel and Blasingame, 2017; Bommer and Bayne, 2018; Vidma and others, 2019). However, the current permit from the North Dakota Department of Mineral Resources for the injection test specifically precludes the injection of water as part of the Liberty pilot test at Stomping Horse. This subactivity used the EDFM models developed in Subactivity 7.1 to conduct a detailed dynamic simulation of alternative rich gas injection scenarios that include the injection of water. The simulation predicted the effects that water injection may have on conformance control in future EOR efforts at different areas of the Bakken.

Examination of past Bakken EOR test results also suggests that injection operations may influence reservoir behavior beyond the boundaries of a DSU (Hoffman and Evans, 2016; Sorensen and Hamling, 2016). In addition to modeling alternative EOR schemes that include water injection, the EERC also conducted simulation activities to examine the potential impact that the scale of a project may have on conformance and sweep efficiency (i.e., a multiwell huff ‘n’ puff [HnP] operation conducted over a domain comprising multiple DSUs). Therefore, the following activities were conducted in this subactivity:

1. EOR performance without conformance control: different rich gas injection scenarios were simulated to obtain the baseline EOR results considering well interference effect (without conformance control) in the Dunn site.

2. Conformance control with water injection: conformance control strategies using water injection were specifically designed for hydraulically fractured wells to improve EOR performance in the Bakken. The strategies were applied to the rich gas EOR cases studied in the Dunn site.

3. Upscaling the alternative EOR strategies: the newly developed rich gas EOR strategies with conformance control were upscaled from a single-well HnP operation to a multiple-well HnP operation in a domain comprising multiple DSUs in the Williams site.

EOR Performance Considering Well Interference in the Dunn Site

First, a series of simulation cases were designed to study the rich gas EOR performance in the Dunn site where Well MB2 was used as an HnP well for EOR operations. Sensitivity analysis was performed to identify the most important factor for the EOR pilot test. Based on the previous and ongoing pilot tests in the Bakken and Eagle Ford unconventional plays, key operational parameters, including injection rate, injection time, soaking time, and production time, etc., were considered in the simulation study, as shown in Table 19. The reason for selecting Well MB2 for HnP operation is that Wells TF2, MB2, TF3, and MB3 are parent wells completed on/before 2015. The production rates of these wells are relatively low so that they were considered more suitable for EOR operations. The newer wells in this DSU could be deferred for EOR operations because of their high current production rates. Wells TF2 and MB3 are close to the newly completed wells, so gas injection could impact production in these high-rate wells. Well TF3 might be depleted more than other wells because of its longer production history and fewer fracture stages. Well MB2 is in the middle of the DSU with a moderate oil production rate, so this well was selected to conduct the detailed EOR prediction and sensitivity study.

Table 19. Operational Parameters Considered in the EOR Sensitivity Study

Parameter	**Value**
Injection Rate, MMscfd	2~45
HnP Well	MB2
EOR Operational Time, years	2
Injection Time, days/cycle	15, 30, 60
Soaking Time, days/cycle	0, 7, 14
Production Time, days/cycle	30, 60, 90
Injection Gas Composition (C1:C2:C3)	60:25:15
Maximum Injection Pressure (BHP), psi	7500
Minimum Production Pressure (BHP), psi	100

The detailed results are presented and analyzed in Subactivity 8.1. An example is presented here to illustrate the EOR performance considering the well interference effect with the following parameters:

- HnP well: MB2
- EOR operational time: 2 years

- Injection rate: 3 MMscfd
- Injection time: 30 days/cycle
- Soaking time: 7 days/cycle
- Production time: 60 days/cycle
- Maximum injection pressure constraint: 7500 psi
- Minimum production pressure constraint: 100 psi

Figure 77 shows the BHP of the HnP well (MB2) and its adjacent offset wells (TF2 and TF3) in the first year of EOR operations. The measured MMP between the oil and injection gas in this site is between 2200 and 2300 psi. Because of the high initial reservoir pressure (~8100 psi), relatively short production history, and well-managed production schedule, the reservoir was not fully depleted to a low-pressure level before the EOR operation. Therefore, the BHP in the HnP well increased effectively with gas injection; however, the BHP also decreased rapidly in the HnP well during the soaking period when the injected gas flowed into the depleted volume around the well. Since Wells TF2 and TF3 are hydraulically connected with the injector, the BHP in these two offset wells also increased above MMP in the injection and soaking cycles. As a result, miscible EOR was reached in the EOR operations when rich gas was injected at 3 MMscfd.

The production pressure was set at 100 psi to maximize the oil production rate so that the lost oil production during the injection and soaking cycles could be made up in the oil production cycle. Figure 78 shows the oil production performance in the HnP well and its adjacent offset wells through the entire EOR process. The higher oil production rate in Well TF2 indicates a gas-flooding effect in the EOR operations; i.e., the injected gas drove oil from the fractures to the well when there was mobile oil in the fractures. A similar oil response was observed in previous gas EOR pilots in the Bakken and Eagle Ford reservoirs (Nagarajan and others, 2020; Litvak and others, 2020). Another possible reason is that TF2 has more fracture stages than MB2 and TF3 (45 vs. 30 and 19); therefore, TF2 might have a larger stimulated reservoir volume (SRV) around the well for EOR. The oil production performance in these wells indicates that a larger SRV could yield better EOR performance in the miscible EOR process.

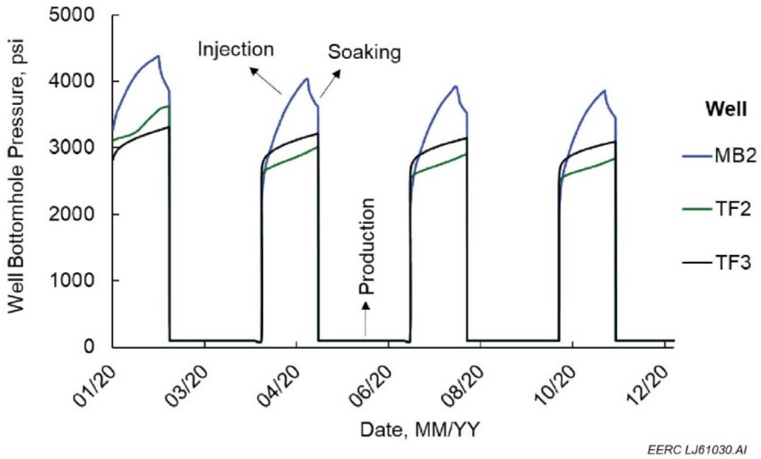

Figure 77. BHP behavior in the HnP well (MB2) and its adjacent offset wells (TF2 and TF3) in the first year of EOR operation when rich gas was injected at 3 MMscfd.

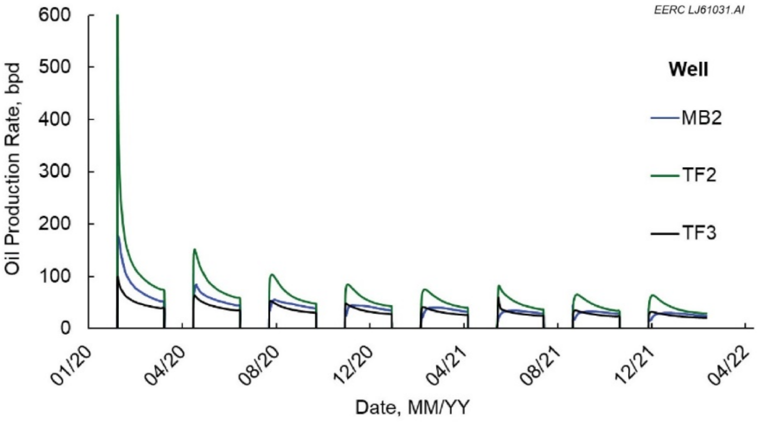

Figure 78. Oil production performance in the HnP well (MB2) and its adjacent offset wells (TF2 and TF3) through the entire EOR process.

Figure 78 also indicates that the EOR effect in the wells becomes weak after the first several injection–production cycles. When the reservoir pressure is high enough to support oil production by primary depletion operations with a moderate production rate, EOR without a long-lasting effect may not be the best choice. Figure 79 shows the comparison of cumulative oil production between a normal pressure depletion and rich gas EOR with a 3-MMscfd injection rate. Results showed that rich gas EOR with a 3-MMscfd gas injection could not produce more oil than the pressure depletion operation since the incremental oil in the production cycle could not offset the lost production in the injection and soaking cycles.

Further analyses of Figures 78 and 79 indicate that rich gas EOR may outperform the pressure depletion in cumulative oil production if the high oil production cycles can be maintained for a longer time. The Eagle Ford pilots showed that a high gas injection rate is beneficial to maintain a high oil production rate in the EOR process. However, compared to the Eagle Ford pilots, gas availability is one of the most critical challenges for EOR operations in the Bakken.

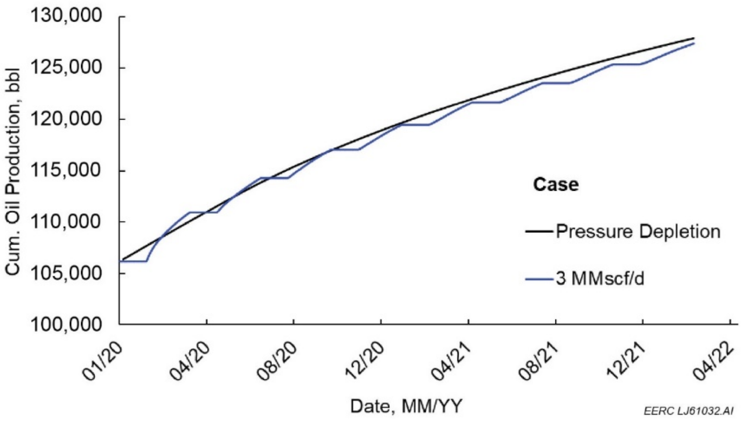

Figure 79. Comparison of cumulative oil production of Well MB2 with pressure depletion and gas EOR (3-MMscf/d injection rate) operations.

There are few large gas storage facilities available near most of the production pads in the Bakken; as a result, continuous injection of rich gas at a high rate becomes difficult in the EOR process because of an inadequate gas supply. Therefore, another case with a moderate injection rate of 6 MMscfd was simulated to verify the assumption. In the meantime, an additional case with a 1-MMscfd gas injection rate was also simulated to have a more detailed comparison between the cases, so that the effect of gas injection on EOR performance can be evaluated more thoroughly. Figure 80 illustrates that a higher BHP could be reached when increasing the gas injection rate, which then yields higher oil production rates and more cumulative oil production, as shown in Figures 81 and 82, respectively.

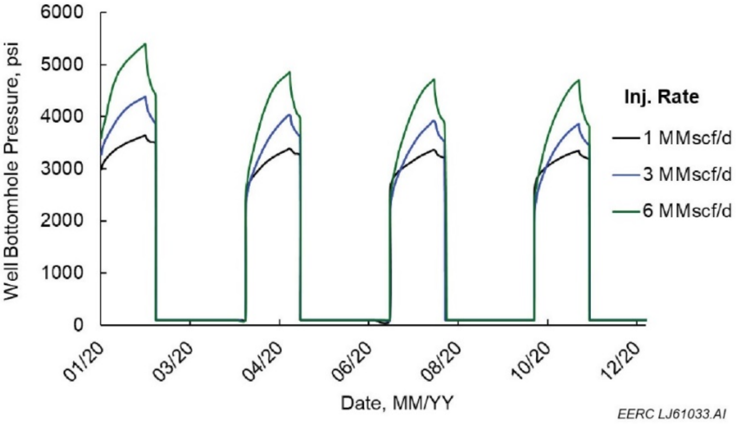

EERC LJ61033.AI

Figure 80. BHP behavior in the HnP well (MB2) with different gas injection rates.

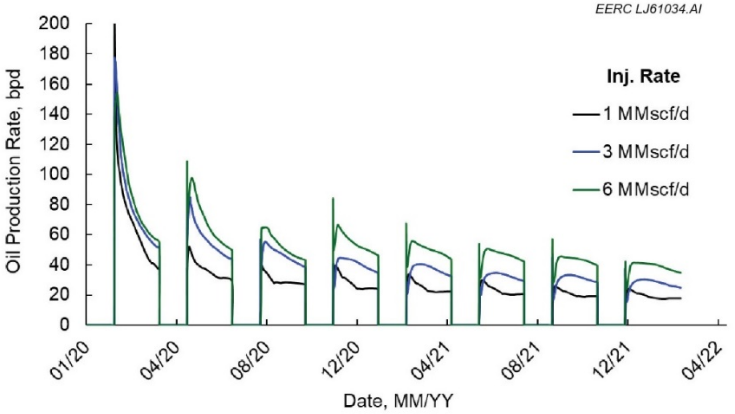
EERC LJ61034.AI

Figure 81. Oil production performance in the HnP well (MB2) with different gas injection rates.

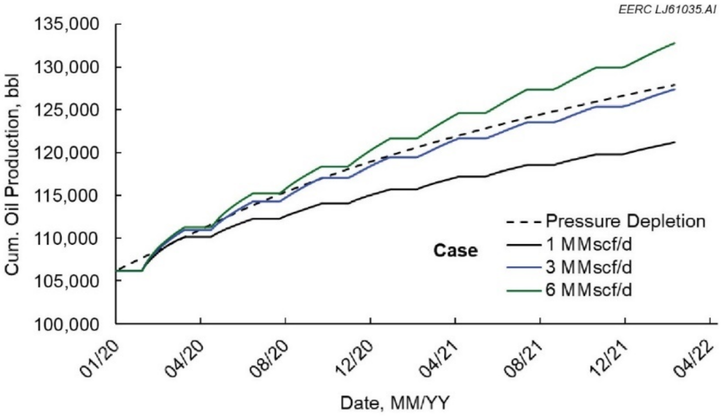

Figure 82. Comparison of oil production performance between pressure depletion and gas injection EOR with different injection rates.

EOR Performance with Conformance Control in the Dunn Site

Figures 80 and 81 illustrate that there is a strong correlation between the well BHP and oil production rate in the rich gas EOR well. Therefore, a direct method to improve the EOR performance is to increase the BHP by using higher gas injection rates with the same injection gas composition. Figure 82 demonstrates the effect of the gas injection rate on EOR performance when no conformance control was applied to confine the injected gas around the HnP well. Considering the gas availability in the Bakken, it is necessary to develop alternative EOR strategies to improve the oil production performance without increasing the gas injection rate significantly. Since BHP is a function of the confined gas quantity around the HnP well, the BHP may increase to a higher level if the injected gas can be kept within a certain volume around the injector in the injection and soaking cycles.

Conformance Control with Water Injection

Figure 82 shows that the oil production performance of pressure depletion and rich gas EOR with a 3-MMscf/d injection rate was similar; thus this EOR case was selected as a base case for a conformance control study. Figure 79 shows that the maximum reachable BHP of the HnP well was around 4400 psi in the injection cycle when rich gas was injected at 3 MMscfd without any conformance control operations. In the meantime, the maximum BHP of the two offset wells, TF2 and TF3, was 3650 and 3300 psi, respectively. The injected gas could easily flow from the injector to these two offset wells because of the pressure difference and high fracture conductivity between these wells. Therefore, a BHP higher than 4400 psi in TF2 and TF3 is required to prevent the injected gas flowing from the HnP well to these two offset wells in the EOR process. One way to achieve this is to inject water in the two adjacent offset wells with controlled pressure as illustrated in Figure 83, where Well MB2 was used for gas EOR with HnP operations and Wells TF2 and TF3 were used to inject water in the injection and soaking cycles of Well MB2 so that the gas injected through this well could be confined in a certain volume around the well without flowing to Wells TF2 and TF3.

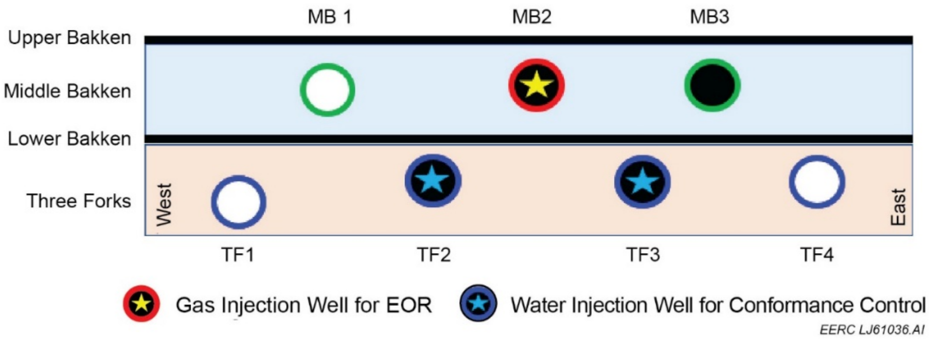

Figure 83. Schematic of gas and water injectors distribution for conformance control in the EOR process at the Dunn site.

Two cases were designed to investigate the effect of water injection in offset wells on pressure behavior in the HnP well where the gas injection rate was fixed at 3 MMscfd. The first case used a constant-pressure water injection of 4500 psi in Wells TF2 and TF3 during the injection and soaking cycles. The second case used 6000-psi water injection in the same two wells to make sure that no gas flowed to them in the EOR process. Figure 84 shows the comparison of the BHP behavior in the HnP well with and without conformance control. It is clear that water injection in the offset wells can improve the BHP in the EOR well effectively. Compared to the maximum BHP of 4400 psi without conformance control, the maximum BHP in the EOR well could reach 4850 and 5400 psi when water was injected at 4500 and 6000 psi, respectively, in the offset wells. Such a pressure increase led to an effective EOR improvement as illustrated in Figure 85. Around 5.5% more oil could be produced from the HnP wells in 2 years of EOR operations when gas was injected at only 3 MMscfd with 6000 psi of water injection in the offset wells. This rate is significantly lower than the reported gas injection rates of 14–25 MMscfd in the Eagle Ford pilots.

Conformance Control with Surfactant Injection

Oil resides in both matrix and fractures in unconventional reservoirs. Oil in hydraulic fractures is relatively easy to produce since the fracture permeability and the pressure difference between reservoir and wellbore is high enough for oil to flow through the fractures. The situation is different for oil in the matrix where a high-pressure difference is required for oil to flow through the tiny pores in the production process. Reservoir pressure continues to drop with production in the pressure depletion stage, especially in the near-fracture and near-wellbore regions. The pressure difference may soon become too low to support the high oil production rate in the pressure depletion operations. As a result, the production rate decreases rapidly in the first several years of production. The depleted volume in the reservoir needs to be recharged so that oil can continue flowing through the matrix and the well can regain oil production. Therefore, oil residing in the tight matrix is the main target for EOR in the Bakken (Jin and others, 2017b, c).

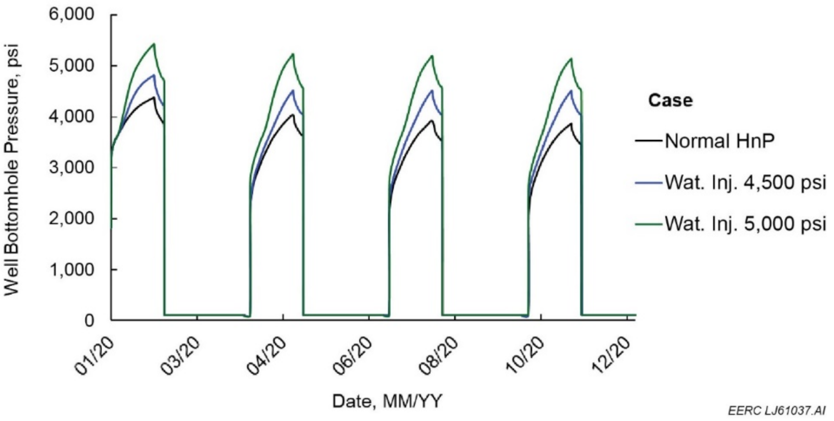

Figure 84. Comparison of BHP behavior in the HnP well (MB2) when the gas injection rate is 3 MMscfd with and without conformance control by water injection in the adjacent offset wells.

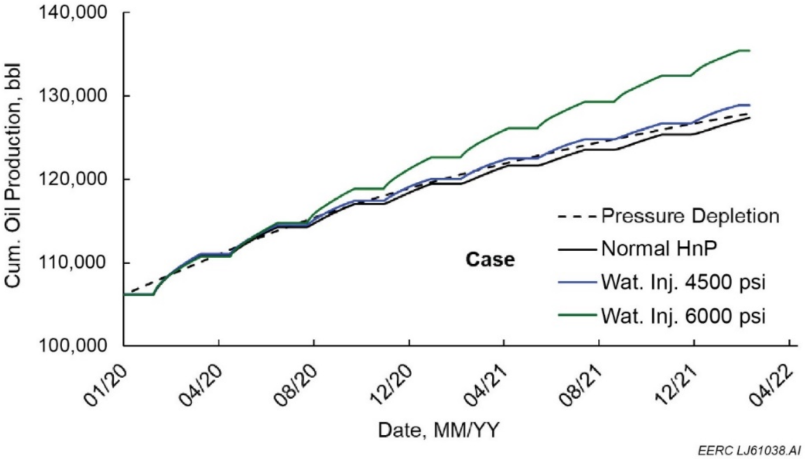

Figure 85. Comparison of oil production performance between pressure depletion and gas EOR (at 3-MMscfd injection rate) with and without conformance control by water injection in the adjacent offset wells.

Figure 86 shows a typical pore-size distribution in the MB and TF measured by the high-pressure mercury injection method. The figure indicates that most of the pore throats have a radius between 5 and 50 nm in the MB, while the values for the TF pores are a little larger, mainly, between 7.5 and 75 nm. Such a tiny pore size could generate high capillary pressure between fluid phases in the matrix based on Equation 6 (Alvarez and others, 2017; Jin and others, 2017c):

$$P_c = \frac{0.29\sigma cos\theta}{r} \quad \text{[Eq. 6]}$$

Where P_c is the capillary pressure, *psi*; σ is the IFT, *dyne/cm*; θ is the contact angle between two phases, *degree*; and r is the pore throat radius, μm.

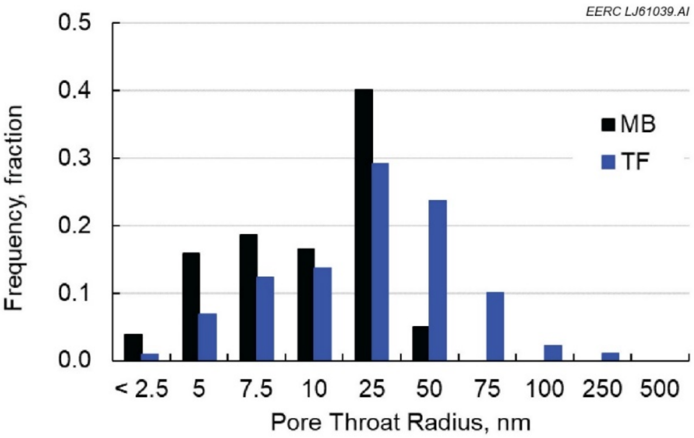

Figure 86. Measurements of pore-size distribution using rocks collected from the MB and Upper TF.

IFTs of oil–water and rich gas–water were also measured considering a wide range of pressure and salinity conditions in the Bakken, as shown in Figure 87. All experiments were conducted with a representative reservoir temperature of 250°F. Based on the experimental measurements and Equation [Eq. 6, capillary pressure could create a high resistance for fluids flowing through the tight matrix. Since pore throat size is an intrinsic rock property, which is difficult to change in the production operations, the IFT and/or CA needs to be reduced for a lower capillary resistance in the EOR process.

Laboratory experiments showed that surfactant can effectively reduce the oil–water CA and IFT in the Bakken (Alvarez and others, 2017; Kazempour and others, 2018). Figure 88 demonstrates the effect of different surfactants on reducing the oil–water CA in the Bakken as reported by Alvarez and others (2017). Kazempour and others (2018) reported that surfactant injection boosted oil production effectively in an EOR pilot in the Bakken. Following the method reported by Kazempour and others (2018), a simplified surfactant injection setting was applied to the model used for conformance control with water injection, as shown in Figure 82. The BHP and EOR performance of rich gas injection combined with conformance control by surfactant injection are shown in Figures 89 and 90, respectively. Results showed that up to 9.2% more oil could be produced from the HnP wells in 2 years of EOR operations when gas was injected at only 3 MMscfd with 6000 psi of surfactant injection in the offset wells. Obviously, surfactant is more effective than water for EOR improvement when used as an injection agent for conformance control in the Bakken.

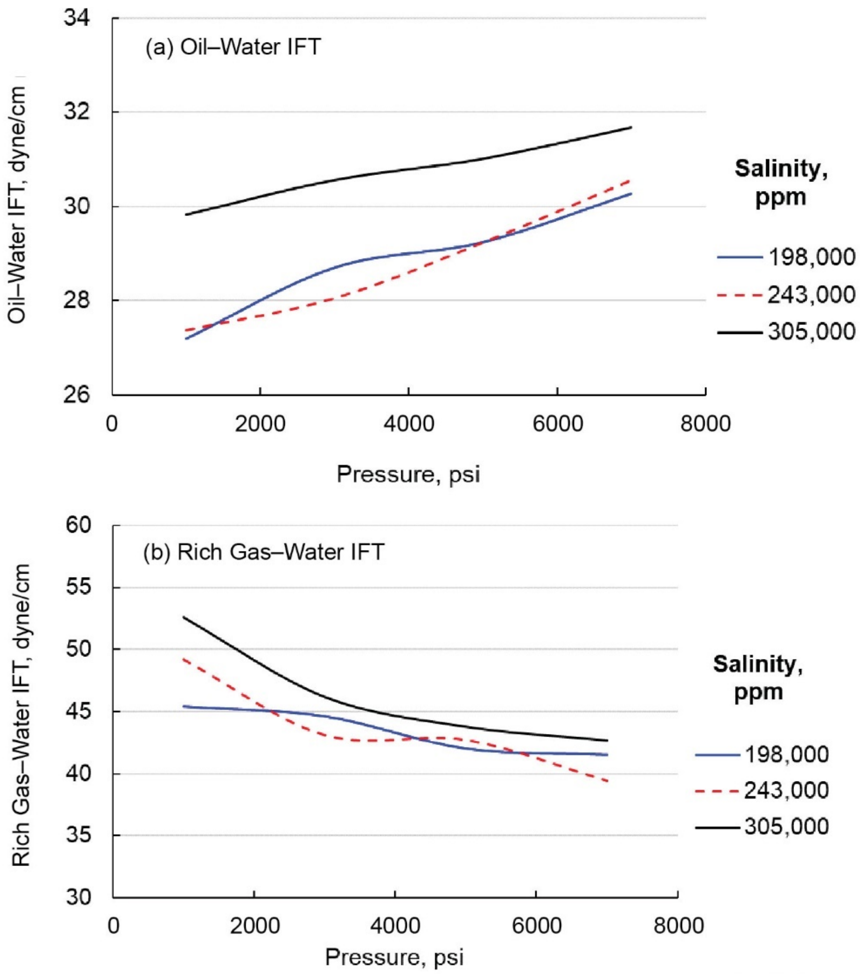

EERC LJ61040.AI

Figure 87. IFT between a) oil and water and b) rich gas and water in the Bakken reservoir considering a wide range of pressure and salinity conditions (temperature at 250°F).

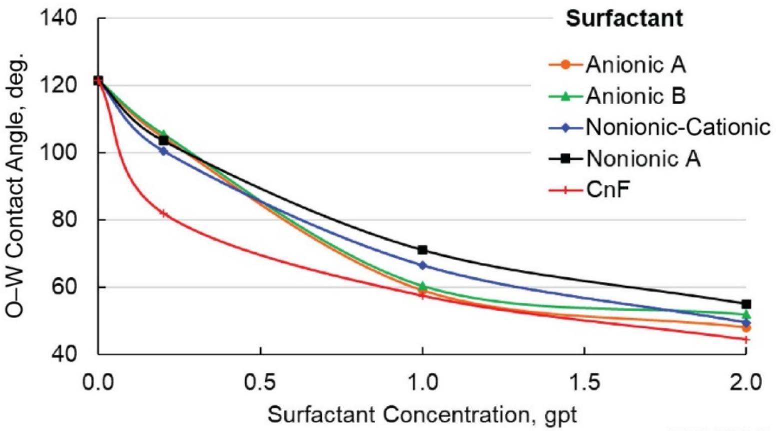

EERC LJ61041.AI

Figure 88. Effect of different surfactants on reducing oil–water CA in the Bakken.

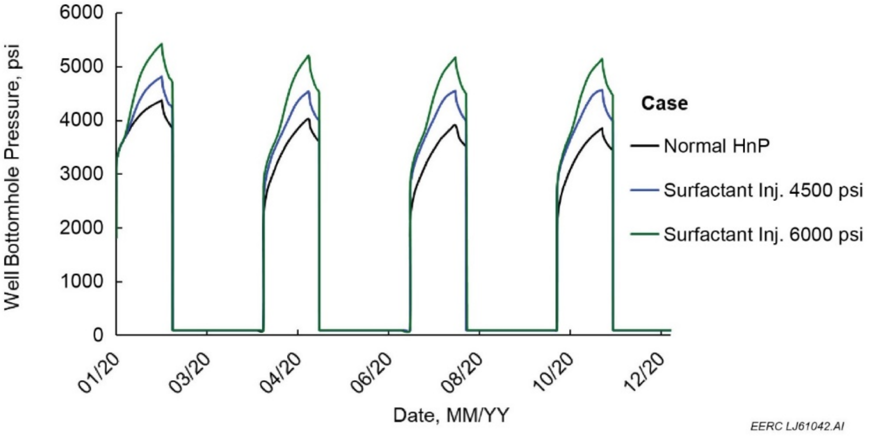

Figure 89. Comparison of BHP behavior in the HnP well (MB2) when the gas injection rate is 3 MMscfd with and without conformance control by surfactant injection in the adjacent offset wells.

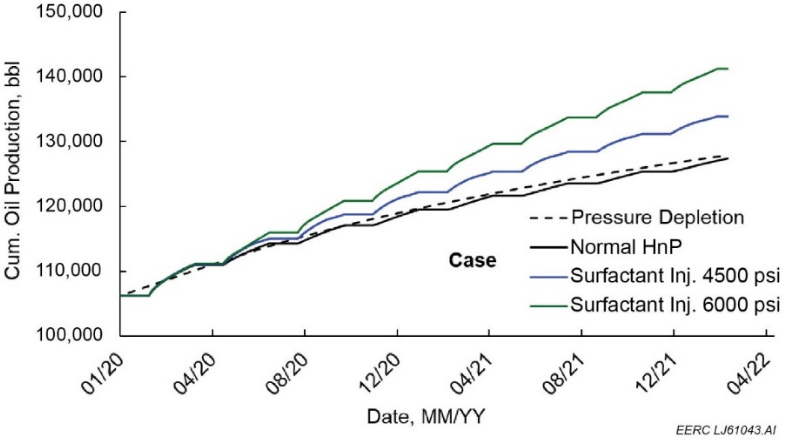

Figure 90. Comparison of oil production performance between pressure depletion and gas EOR (at a 3-MMscfd injection rate) with and without conformance control by surfactant injection in the adjacent offset wells.

EOR Performance in Multiple DSUs with Conformance Control in the Williams Site

The single DSU case in the Dunn site showed that the EOR performance in the HnP well can be improved by either increasing the gas injection rate or confining the injected gas within a certain volume around the gas injector by conformance control. BHP is one of the key factors that impact the EOR results. No matter which method is applied to improve EOR performance, the BHP must be lifted for gas to penetrate the tight matrix deeper so that the gas can contact more oil and extract it out of the tiny pores. It should be noted that the reservoir in the Dunn site has not been depleted completely since the child wells were put on production in or after 2018, as shown in Table 13. Parent wells are located in the middle of the site, as shown in Figure 58, so that the injected gas is relatively easy to control as the reservoir pressure is higher on the two sides of the

DSU. However, the production situation in the Williams site is more complex, as indicated in Table 14. Figure 61 shows that parent and child wells were distributed alternately across the DSUs in the site. Previous EOR tests in this site showed that single-well HnP operations with low rich gas injection rates (0.2–2.2 MMscfd) were difficult to improve oil production significantly because the reservoir was depleted to very low pressure. A considerable volume of gas is needed to fill up the depleted reservoir volume before the BHP can be lifted to a level for an effective EOR. Also, the pressure response to gas injection varied from well to well during the pilot test (Pospisil and others, 2020).

Simulation tests and IFT analysis showed that although water injection can be used to confine the injected gas within the desired reservoir volume, the injected water will also block oil flow around the water injector. Therefore, the EOR and conformance control strategies need to be carefully designed for utilizing the wells reasonably to improve the oil production performance.

Since the wells were completed in different years and have been producing for 5–8 years, the HnP performance for each well was different. Two wells with their adjacent offset wells were selected to demonstrate the different EOR responses to gas and water injection operations. Well 5MBH was completed in the middle of the site with 50 fracture stages in 2014, and Well 12MBH was completed close to the east boundary of the site with 35 fracture stages in 2015. Five operational scenarios were tested: pressure depletion; normal rich gas HnP EOR; and rich gas HnP EOR with conformance control by water injection at 2000, 4000, and 6000 psi in the offset wells. Gas was injected at 10 MMscfd for 60 days in the injection cycle, and then the well was switched to a production cycle for 30 days. Figure 91 shows the comparison of oil responses to different operational conditions in the two wells. Figure 91a shows that normal HnP EOR without conformance control could not improve the oil production performance in Well 5MBH as the injected gas migrated to offset wells quickly. However, the EOR results became better when conformance control was applied to confine the gas around the well. The oil production performance of EOR became better than that of pressure depletion when the water injection pressure reached 4000 psi in the offset wells. Oil production behavior was different in Well 12MBH, as shown in Figure 91b. Normal HnP EOR yielded better oil production than the pressure depletion operation. The EOR results became even better when higher-pressure water injection was used for conformance control. One reason is that Well 12MBH is close to the boundary, so pressure was easier to build up around the well.

Although high-pressure water injection in the offset wells can improve EOR performance in the HnP well, it can also reduce the oil production in the wells that were used for water injection, as shown in Figure 92. The figure shows that the more water was injected through a well, the less oil could be produced in this well. This response fits the oil–water multiple-phase flow theory very well; i.e., water blocks the oil flow path in the tight matrix because of the high capillary pressure caused by the large oil–water IFT and tiny pore throat size. Therefore, the EOR strategies in a site with multiple DSUs need to be carefully designed in order to balance the production gain and loss between different wells. A series of simulations were performed to improve the overall EOR performance in the Williams site. Different combinations of operational parameters, including injection rate, injection time, soaking time, production time, water injection wells, water injection pressure, injector and producer numbers, etc., were tested to observe the EOR response in multiple DSUs.

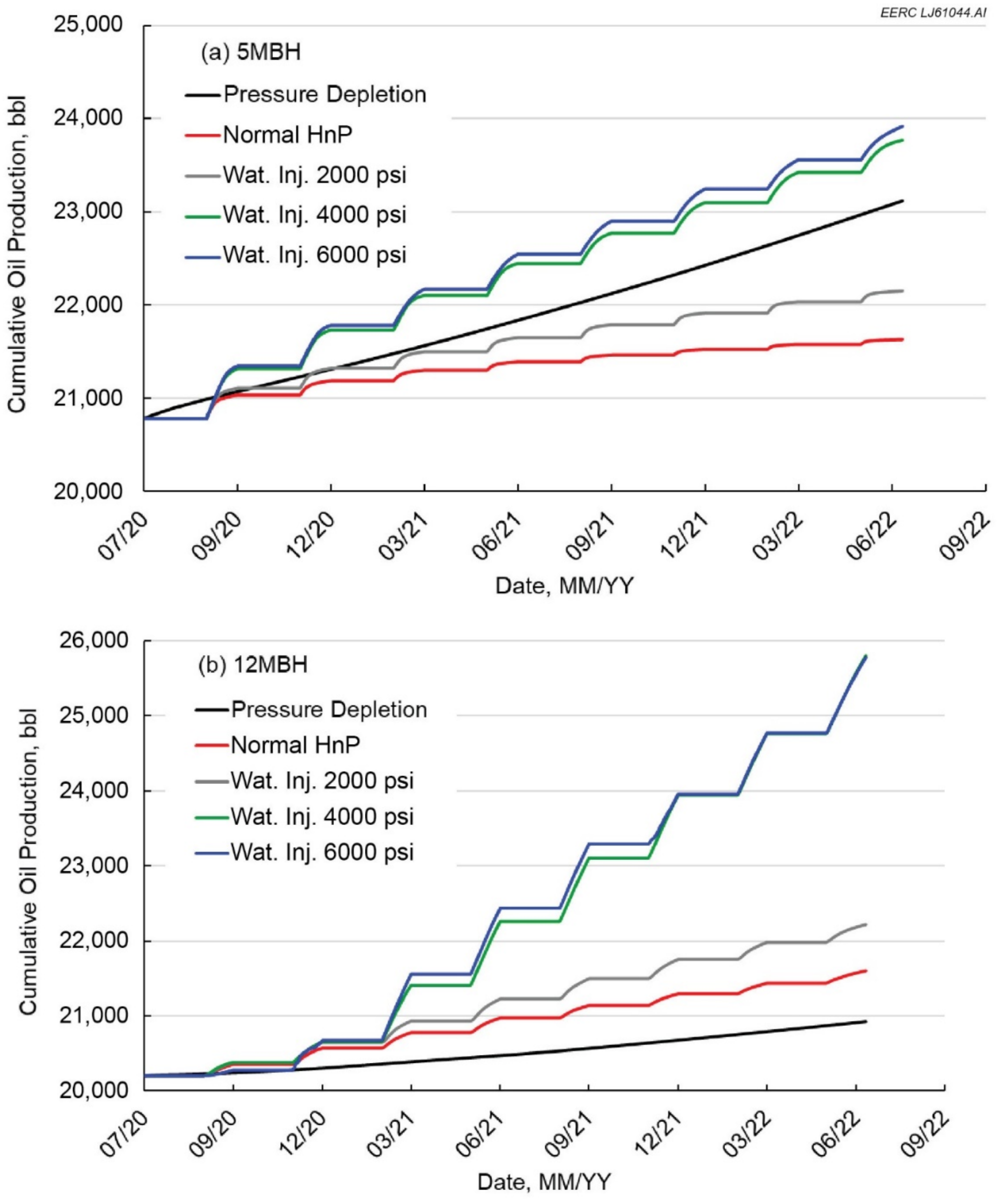

Figure 91. Comparison of oil production performance in gas EOR wells a) 5MBH and b) 12MBH. The wells were operated by pressure depletion and gas EOR (at 10-MMscfd gas injection rate) with and without conformance control by water injection in the adjacent offset wells.

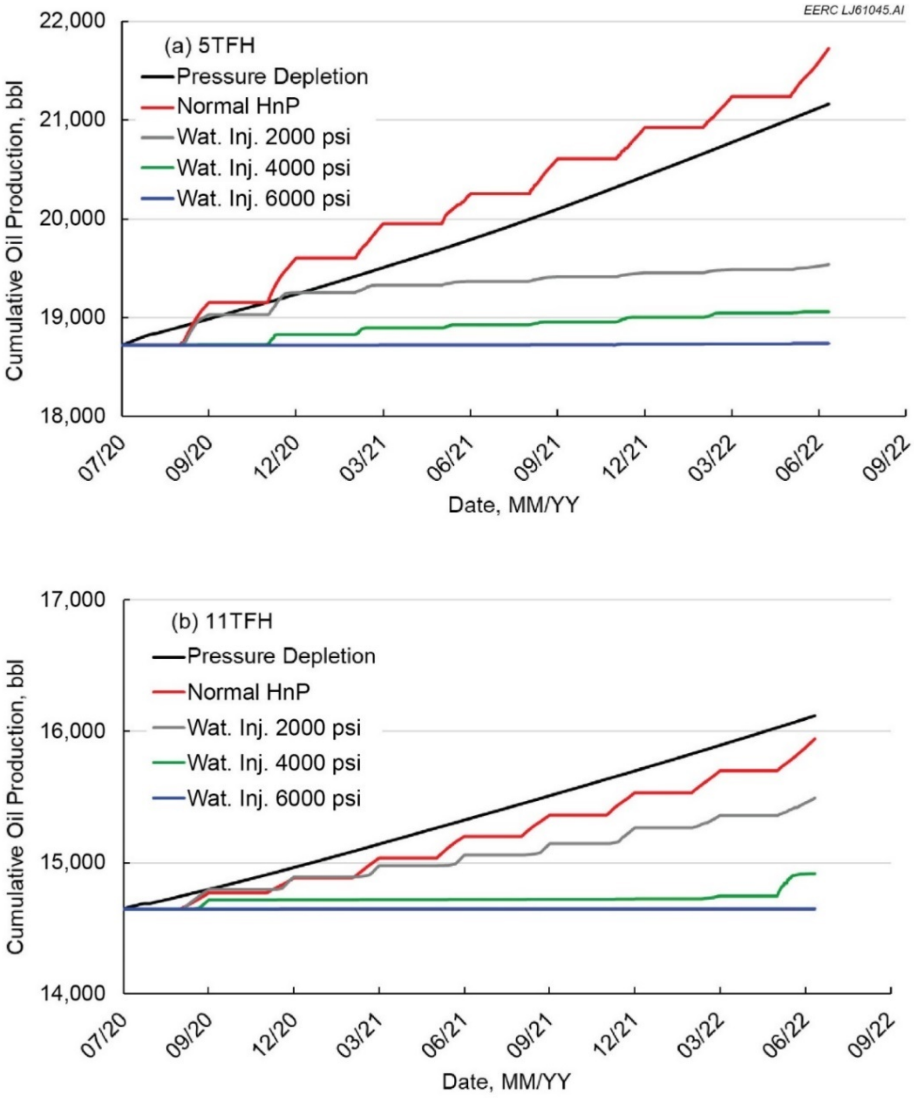

Figure 92. Comparison of oil production performance in conformance control wells a) 5TFH and b) 11TFH. The wells were used to inject water in the cases with conformance control operations. They were regular producers with pressure depletion only when no conformance control was used.

After testing numerous operational combinations were tested, the design in Figure 93 was adopted to upscale the alternative EOR strategies with conformance control from a single DSU to multiple DSUs. The corresponding designing parameters are shown in Table 20. Four types of wells were set up in the design: HnP wells for gas injection and oil production, water injection wells for conformance control, producers with high oil production rates which were kept open all the time, and producers next to the HnP wells that were only open during the production cycle of the HnP wells. Figure 94 illustrates the comparison of oil production performance with different operational strategies. Results showed that the best EOR effect was not yielded by the case with the most gas injection volume; i.e., every well was used for gas HnP EOR. A reasonable arrangement of production strategy could yield 7.44% of incremental oil production in 2 years of operation. Further optimization of the EOR strategies could yield more incremental oil production.

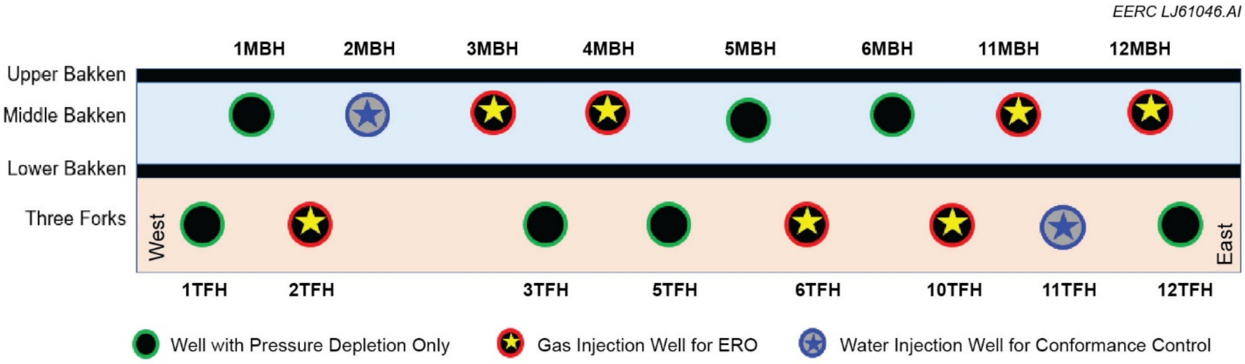

Figure 93. Schematic of producer and injector distribution for rich gas EOR with conformance control in multiple DSUs at the Williams site.

Table 20. Parameters for Rich Gas EOR with Conformance Control in the Williams Site

Parameter	Value
Gas HnP Wells	2TFH, 3MBH, 4MBH, 6TFH, 10TFH, 11MBH, 12MBH
Water Injection Wells	2MBH, 11TFH
Wells with Pressure Depletion Only	1TFH, 1MBH, 3TFH, 5TFH, 5MBH, 6MBH, 12TFH
Gas Injection Rate	10 MMscfd for each well
Injection Time	30 days/cycle
Soaking Time	0 days/cycle
Production Time	60 days/cycle
Injection Gas Composition (C1:C2:C3)	7:2:1
Maximum Gas Injection Pressure Constraint	7500 psi
Maximum Water Injection Pressure	4000 psi
Minimum Production Pressure	300 psi
EOR Operational Time	2 years

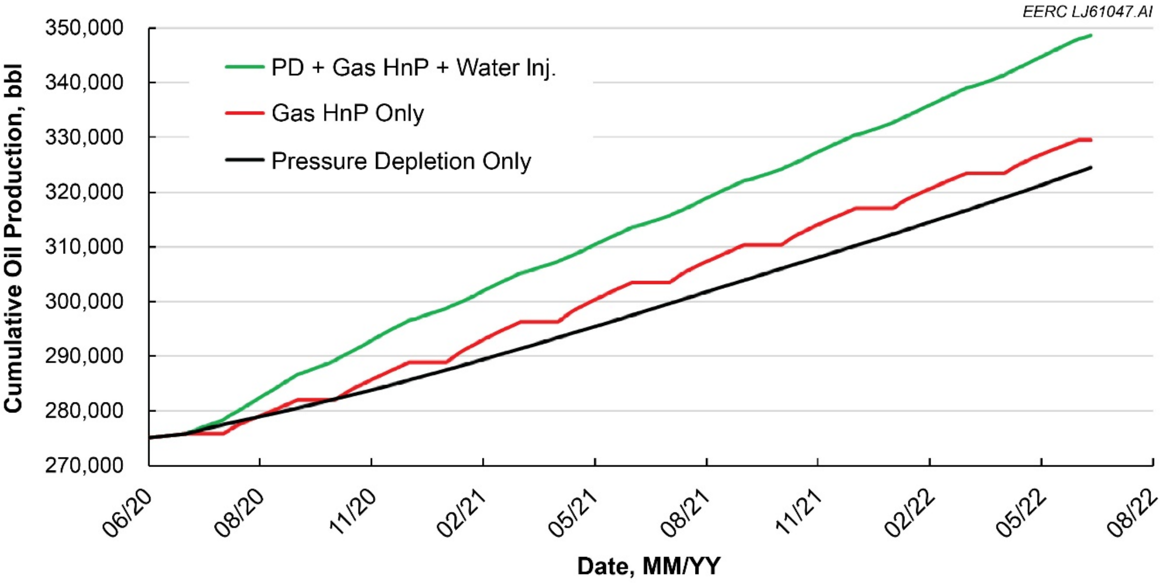

Figure 94. Comparison of oil production performance with different operational strategies in the Williams site with multiple DSUs.

Conclusions

A systematic simulation study was conducted in this activity to investigate the gas EOR strategies in the Bakken Formation. The conformance issue caused by well interference was thoroughly studied based on field observations. Two sites with clear well interference effects were selected for detailed analyses of crossflow between wells in different areas. A highly efficient fracture modeling method, EDFM, was employed to develop two multiple-well, multiple-fracture models. These models captured the well interference and conformance issues in the Bakken effectively and thus made it possible to investigate the complex flow behavior between wells in the EOR processes. Alternative EOR and conformance control strategies were developed to improve the oil production performance in both single-well and multiple DSUs. Results showed the following:

- A large volume of gas needs to be injected into the reservoir in order to lift the BHP and yield meaningful EOR response.

- The EOR response in each well could be different even though the wells are located in the same DSU. Many factors, including completion time and formation, number of fractures, offset wells, and production history, etc., could impact the EOR results.

- Water injection can be used for conformance control in the Bakken because of its relatively low mobility compared to gas.

- Water injection could also block oil flow around the wells used for conformance control because of the high IFT between oil and water as well as the tiny pore throat size in the tight matrix.

- Not all of the wells are suitable for EOR operations in the Bakken, so gas and water injectors need to be carefully selected for EOR design. EOR performance can be improved considerably by optimizing the EOR strategies.

- Surfactant is more effective than water for improving gas EOR performance when used as a conformance control agent.

ACTIVITY 8.0 – MACHINE LEARNING AND BIG DATA ANALYTICS FOR UNCONVENTIONAL EOR STRATEGIES

Two of the objectives of Subtask 3.1 are to optimize future commercial-scale tight oil EOR design and operations and to establish the effectiveness of monitoring techniques for reservoir surveillance and injection conformance modeling. Activity 8.0, comprising two subactivities, applied ML and BDA methods to facilitate progress for both of the following objectives. The following provides a summary of the activities.

Subactivity 8.1 – Virtual Learning

Introduction

An evaluation of modeling and simulation results from rich gas injection tests in the Bakken and Eagle Ford suggested that adding a water injection component to the EOR reservoir management strategy may be an effective method for reducing breakthrough time. Furthermore, the results of laboratory studies suggested that beginning EOR operations earlier in the lifetime of a DSU, when reservoir pressures are not significantly below MMP, may improve the economics of EOR and lead to higher ultimate recovery values. Other factors, such as the number of wells within the DSU, injection time (sometimes called the “huff period” or the days of gas injection), soak time (the days between the huff period and the “puff period”), production time (sometimes called the puff period or the days of gas production after the soaking time), and cycle time (sum of the injection time, soak time, and production time), likely all contribute to the overall performance of a DSU in response to rich gas injection. Subactivity 8.1 used virtual learning methods to investigate model simulations of alternative rich gas injection scenarios to quantify the effect of the aforementioned factors that potentially contribute to DSU incremental production of oil, gas, and water (hereafter “oil, gas, or water production”). The technical approach for Subactivity 8.1 comprises the generation of reservoir simulations followed by the application of applied statistical and ML methods to the reservoir simulation outputs to quantify the effects of different factors on oil, gas, and water production and to identify optimal configurations of the different inputs. A summary of findings are provided below.

Geologic Model and Reservoir Simulation

The geologic model (geomodel) and reservoir simulations examined as part of Subactivity 8.1 were previously described under Activity 7. The geomodel addressed a reference DSU comprising seven wells, with three wells completed in the MB Formation (MB1, MB2, and MB3) and four wells completed in the TF Formation (TF1, TF2, TF3, and TF4) (Figure 95). Two alternative DSU configurations that were geomodeled are also shown in Figure 95 and include both five- and six-well configurations. The reservoir simulations used different combinations of wells and operating parameters to generate sets of outputs for the data analysis. Subactivity 8.1 included two sets of reservoir simulation cases for the reference seven-well DSU: Set 1 and Set 2. These sets were used to evaluate different components of DSU development and operation, as described below.

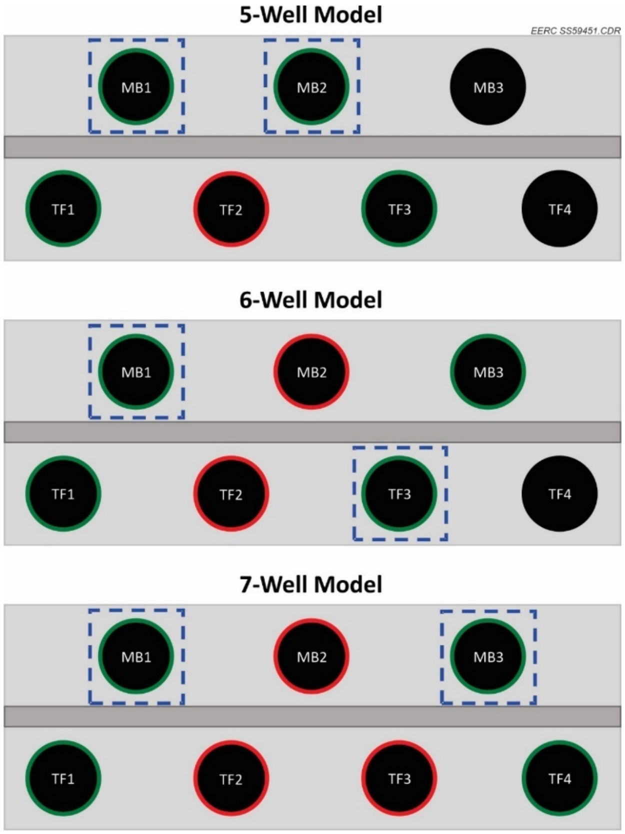

Figure 95. Illustration of the DSU models identifying the MB and TF wellbores included in each model and the wells that were used for rich gas injection (red outline) or production (green outline). The blue dashed boxes indicate wells used for water injection during gas and water injection scenarios, as described in the text.

Simulation Case Matrices – Set 1 Simulations: DSU Development

The Set 1 simulations evaluated the effect of three potential DSU development factors based on oil, gas, and water production: 1) well count, 2) EOR development schedule, and 3) injectate. Using the well configurations shown in Figure 95, three levels of EOR development timeline were considered: early (BHP 500 psi below the MMP), middle (oil rate less than 100 stock tank barrels per day [stbd], and late (oil rate less than 50 stbd). Lastly, the injectate factor had two levels: gas-only injection or gas and water injection. This yielded a test matrix comprising 18 individual cases, as described in Table 21.

In recognition of the fact that it is impracticable to simulate all possible combinations of wells, gas injectors, water injectors, and operating conditions for a seven-well DSU, the 18 individual cases in the Set 1 case matrix were defined to balance the number of simulations against computational limitations and produce a data set that could provide insights into the relative effects of well count; EOR development strategy; and EOR injectate on oil, gas, and water production as well as inform subsequent simulations for simulation case matrix Set 2.

Table 21. Set 1 Reservoir Simulation Case Matrix Referencing the Well Counts Shown in Figure 94

Case ID	DSU Well Count	EOR Timeline	Injectate
1	5	Early	Gas
2	6	Early	Gas
3	7	Early	Gas
4	5	Early	Gas + water
5	6	Early	Gas + water
6	7	Early	Gas + water
7	5	Middle	Gas
8	6	Middle	Gas
9	7	Middle	Gas
10	5	Middle	Gas + water
11	6	Middle	Gas + water
12	7	Middle	Gas + water
13	5	Late	Gas
14	6	Late	Gas
15	7	Late	Gas
16	5	Late	Gas + water
17	6	Late	Gas + water
18	7	Late	Gas + water

Simulation Case Matrices – Set 2 Simulations – DSU Operation

The Set 2 simulations evaluated the reference seven-well DSU, the early EOR development timeline (BHP 500 psi below the MMP), and gas-only injection (i.e., no water injection wells) with a focus on the effect of four potential operational factors on oil, gas, and water production: 1) injection rate, 2) injection time, 3) soak time, and 4) production time. The sum of injection time, soak time, and production time yields the cycle time. A total of 267 cases were evaluated. As was the case with the Set 1 simulations, the Set 2 case matrix was selected to balance the number of simulations against computational limitations and produce a data set that effectively sampled the operational parameter space (i.e., the range of combinations of the operational factors) and provided inputs to ML-based approaches for evaluating the results. Table 22 provides descriptive statistics for the 267 simulations.

Table 22. Descriptive Statistics for Set 2 Reservoir Simulation Case Matrix. All 267 cases used the full seven-well DSU, the early EOR development timeline, and gas-only injection (min = minimum, P25 = 25th percentile, std. dev. = standard deviation, P75 = 75th percentile, and max = maximum).

Variable	Min	P25	Median	Mean	Std. Dev.	P75	Max
Gas Injection Rate (MMscfd)	3	9	11	12.9	6.4	16	35
Injection Time (days)	10	26	33	37.0	15.2	48	90
Soak Time (days)	0	6	12	11.3	5.9	16	21
Production Time (days)	21	42	60	60.2	19.6	78	96
Cycle Time (days)	45	87	110	108.4	26.8	127	207
DSU Incremental Oil (Mbbl)	211	226	229	229.8	6.3	233	245
DSU Incremental Gas (Bcf)	1.0	1.3	1.4	1.5	0.3	1.6	2.4
DSU Incremental Water (Mbbl)	372	448	473	471.3	33.4	495	546

Target Variables

The target variables (response variables) were DSU incremental oil, water, and gas production at the end of the 2-year EOR period (i.e., the sum of oil, water, and gas production across all wells over the 2-year EOR period). The oil, water, and gas production were natural log-transformed for all data analysis methods to make the target variables closer to a normal distribution.[1]

The configuration of DSU development that resulted in the greatest oil production was associated with commensurately greater water and gas production, which are potentially negative outcomes that affect the overall DSU performance. Therefore, the oil and water production were translated into net revenue to provide a multiobjective target variable that rewarded oil production and penalized water production. For this assessment, gas production was not included in the net revenue calculations, since gas production can be a source of revenue only if the infrastructure exists to gather and sell the produced gas and/or the produced gas represents a source of recycled injectate for the rich gas EOR; alternatively, it could result in a financial loss if the produced gas must be vented/flared or forces the shut-in of one or more production wells. Therefore, as a simplifying assumption, gas production was omitted from the current analysis. However, supplemental calculations were done to assess the volumes of recycled gas (produced gas) for each case.

The net revenue calculations evaluated conditions that weighted the relative value of oil and water production differently. For the regression modeling, the first case assumed \$60/stb oil price and \$3/bbl water disposal cost (\$60oil_\$3wtr), and the second case assumed \$50/stb oil price and

---

[1] The nonlinearity of the relationship between oil, water, and gas production as a function of the DSU development or operational variables was obvious from exploratory plots and indicated that some type of transformation should be applied to attempt to linearize the relation and minimize heteroscedasticity before continuing. A good transformation would be one in which we exponentiate oil, water, and gas production with an exponent less than 1. The most common transformation for data with this nonlinear pattern is the logarithm transformation. In this work, the natural log of oil, water, and gas production was used to linearize the relation (Helsel and others, 2020).

$4/bbl water disposal cost. Therefore, while the first scenario weighted the cost of water disposal at 5% of the revenue from oil production (3 ÷ 60 = 5%), the second scenario weighted the cost of water disposal at 8% of the revenue from oil production (4 ÷ 50 = 8%). The disposal cost for produced water was adapted from Glazewski and others (2020), which estimated that produced water transport and disposal costs were generally $2/bbl to $4/bbl of produced water. Additional values were also used to evaluate the sensitivity of the net revenue variable to oil price and water disposal cost. The net revenue calculations were done using the nominal value (i.e., the current monetary value) and did not adjust for the effects of inflation since the EOR period of the study was only 2 years.

Therefore, the primary target variables for the data analysis methods were 1) oil, gas, and water production; 2) Net Revenue One ($60oil_$3wtr); and 3) Net Revenue Two ($50oil_$4wtr).

Data Analysis

The data analysis for the case matrices used two complementary approaches:

1. Linear regression to draw inferences about the effects of each DSU development or operational factor on DSU performance (oil, gas, and water production).

2. ML-based approaches to create predictive models and explore DSU performance with the goal of identifying optimal parameter configurations (i.e., optimal values of injection rate, injection time, soak time, and production time).

Linear Regression for Statistical Inference

Linear regression was used for statistical inference about the effects of each parameter on DSU performance. While the linear models provide a practical starting point for analyzing the simulation cases, several of the predictor–response relationships in Set 2 did not conform to the underlying assumptions of linear regression; therefore, alternative methods were used to assess Set 2 (see "Machine Learning Methods for Predictive Modeling").[2]

For Set 1, each of the features was treated as a factor variable (categorical variable) in the regression. Therefore, no transformations of the features were necessary for Set 1. For example, well count, EOR development timeline, and injectate remained as presented Table 21. The base case regression model was established as a five-well DSU with an early EOR development timeline and gas-only injection, and the Set 1 regression models quantified the change in performance from baseline as a function changing the factors, e.g., going from five to six to seven wells.

For Set 2, the features were numeric and, therefore, scaled by subtracting the mean and dividing by two standard deviations (z-score approach). Dividing by two standard deviations means that a one-unit change in the scaled predictor corresponds to a change from one standard

---

[2] Underlying assumptions of linear regression: a) model form is correct: y is linearly related to x; b) variance of the residuals is constant (homoscedastic) and does not depend on x or on anything else, such as time; c) the residuals are independent of x; and d) the residuals are normally distributed (Helsel and others, 2020).

deviation below the mean to one standard deviation above the mean (Gelman and Hill, 2007). For example, the scaled input for "injection time" was calculated as:

$$\text{z.inj.time} = \frac{[\text{inj.time} - \text{mean(inj.time)}]}{[2 \times \text{stdev(inj.time)}]} \qquad \text{[Eq. 7]}$$

Where:

z.inj.time = the standardized value of injection time
mean(inj.time) = the average of injection time
stdev(inj.time) = the standard deviation of injection time

In addition to placing the features onto the same scale with mean zero and ±2 standard deviations, scaling the input variables makes the base case model output easier to interpret, as the base case represents estimated DSU performance when all inputs are at their mean value.[3] Diagnostic plots were used to assess the fitted regression models. The diagnostic plots included assessments of the normality of the regression residuals and crossplots of the residuals versus their fitted values and the order of the data. The diagnostic plots were used to evaluate whether potential trends in the residuals would confound inferences drawn from the fitted regression models.

Machine Learning Methods for Predictive Modeling

ML-based methods were used to evaluate Set 2 and extend the statistical inference developed from the linear regression modeling. The technical approach for the ML-based approaches included four steps: 1) train and test ML-based predictive models using the 267 cases from Set 2; 2) create a new full operational matrix covering all possible combinations of the input variables based on the range (minimum to maximum values) of the four input parameters across the 267 cases: injection rate, injection time, soak time, and production time; 3) apply the developed predictive models from No. 1 to the full operational matrix from No. 2 to predict DSU performance over all possible combinations of input variables; and 4) visualize and analyze the results of the predictive model outputs from No. 3 to identify optimal configurations of the input parameters.

The workflow for fitting ML models included two preprocessing steps: 1) the features were standardized using the z-score approach (Equation 7) and 2) the 267 cases were randomly split into training and testing data sets by 0.8:0.2 (i.e., 80% of the cases were used to train the models, and 20% of the cases were used to test the models). The training data set was used to develop the ML model, and the model performance was evaluated using the test data set. Model performance can largely depend on how the data are split between training and test sets, such that different data splits may lead to models with different test set performances. To overcome the issue of improper/imbalanced data set splitting, a *k*-fold cross validation approach was used. Cross validation is a resampling procedure used to evaluate a model by omitting a portion of the training data set used to train the model and later using this sample for testing/validating. The term "*k*-fold"

---

[3] Linear regression was implemented in Minitab 19 Statistical Software (2020). The regression models started with a "full model" of all features and their interactions. Model selection was done using forward- and backward-selection to minimize the Bayesian information criterion (BIC) (sometimes referred to as the "Schwarz information criterion"). The BIC scores the models on how well they fit the data (goodness-of-fit) but also penalizes the score for the number of parameters used in the model. The combination of goodness-of-fit and parameter penalty means that BIC helps identify the most parsimonious model, i.e., the simplest model that provides a good fit to the data (Akaike, 1973; Schwarz, 1978; McElreath, 2016).

cross validation refers to splitting the data set into a *k* number of sections/folds, where each fold is used as a testing set at some point. The *k* is predefined, and by convention, $k = 5$ is used in this project for model development (Zhang, 2012).

Four models were used for the ML-based predictive modeling including 1) linear regression, 2) support vector machine regression (SVM), 3) random forest (RF), and 4) extreme gradient boosting (XGBoost). Additional details for each model are provided in Appendix A.

Full Operational Matrix

A full operational matrix was created covering all combinations of operation conditions from the Set 2 simulations. The levels (number of discrete values) for the four operational parameters are injection rate (32 levels), injection time (80 levels), soak time (21 levels), and production time (75 levels). Therefore, the resulting size of the full operational matrix is 4,032,000 ($32 \times 80 \times 21 \times 75$). Developing and executing over 4 million unique reservoir simulations would be computationally infeasible, which highlights the benefit of using a set of simulations to train ML-based predictive models and then utilizing the ML-based predictive models for subsequent evaluations. The full operational matrix was used to generate predictions across all 4,032,000 combinations, which were then used to create contour plots to provide insights about optimal parameter configurations for maximizing DSU performance.

Global Sensitivity Analysis

Sensitivity analysis was performed to estimate the uncertainty of the modeling output because of the uncertainty of the inputs (Salciccioli and others, 2016). The Sobol method is a powerful variance-based sensitivity analysis that quantifies the input and output uncertainties as probability distributions and decomposes the output variance into parts attributable to input variables and combinations of variables. Therefore, the sensitivity of the output to an input parameter is measured by the amount of variance in the output caused by that input (Sobol, 1993; 2001). The Sobol sensitivity indices include the following:

1. First-order indices: measure the contribution to the output variance attributable to a single input parameter.
2. Second-order indices: measure the contribution to the output variance attributable to the interaction of two input parameters.
3. Total-effect indices: sum of indices from any order that measures the contribution of the output variance caused by a single input parameter.

The sum of the total-effect indices equals to 1, and the sum of any order of sensitivity indices equals to 1. Therefore, the first-order, second-order, and total-effect indices show the fractional contribution of each input parameter (or interaction term) to the total variance in the target variable. Detailed descriptions and mathematical background of the Sobol method can be found in Sobol (1993, 2001) and Pappenberger and others (2008). The Python package SALIb was used to perform the Sobol method sensitivity analysis (Herman and Usher, 2017). The procedures to perform the Sobol method sensitivity analysis using the SALIb package were:

1) Define the model inputs and create sampling bounds (ranges) of the four operational parameters.

2) Generate parameter sets using the Sobol sequence based on the sampling bounds. In this study, 1000 parameter sets were generated from the Sobol sequence. The cross-sampling scheme creates 1000*(4 + 1) = 5000 total model runs.

3) Run the parameter sets through the ML predictive model (i.e., linear regression, SVM, RF, or XGBoost). In this study, the SVM models were used for the Sobol sensitivity analysis.

4) Calculate the Sobol sensitivity indices.

5) Visualize and interpret the sensitivity analysis results.

Results – Linear Regression

Set 1 Simulations

Diagnostic plots for the Set 1 regression models are provided in Appendix A. These diagnostic plots show that the Set 1 linear regression models are reasonable—the residuals follow a normal distribution, and there are no visible trends in the residuals; therefore, inferences drawn from these models are valid interpretations of the Set 1 simulation case matrix.

DSU Incremental Oil Production

Figure 96 summarizes the fitted regression model for oil production. The exponentiation of the constant term in the fitted regression model, exp(Coef), represents the expected value for the Set 1 base case: a five-well DSU with an early EOR development timeline and gas-only injection, which is exp(11.864) = 142,059 bbl.

The exponentiation of the additional factors (expressed as exp(Coef) – 1) in the regression summary represents the estimated percentage effect of going from the base case to the stated factor condition. For example, increasing from the base case five-well DSU to the six- or seven-well DSU configurations is expected to ***increase*** oil production by +24.2% or +59.2%, respectively. Similarly, delaying the start of the rich gas EOR from the base case early scenario to the middle or late scenario is expected to ***decrease*** oil production by −26.6% or −47.6%, respectively. Lastly, switching from the base case injectate of gas-only injection to gas and water injection would be expected to ***decrease*** oil production by −25.1%. The bars in the far-right column of Figure 96 provide a visual summary of the sign (blue is a positive effect, and red is a negative effect) and magnitude (the bar length is proportional to the effect size) of the factor in switching from the base case to the stated factor condition, i.e., the relative importance of each factor on oil production.

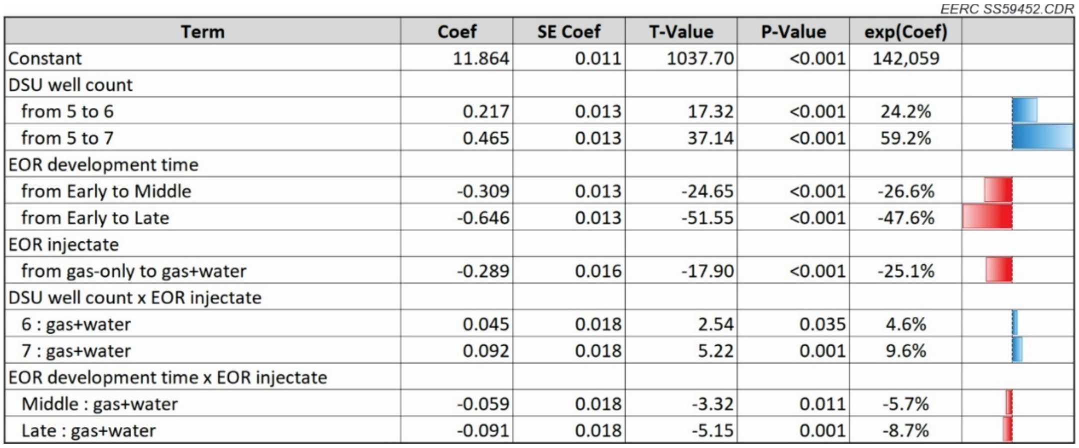

Term	Coef	SE Coef	T-Value	P-Value	exp(Coef)	
Constant	11.864	0.011	1037.70	<0.001	142,059	
DSU well count						
from 5 to 6	0.217	0.013	17.32	<0.001	24.2%	
from 5 to 7	0.465	0.013	37.14	<0.001	59.2%	
EOR development time						
from Early to Middle	-0.309	0.013	-24.65	<0.001	-26.6%	
from Early to Late	-0.646	0.013	-51.55	<0.001	-47.6%	
EOR injectate						
from gas-only to gas+water	-0.289	0.016	-17.90	<0.001	-25.1%	
DSU well count x EOR injectate						
6 : gas+water	0.045	0.018	2.54	0.035	4.6%	
7 : gas+water	0.092	0.018	5.22	0.001	9.6%	
EOR development time x EOR injectate						
Middle : gas+water	-0.059	0.018	-3.32	0.011	-5.7%	
Late : gas+water	-0.091	0.018	-5.15	0.001	-8.7%	

Figure 96. Summary of the fitted regression model output for Set 1 for the target variable: **DSU incremental oil production (bbl)**. Coef = coefficient, SE Coef = standard error of the coefficient, T-Value = the *t*-statistics of the coefficient, P-Value = the *p*-value of the student's *t*-distribution for the coefficient, and exp(Coef) = exponentiation of the Coef for the constant term and (exp(Coef) – 1) for the additional factors.

The interaction terms in Figure 96 (i.e., 6: gas+water, 7: gas+water, Middle: gas+water, and Late: gas+water) are better described using factorial plots. Figure 97 shows factorial plots for both the main effects (top) and the interactions (bottom) for the fitted regression model for oil production. Analogous to the bars in the regression coefficient summary, the factorial plots show large main effects on oil production associated with going from five to six to seven wells on the DSU (left panel), early to middle to late EOR development timeline (middle panel), and gas-only injection to gas and water injection (right panel). The interaction plots show how the relationship between one categorical factor and a continuous response depends on the value of the second categorical factor. For example, the lower left-hand panel in the interaction plots shows how both well count (five, six, or seven wells) and injectate (gas-only or gas and water) relate to oil production. For the five-well, gas-only injectate scenario, the average oil production is 103,300 bbl, which increases to 164,500 for the seven-well case. These outcomes are greater than the main effect plot, which starts at 87,200 bbl for the five-well case and increases to 145,400 bbl for the seven-well case. Conversely, the five-well, gas and water injectate scenario average oil production is 73,600 bbl and increases to 128,500 bbl for the seven-well case. Therefore, the interaction between the DSU well count and injectate creates a different expected value, and the interaction plots help elucidate these relationships. The fitted regression model did not include an interaction term for (DSU well count × EOR development timeline) because this term was not significant, and the BIC selection dropped the term from the final model, which is why the upper left-hand panel in the interaction plot is blank.

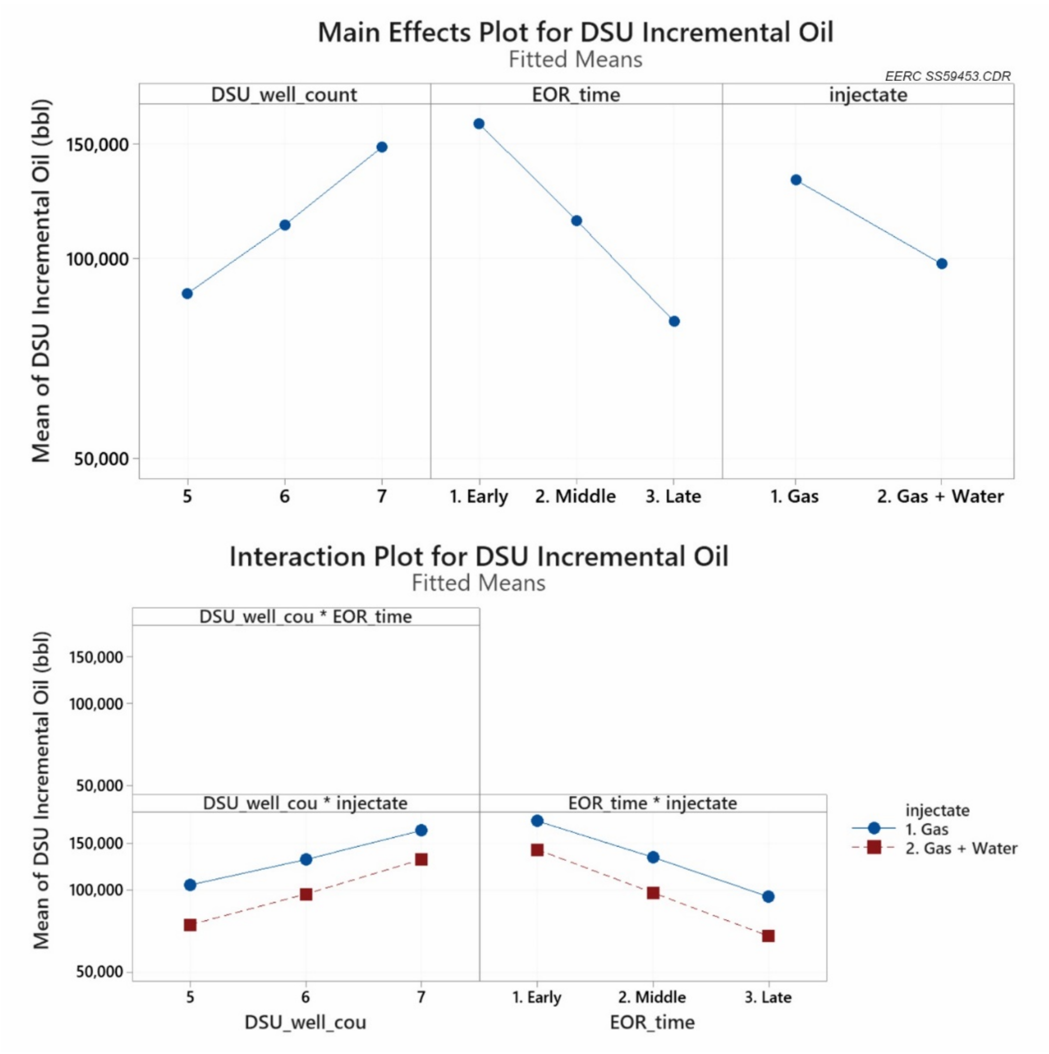

Figure 97. Factorial plots for main effects (top) and interactions (bottom) for DSU well count, EOR development timeline, and injectate from the fitted regression model for Set 1 for the target variable: **DSU incremental oil production (bbl)**.

DSU Incremental Water Production

Figure 98 summarizes the fitted regression model for water production. The expected DSU incremental water production for the Set 1 base case is 209,966 bbl. Increasing from the base case five-well DSU to the six- or seven-well DSU configurations is expected to ***increase*** water production by +15.3% and +47.2%, respectively. Similarly, delaying the start of the rich gas EOR from the base case early scenario to the middle or late scenario is expected to ***decrease*** water production by −24.4% and −48.7%, respectively. Lastly, as would be anticipated, switching from the base case injectate of gas-only injection to gas and water injection has an enormous effect on water production and would be expected to ***increase*** water production by +282.5%.

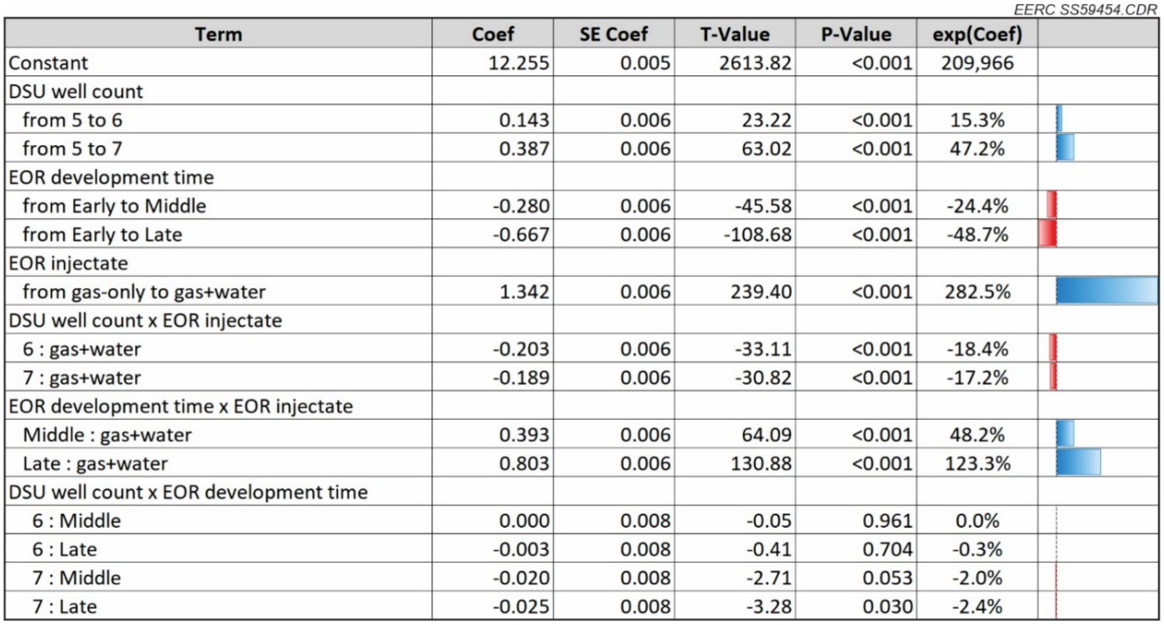
EERC SS59454.CDR

Term	Coef	SE Coef	T-Value	P-Value	exp(Coef)
Constant	12.255	0.005	2613.82	<0.001	209,966
DSU well count					
from 5 to 6	0.143	0.006	23.22	<0.001	15.3%
from 5 to 7	0.387	0.006	63.02	<0.001	47.2%
EOR development time					
from Early to Middle	-0.280	0.006	-45.58	<0.001	-24.4%
from Early to Late	-0.667	0.006	-108.68	<0.001	-48.7%
EOR injectate					
from gas-only to gas+water	1.342	0.006	239.40	<0.001	282.5%
DSU well count x EOR injectate					
6 : gas+water	-0.203	0.006	-33.11	<0.001	-18.4%
7 : gas+water	-0.189	0.006	-30.82	<0.001	-17.2%
EOR development time x EOR injectate					
Middle : gas+water	0.393	0.006	64.09	<0.001	48.2%
Late : gas+water	0.803	0.006	130.88	<0.001	123.3%
DSU well count x EOR development time					
6 : Middle	0.000	0.008	-0.05	0.961	0.0%
6 : Late	-0.003	0.008	-0.41	0.704	-0.3%
7 : Middle	-0.020	0.008	-2.71	0.053	-2.0%
7 : Late	-0.025	0.008	-3.28	0.030	-2.4%

Figure 98. Regression output summary for Set 1 for the target variable: **DSU incremental water production (bbl)**. Coef = coefficient, SE Coef = standard error of the coefficient, T-Value = the *t*-statistics of the coefficient, P-Value = the *p*-value of the student's *t*-distribution for the coefficient, and exp(Coef) = exponentiation of the Coef for the constant term and (exp(Coef) – 1) for the additional factors.

Figure 99 shows factorial plots for both the main effects (top) and the interactions (bottom) for the fitted regression model. The factorial plots show relatively small main effects on water production associated with going from five to six to seven wells on the DSU (left panel) and early to middle to late EOR development timeline (middle panel). However, going from gas-only injection to gas and water injection (right panel) results in a significant increase in water production, which is to be expected. The interaction plots also show that changing the injectate from gas-only to gas and water provides the largest effect on water production, as the other factors do not affect water production nearly as much.

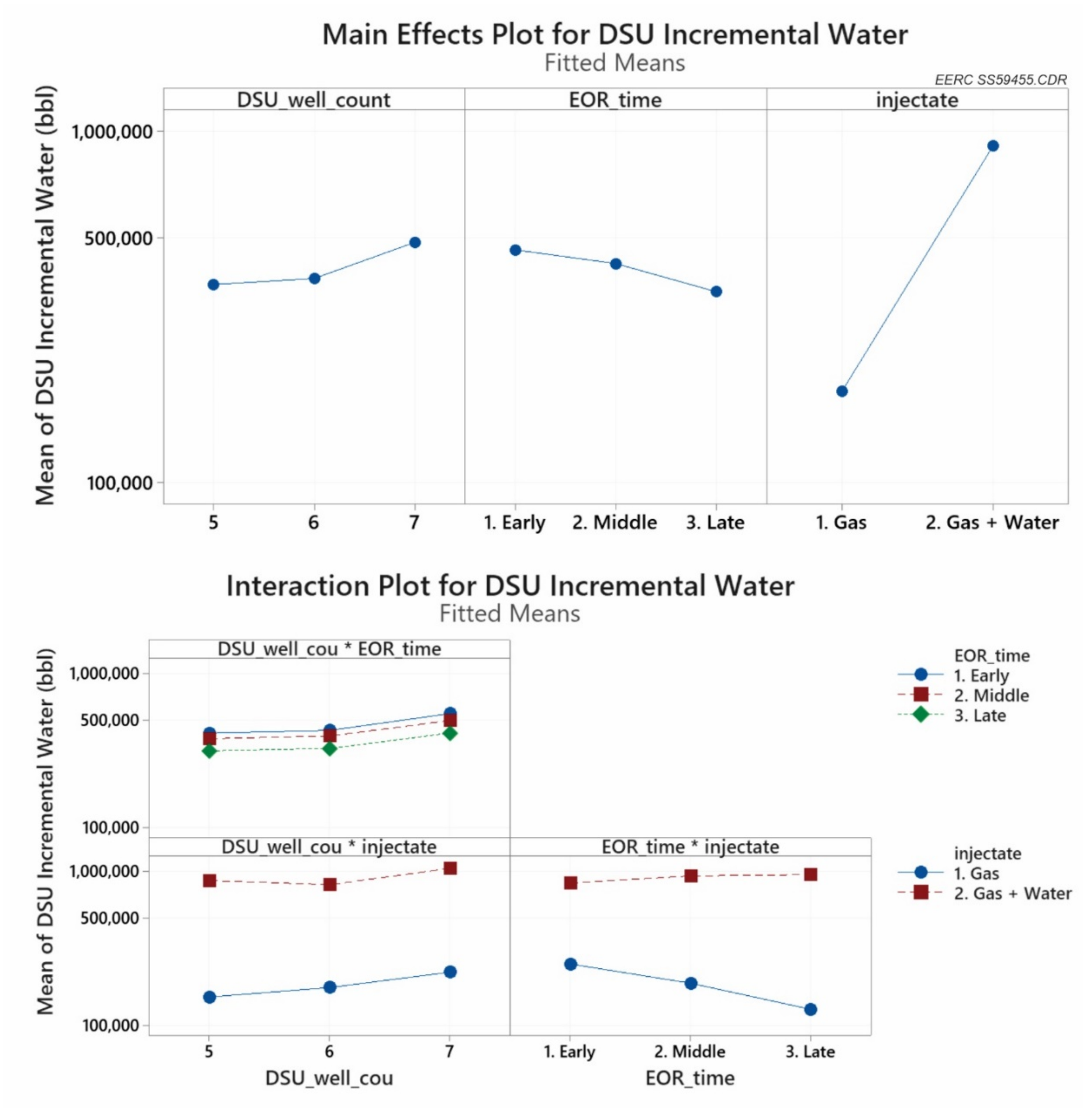

Figure 99. Factorial plots for main effects (top) and interactions (bottom) for DSU well count, EOR development timeline, and injectate from the fitted regression model for Set 1 for the target variable: **DSU incremental water production (bbl)**.

DSU Incremental Gas Production

Figure 100 summarizes the fitted regression models for gas production. The expected gas production for the Set 1 base case is 835 MMscf. Increasing from the base case five-well DSU to the six- or seven-well DSU configurations is expected to ***increase*** gas production by +81.2% and +165.3%, respectively. The other factors have a significantly smaller effect on gas production. For example, delaying the start of the rich gas EOR from the base case early scenario to the middle or late scenario is expected to ***decrease*** gas production by −2.8% and −7.5%, respectively. Lastly, switching from the base case injectate of gas-only injection to gas and water injection would be expected to ***decrease*** gas production by −8.7%.

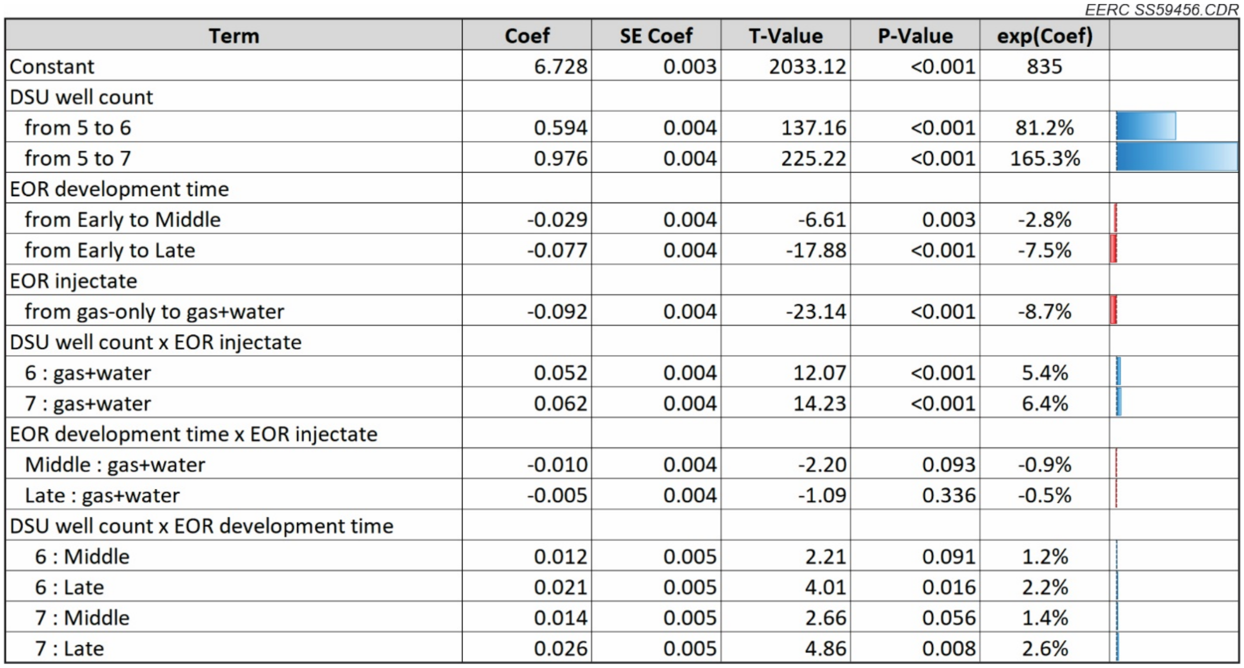

EERC SS59456.CDR

Term	Coef	SE Coef	T-Value	P-Value	exp(Coef)
Constant	6.728	0.003	2033.12	<0.001	835
DSU well count					
from 5 to 6	0.594	0.004	137.16	<0.001	81.2%
from 5 to 7	0.976	0.004	225.22	<0.001	165.3%
EOR development time					
from Early to Middle	-0.029	0.004	-6.61	0.003	-2.8%
from Early to Late	-0.077	0.004	-17.88	<0.001	-7.5%
EOR injectate					
from gas-only to gas+water	-0.092	0.004	-23.14	<0.001	-8.7%
DSU well count x EOR injectate					
6 : gas+water	0.052	0.004	12.07	<0.001	5.4%
7 : gas+water	0.062	0.004	14.23	<0.001	6.4%
EOR development time x EOR injectate					
Middle : gas+water	-0.010	0.004	-2.20	0.093	-0.9%
Late : gas+water	-0.005	0.004	-1.09	0.336	-0.5%
DSU well count x EOR development time					
6 : Middle	0.012	0.005	2.21	0.091	1.2%
6 : Late	0.021	0.005	4.01	0.016	2.2%
7 : Middle	0.014	0.005	2.66	0.056	1.4%
7 : Late	0.026	0.005	4.86	0.008	2.6%

Figure 100. Regression output summary for Set 1 for the target variable: **DSU incremental gas production (MMscf)**. Coef = coefficient, SE Coef = standard error of the coefficient, T-Value = the *t*-statistics of the coefficient, P-Value = the *p*-value of the student's *t*-distribution for the coefficient, and exp(Coef) = exponentiation of the Coef for the constant term and (exp(Coef) – 1) for the additional factors.

Figure 101 shows factorial plots for both the main effects (top) and the interactions (bottom) for the fitted regression model. The factorial plots show large main effects on gas production associated with going from five to six to seven wells on the DSU (left panel). However, going from early to middle to late EOR development timeline (middle panel) or from gas-only injection to gas and water injection (right panel) results in a small decrease in gas production.

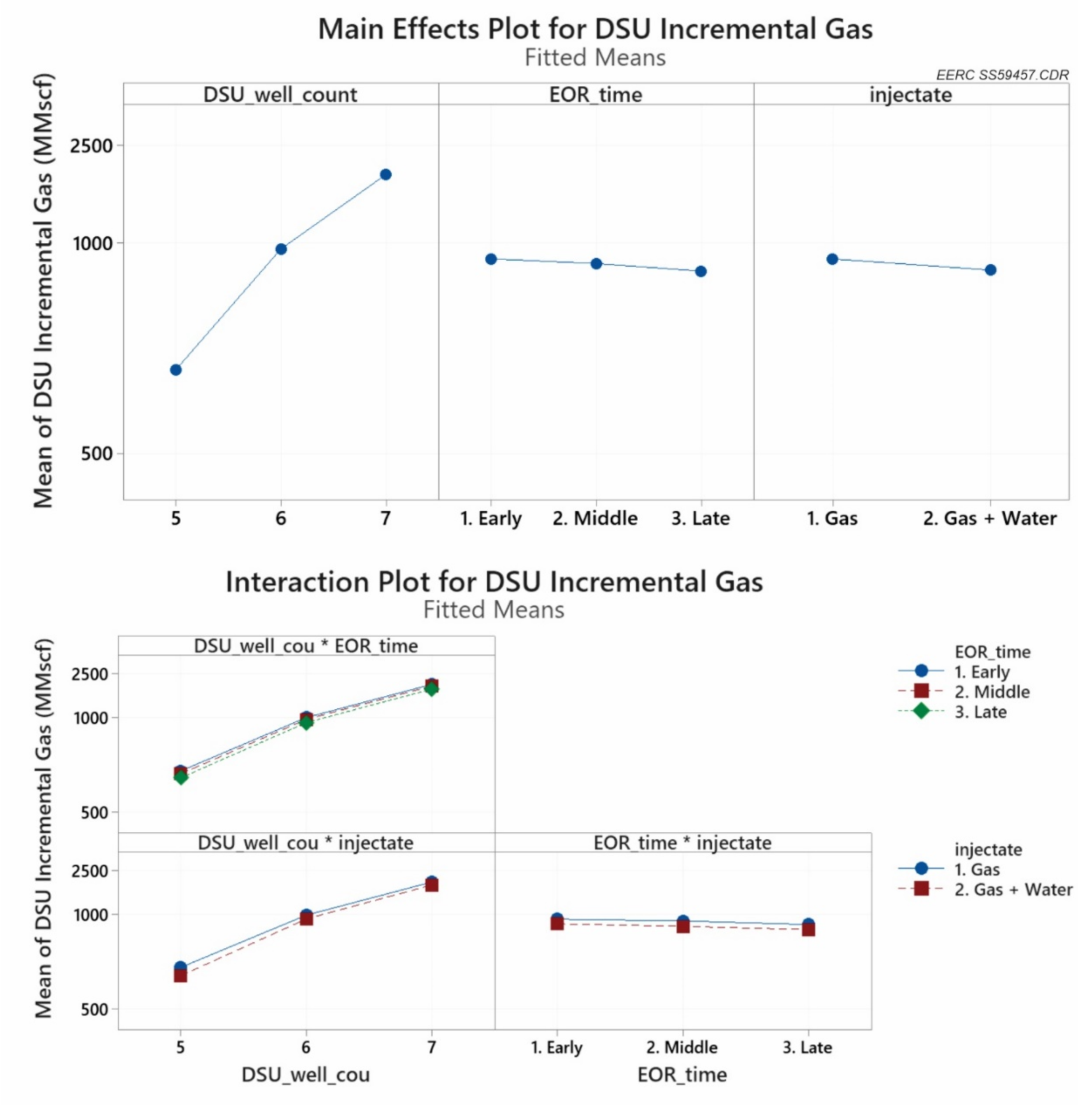

Figure 101. Factorial plots for main effects (top) and interactions (bottom) for DSU well count, EOR development timeline, and injectate from the fitted regression model for Set 1 for the target variable: **DSU incremental gas production (MMscf)**.

DSU Incremental Net Revenue

For the two net revenue scenarios, \$60/bbl oil price and \$3/bbl water disposal cost (\$60oil_\$3wtr) or \$50/bbl oil price and \$4/bbl water disposal cost (\$50oil_\$4wtr), the latter resulted in a negative outcome for two cases. The logarithm of a negative number is undefined; therefore, both net revenue scenarios were modeled using a normal distribution and were not natural log-transformed prior to fitting the regression models. Consequently, interpretation of the coefficients is slightly different from the preceding models that used a natural log-transformed oil, water, or gas production as the response variable.

Figure 102 shows the fitted regression models for the two net revenue scenarios. The patterns in the regression coefficients are similar; however, the net revenue estimates differ because of the higher penalty for the cost of produced water transport and disposal for \$50oil_\$4wtr as compared to \$60oil_\$3wtr. For example, the expected value for the base case is \$7.86 million (MM) dollars for the \$60oil_\$3wtr case and \$6.22MM for the \$50oil_\$4wtr case, illustrating the effect of the higher penalty for the cost of produced water transport and disposal (\$1.64MM in additional costs over 2 years).

The patterns for the different factors are like those for oil production, since the higher oil price relative to the cost of produced water transport and disposal means that oil production largely drives the net revenue result. Increasing from the base case five-well DSU to the six- or seven-well DSU configurations is expected to ***increase*** net revenue by +26.1% and +61.4%, respectively, for \$60oil_3wtr and only slightly less for \$50oil_\$4wtr: +21.2% and +49.5%, respectively. The EOR development time has a large effect on net revenue, as delaying the start of the rich gas EOR from the base case early scenario to the middle or late scenario is expected to ***decrease*** net revenue by −26.5% and −47.3%, respectively, for \$60oil_\$3wtr and by −21.0% and −37.3%, respectively, for \$50oil_\$4wtr. Lastly, the EOR injectate also has a large effect on net revenue, as switching from the base case injectate of gas-only injection to gas and water injection would be expected to ***decrease*** \$60oil_\$3wtr by −49.2% and \$50oil_4\$wtr by −52.1%.

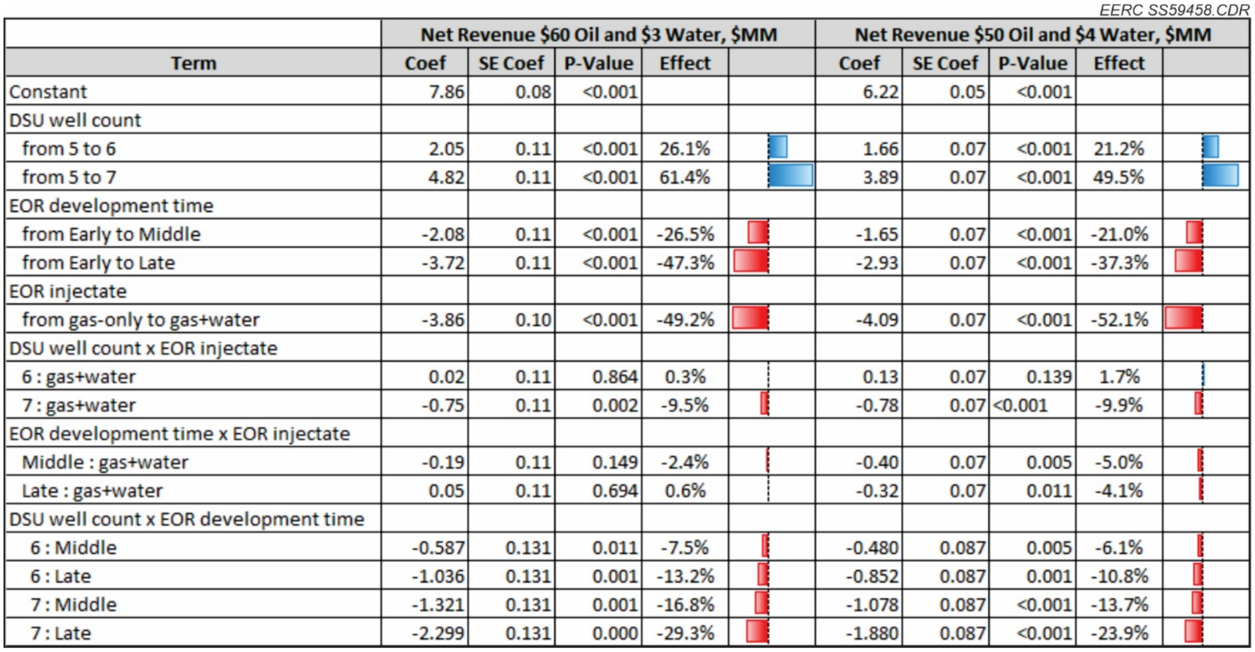
EERC SS59458.CDR

	Net Revenue \$60 Oil and \$3 Water, \$MM					Net Revenue \$50 Oil and \$4 Water, \$MM				
Term	Coef	SE Coef	P-Value	Effect		Coef	SE Coef	P-Value	Effect	
Constant	7.86	0.08	<0.001			6.22	0.05	<0.001		
DSU well count										
from 5 to 6	2.05	0.11	<0.001	26.1%		1.66	0.07	<0.001	21.2%	
from 5 to 7	4.82	0.11	<0.001	61.4%		3.89	0.07	<0.001	49.5%	
EOR development time										
from Early to Middle	-2.08	0.11	<0.001	-26.5%		-1.65	0.07	<0.001	-21.0%	
from Early to Late	-3.72	0.11	<0.001	-47.3%		-2.93	0.07	<0.001	-37.3%	
EOR injectate										
from gas-only to gas+water	-3.86	0.10	<0.001	-49.2%		-4.09	0.07	<0.001	-52.1%	
DSU well count x EOR injectate										
6 : gas+water	0.02	0.11	0.864	0.3%		0.13	0.07	0.139	1.7%	
7 : gas+water	-0.75	0.11	0.002	-9.5%		-0.78	0.07	<0.001	-9.9%	
EOR development time x EOR injectate										
Middle : gas+water	-0.19	0.11	0.149	-2.4%		-0.40	0.07	0.005	-5.0%	
Late : gas+water	0.05	0.11	0.694	0.6%		-0.32	0.07	0.011	-4.1%	
DSU well count x EOR development time										
6 : Middle	-0.587	0.131	0.011	-7.5%		-0.480	0.087	0.005	-6.1%	
6 : Late	-1.036	0.131	0.001	-13.2%		-0.852	0.087	0.001	-10.8%	
7 : Middle	-1.321	0.131	0.001	-16.8%		-1.078	0.087	<0.001	-13.7%	
7 : Late	-2.299	0.131	0.000	-29.3%		-1.880	0.087	<0.001	-23.9%	

Figure 102. Regression output summary for Set 1 for the target variable: **DSU Net Revenue at \$60oil_\$3wtr (\$MM, left) and DSU Net Revenue at \$50oil_\$4wtr (\$MM, right)**. Coef = coefficient, SE Coef = standard error of the coefficient, P-Value = the *p*-value of the student's *t*-distribution for the coefficient, and Effect = the percentage change from the base case.

Figure 103 shows factorial plots for both the main effects (top) and the interactions (bottom) for the fitted regression model. The main effects plots show the large effects of well count, EOR development time, and EOR injectate for both net revenue scenarios. The interaction plots show slightly different slopes for the different factors, highlighting the interactions among factors. For example, the early EOR development timeline accelerates revenues from oil production, leading to a steeper slope than the late EOR development timeline as the DSU well count increases from five to six to seven wells.

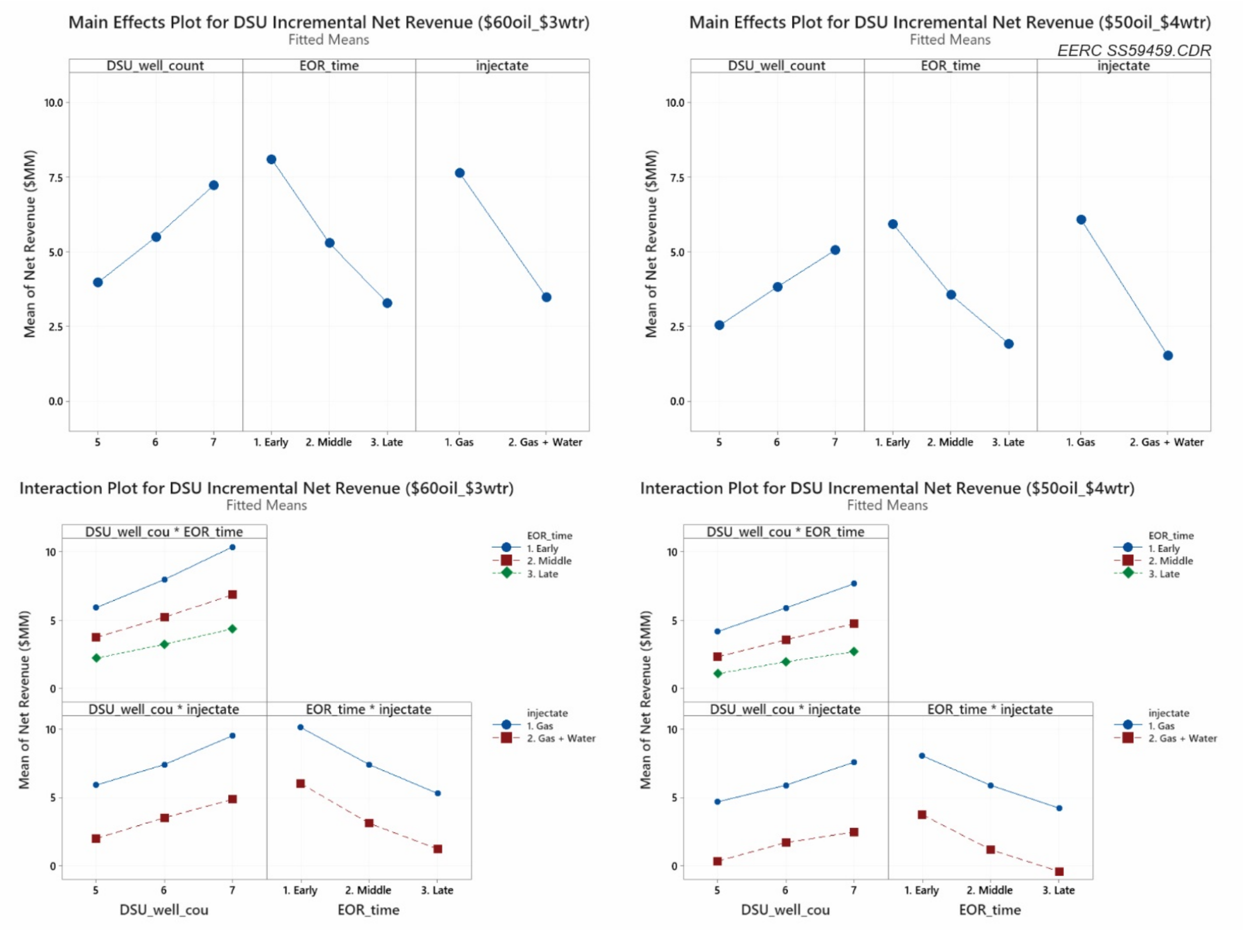

Figure 103. Factorial plots for main effects (top) and interactions (bottom) for DSU well count, EOR development timeline, and injectate from the fitted regression model for Set 1 for the target variable: $**60oil_$3wtr ($MM, left) and $50oil_$4wtr ($MM, right)**.

Set 2 Simulations

The results of the Set 1 simulations showed that a seven-well DSU with an early EOR development timeline and gas-only injection performs best for both oil production and net revenue. Therefore, the Set 2 simulations all used a seven-well DSU with an early EOR development timeline and gas-only injection for all simulations and instead varied four operational factors: injection rate, injection time, soak time, and production time.

Diagnostic plots for the Set 2 regression models are provided in Appendix A. These diagnostic plots show that some of the Set 2 linear regression models demonstrate deviations from the underlying assumptions of linear regression—some of the residuals are outliers and do not follow a normal distribution, and cases with injection rates greater than 20 MMscf show slightly larger residuals than cases with lower injection rates. Therefore, inferences drawn from these linear regression models beyond the mean ±1 standard deviation should be made with caution, and the ML-based methods in Section 4 are used to supplement the linear regression interpretations.

DSU Incremental Oil Production

Figure 104 summarizes the fitted regression model for oil production. Like the preceding figures for Set 1, the bars in the rightmost column provide a visual summary of the sign (blue is a positive effect, and red is a negative effect) and magnitude (the bar length is proportional to the effect size) of the operational variable, i.e., the relative importance of each variable on oil production. Unlike the Set 1 regression models, which used factor (categorical) variables in the models, the Set 2 regression models used scaled numeric variables of injection rate, injection time, soak time, and production time. In Figure 104, the prefix "z" denotes the scaled variable using the formula shown in Equation 7. Therefore, the column "exp(Coef)" for the scaled variables shows the percentage change in DSU incremental oil production given a one-unit change in the scaled variable, i.e., a change from one standard deviation below the mean to one standard deviation above.

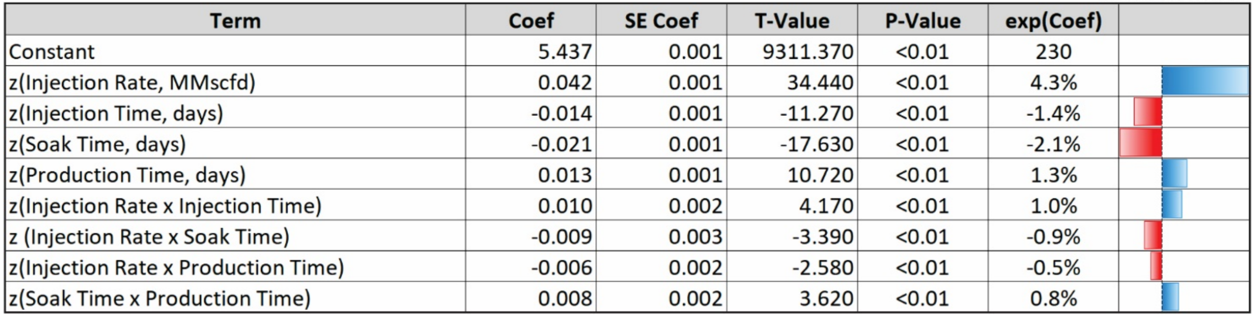

EERC SS59460.CDR

Term	Coef	SE Coef	T-Value	P-Value	exp(Coef)	
Constant	5.437	0.001	9311.370	<0.01	230	
z(Injection Rate, MMscfd)	0.042	0.001	34.440	<0.01	4.3%	
z(Injection Time, days)	-0.014	0.001	-11.270	<0.01	-1.4%	
z(Soak Time, days)	-0.021	0.001	-17.630	<0.01	-2.1%	
z(Production Time, days)	0.013	0.001	10.720	<0.01	1.3%	
z(Injection Rate x Injection Time)	0.010	0.002	4.170	<0.01	1.0%	
z (Injection Rate x Soak Time)	-0.009	0.003	-3.390	<0.01	-0.9%	
z(Injection Rate x Production Time)	-0.006	0.002	-2.580	<0.01	-0.5%	
z(Soak Time x Production Time)	0.008	0.002	3.620	<0.01	0.8%	

Figure 104. Summary of the fitted regression model output for Set 2 for the target variable: **DSU incremental oil production (Mbbl)**. Coef = coefficient, SE Coef = standard error of the coefficient, T-Value = the *t*-statistics of the coefficient, P-Value = the *p*-value of the student's *t*-distribution for the coefficient, and exp(Coef) = exponentiation of the Coef for the constant term and (exp(Coef) – 1) for the additional variables.

The exponentiation of the constant term in the fitted regression model, exp(Coef), represents the expected value for the Set 2 base case: a seven-well DSU with an early EOR development timeline and gas-only injection, which is exp(5.437) = 230 Mbbl. The exponentiation of the additional factors (expressed as exp(Coef) – 1) in the regression summary represents the estimated effect of a one-unit change in the operational variable. For example, the largest effect is for injection rate, and going from one standard deviation below the mean (6.5 MMscfd) to one standard deviation above the mean (19 MMscfd) is expected to ***increase*** oil production by +4.3% (from 230 Mbbl to 240 Mbbl). Soak time has the next largest effect, and going from one standard deviation below the mean (5 days) to one standard deviation above the mean (17 days) is expected to ***decrease*** oil production by −2.1%. The other effect sizes for main effects are relatively small, with a −1.4% effect for injection time (going from 22 to 52 days) and +1.3% effect for production time (going from 41 days to 80 days).

The effect sizes for interactions are also relatively small (≤1%); however, the interactions between (injection rate × injection time), (injection rate × soak time), (injection rate × production time), and (soak time × production time) are all statistically significant (*p*-value ≤0.05).

Figure 105 shows factorial plots for both the main effects (top) and the interactions (bottom) for the fitted regression model for oil production. Analogous to the bars in the regression coefficient summary, the factorial plots show large positive main effects on oil production associated with higher injection rates, relatively small negative effects of longer injection and soak time, and relatively small positive effects of longer production time. The interaction plots show how the relationship between one variable and a continuous response depends on the value of the variable. For example, the upper left-hand panel in the interaction plots shows how the increase in oil production with higher injection rate varies (different slope) depending on the interaction between (injection rate × injection time). The fitted regression model did not include an interaction term for (injection time × soak time) or (injection time × production time) because these terms were not significant, and the BIC selection dropped the terms from the final model, which is why the middle panels in the interaction plot are blank.

DSU Incremental Water Production

Figure 106 summarizes the fitted regression model for water production. The exponentiation of the constant term in the fitted regression model, exp(Coef), represents the expected value for the Set 2 base case: a seven-well DSU with an early EOR development timeline and gas-only injection, which is exp(5.437) = 469 Mbbl. The exponentiation of the additional factors (expressed as exp(Coef) – 1) in the regression summary represents the estimated effect of a one-unit change in the operational variable. For example, the largest effect is for injection time, and going from one standard deviation below the mean (22 days) to one standard deviation above the mean (52 days) is expected to ***decrease*** water production by −9.8% (from 469 to 423 Mbbl). Production time has the next largest effect, and going from one standard deviation below the mean (41 days) to one standard deviation above the mean (80 days) is expected to ***increase*** water production by +7.6%. The other effect sizes for main effects are relatively small, with a −3.5% effect for injection rate (going from 6.5 to 19 MMscfd) and −3.4% effect for soak time (going from 5 days to 17 days).

The effect sizes for interactions are also relatively small (≤2.1%); however, the interactions between (injection rate × injection time), (injection time × soak time), and (injection time × production time) are all statistically significant (*p*-value ≤0.05).

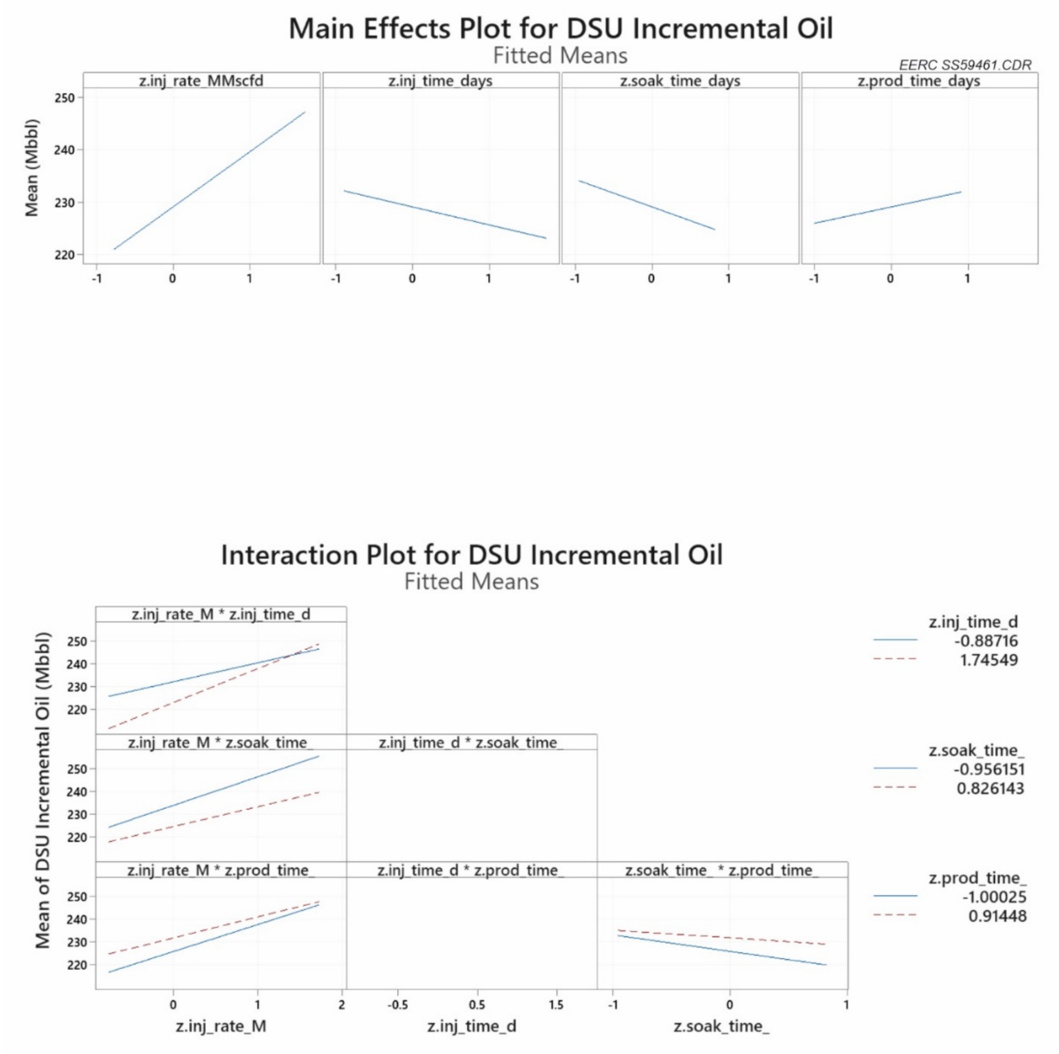

Figure 105. Factorial plots for main effects (top) and interactions (bottom) for injection rate, injection time, soak time, and production time from the fitted regression model for Set 2 for the target variable: **DSU incremental oil production (Mbbl)**.

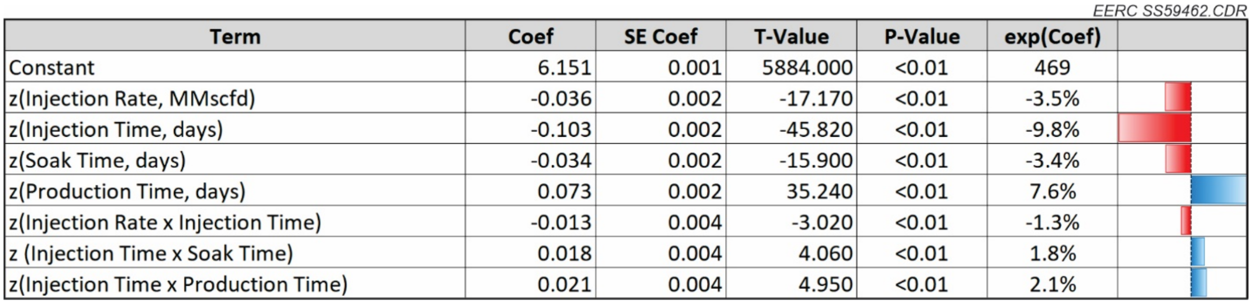
EERC SS59462.CDR

Term	Coef	SE Coef	T-Value	P-Value	exp(Coef)	
Constant	6.151	0.001	5884.000	<0.01	469	
z(Injection Rate, MMscfd)	-0.036	0.002	-17.170	<0.01	-3.5%	🟥
z(Injection Time, days)	-0.103	0.002	-45.820	<0.01	-9.8%	🟥
z(Soak Time, days)	-0.034	0.002	-15.900	<0.01	-3.4%	🟥
z(Production Time, days)	0.073	0.002	35.240	<0.01	7.6%	🟦
z(Injection Rate x Injection Time)	-0.013	0.004	-3.020	<0.01	-1.3%	🟥
z (Injection Time x Soak Time)	0.018	0.004	4.060	<0.01	1.8%	🟦
z(Injection Time x Production Time)	0.021	0.004	4.950	<0.01	2.1%	🟦

Figure 106. Summary of the fitted regression model output for Set 2 for the target variable: **DSU incremental water production (Mbbl)**. Coef = coefficient, SE Coef = standard error of the coefficient, T-Value = the *t*-statistics of the coefficient, P-Value = the *p*-value of the student's *t*-distribution for the coefficient, and exp(Coef) = exponentiation of the Coef for the constant term and (exp(Coef) – 1) for the additional variables.

Figure 107 shows factorial plots for both the main effects (top) and the interactions (bottom) for the fitted regression model for water production. Analogous to the bars in the regression coefficient summary, the factorial plots show large negative main effects on water production associated with longer injection time, relatively small negative effects of higher injection rate and longer soak time, and modest positive effects of longer production time. The interaction plots show how the relationship between one variable and a continuous response depends on the value of the variable. For example, the uppermost middle panel in the interaction plots shows how the decrease in water production with higher injection time varies (different slope) depending on the interaction between (injection time × soak time). The fitted regression model did not include an interaction term for (injection rate × soak time), (injection rate × production time), or (soak time × production time) because these terms were not significant, and the BIC selection dropped the terms from the final model, which is why those panels in the interaction plot are blank.

DSU Incremental Gas Production

Figure 108 summarizes the fitted regression model for gas production. The exponentiation of the constant term in the fitted regression model, exp(Coef), represents the expected value for the Set 2 base case: a seven-well DSU with an early EOR development timeline and gas-only injection, which is exp(5.437) = 1443 MMscf. The exponentiation of the additional factors (expressed as exp(Coef) – 1) in the regression summary represents the estimated effect of a one-unit change in the operational variable. For example, the largest effect was for injection rate, and going from one standard deviation below the mean (6.5 MMscfd) to one standard deviation above the mean (19 MMscfd) is expected to ***increase*** gas production by +33.2% (from 1443 MMscf to 1922 Mbbl). Injection time, soak time, and production time had lower and similar effect sizes, with a positive effect of +7.7%, negative effect of −7.9%, and negative effect of −7.7%, respectively.

The effect sizes for interactions were larger than the interactions for oil or water production, with a negative effect of −5.8% for (injection time × soak time) and positive +6.7% for (soak time × production time).

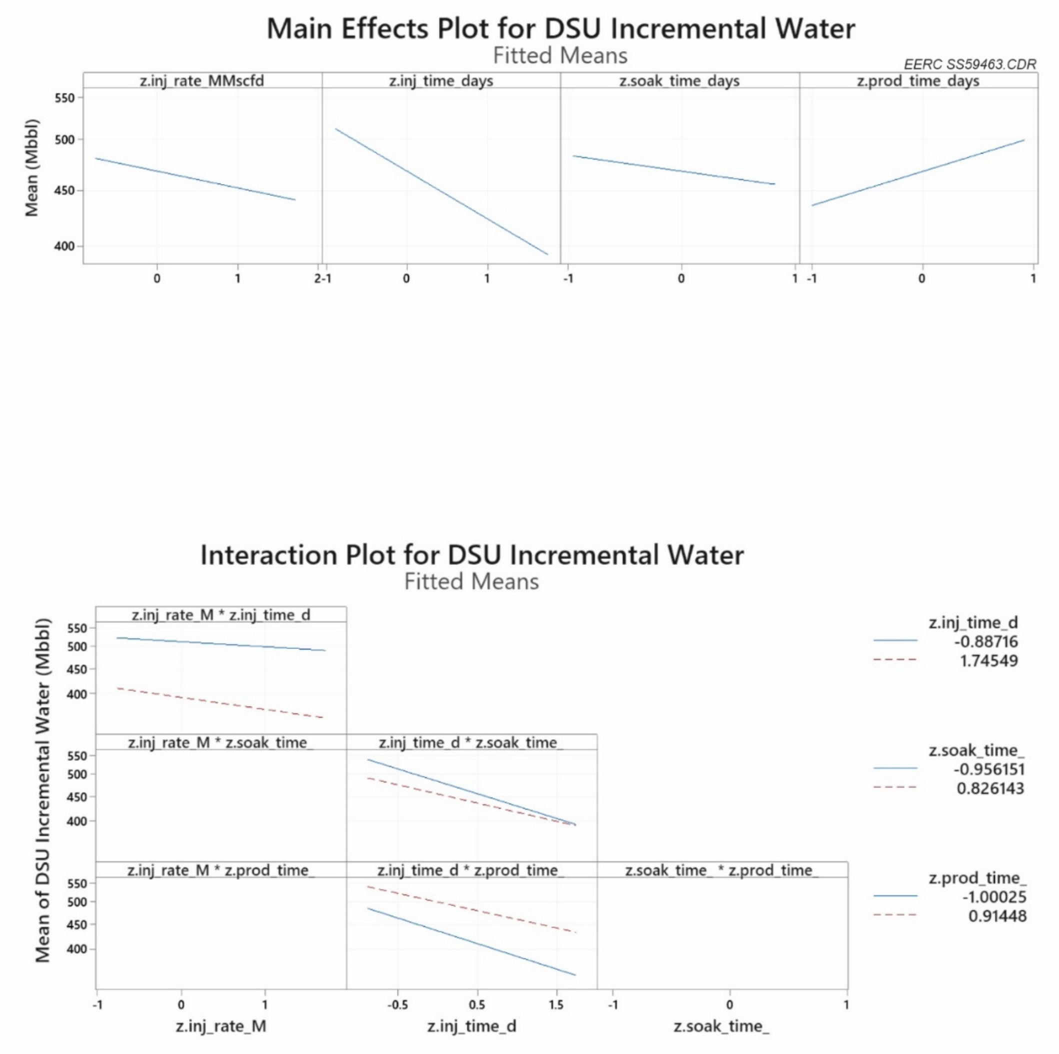

Figure 107. Factorial plots for main effects (top) and interactions (bottom) for injection rate, injection time, soak time, and production time from the fitted regression model for Set 2 for the target variable: **DSU incremental water production (Mbbl)**.

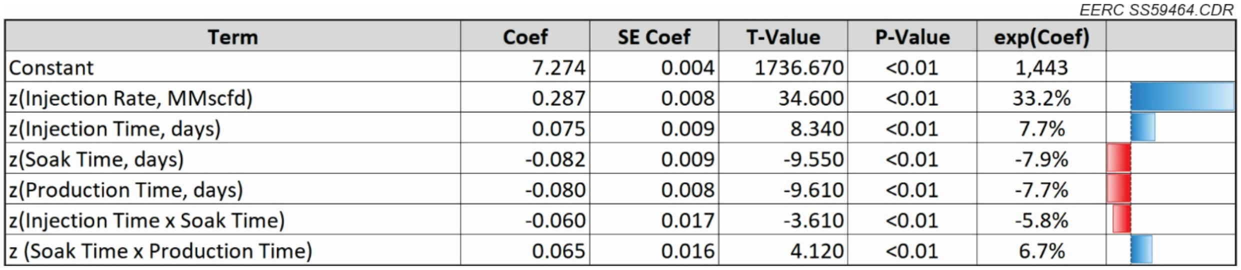

EERC SS59464.CDR

Term	Coef	SE Coef	T-Value	P-Value	exp(Coef)	
Constant	7.274	0.004	1736.670	<0.01	1,443	
z(Injection Rate, MMscfd)	0.287	0.008	34.600	<0.01	33.2%	
z(Injection Time, days)	0.075	0.009	8.340	<0.01	7.7%	
z(Soak Time, days)	-0.082	0.009	-9.550	<0.01	-7.9%	
z(Production Time, days)	-0.080	0.008	-9.610	<0.01	-7.7%	
z(Injection Time x Soak Time)	-0.060	0.017	-3.610	<0.01	-5.8%	
z (Soak Time x Production Time)	0.065	0.016	4.120	<0.01	6.7%	

Figure 108. Summary of the fitted regression model output for Set 2 for the target variable: **DSU incremental gas production (MMscf)**. Coef = coefficient, SE Coef = standard error of the coefficient, T-Value = the *t*-statistics of the coefficient, P-Value = the *p*-value of the student's *t*-distribution for the coefficient, and exp(Coef) = exponentiation of the Coef for the constant term and (exp(Coef) – 1) for the additional variables.

Figure 109 shows factorial plots for both the main effects (top) and the interactions (bottom) for the fitted regression model for gas production. Analogous to the bars in the regression coefficient summary, the factorial plots show large positive main effects on water production associated with higher injection rate, relatively modest positive effects of longer injection time, and modest negative effects of longer soak and production time. The interaction plots show how the relationship between one variable and a continuous response depends on the value of the variable. For example, the upper left-hand panel in the interaction plots shows how the increase in gas production with higher injection time varies (different slope) depending on the interaction between (injection time × soak time). The fitted regression model did not include an interaction term for (injection time × production time) because this term was not significant, and the BIC selection dropped the term from the final model, which is why that panel in the interaction plot is blank.

DSU Incremental Net Revenue

Figure 110 shows the fitted regression models for the two net revenue scenarios: $60/bbl oil price and $3/bbl water disposal cost ($60oil_$3wtr) or $50/bbl oil price and $4/bbl water disposal cost ($50oil_$4wtr). The patterns in the regression coefficients are similar; however, the net revenue estimates differ because of the higher penalty for the cost of produced water transport and disposal for $50oil_$4wtr as compared to $60oil_$3wtr. For example, the expected value for the base case is exp(2.476) = $11.9MM for the $60oil_$3wtr case and exp(2.262) = $9.6MM for the $50oil_$4wtr case, illustrating the effect of the higher penalty for the cost of produced water transport and disposal ($2.3MM in additional costs over 2 years).

The patterns for the different factors are like those for oil production, since the higher oil price relative to the cost of produced water transport and disposal means that oil production largely drives the net revenue result. Increasing the injection rate by a one-unit change is expected to ***increase*** net revenue by +5.6% and +5.9%, respectively, for $60oil_3wtr and $50oil_$4wtr scenarios. Soak time had the next largest effect, and a one-unit change is expected to ***decrease*** oil production by −1.9% and −1.8%, respectively, for $60oil_3wtr and $50oil_$4wtr scenarios. The other effect sizes for main effects were relatively small, with a 0.0% and 0.4% effect for injection time and a 0.3% and 0.1% effect for production time.

The effect sizes for interactions were also relatively small (≤1.4%), and only the interactions between (injection rate × injection time), (injection rate × soak time), and (soak time × production time) had *p*-values ≤0.05.

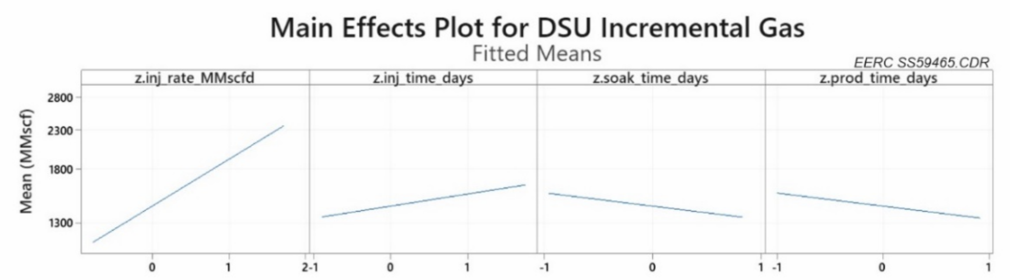

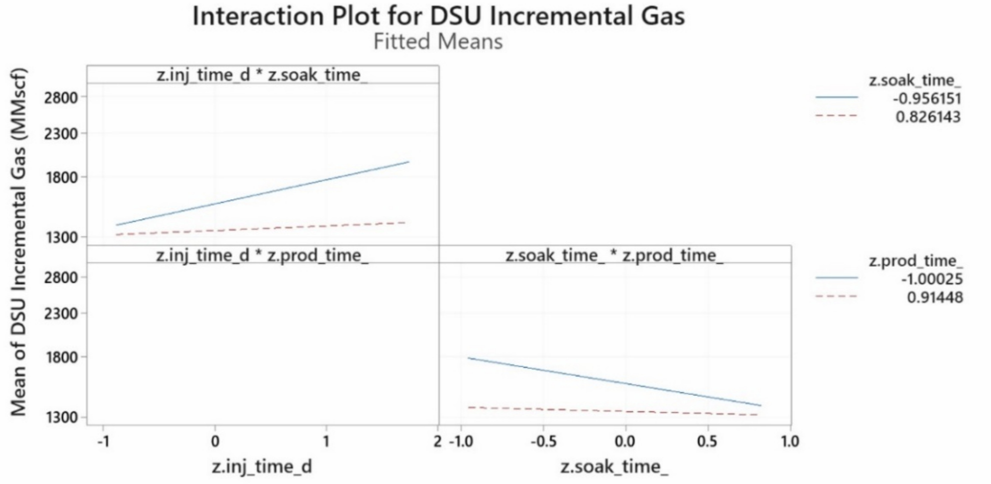

Figure 109. Factorial plots for main effects (top) and interactions (bottom) for injection rate, injection time, soak time, and production time from the fitted regression model for Set 2 for the target variable: **DSU incremental gas production (MMscf)**.

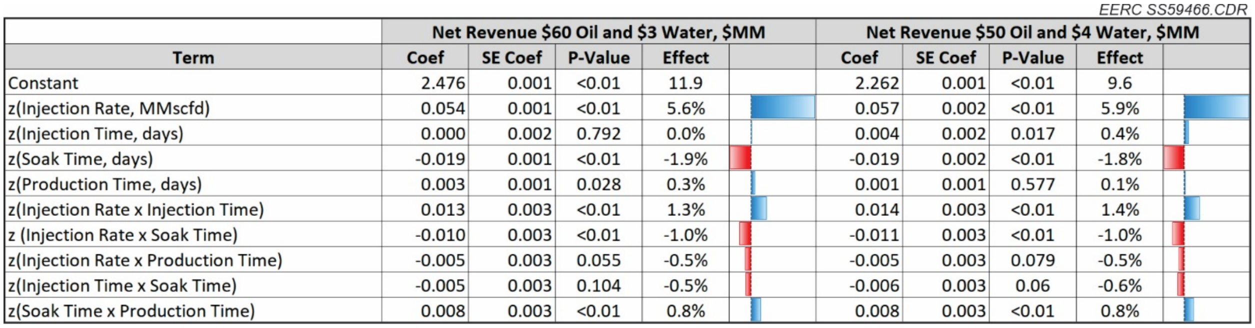

EERC SS59466.CDR

	Net Revenue $60 Oil and $3 Water, $MM					Net Revenue $50 Oil and $4 Water, $MM				
Term	**Coef**	**SE Coef**	**P-Value**	**Effect**		**Coef**	**SE Coef**	**P-Value**	**Effect**	
Constant	2.476	0.001	<0.01	11.9		2.262	0.001	<0.01	9.6	
z(Injection Rate, MMscfd)	0.054	0.001	<0.01	5.6%		0.057	0.002	<0.01	5.9%	
z(Injection Time, days)	0.000	0.002	0.792	0.0%		0.004	0.002	0.017	0.4%	
z(Soak Time, days)	-0.019	0.001	<0.01	-1.9%		-0.019	0.002	<0.01	-1.8%	
z(Production Time, days)	0.003	0.001	0.028	0.3%		0.001	0.001	0.577	0.1%	
z(Injection Rate x Injection Time)	0.013	0.003	<0.01	1.3%		0.014	0.003	<0.01	1.4%	
z (Injection Rate x Soak Time)	-0.010	0.003	<0.01	-1.0%		-0.011	0.003	<0.01	-1.0%	
z(Injection Rate x Production Time)	-0.005	0.003	0.055	-0.5%		-0.005	0.003	0.079	-0.5%	
z(Injection Time x Soak Time)	-0.005	0.003	0.104	-0.5%		-0.006	0.003	0.06	-0.6%	
z(Soak Time x Production Time)	0.008	0.003	<0.01	0.8%		0.008	0.003	<0.01	0.8%	

Figure 110. Summary of the fitted regression model output for Set 2 for the target variable: **DSU Net Revenue at $60oil_$3wtr ($MM, left) and DSU Net Revenue at $50oil_$4wtr ($MM, right)**. Coef = coefficient, SE Coef = standard error of the coefficient, T-Value = the *t*-statistics of the coefficient, P-Value = the *p*-value of the student's *t*-distribution for the coefficient, and exp(Coef) = exponentiation of the Coef for the constant term and (exp(Coef) – 1) for the additional variables.

Figure 111 shows factorial plots for both the main effects (top) and the interactions (bottom) for the fitted regression model for oil production. Analogous to the bars in the regression coefficient summary, the factorial plots show large positive main effects on net revenue associated with higher injection rates, relatively small positive effects of longer injection and production time, and relatively moderate negative effects of longer soak time. The interaction plots show how the relationship between one variable and a continuous response depends on the value of the variable. For example, the upper left-hand panel in the interaction plots shows how the increase in net revenue with a higher injection rate varies (different slope) depending on the interaction between (injection rate × injection time). The fitted regression model did not include an interaction term for (injection time × production time) because this term was not significant, and the BIC selection dropped the term from the final model, which is why the bottom middle panel in the interaction plots are blank.

Linear Regression Summary

The Set 1 and Set 2 linear regression models showed the following:

- Among the Set 1 simulations for i) five-, six-, and seven-well DSU configurations; ii) early, middle, and late EOR development timelines; and iii) gas-only or gas and water injection the seven-well DSU with early EOR development timeline and gas-only injection had the best oil production and net revenue.

- In the Set 1 simulation, i) increasing the well count from five to seven wells significantly increased oil production, ii) delaying the start of the EOR development significantly reduced oil production, and iii) switching from gas-only to gas and water injection significantly reduced oil production.

- Among the Set 2 simulations of a seven-well DSU, early EOR development timeline, gas-only injection, and the operational variables tested (injection rate, injection time soak time, and production time), the variable with the greatest effect on oil production was the injection rate. However, higher injection rates were also associated with significantly greater gas production.

- For the Set 2 simulations, injection time, soak time, and production time had a relatively small effect on oil production (<2.1% effect over a one-unit change in the variables). Longer injection time had a negative effect on water production (i.e., longer injection time equated with lower water production) and longer production time had a positive effect on water production (i.e., longer production time equated with greater water production). Conversely, longer injection time had a positive effect on gas production (i.e., longer injection time equated with higher gas production) and longer soak and production times had a negative effect on gas production (i.e., longer soak and production times equated with lower gas production).

- For the Set 2 simulations, the operational variables injection rate, injection time, soak time, and production time showed significant interactions (second-order effects) and

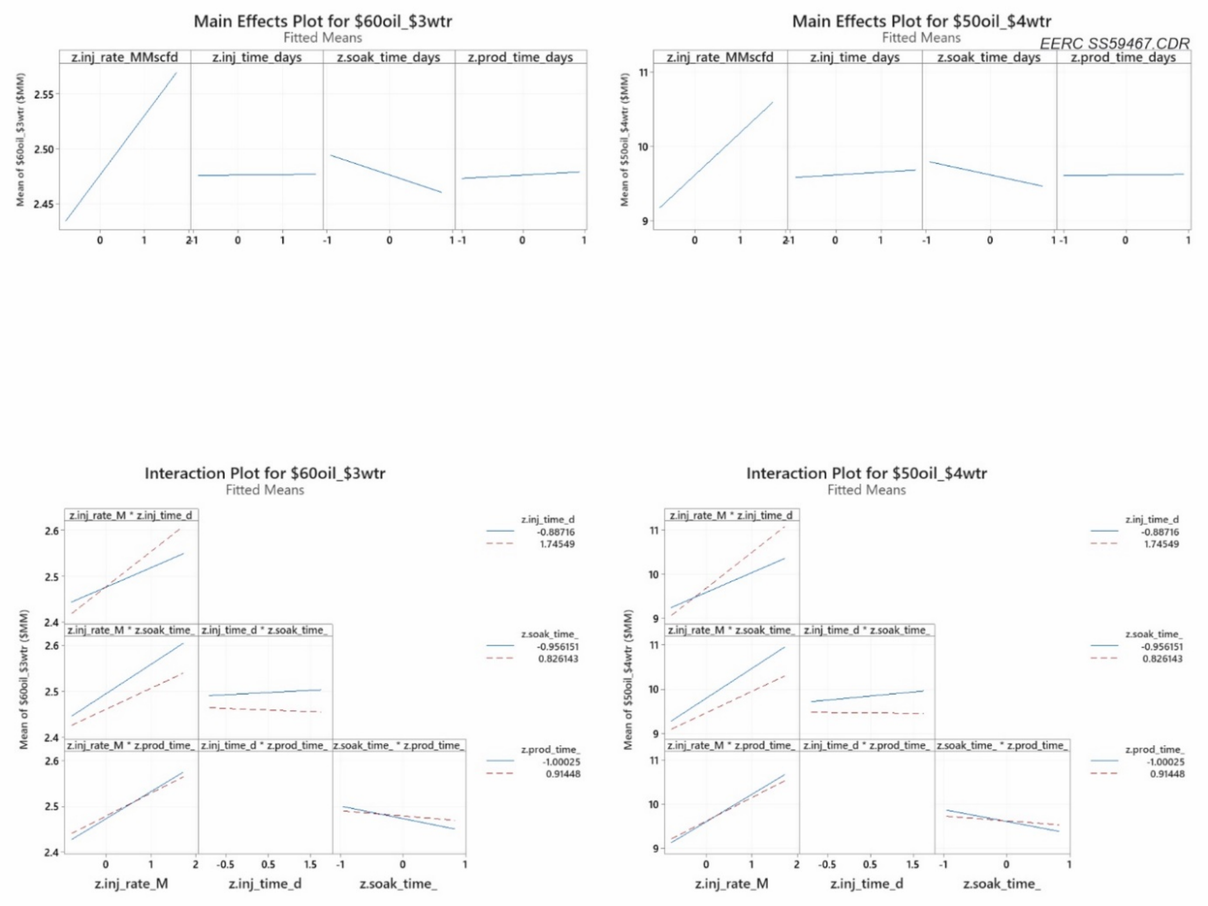

Figure 111. Factorial plots for main effects (top) and interactions (bottom) for injection rate, injection time, soak time, and production time from the fitted regression model for Set 2 for the target variable: $60oil_$3wtr ($MM, left) and $50oil_$4wtr ($MM, right).

some of the higher injection rate cases did not conform to the underlying assumption of linear regression, which together point toward nonlinear effects between the operational variables and the target variables of oil, gas, and water production that would be better modeled using alternative methods like those presented in Section 4 (see *Section 4: Results – Machine Learning*).

Results – Machine Learning

ML-based methods were used to evaluate the Set 2 simulations and extend the statistical inferences developed from the linear regression modeling. The ML results are presented in three parts: i) exploratory data analysis of correlations among the four operational parameters (injection rate, injection time, soak time, and production time) and the three DSU incremental production metrics (oil, gas, and water); ii) fitting predictive models to the training and test data sets and the identification of the best-performing models, and iii) full operational matrix predictive modeling to examine all combinations of operational parameters, develop optimization contours, and compute global sensitivity metrics across the simulations.

Exploratory Analysis

Figure 112 shows pairwise plots of the three DSU production metrics and four EOR operational parameters. The histograms of the variables are shown on the diagonal. The density distributions of the paired variables are presented to the left and below the histograms, and the scatterplots of the paired variables, along with the Pearson correlation coefficients on top of these plots, are presented to the right and above the histograms.

The production metrics (oil, gas, and water) are moderately correlated. For example, oil production is positively correlated with gas production (correlation coefficient r: 0.73) and water production (r: 0.22), and gas production is negatively correlated with water production (r: −0.48). The moderate correlations among the production metrics indicate that the optimum operational conditions are different for different production metrics. For example, the optimum combination of operational parameters for maximizing oil production may not yield maximized gas and/or water production and vice versa.

Other observations of correlations of the production metrics and operational parameters are as follows (Figure 112):

- Both oil production and gas production are positively correlated with injection rate (r: 0.77 and 0.85, respectively), but water production is not correlated with injection rate (r: −0.27).

- Oil and water production are negatively correlated with injection time (r: −0.44 and −0.72, respectively), while gas production is not correlated with injection time (r: 0.05).

- Oil and water production are moderately negatively correlated with soak time (r: −0.39 and −0.36), while gas production is not correlated with soak time (r: −0.18).

- Lastly, production time is not correlated with oil production (r: 0.05) but slightly negatively correlated with gas production (r: −0.40) and positively correlated with water production (r: 0.54).

These correlations among the production metrics and the operational parameters suggest that the relationship of production and operations is not linear. However, the high correlation between oil and gas production and injection rate suggests that injection rate is likely to be the most important factor for predicting oil and gas production.

Predictive Model Performance – Training and Testing Data Sets

Separate predictive models using each of the four ML algorithms were developed for oil production, water production, gas production, and net revenue. The individual modeling performance is evaluated based on the model performance on both training and test sets. Since the model development and evaluation process is the same for oil production, water production, and net revenue, only the oil production models are presented in detail in this report. The remaining models are included in the optimization results (see *Contour Plots*).

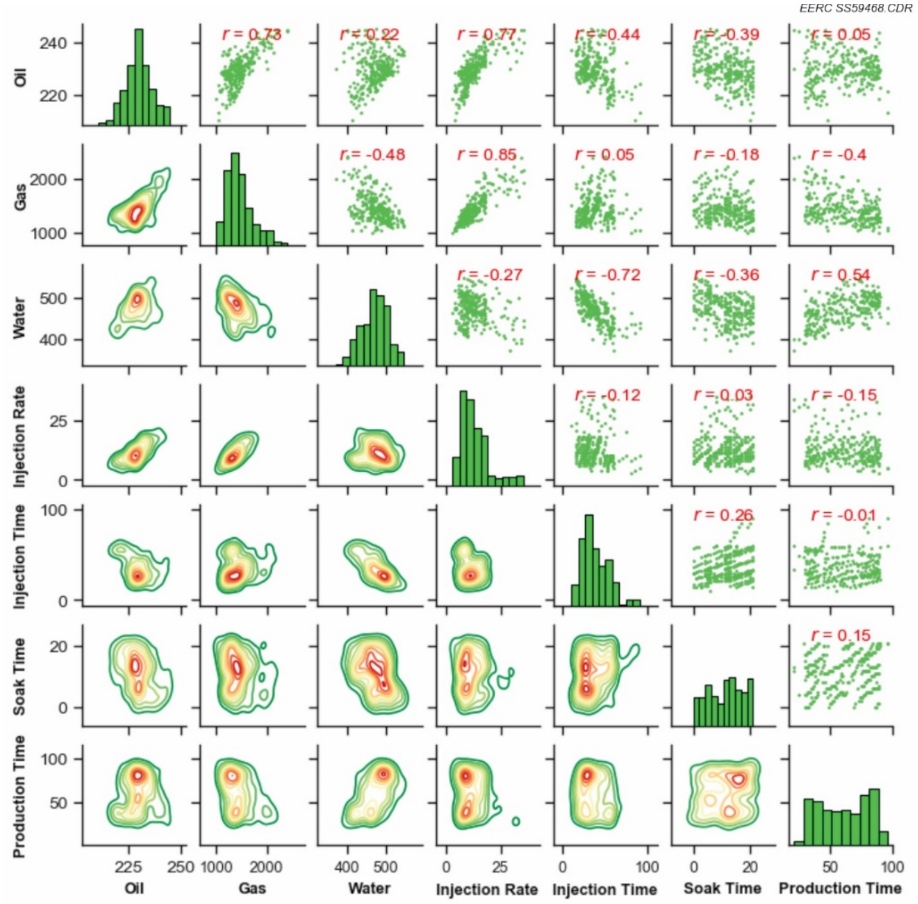

Figure 112. Pairwise plots of the three DSU production metrics (oil [Mbbl], gas [MMcf] and water [Mbbl]) and four EOR operational parameters (injection rate [Mcfd], injection time [d], soaking time [d], and production time [d]). The histograms of the variables are shown on the diagonal. The density distributions of the paired variables are presented to the left and below the histograms, and the scatterplots of the paired variables, along with the Pearson correlation coefficients on top of these plots, are presented to the right and above the histograms.

Results from fitting the four ML algorithms to the training set show that linear regression, SVM, RF, and XGBoost all provide excellent predictive performance of oil production, with r^2 values of 0.932, 0.984, 0.992, and 1.00 Mbbl, and RMSE (root mean square error) values of 2.21, 1.09, 0.78, and 0.14 Mbbl, respectively (Figure 113). The model hyperparameters were fit to the training set and then evaluated on the test set. All four models performed well on the test set, with r^2 values of 0.915, 0.982, 0.969, and 0.965 Mbbl and RMSE values of 2.84, 1.32, 1.90, and 1.93 Mbbl, respectively, for linear regression, SVM, RF, and XGBoost (Figure 114).

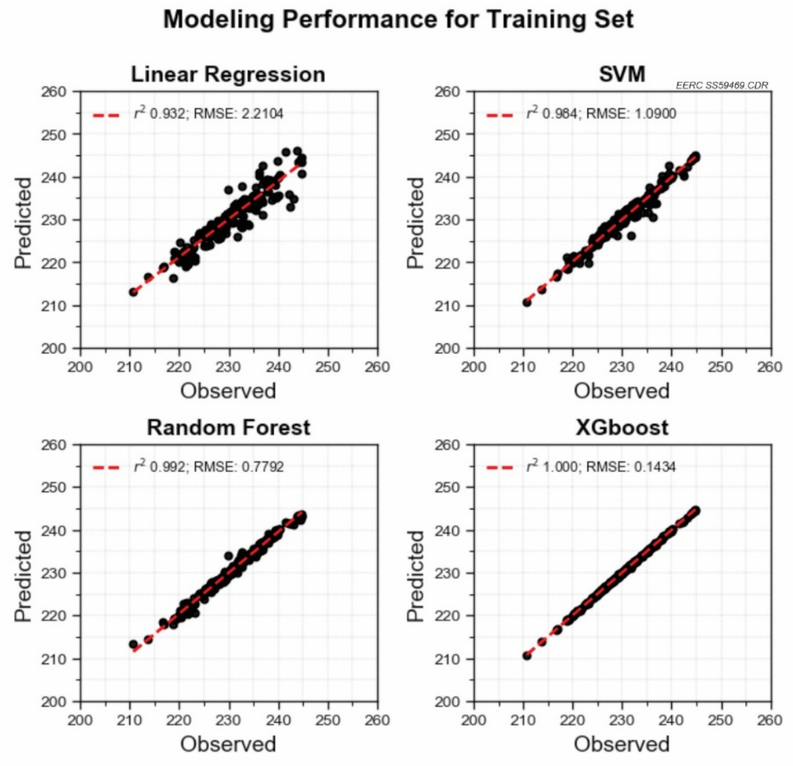

Figure 113. Crossplots of observed (simulated using CMG GEM) (*x*-axis) and predicted (using the fitted ML algorithm) DSU incremental oil production (Mbbl) from four ML algorithms fitted to the training set. The dashed diagonal line represents the 1:1 line between the observed and predicted values. The r^2 and RMSE values are presented for each model. The unit for the RMSE value is Mbbl.

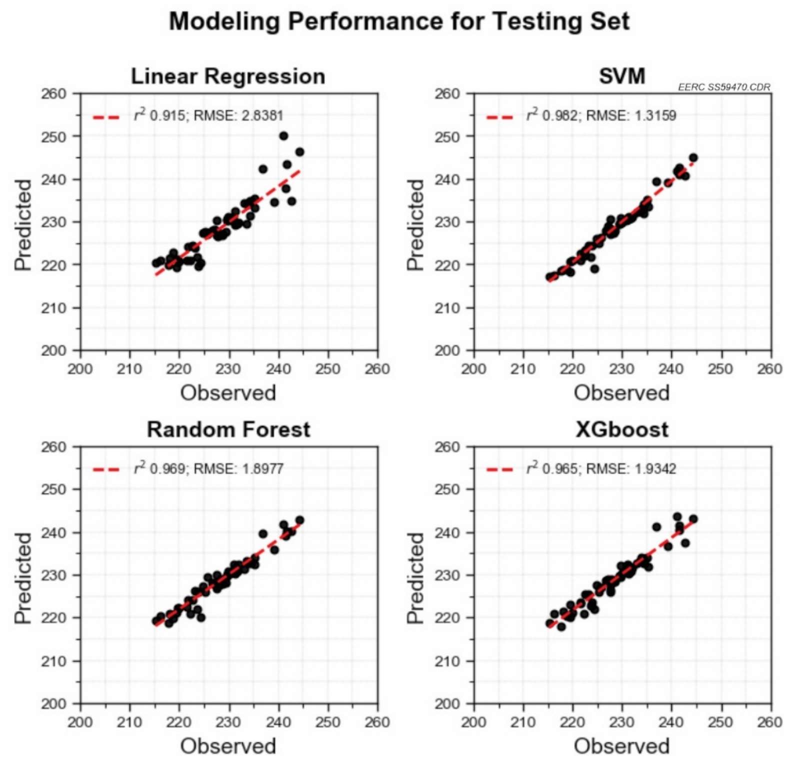

Figure 114. Crossplots of observed (simulated using CMG GEM) (*x*-axis) and predicted (using the fitted ML algorithm) DSU incremental oil production (Mbbl) from four ML algorithms fitted to the training data set, and then evaluated on the test set. The dashed diagonal line represents the 1:1 line between the observed and predicted values. The r^2 and RMSE values are presented for each model. The unit for the RMSE value is Mbbl.

All models performed well in predicting oil production. However, linear regression was the weakest among the four models, with both the lowest r^2 in the test set (0.915) and highest RMSE in the test set (2.838). While XGBoost had the best performance for predicting oil in the training data set ($r^2 = 1.000$ and RMSE = 0.143), the model performance significantly decreased for the test set ($r^2 = 0.965$ and RMSE = 1.934), which suggest overfitting of the XGBoost algorithm. The RF algorithm provided more consistent predictions in both training and test data sets; however, there was also evidence of slight overfitting. The SVM model was the overall best-performing algorithm for both the training and test sets. Similar results for the training and test sets were observed for the other target variables of water production, gas production, and net revenue (Table 23, Figure 115).

Variable Importance

Figure 116 shows the relative importance of the four operational parameters in predicting oil production from the four models. The variable importance plots for all models show that injection rate is the most important variable. Depending on the model, injection time, soak time, and production time had different relative importance.

Table 23. Performance on the Training and Test Sets for Each of the Four Algorithms for the Target Variables of Oil, Water, and Gas Production and Net Revenue

		r^2		RMSE	
Target	**Model**	**Training**	**Test**	**Training**	**Test**
DSU Oil Production	Linear regression	0.932	0.915	2.210	2.838
	SVM	0.984	0.962	1.090	1.316
	RF	0.992	0.969	0.779	1.898
	XGBoost	1.000	0.965	0.143	1.934
DSU Water Production	Linear regression	0.935	0.887	0.023	0.064
	SVM	0.991	0.986	0.009	0.023
	RF	0.994	0.941	0.007	0.045
	XGBoost	1.000	0.961	0.002	0.037
DSU Gas Production	Linear regression	0.975	0.960	0.030	0.018
	SVM	0.991	0.984	0.017	0.012
	RF	0.969	0.982	0.030	0.012
	XGBoost	0.975	0.999	0.028	0.003
DSU Net Revenue	Linear regression	0.935	0.886	0.023	0.063
	SVM	0.974	0.974	0.015	0.030
	RF	0.994	0.943	0.007	0.043
	XGBoost	0.999	0.948	0.002	0.042

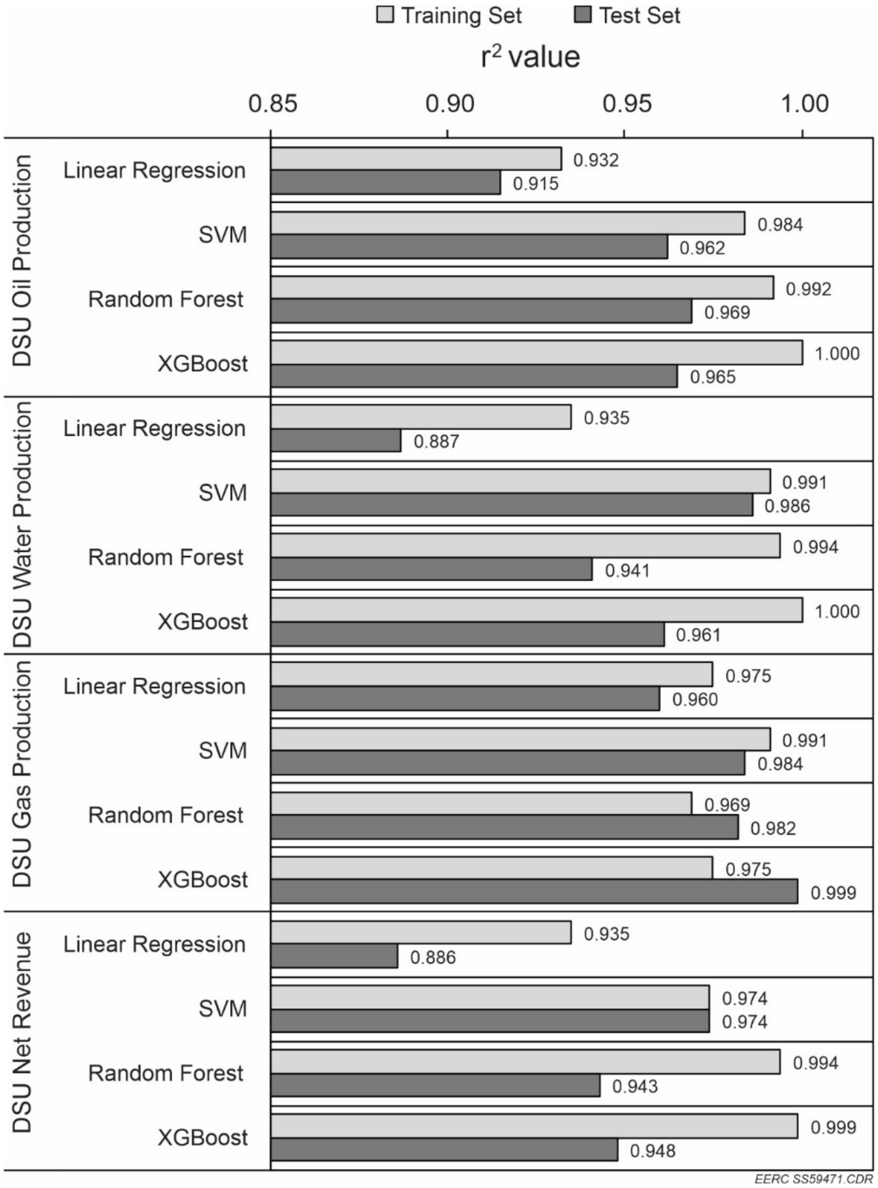

Figure 115. Bar charts showing the r^2 values between training and test sets for each of the four ML models (linear regression, SVM, RF, and XGBoost) for predicting DSU oil, water, gas production, and net revenue.

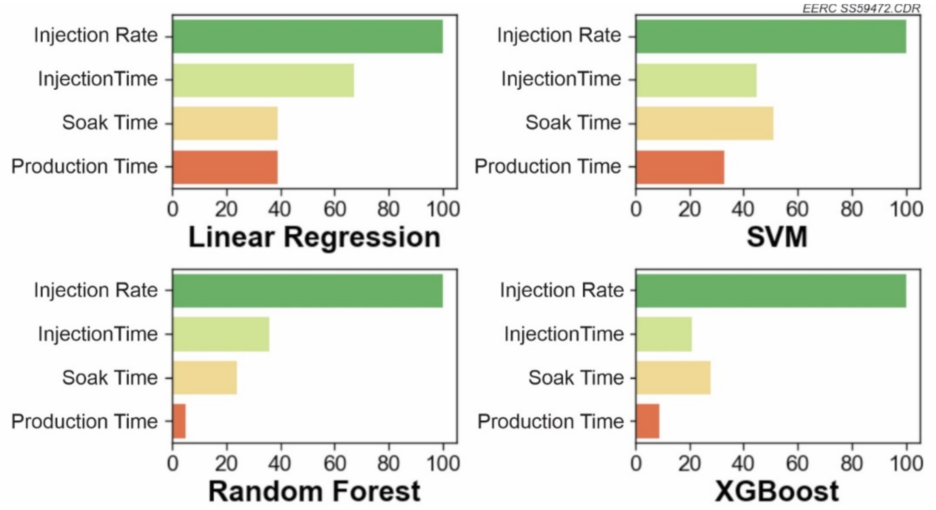

Figure 116. Variable importance diagram for the four ML models (linear regression, SVM, RF, and XGBoost) for predicting oil production.

Full Operational Matrix Results

Figure 117 shows histograms of the predicted oil production for all 4,032,000 cases for each of the four predictive models. Oil production predictions from the four models are different. The histograms of predictions from the linear regression and SVM models more closely follow a normal distribution, while the histogram of predictions from the RF and XGBoost predictions do not follow a normal distribution and instead appear bimodal. However, the average predicted value across all models is relatively similar, with 230, 231, 231, and 237 Mbbl for the linear regression, SVM, RF, and XGBoost models, respectively.

Figure 118 shows the correlation matrix between the four operational variables and the four predictive models, which provides insights into which variables drive the predictions in each model. As previously described with the variable importance plots, the correlation matrix shows that injection rate is the dominant predictive variable, with Pearson correlation coefficients ranging from 0.82 to 0.88 across the four models. The remaining operational variables have similar correlation coefficients; however, there are differences in how each model utilizes injection time, soak time, and/or production time. For example, the linear regression model places the greatest emphasis on soak time (r = −0.42), while the RF model places little emphasis on production time (r = 0.082).

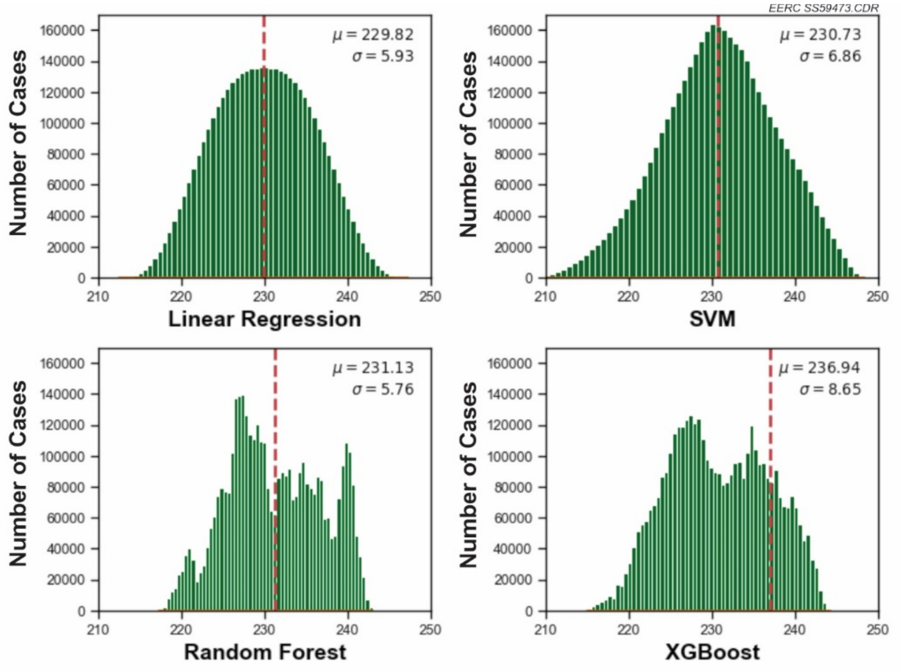

Figure 117.Predicted DSU incremental oil production (Mbbl) based on the predictive models built using four ML algorithms: linear regression, SVM, RF, and XGBoost.

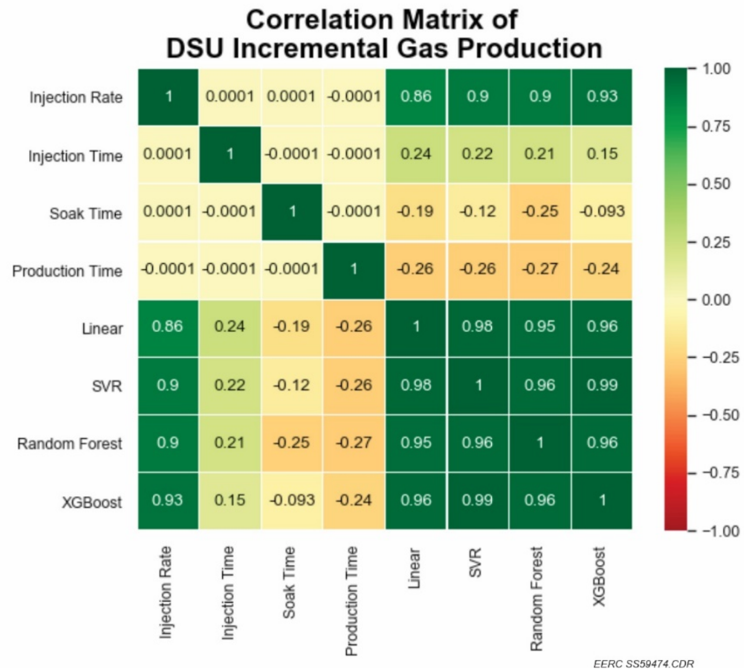

	Injection Rate	Injection Time	Soak Time	Production Time	Linear	SVR	Random Forest	XGBoost
Injection Rate	1	0.0001	0.0001	-0.0001	0.86	0.9	0.9	0.93
Injection Time	0.0001	1	-0.0001	-0.0001	0.24	0.22	0.21	0.15
Soak Time	0.0001	-0.0001	1	-0.0001	-0.19	-0.12	-0.25	-0.093
Production Time	-0.0001	-0.0001	-0.0001	1	-0.26	-0.26	-0.27	-0.24
Linear	0.86	0.24	-0.19	-0.26	1	0.98	0.95	0.96
SVR	0.9	0.22	-0.12	-0.26	0.98	1	0.96	0.99
Random Forest	0.9	0.21	-0.25	-0.27	0.95	0.96	1	0.96
XGBoost	0.93	0.15	-0.093	-0.24	0.96	0.99	0.96	1

Figure 118. Correlation matrix plot of the full operational matrix and the predicted oil production from each of the four predictive models: linear regression, SVM, RF, and XGBoost. The numbers in each grid cell are the Pearson correlation coefficients, which are plotted using a color ramp from −1.00 (perfect negative correlation – red) to +1.00 (perfect positive correlation – green).

Contour Plots

DSU Incremental Oil Production

In each of the predictive models, four independent parameters are used to predict DSU incremental oil production: injection rate, injection time, soak time, and production time. To visualize the relationships of these four parameters with the predicted oil production across the full operational matrix, contour plots were created to visualize relationships between combinations of two parameters and DSU incremental oil production. For the contour plots, the *y*-axes are always injection rate and the *x*-axes are injection time, soak time, or production time. The *z*-axis (color ramp contour) is the predicted oil production and shows a color ramp from the minimum (210 Mbbl) to maximum (248 Mbbl) values. Figure 119 shows the oil production contour plots for each of the four predictive models and three combinations of input parameters: injection rate vs. injection time (top row), injection rate vs. soak time (middle row), and injection rate vs. production time (bottom row).

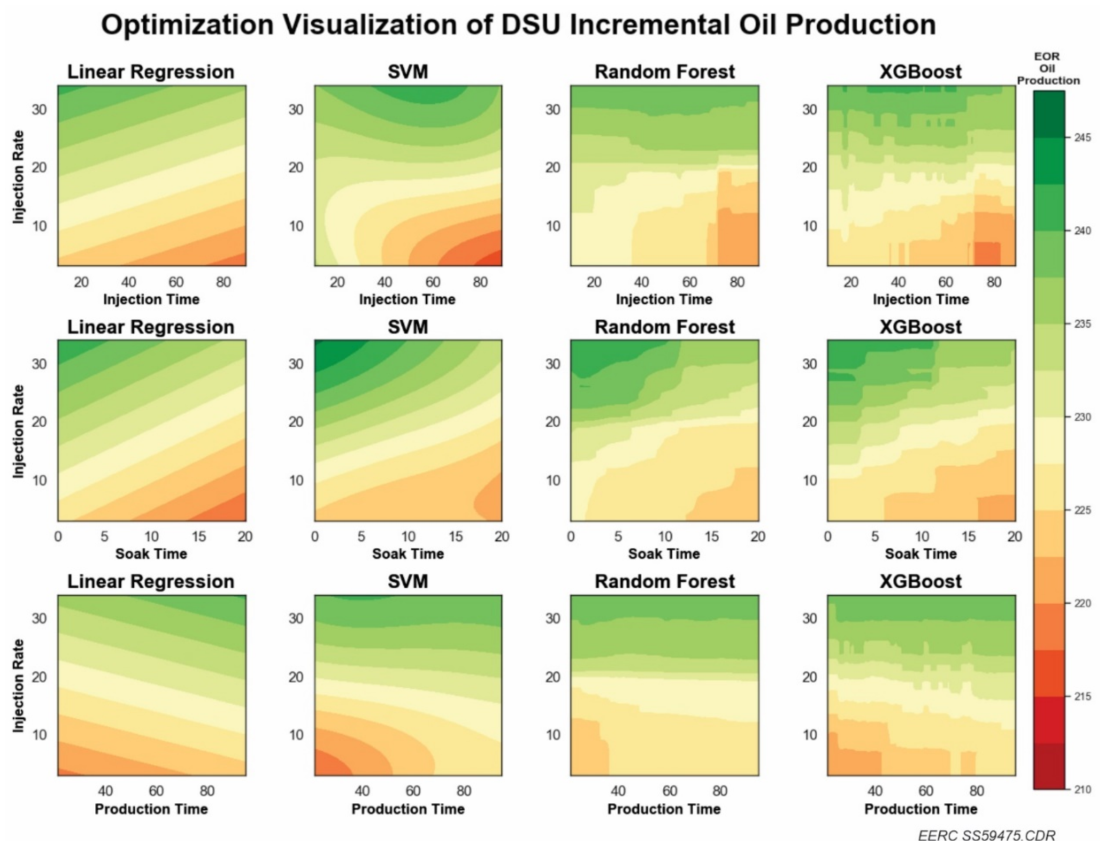

EERC SS59475.CDR

Figure 119. Contour plots of predicted DSU incremental oil production for three combinations of input parameters: injection rate (MMscfd) vs. injection time (days) (top row), injection rate vs. soak time (days) (middle row), and injection rate vs. production time (days) (bottom row) for each of the four ML algorithms.

The four predictive models show similar contour trends; however, the linear regression model does not capture the nonlinear behavior between operational parameters and oil production, as shown by the straight lines in each contour plot. The SVM, RF, and XGBoost contour plots are very similar, with the RF and XGBoost models having more granular predictions across the full operational matrix. The following interpretations are based on the SVM contour plot (second column in Figure 119):

- **Injection rate:** Regardless of injection, soak, or production time, higher injection rates correspond to higher oil production, as the oil production color ramp trends from red (minimum) to green (maximum) going vertically along the *y*-axis from low to high injection rate. However, the curvature of the oil production contour lines shows interactions between injection rate and the other operational parameters.

- **Injection time (top SVM panel):** At higher injection rates above 20 MMscfd, oil production is best when injection time is between approximately 30 and 80 days, with maxima near 60 days. However, lower injection rates less than 20 MMscfd perform worse when injection time increases, with the lowest oil production associated with the longest injection time (red region of the lower right-hand corner of the panel).

- **Soak time (middle SVM panel):** Oil production shows a nearly linear relationship between the combination of soak time and injection rate, with the greatest oil production occurring at the highest injection rate and shortest soak time (upper left-hand corner of the panel) and the lowest oil production occurring at the lowest injection rate and longest soak time (lower right-hand corner of the panel).

- **Production time (bottom SVM panel):** At higher injection rates above 20 MMscfd, oil production is nearly invariant to production time, with shallow slopes to the contour lines. However, lower injection rates less than 20 MMscfd follow the opposite trend of soak time and perform better when production time increases.

Based on these relationships, the optimal operating regions for ***maximizing oil production***, regardless of water and gas production, are higher injection rate, moderate injection time, short soak time, and moderate production time.

To avoid the interactions of multiple variables for the prediction of oil production, a second set of predictions was created by using subsets of the full operational matrix and fixing the production time at its median value (60 days) and the soak time at either its 25th percentile value (5 days) or its maximum value (20 days). The optimization contour plots of oil production based on the subset data are presented in Figure 120. Once again, the linear regression model does not capture the nonlinear behavior between operational parameters and oil production, as shown by the straight lines in each contour plot. The SVM, RF, and XGBoost contour plots are, again, very similar, with the RF and XGBoost models having more granular predictions. As shown in the contour subsets, higher oil production could be achieved via higher injection rates, while longer injection time does not necessarily correspond to higher oil production, especially when the injection rate is less than approximately 20 MMscfd.

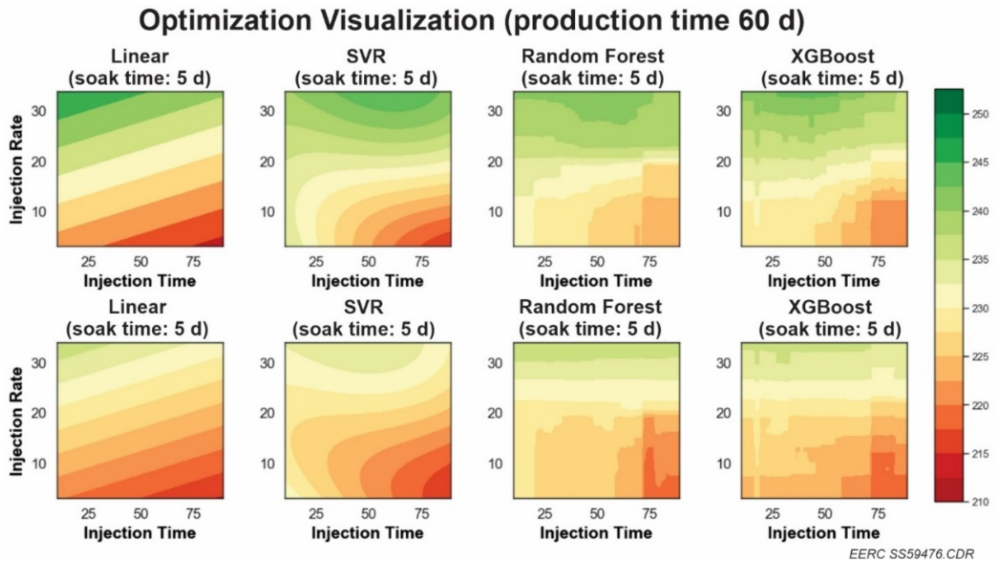

Figure 120. Contour plots of predicted DSU incremental oil production for each of the four ML algorithms, showing injection rate on the *y*-axis (MMscfd), production time fixed at the median value (60 days), and soak time fixed at either 5 days (top row) or 20 days (bottom row).

DSU Incremental Water Production

Figure 121 shows the correlation matrix between the four operational variables and the four predictive models for water production, which provides insights into which variables drive the predictions in each model. The correlation matrix shows that injection time is the dominant predictive variable, with Pearson correlation coefficients ranging from −0.72 to −0.78. The remaining operational variables have similar correlation coefficients (−0.15 to +0.56) and each model weights injection time, soak time, and/or production time similarly.

Figure 122 shows the water production contour plots for each of the four predictive models and three combinations of input parameters: injection rate vs. injection time (top row), injection rate vs. soak time (middle row), and injection rate vs. production time (bottom row). The four predictive models show similar contour trends; however, the linear regression and SVM models show smooth trends while the RF and XGBoost models show more granular predictions across the full operational matrix. The following interpretations are based on the SVM contour plot (second column in Figure 122):

- **Injection rate**: Water production shows a diagonal trend with injection rate, either decreasing from lower left to upper right or vice versa, illustrating an interaction between injection rate and injection, soak, or production time.

- **Injection time** (top SVM panel): Injection time is inversely related to water production, with the greatest water production occurring with the shortest injection times (less than 20 days) and the lowest water production occurring with the longest injection times (greater than 60 days). There is also an interaction with injection rate, as lower injection rates correspond to greater water production (lower left-hand corner) and higher injection rates correspond to lower water production (upper right-hand corner).

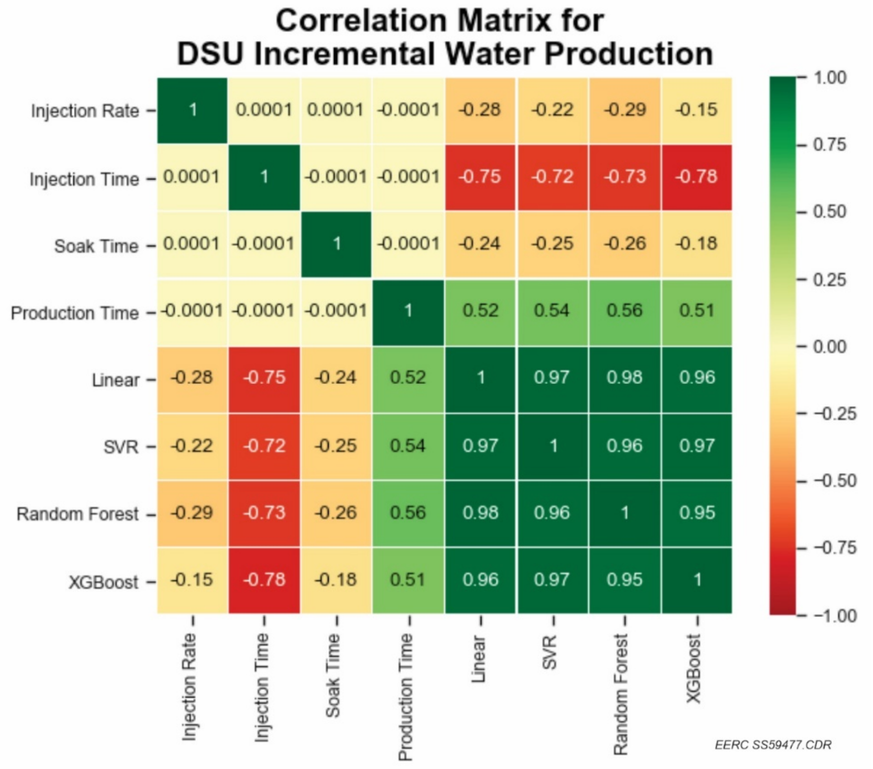

	Injection Rate	Injection Time	Soak Time	Production Time	Linear	SVR	Random Forest	XGBoost
Injection Rate	1	0.0001	0.0001	-0.0001	-0.28	-0.22	-0.29	-0.15
Injection Time	0.0001	1	-0.0001	-0.0001	-0.75	-0.72	-0.73	-0.78
Soak Time	0.0001	-0.0001	1	-0.0001	-0.24	-0.25	-0.26	-0.18
Production Time	-0.0001	-0.0001	-0.0001	1	0.52	0.54	0.56	0.51
Linear	-0.28	-0.75	-0.24	0.52	1	0.97	0.98	0.96
SVR	-0.22	-0.72	-0.25	0.54	0.97	1	0.96	0.97
Random Forest	-0.29	-0.73	-0.26	0.56	0.98	0.96	1	0.95
XGBoost	-0.15	-0.78	-0.18	0.51	0.96	0.97	0.95	1

Figure 121. Correlation matrix plot of the full operational matrix and the predicted water production from each of the four predictive models: linear regression, SVM, RF, and XGBoost. The numbers in each grid cell are the Pearson correlation coefficients, which are plotted using a color ramp from −1.00 (perfect negative correlation – red) to +1.00 (perfect positive correlation – green).

- **Soak time** (middle SVM panel): Like injection time, soak time is inversely related to water production and more strongly interacts with injection rate, with the greatest water production occurring at the lowest injection rate and shortest soak time (lower left-hand corner) and the lowest water production occurring at the highest injection rate and longest soak time (upper right-hand corner).

- **Production time** (bottom SVM panel): Production time and injection rate also interact, and the relationship between water production and injection rate/production time is the opposite trend from injection and soak time, with the greatest water production occurring at the lowest injection rate and longest production time (lower right-hand corner) and the lowest water production occurring at the highest injection rate and shortest production time (upper left-hand corner).

Based on these relationships, the optimal operating regions for ***minimizing water production***, regardless of oil and gas production, are higher injection rate, longer injection time and soak time, and shorter production time.

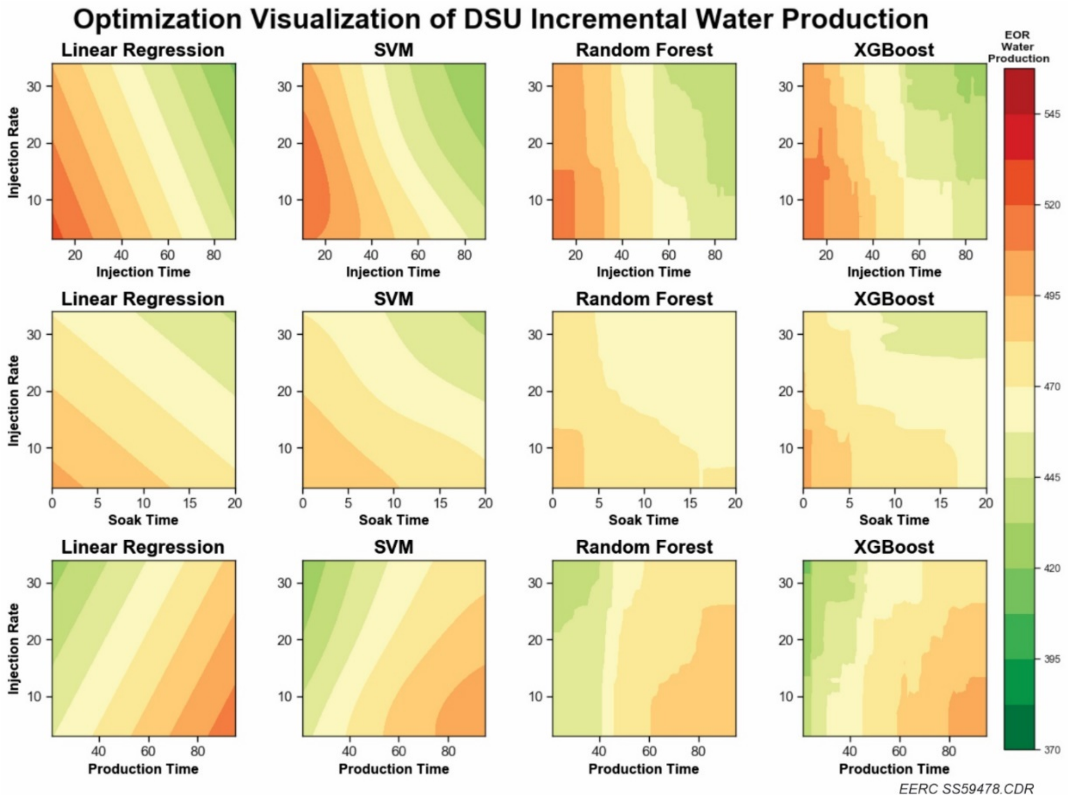

Figure 122. Contour plots of predicted DSU incremental water production for each of the four ML algorithms and three combinations of input parameters: injection rate (MMscfd) vs. injection time (days) (top row), injection rate vs. soak time (days) (middle row), and injection rate vs. production time (days) (bottom row).

DSU Incremental Gas Production

As described in the introduction, the overall goal of the project is to determine the feasibility of reinjecting captured rich gas (produced gas) into a Bakken reservoir for EOR. As shown in the preceding section, regardless of injection, soak, or production time, higher injection rates correspond to higher oil production. However, higher injection rates are also associated with higher produced gas. The total gas injected comprises both purchased gas (new gas brought to the oil field) and recycled gas (produced gas that is collected on-site from production wells, separated, processed, and reinjected into the reservoir) (Equation 8):

$$\text{Total Gas Injection (MMscf)} = \text{Purchased Gas (MMscf)} + \text{Recycled Gas (MMscf)} \quad \text{[Eq. 8]}$$

More detailed simulations and analysis on the behavior of recycled and purchased gas will be presented in Subactivity 8.2 – *Real-Time Forecasting, Visualization, and Control*. This report focuses on DSU incremental gas production (produced or recycled gas).

Figure 123 shows the correlation matrix between the four operational variables and the four predictive models for gas production, which provides insights into which variables drive the predictions in each model. The correlation matrix shows that injection rate is the dominant predictive variable, with Pearson correlation coefficients ranging from +0.86 to +0.93. The linear regression, SVM, and RF models have similar correlation coefficients for the remaining operational variables; however, the XGBoost model uses smaller weights for injection time and soak time.

Figure 124 shows the gas production contour plots for each of the four predictive models and three combinations of input parameters: injection rate vs. injection time (top row), injection rate vs. soak time (middle row), and injection rate vs. production time (bottom row). The four predictive models show similar contour trends; however, the linear regression and SVM models show smooth trends while the RF and XGBoost models show more granular predictions across the full operational matrix. The following interpretations are based on the SVM contour plot (second column in Figure 124):

- **Injection rate:** Higher injection rates correspond to higher gas production in all contour plots, as the recycled gas production color ramp trends from red (minimum) to green (maximum) going vertically along the *y*-axis from low to high injection rate. However, the curvature of the recycled gas production contour lines shows interactions between injection rate and the other operational parameters.

- **Injection time (top SVM panel):** At higher injection rates above 20 MMscfd, higher gas production occurs at injection times of approximately 40–80 days. However, at lower injection rates less than 10 MMscfd, gas production decreases with longer injection time, with the minimum gas production near 60 days (red region of the bottom right-hand portion of the panel).

- **Soak time (middle SVM panel):** At higher injection rates above 20 MMscfd, there is a negative relationship between soak time and gas production, with the greatest gas production occurring at the higher injection rate and shortest soak time (upper left-hand corner of the panel). However, at lower injection rates less than 10 MMscfd, this negative relationship declines, and gas production is predominantly driven by injection rate, independent of soak time.

- **Production time (bottom SVM panel):** The patterns between gas production and production time are like those for gas production and soak time. At higher injection rates above 20 MMscfd, there is a negative relationship between production time and gas production, with the greatest gas production occurring at the higher injection rate and shortest production time (upper left-hand corner of the panel). However, at lower injection rates less than 10 MMscfd, gas production is predominantly driven by injection rate, independent of production time.

Based on these relationships, the optimal operating regions for ***maximizing gas production***, regardless of oil and water production, were higher injection rate, longer injection time, shorter soak time, and shorter production time. However, maximizing gas production may not always be an operational goal.

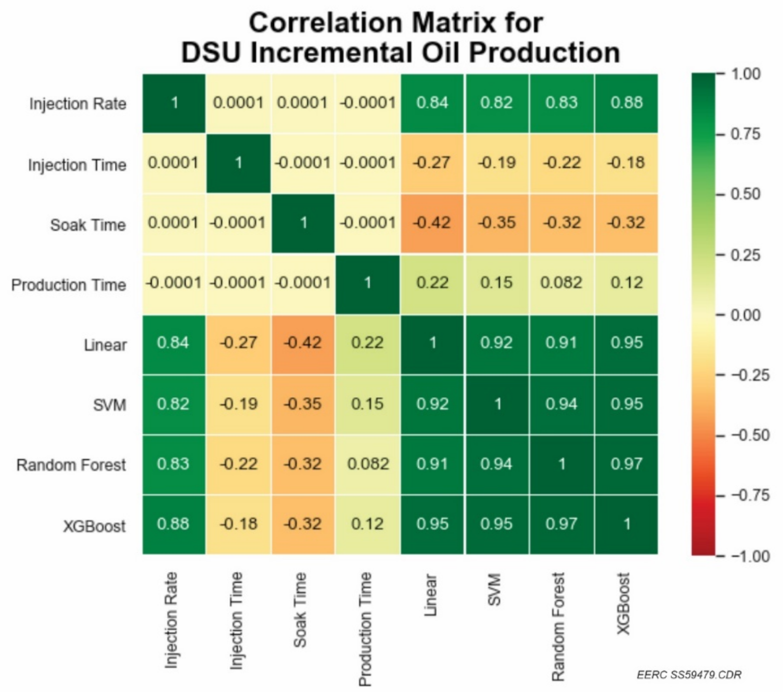

Figure 123. Correlation matrix plot of the full operational matrix and the predicted gas production from each of the four predictive models: linear regression, SVM, RF, and XGBoost. The numbers in each grid cell are the Pearson correlation coefficients, which are plotted using a color ramp from −1.00 (perfect negative correlation – red) to +1.00 (perfect positive correlation – green).

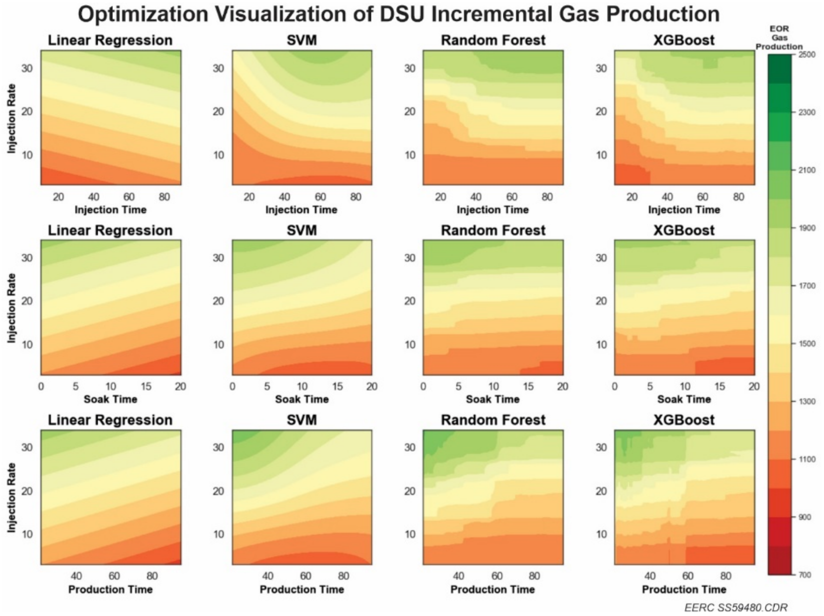

Figure 124. Contour plots of predicted DSU incremental gas production for each of the four ML algorithms three combinations of input parameters: injection rate (MMscfd) vs. injection time (days) (top row), injection rate vs. soak time (days) (middle row), and injection rate vs. production time (days) (bottom row).

DSU Incremental Net Revenue

For the optimization visualizations, the net revenue calculations evaluated several cases that weighted the relative value of oil and water production differently, which expands upon the two cases used for the regression models. A base case of \$60/stb oil and \$4/bbl water was explored along with five additional cases: (Case 1) \$40/stb oil and \$4/bbl water, (Case 2) \$40/stb oil and \$2/bbl water, (Case 3) \$50/stb oil and \$4/bbl water, (Case 4) \$50/stb oil and \$2/bbl water, and (Case 5) \$60/stb oil and \$2/bbl water.

Figure 125 shows each of the additional net revenue cases (*y*-axis) compared to the base case net revenue outcome (*x*-axis). As shown in the figure, net revenue is mainly driven by oil production and less influenced by water production because the monetary reward (revenue) is much larger for oil production than the penalty for water production (cost). For example, Case 5 has the greatest net revenue because it has both the highest oil price (\$60/stb oil) and lowest water cost (\$2/bbl water). The next highest case is the base case, which has the highest oil price (\$60/stb oil) but highest water cost (\$4/bbl water). The other cases with lower oil prices have significantly lower net revenue, regardless of the water cost. Consequently, contour plots for net revenue closely track oil production.

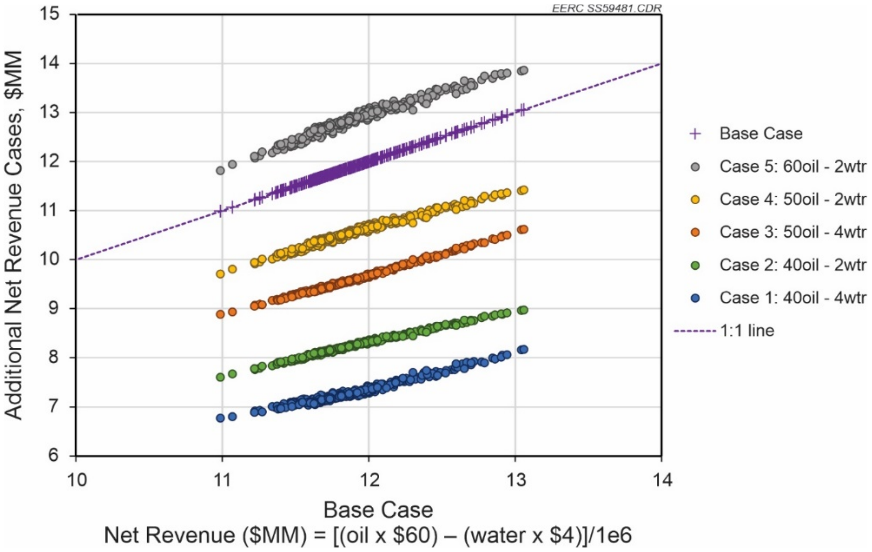

Figure 125. Comparison of five cases for calculating net revenue (*y*-axis, \$MM) against the base case of \$60/stb oil and \$/bbl water (*x*-axis, \$MM). See legend for case definitions.

Figure 126 shows the net revenue contour plots for each of the four predictive models and three combinations of input parameters: injection rate vs. injection time (top row), injection rate vs. soak time (middle row), and injection rate vs. production time (bottom row). Like the preceding plots for oil, water, and gas production, the four predictive models for net revenue show similar contour trends. The following interpretations are based on the SVM contour plot (second column in Figure 126):

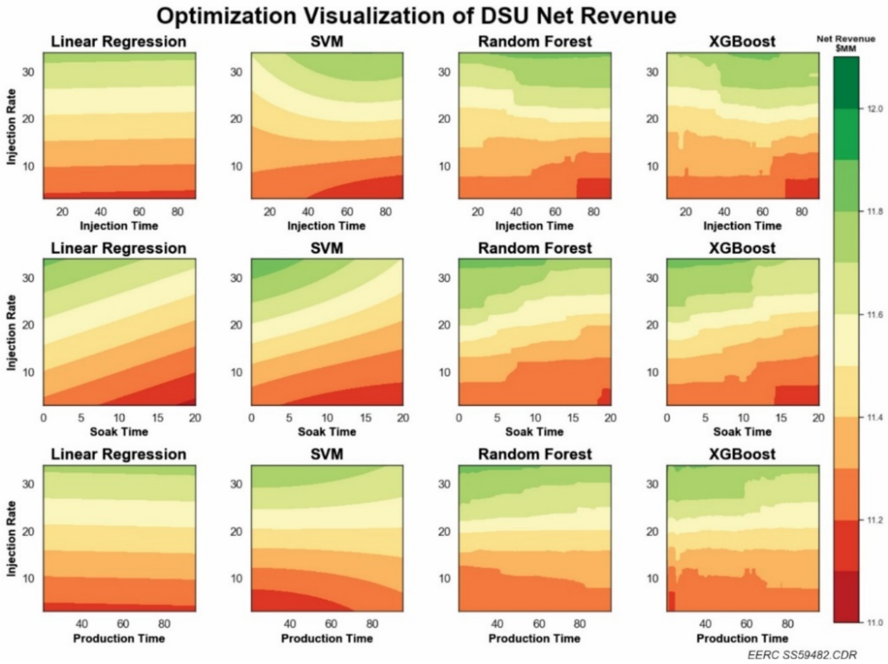

Figure 126. Contour plots of predicted DSU net revenue (base case: $60/stb oil and $4/bbl water) for each of the four ML algorithms and three combinations of input parameters: injection rate (MMscfd) vs. injection time (days) (top row), injection rate vs. soak time (days) (middle row), and injection rate vs. production time (days) (bottom row).

- **Injection rate:** Regardless of injection, soak, or production time, higher injection rates correspond to higher net revenue, as the net revenue color ramp trends from red (minimum) to green (maximum) going vertically along the *y*-axis from low to high injection rate. However, the curvature of the net revenue contour lines shows interactions between injection rate and the other operational parameters.

- **Injection time (top SVM panel):** At higher injection rates above 20 MMscfd, net revenue is best when injection time is between approximately 40 and 80 days, with maxima near 70 days. However, lower injection rates less than 20 MMscfd perform worse when injection time increases, with the lowest oil production associated with the longest injection time (red region of the lower right-hand corner of the panel).

- **Soak time (middle SVM panel):** Net revenue shows a nearly linear relationship between the combination of soak time and injection rate, with the greatest net revenue occurring at the highest injection rate and shortest soak time (upper left-hand corner of the panel) and the lowest net revenue occurring at the lowest injection rate and longest soak time (lower right-hand corner of the panel).

- **Production time (bottom SVM panel):** At injection rates between 15 and 25 MMscfd, net revenue is nearly invariant to production time, with shallow slopes to the contour lines (nearly horizontal). However, higher injection rates greater than 25 MMscfd show greater net revenue at lower injection times, and conversely, at lower injection rates less than 15 MMscfd, longer injection times are associated with greater net revenue.

The optimal operation regions for ***maximizing net revenue*** essentially mirrors oil production, since the higher oil price estimates ($40 to $60/stb oil) relative to the cost of produced water transport and disposal ($2 to $4/bbl water) means that oil production largely drives the net revenue result.

Sobol Sensitivity Indices

Figure 127 shows the total-effect, first-order, and second-order Sobol sensitivity indices for predicting oil production using the SVM algorithm. The *y*-axes show the fractional contribution of each operational variable to the output variance. For the Set 2 simulations and SVM predictive model, the total-effect indices are essentially equivalent to the first-order indices, as the second-order indices, other than perhaps (injection rate × injection time) and (injection rate × production time), do not significantly contribute to the oil production variance (less than 2% of the total variance). Like the preceding variable importance plots and correlation matrices, injection rate is the most important variable for predicting oil production. For example, 75% of the first-order indices are attributable to injection rate, and the next highest first-order index is soak time (10%). The first-order indices for injection and production time are both less than 5%.

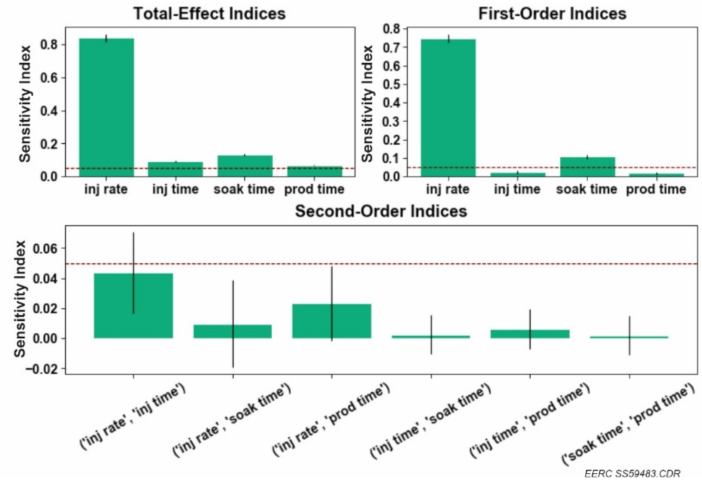

Figure 127. Sobol sensitivity indices for the SVM model for predicting DSU incremental oil production. The horizontal line represents sensitivity index = 0.05, which is a conventional threshold to determine the importance of a parameter.

ML Summary

The Set 2 ML models showed the following:

- All of the models performed well in predicting oil production. However, linear regression was the weakest among the four models, with both the lowest r^2 and highest RMSE. While XGBoost had the best performance for the training data set, the model performance decreased for the test data set, which suggests mild overfitting of the XGBoost algorithm.

The RF algorithm provided more consistent predictions in both training and test data sets; however, there was also evidence of slight overfitting. SVM was the overall best-performing algorithm for both the training and test sets. Similar results were achieved for the other target variables of water production, gas production, and net revenue.

- The variable importance plots, correlation matrices, and Sobol sensitivity indices showed similar results and clearly showed that injection rate is the most important operational variable for predicting oil production among injection rate, injection time, soak time, and production time. For example, 75% of the first-order indices were attributable to injection rate, and the next highest first-order index was soak time (10%). The first-order indices for injection and production time were both less than 5%.

The optimal operating regions for various performance metrics are as follows:

- ***Maximizing oil production***, regardless of water and gas production: higher injection rate, moderate injection time, short soak time, and moderate production time.

- ***Minimizing water production***, regardless of oil and gas production: higher injection rate, longer injection time and soak time, and shorter production time.

- ***Maximizing gas production***, regardless of oil and water production: higher injection rate, longer injection time, shorter soak time, and shorter production time; however, maximizing gas production may not always be an operational goal.

- ***Maximizing net revenue:*** mirrors oil production, since the higher oil price estimates ($40 to $60/stb oil) relative to the cost of produced water transport and disposal ($2 to $4/bbl water) means that oil production largely drove the net revenue result.

The different contours for oil, water, and gas production illustrate that the optimal operating envelope for injection rate, injection time, soak time, and production time depend upon the site-specific objectives and constraints of the project. For example, if the rich gas supplies limit the maximum injection rate to <5 MMscfd and the infrastructure to recycle produced gas is limited, so, therefore, gas production must be minimized, then the optimal operating region is an injection time between 40 and 80 days, soak time between 5 and 20 days, and production time between 40 and 80 days (i.e., cycle times from 85 to 180 days). However, if the rich gas supply is abundant and on-site recycling facilities can accommodate large gas volumes, then the optimal operating region for maximizing oil production is an injection time between 40 and 80 days, soak time less than 7 days, and production time between 30 and 50 days (i.e., cycle times from 77 to 137 days). Therefore, the contour plots shown in Figures 119, 122, 124, and 126 provide response surfaces: estimates of how oil, water, and gas production will respond to the operating variables. However, the "optimal" configuration of operational variables is a multiobjective optimization problem specific to the site-specific project constraints.

Summary and Conclusions

The Subactivity 8.1 work demonstrated how to integrate physics-based reservoir simulations for an unconventional reservoir with statistics and ML to investigate sets of rich gas injection scenarios used to quantify the effect of DSU development and operational factors on DSU production of oil, gas, and water. The workflows developed for the Set 1 and Set 2 simulations and analyses provide a template for future virtual-learning work. The process relies on commercial modeling and simulation outputs combined with open-sourced ML techniques in R. The workflow may be expanded to include sets of DSUs (as opposed to a single DSU) and to include additional variables beyond those included in the current study.

Subactivity 8.2.1 – Real-Time Visualization, Forecasting, and Control

Introduction

To support DOE NETL's goal to enhance resource production in the Bakken, the EERC is currently conducting a project as part of the EERC–DOE Joint Cooperative Agreement Subtask 3.1 entitled "Bakken Rich Gas Enhanced Oil Recovery Project." The overall goal of the project is to determine the feasibility of reinjecting captured rich gas (produced gas) into a Bakken reservoir for EOR. The focus of this section is on one component of the broader EERC effort: Subactivity 8.2.1 – Real-Time Visualization, Forecasting, and Control.

The goal of Subactivity 8.2.1 is to explore real-time visualization, forecasting, and control methods (RTVFC) for improved reservoir surveillance during rich gas EOR. In this context, the definition of these terms are as follows:

- "Visualization" refers to time-series plots of reservoir surveillance data or analytics (reexpressions of the data that provide better insights than the raw measurement) that can inform the EOR site operator of downhole conditions (e.g., gas breakthrough from the injection well[s] to the offset production well[s]) that could affect the performance of the EOR project.

- "Forecasting" refers to predictive modeling for the purpose of rapidly generating a prediction about future performance that the EOR site operator can compare against the observed performance.

- "Control" methods refer to operational changes that the EOR site operator can enact (e.g., changing gas-injection rates) to affect the observed performance and potentially improve the EOR outcome.

The integration of these three pieces—visualizing reservoir surveillance data in real-time, rapidly forecasting reservoir performance, and deploying operational changes to affect EOR performance—constitute RTFVC.

Subactivity 8.2.1 started with a detailed review of reservoir surveillance data generated over the course of previous Bakken EOR pilot tests (small-scale gas-injection EOR projects) that used rich gas, carbon dioxide, surfactant, water, or combinations of these fluids. These historical operational data were used to screen candidate RTVFC methods, which were then applied to an extensive set of reservoir simulation outputs of a reference gas EOR project to evaluate gas breakthrough at offset production wells.

The remainder of this report summarizes the pilot test screening process, the reservoir simulation outputs for the reference rich gas EOR project, and the results of applying RTVFC methods to the simulated outputs.

Pilot Test Screening

The EERC project team compiled a database comprising publicly available Bakken EOR pilot test data (M12: "Pilot Test Database Complete" [3/31/2020]), which were used to screen candidate RTVFC methods. Table 24 summarizes each pilot test in that database showing the pilot test name, injectate (water, surfactant, CO_2, propane, or rich gas), state and county (if available), and operator/reporter.

Table 24. Summary of Bakken EOR Pilot Tests Used to Screen Candidate RTVFC Methods.[4]

Case No.	Injectate	Operational Method	Pilot Start Year	State/ County	Operator/ Reporter
1	Water	HnP	1994	ND/McKenzie	Meridian
2	Water	HnP	2012	ND/Mountrail	EOG
3	Water	Flooding	2014	MT/(county N/A)	Montana Tech
4	Surfactant	HnP	2015	ND/(county N/A)	Nalco Champion
5	CO_2	HnP	2008	ND/Mountrail	EOG
6	CO_2	HnP	2009	MT/(county N/A)	Continental
7	CO_2	Flooding/injectivity	2014	ND/Mountrail	Whiting
8	CO_2	Injectivity	2017	ND/Dunn	XTO
9	Propane	Flooding	2017	ND/Mountrail	Hess
10	Rich gas	Flooding	2014	ND/Mountrail	EOG
11	Rich gas	HnP	2018	ND/Williams	Liberty

---

[4] Notes: "HnP" refers to a cyclic EOR operational method comprising injection time (sometimes called the "huff period" or the days of gas injection), soak time (the days between the "huff period" and the "puff period"), production time (sometimes called the puff period or the days of gas production after the soaking time), and cycle time (sum of the injection time, soak time, and production time). "Flooding" refers to EOR water (or gas) flooding where water (or gas) is injected into the oil reservoir to increase output when extracting oil, especially in reservoirs where production rates have declined over time. "Injectivity" (water or gas) is defined as the rate of water (or gas) injection over the pressure differential between the injector and the producer (or the formation). The parameter is used to evaluate how easily a fluid can be injected through an injector and the ability of a formation to accept external fluid. An injectivity test can be performed before large-scale flooding operations to optimize the flooding design. Finally, "Flooding/ Injectivity" refers to an EOR that had both flooding and injectivity, as defined above.

While many different technologies have been developed and applied to monitor the EOR process in conventional reservoirs (Michael and others, 2010; Zhang and others, 2014; Alfi and others, 2015; Zaluski and others, 2016; Jervis and others, 2018; Mur and others, 2020; Jin and others, 2021), comparatively fewer technologies were used in the historical Bakken EOR pilot tests to monitor the injection and production behavior (Hoffman and Evans, 2016; Kazempour and others, 2018; Sorensen and others, 2018; Nagarajan and others, 2020; Pospisil and others, 2020). As shown in Table 25, most of the Bakken EOR pilot studies included monthly production and/or injection rate (oil, gas, and water volumes) and well logs, and a few had daily production/injection rates (five of 11 cases, 45%) and downhole pressure measurements (three of 11 cases, 27%). A handful of the historical pilot studies included gas composition monitoring (three of 11 cases, 27%) or tracer testing (two of 11 cases, 18%). Therefore, the screening of candidate RTVFC methods was constrained by data availability, so the pilot test screening evaluated the best methods given the available reservoir surveillance data.

Figure 128 shows that 64% (seven of 11) of the Bakken EOR pilot tests employed gas injection (propane, rich gas, or CO_2). Two successful cases (Case Nos. 8 and 9 in Tables 24 and 25) were reported using propane and CO_2 injection in the Bakken (Sorensen and others, 2018; Nagarajan and others, 2020). Although water could be injected into the reservoir through fractures, the EOR performance by water injection was not encouraging, likely because it is extremely difficult for water to penetrate the Bakken matrix and recover oil from the formation in a short timespan because of the tiny pore throats and the high IFT between oil and water, as reported in Activity 7. Since IFT between gas and oil reduces with pressure, gas more easily penetrates the oil-bearing Bakken matrix and extracts oil out of the rock under high-pressure reservoir conditions when given enough contact time (weeks to months). Therefore, these physical constraints suggest that it is advisable to use gas as an injectate instead of water, assuming no surfactant is added to the injection water. However, if properly executed, then a surfactant can reduce the IFT between oil and water and increase oil production by potentially changing the wettability of rock from oil-wet to water-wet. For example, Kazempour and others (2018) reported on a pilot test where high-pressure surfactant injection effectively boosted the oil production (Case No. 4 in Tables 24 and 25). However, the relatively high cost and the high-salinity and high-temperature reservoir environment in the Bakken create challenges for broadly applying surfactant EOR with currently available technologies.

Although a few encouraging EOR cases using a gas injectate (hereafter, "gas EOR") were reported, most of the Bakken pilot tests did not show a clear incremental oil response to these EOR processes. Premature gas breakthrough and poor conformance control have been identified as two of the most critical factors for these underperforming gas EOR tests (Hoffman and Evans, 2016; Sorensen and Hamling, 2016; Pospisil and others, 2020). This lack of performance is attributed to the fact that gas EOR relies on gas–oil interactions in the reservoir where high pressure is required to make the interactions happen at a reasonable rate. An uncontrolled gas crossflow between the injector and offset wells interferes with the rate and extent of the pressure buildup and leads to an unsuccessful EOR test. Therefore, effective detection of gas breakthrough to the offset wells becomes important for gas EOR monitoring.

Table 25. Summary of Available Data for the Previous Bakken EOR Pilot Tests

Case No.	Injectate	Routine Data	Monitoring Methods/Data Reported	Data Source
1	Water	MPIR,* well logs		NDIC
2	Water	MPIR, well logs		NDIC
3	Water	MPIR	Daily injection rate	NDIC, Hoffman and Evans (2016)
4	Surfactant	MPIR		Kazempour and others (2018)
5	CO_2	MPIR, well logs		NDIC
6	CO_2	MPIR		Hoffman and Evans (2016)
7	CO_2	MPIR, well logs	Daily injection rate, surface injection pressure, gas composition	NDIC
8	CO_2	MPIR, well logs	Daily injection rate, bottomhole injection pressure, oil composition	NDIC, Sorensen and others (2018)
9	Propane	MPIR, well logs	Daily production/injection rates, bottomhole injection pressure, gas composition, tracer testing	NDIC, Nagarajan and others (2020)
10	Rich gas	MPIR, well logs		NDIC
11	Rich gas	MPIR, well logs	Daily production/injection rates, bottomhole injection pressure, gas composition, tracer testing	NDIC, Pospisil and others (2020)

* MP(I)R – monthly production (and injection) rates.

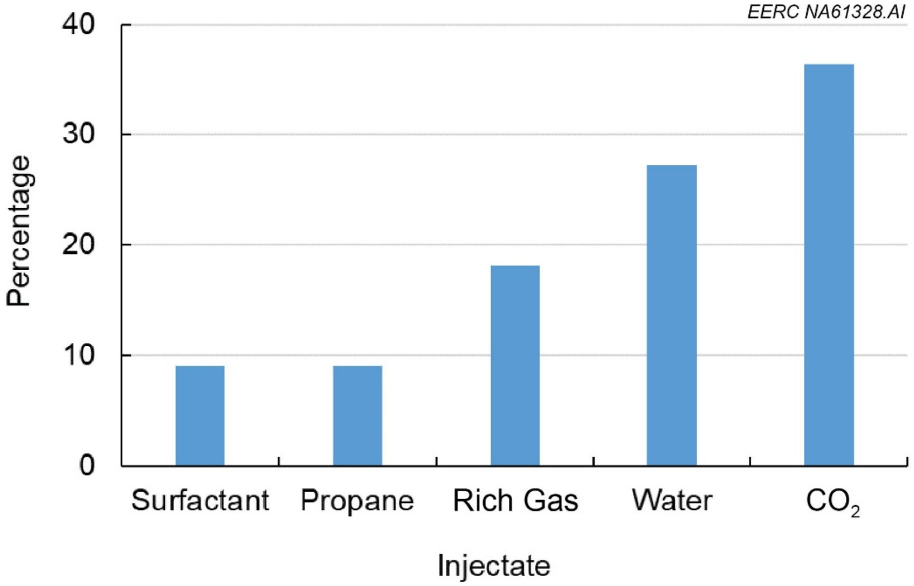

Figure 128. Percentage of Bakken EOR pilot tests by EOR injectate types (total of 11 EOR pilot tests—see Table 24).

A variety of monitoring technologies have been used to detect fluid breakthrough behavior in conventional reservoirs when water-flooding or gas-flooding operations are implemented (Michael and others, 2010; Zhang and others, 2014; Alfi and others, 2015; Jervis and others, 2018; Zaluski and others, 2016). For example, pulsed-neutron logs and seismic surveys are frequently used to detect whether gas has entered a producer well or passed a certain location in a CO_2 flooding process (Zaluski and others, 2016; Jin and others, 2021). However, such methods usually require days to weeks to interpret the measured data; i.e., these methods do not produce "near-real-time" data/information. In addition, EOR implemented in conventional reservoirs typically utilize vertical wells arranged in flood patterns, as opposed to unconventional Bakken reservoir development, which utilizes long horizontal wells (laterals) with 10,000 feet or more of completed lateral. Using conventional production logs is challenging to evaluate the flow behavior in long horizontal wells with several to tens of fracture stages (Hoffman and Evans, 2016). The complex completion methods for unconventional reservoirs, like the Bakken, combined with reservoir heterogeneity make regular production data (oil/gas/water rates) too noisy to accurately detect gas breakthrough.

Figure 129 illustrates the distribution of the gas injector and its offset producers in the propane EOR pilot test (Case No. 9, Table 24) conducted in the Bakken in 2017. A vertical well "C3_Inj" was used to inject propane, and oil/gas/water production rates were monitored at the offset producer wells, M1–M6, which were connected to horizontal laterals of different lengths. Well M1 was the closest producer to the propane injector (0.3 miles [1584 ft]). A total of 19.88 MMscf propane was intermittently injected into the C3_Inj from May 2017 to August 2018. The injection rate varied from month to month, as shown in Figure 130.

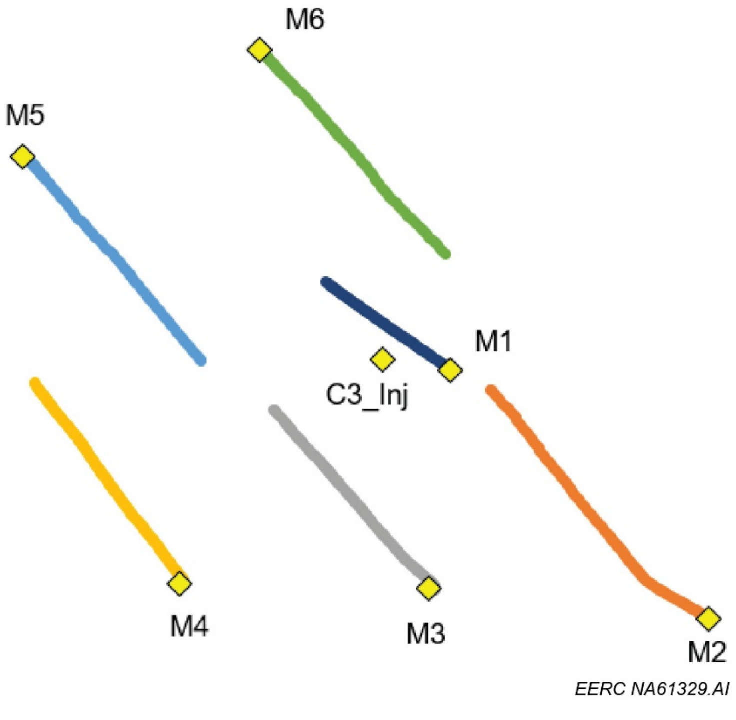

Figure 129. Schematic of the gas injector (C3_Inj) and offset producer wells (M1–M6) and horizontal laterals in the Hess propane EOR pilot test (Case No. 9).

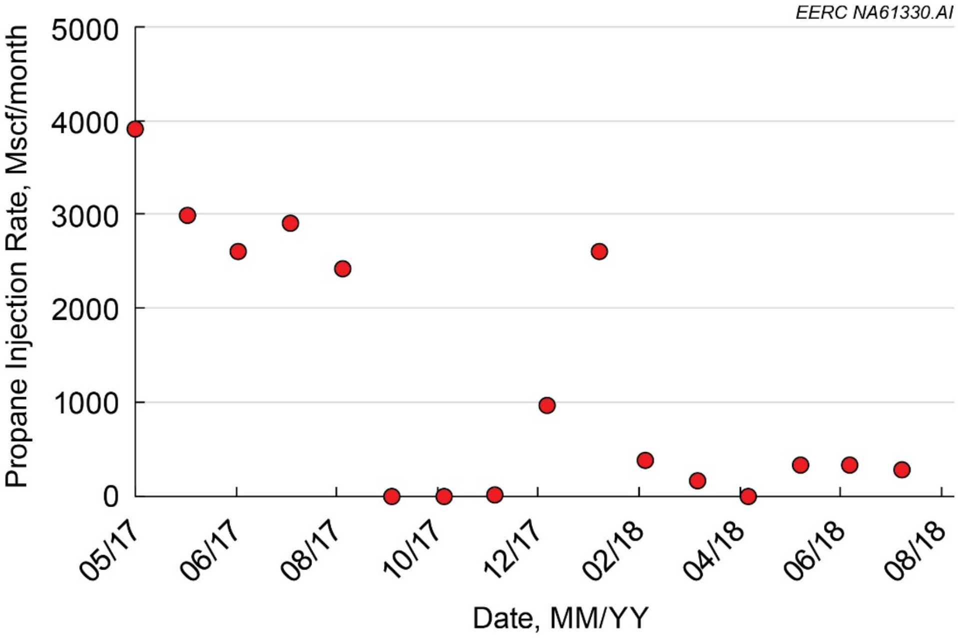

Figure 130. Monthly gas injection rate in the Hess propane EOR pilot test (Case No. 9).

Figure 131 shows the available daily fluid production rates (gas, oil, and water) for M1 and the propane injection rate in C3-Inj for the Hess propane EOR pilot test (Case No. 9). As shown in the figure, the fluid production rates do not provide sufficient information to determine if and/or when the injected propane breakthrough occurred in the offset production well, M1. In contrast, compositional measurements of gas stream produced from M1 provided robust signals for gas breakthrough diagnosis. The propane concentration (in mole percentage) in the produced gas stream from a normal Bakken producer is usually below 20 mol% based on many PVT reports collected from the Bakken. This concentration can be relatively stable for a long time during the normal production process. Accordingly, a propane concentration in the produced gas stream of an offset well that is significantly higher than 20 mol% could be a clear signal of propane breakthrough. Figure 132 demonstrates how the propane concentration changed in the produced gas stream of M1 during the monitoring period. The data showed that the propane concentration exceeded 93 mol% on October 10, 2017, which clearly indicated that the injected propane had breakthrough to the M1 as most of the produced gas was propane. Since 19.88 MMscf propane was injected into the formation near M1, the propane production from this well could last for months after injection operations cease. Therefore, propane concentration was selected as one of the monitoring parameters for gas breakthrough detection in this study.

As noted above, the screening of candidate RTVFC methods was constrained by the availability of reservoir surveillance data of the pilot tests. Therefore, the historical data sets of the Bakken EOR pilot tests were supplemented with an extensive set of reservoir simulations to permit the evaluation of gas breakthrough at offset production wells, as described in the next section.

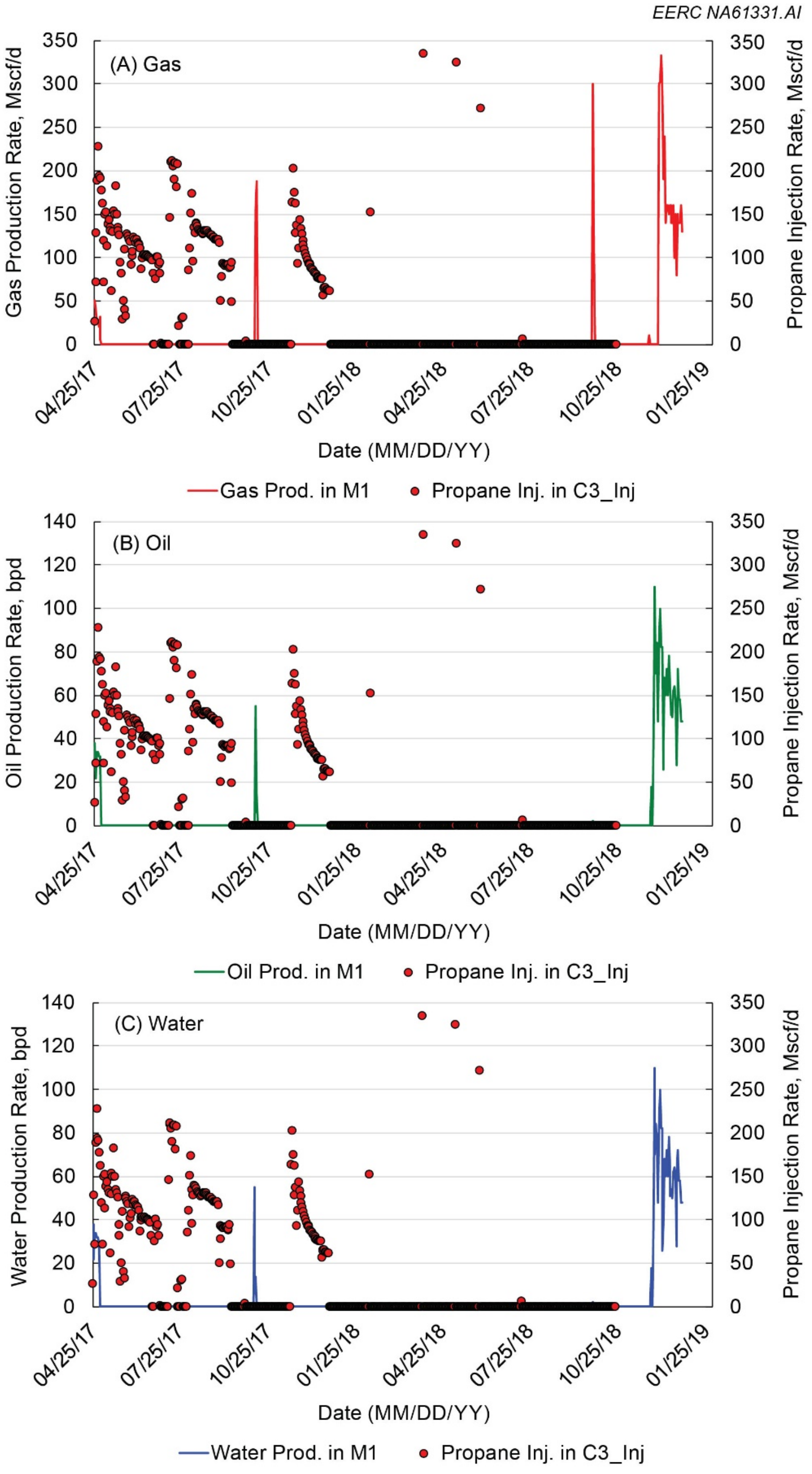

Figure 131. The daily fluid production rate and propane injection rate in M1 and C3_Inj, respectively, for the Hess propane EOR pilot test (Case No. 9): A, gas; B, oil; and C, water.

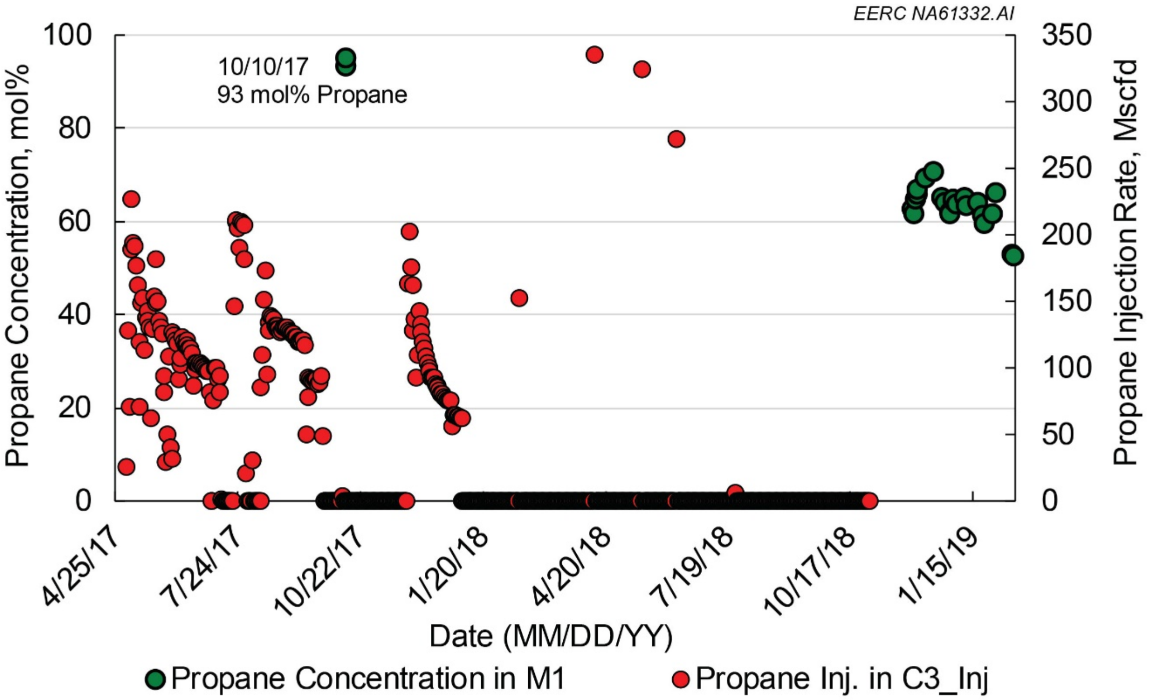

Figure 132. Monitoring of propane concentration in the gas stream produced from M1 (mole %, left *y*-axis) and the propane injection rate in C3_Inj (right *y*-axis) for the Hess propane EOR pilot test (Case No. 9).

Geologic Model and Reservoir Simulation

Geologic Model of the 7-Well DSU

The geologic model (geomodel) and reservoir simulation approaches used for Subactivity 8.2 were previously described under Activity 7. The single DSU model for the Dunn site was adopted for the RTVFC study in Subactivity 8.2. The detailed geologic properties of the model can be found in Subactivity 7.1.

The geomodel included seven wells (three wells completed in the MB Formation (MB1, MB2, and MB3) and four wells completed in the TF Formation (TF1, TF2, TF3, and TF4) arranged in a "wine rack" geometric configuration (Figure 133). The geomodel was used to simulate gas injection at MB2 (outlined in red in Figure 133) and the resultant responses in the Offset Wells MB1, MB3, and TF1–TF4 (outlined in green in Figure 133).

The reservoir simulations (utilizing the model described on page 86, "Reservoir Simulation Model for the Single DSU Site") evaluated scenarios with all wells open (i.e., Offset Wells MB1, MB3, TF1, TF2, TF3, and TF4 open) and scenarios with the exterior offset wells closed (i.e., Offset Wells MB1, MB3, TF1, and TF4 shut-in and Offset Wells TF2 and TF3 open [producing]), as denoted by the dashed and solid outlines in Figure 133. The yellow arrows in Figure 133 illustrate potential gas breakthrough from the injection well (MB2) to the offset production wells.

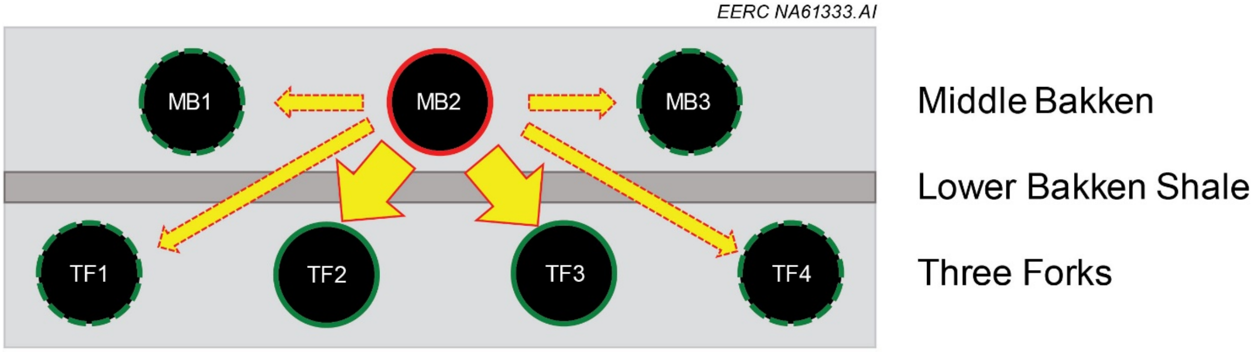

Figure 133. Illustration of the 7-well DSU model identifying the MB and TF wellbores and the wells that were used for rich gas injection (MB2 – red outline) or production (MB1, MB3, TF1 to TF4, green outline), as described in the text. Dashed outlines refer to the "Open" scenarios that included Wells TF2 and TF3 as well as MB1, MB2, TF1, and TF4, while solid outlines refer to the "Closed" scenarios that shut in the four dash-outlined wells.

Reservoir Simulation

A high-efficient fracture simulation method—EDFM—was used to set up complex fractures in the simulation model. Hydraulic fractures were distributed along the wellbore based on the fracturing data. Some of the fractures were connected in the model based on the history match of the production data collected for each well. The well interference effects were captured after carefully tuning the reservoir and fracture properties. The detailed reservoir and fracture calibration process can also be found in Subactivity 7.1 of the main report. The EDFM-integrated simulation model can mimic the crossflow between wells when gas injection is used for EOR.

One of the objectives for Subactivity 8.2 is to rapidly detect gas breakthrough during the gas EOR process. As summarized in the preceding section, the results of the pilot test screening showed that propane concentration (i.e., gas composition) can be used to detect gas breakthrough behavior more effectively than fluid production rates (oil, gas, or water). Based on the same logic, if another pure gas like methane or ethane is injected for EOR operations, then its concentration could also be used for gas breakthrough detection. Therefore, the gas components were set up individually in the EOS so that pure-component gas injection scenarios could be simulated for methane (C1), ethane (C2), and propane (C3).

Produced gas from the Bakken is usually relatively enriched in ethane and propane (i.e., ethane and propane constitute 30–40 mol% of the produced gas). As shown in Table 24, the produced (or rich) gas has also been used as an injectate for EOR operations. Although methane in the rich gas leads to a higher MMP, therefore requiring higher injection pressure for gas EOR purposes, reinjecting the produced gas without separation of the methane component reduces the EOR operational costs. However, if the composition of injection gas is like that of the produced gas from an offset well, then it may no longer be possible to detect the gas breakthrough by monitoring the concentration change of an individual gas component. In other words, the produced gas from gas breakthrough would be chemically indistinguishable from the produced gas without gas breakthrough.

Tracer testing has been used in the oil and gas industry for many years with a range of applications, including evaluation of reservoir heterogeneity, determination of connectivity between wells/fractures, identification of thief zones (as well as flow barriers) in a reservoir, and estimation of sweep efficiency (Kumar and Sharma, 2018; Tayyib and others, 2019; Al-Qasim and others, 2019, 2020). The fast evolution of tracer technologies has made tracer testing an important monitoring and surveillance method for field practices, including various EOR operations (Sharma and others, 2014; Sanni and others, 2017). A variety of tracers have been developed in the past decades, and different tracers can be used to rapidly identify and characterize the movement of gas, oil, or water, depending on the project requirements (Huseby and others, 2010; Yuncong and others, 2014; Sanni and others, 2017; Al Abbad and others, 2019; Nagarajan and others, 2020; Chen and others, 2021).

In unconventional reservoirs, a short tracer breakthrough time observed in an offset well may indicate that the well is connected to the injector through fractures. For example, the tracer tests in the Liberty rich gas pilot test (Case No. 11) showed that the wells were highly interconnected through fractures in the reservoir (Pospisil and others, 2020). Therefore, tracer tests were included in the reservoir simulations for rich gas EOR to evaluate how the addition of a tracer gas would improve RTVFC as compared to rich gas or single-component gas injection without a tracer. Based on the rich gas composition (60 mol% of methane, 25 mol% of ethane, and 15 mol% of propane) simulated in this study, three tracers were attached to three individual gas components, as shown in Table 26: Tracers TRC-C1, TRC-C2, and TRC-C3 were attached to methane, ethane, and propane, respectively. Both pure propane and rich gas (with tracers) EOR scenarios were simulated using CMG's GEM V2020.

Table 26. Composition of the EOS for Gas Breakthrough and EOR Simulations[5]

No.	Component	Tracer Attached	No.	Component	Tracer Attached
1	N_2	N/A	5	IC_4 to NC_4	N/A
2	CH_4	TRC-C1	6	IC_5 to C_{12}	N/A
3	C_2H_6	TRC-C2	7	C_{13} to C_{19}	N/A
4	C_3H_8	TRC-C3	8	C_{20} to C_{30}	N/A

Subactivity 8.2 included two sets of reservoir simulation cases for the seven-well DSU: 1) propane (C3) injection and 2) rich gas injection with a tracer (hereafter "tracer injection"). These sets were used to evaluate gas breakthrough from the gas injection well (MB2) to the offset production wells (MB1, MB3, and TF1-4) under different operating conditions, as described below.

Propane Injection

Table 27 shows the simulation case matrix for the propane injection scenarios, which injected at well MB2 and utilized varying injection rates from 0.5 to 18 million standard cubic feet

---

[5] "IC" refers to isoalkanes with C equal to the carbon-number. "NC" refers to normal alkanes. "C" with no "I" or "N" prefix refers to either iso- or normal alkanes within the specific carbon-number range.

Table 27. Propane Injection Reservoir Simulation Case Matrix for the 28 Simulations. The 28 runs were executed with Offset Wells MB1, MB3, TF1, and TF4 closed (shut-in) and again with the wells open (producing), for a total of 56 simulations.

Simulation Case Number	Inj. Rate (MMscfd)	Max Inj. BHP (psi)
1	0.5	1500
2	0.5	3000
3	0.5	5500
4	0.5	7500
5	1.5	1500
6	1.5	3000
7	1.5	5500
8	1.5	7500
9	3	1500
10	3	3000
11	3	5500
12	3	7500
13	6	1500
14	6	3000
15	6	5500
16	6	7500
17	8	1500
18	8	3000
19	8	5500
20	8	7500
21	10	1500
22	10	3000
23	10	5500
24	10	7500
25	18	1500
26	18	3000
27	18	5500
28	18	7500

per day (MMscfd) and varying maximum injection BHP from 1500 to 7500 psi across 28 runs. The rate and pressure settings were designed to cover representative operational ranges for the unconventional Bakken reservoir. The 28 runs were executed with Offset Wells MB1, MB3, TF1, and TF4 closed (shut-in) during the injection and soaking stages and again with the wells open (producing), for a total of 56 runs for the propane injection. The minimum production BHP (100 psi), injection time (30 days), soaking time (7 days), and production time (60 days) (cycle time of 97 days) were held constant across all 56 runs. The injection–soaking–production cycles through 2 years of prediction can be found in Table 28.

Table 28. Injection–Soaking–Production Cycles in the HnP Process

Date (MM/DD/YY)	Cycle							
	1	2	3	4	5	6	7	8
Injection Start	01/01/20	04/07/20	07/13/20	10/18/20	01/23/21	04/30/21	08/05/21	11/10/21
Injection End	01/30/20	05/06/20	08/11/20	11/16/20	02/21/21	05/29/21	09/03/21	12/09/21
Soaking Start	01/31/20	05/07/20	08/12/20	11/17/20	02/22/21	05/30/21	09/04/21	12/10/21
Soaking End	02/06/20	05/13/20	08/18/20	11/23/20	02/28/21	06/05/21	09/10/21	12/16/21
Production Start	02/07/20	05/14/20	08/19/20	11/24/20	03/01/21	06/06/21	09/11/21	12/17/21
Production End	04/06/20	07/12/20	10/17/20	01/22/21	04/29/21	08/04/21	11/09/21	12/31/21

The wells were operated differently in the offset well open and closed scenarios. For cases with offset wells open, Wells MB1, MB3, TF1, TF2, TF3, and TF4 were open all the time (producing), and only Well MB2 changed its status with cycles, as shown in Table 29. For cases with offset wells closed, Wells TF1, MB1, MB3, and TF4 were closed all the time (shut-in), and other wells changed their status with HnP stages, as shown in Table 30.

Table 29. Change of Well Status for MB2 in Different HnP Stages When All of the Offset Wells MB1, MB3, TF1, TF2, TF3, and TF4 Were Kept Open (producing)

Stage	Cycle 1 As an Example	Well Status	
	Date (MM/DD/YY)	Open	Closed
Injection	01/01/20 to 01/30/20	MB2 (injecting)	
Soaking	01/31/20 to 02/06/20		MB2
Producing	02/07/20 to 04/06/20	MB2	

Table 30. Change of Well Status for MB2, TF2, and TF3 in Different HnP Stages When External Offset Wells MB1, MB2, TF1, TF2, TF3, and TF4 Were Closed (shut-in)

Stage	Cycle 1 As an Example	Well Status	
	Date (MM/DD/YY)	Open	Closed
Injection	01/01/20 to 01/30/20	MB2 (injecting)	TF2, TF3
Soaking	01/31/20 to 02/06/20		TF2, MB2, TF3
Producing	02/07/20 to 04/06/20	TF2, MB2, TF3	

Tracer Injection

The simulation case matrix for the tracer injection scenarios also injected at Well MB2 and utilized the same varying injection rates (0.5 to 18 MMscfd) and varying maximum injection BHP (1500 to 7500 psi) as the propane injection runs. Like the propane injection runs, the 28 tracer injection runs were executed with Offset Wells MB1, MB3, TF1, and TF4 closed (shut-in) in the injection and soaking stages and again with the wells open (producing), for a total of 56 runs. As with the propane injection run, for the tracer injection runs, the minimum production BHP (100 psi), injection time (30 days), soaking time (7 days), and production time (60 days) were held constant across all 56 runs.

The propane injection runs (28 closed + 28 open = 56 total) and tracer injection runs (28 closed + 28 open = 56 total) provided a total of 112 simulations for the RTVFC inputs.

Data Extraction and Preprocessing

Data Extraction

The reservoir simulation output data for each of the 112 cases were stored in .sr3 file format (i.e., 112 separate .sr3 files). Traditionally, the user opens each .sr3 file with CMG software, manually selects wells and parameters, and exports the data to an Excel (.xlxs) or text (.txt) file for subsequent visualization or data analysis in a third-party software. However, the traditional data extraction approach is inefficient and potentially error-prone when dealing with many cases, because 1) manually opening and exporting many .sr3 files is labor-intensive and 2) errors can be introduced during the manual data extraction process. To overcome these limitations, a semiautomated approach was developed for the data extraction that included the following steps:

1 Create a result file (i.e., .rwd file) that stores output parameters for each reservoir simulation .sr3 file. The .rwd files were created using customized Python code to reduce manual work and human error.

2 Extract the data from the .rwd files using CMG software. This process required opening the .rwd file in the "Result Report" tool in the CMG software and using a customized query to extract the data from the .rwd file to a .csv file.

3 Compile the exported .csv files into a structured tabular data set using a customized Python script.

The Step 1 and Step 3 steps were automated via Python scripts, and Step 2 required minimum human assistance. This data extraction workflow permits more expansive integration of physics-based reservoir simulation results with data visualization and machine learning and is a significant improvement over the traditional approach—i.e., faster and more accurate.

Data Preprocessing

The reservoir simulation data included both primary production and EOR. The data were filtered to the range of January 1, 2020 (injection start date for the first cycle), to December 31, 2021 (production end date for the last cycle, Cycle 8), to limit the visualizations to the 2-year EOR period. The primary production was subtracted from the EOR production to yield the incremental production attributable to EOR.

The output data from the reservoir simulations had irregular time steps to the scale of minutes because of different convergence criteria within the numerical simulator for each case. To simplify the visualization and forecasting, the data were aggregated to the scale of days by calculating the daily maximum value. A standardized daily database was created from January 1, 2020, to December 31, 2021, and the reservoir simulation daily data were mapped to this standard daily timeline. Days with no reservoir simulation output were treated as missing values.

After aggregating the 112 reservoir simulations and mapping these to a standardized daily timeline, a minimum treatment of the data was performed to remove outliers by visual inspection—plotting the time-series data and removing erroneously low or high values. The resultant aggregated and cleaned database provided the inputs to the real-time visualization.

Real-Time Visualization and Forecasting

As previously discussed, "visualization" in RTVFC refers to time-series plots of reservoir surveillance data or analytics (reexpressions of the data that provide better insights than the raw measurement) that can inform the EOR site operator of downhole conditions (e.g., gas breakthrough from the injection well[s] to the offset production well[s]) that could affect the performance of the EOR project. In this proof of concept, the real-time visualization allows the user to display the simulation results for selected EOR operating parameters and target variables. The visualization process is meant to emulate "real-time" data that are consistent with similar processes that the EERC has used on other gas injection projects. For example, a typical field project for rich gas EOR might include the following sequence of steps: 1) acquisition of injection rates, production rates, and well BHPs whenever new data are available, which provides the foundation of real-time visualization; 2) data preprocessing to deal with missing and outlier values; 3) compilation of the various data sets into a coherent structured data format based on well identifiers, operating scheme, and acquisition timestamp; 4) appending of new data to the existing data set; and 5) creating visualizations and/or updating visualizations based on the updated data set.

For the purposes of this proof-of-concept study, the process was started with the data already acquired, transferred, aggregated, and cleaned, and the full 2-year EOR outputs were used in the visualizations. However, the process may be adapted to "real-time" and can upload and plot the data at whatever acquisition frequency the field operator would like to implement (e.g., hourly, daily, weekly, etc.).

The EOR operating parameters for the reservoir simulations included external offset well status (MB1, MB3, TF1, and TF4 closed or open), injectate (rich gas or propane), injection rate (0.5, 1.5, 3.0, 6.0, 8.0, 10, or 18 MMscfd), and injection pressure (1500, 3000, 5500, or 7500 psi). The target variables for visualization included the following measurements at each of the seven wells (MB1, MB2 [injection well], MB3, TF1, TF2, TF3, and TF4): production (oil, gas, and water production rates and cumulative production), BHP, and tracer (rich gas or propane) production rate and cumulative production.

An online dashboard was created using R-shiny (Chang and others, 2021), where users can interactively customize the display. The website address of the dashboard is https://eerc-ai-team.shinyapps.io/EORWellPerformance/. The online dashboard was developed by creating 1) a server that provides the backbone of the visualizations and 2) a user interface (UI) where pages show different time-series visualizations of the well performance based on a set of user-defined selections.

Server Creation

Interactive Data Set

The aggregated and cleaned data set of the 112 reservoir simulations described in Section 4 was imported into the R-shiny server. To ensure responsive selection of wells and target variables, the data were arranged in "long" format, where the variables from the same group were arranged in the same column. For example, for the variable "well," data associated with the seven wells were arranged vertically instead of horizontally. The benefit of long-format data is that the data can be subset interactively. For example, the users can subset data by selecting Wells "MB2" out of the seven wells.

Interactive Visualization

The interactive function of the input data was accomplished by controllers in R-shiny, which allow the users to query and extract data from the server. Controllers were created via "CheckboxInput" and/or "RadioButtons" for discrete variables and "SliderInput" for continuous variables.

The time-series plots of the well performance variables were created using the R package, ggplot (R Core Team, 2021; Wickham, 2016). The "grid_wrap" function was used so that the data from different wells could be visualized vertically and interactively.

User Interface

The UI has four pages: 1) Welcome, 2) Tracer Injection, 3) Propane Injection, and 4) Prediction. Detailed descriptions of the four pages are provided below.

Welcome Page

The Welcome page provides a high-level introduction to the project and instructions about how to use the dashboard (Figure 134).

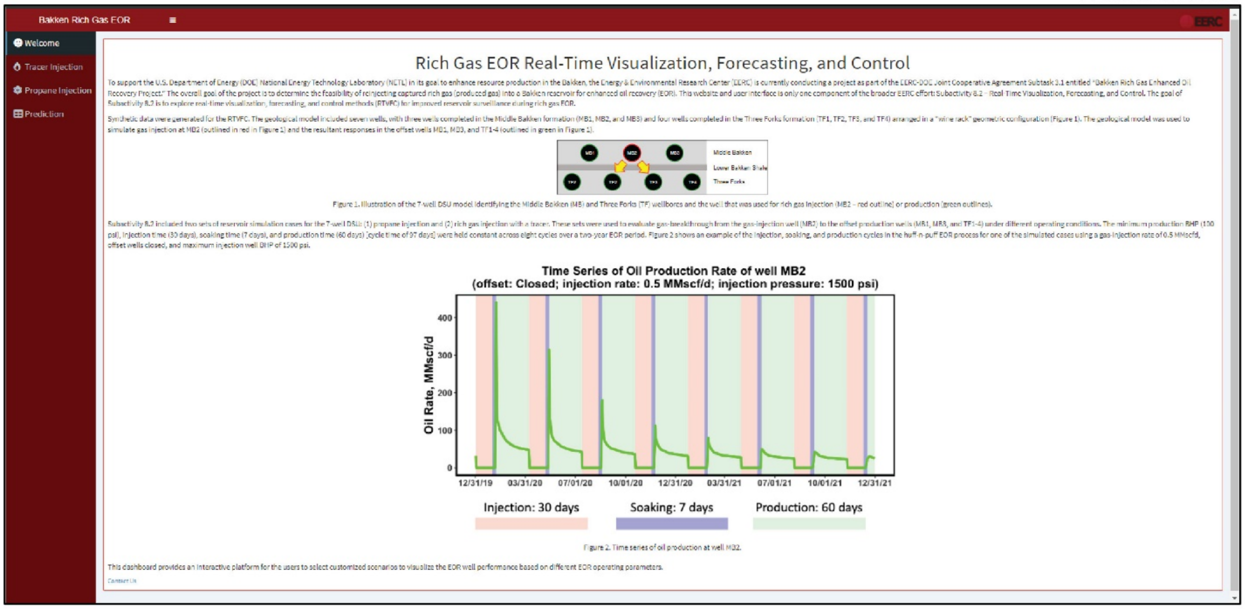

Rich Gas EOR Real-Time Visualization, Forecasting, and Control

To support the U.S. Department of Energy (DOE) National Energy Technology Laboratory (NETL) in its goal to enhance resource production in the Bakken, the Energy & Environmental Research Center (EERC) is currently conducting a project as part of the EERC-DOE Joint Cooperative Agreement Subtask 3.1 entitled "Bakken Rich Gas Enhanced Oil Recovery Project." The overall goal of the project is to determine the feasibility of reinjecting captured rich gas (produced gas) into a Bakken reservoir for enhanced oil recovery (EOR). This website and user interface is only one component of the broader EERC effort: Subactivity 8.2 – Real-Time Visualization, Forecasting, and Control. The goal of Subactivity 8.2 is to explore real-time visualization, forecasting, and control methods (RTVFC) for improved reservoir surveillance during rich gas EOR.

Synthetic data were generated for the RTVFC. The geological model included seven wells, with three wells completed in the Middle Bakken formation (MB1, MB2, and MB3) and four wells completed in the Three Forks formation (TF1, TF2, TF3, and TF4) arranged in a "wine rack" geometric configuration (Figure 1). The geological model was used to simulate gas injection at MB2 (outlined in red in Figure 1) and the resultant responses in the offset wells MB1, MB3, and TF1-4 (outlined in green in Figure 1).

Figure 1. Illustration of the 7-well DSU model identifying the Middle Bakken (MB) and Three Forks (TF) wellbores and the well that was used for rich gas injection (MB2 – red outline) or production (green outlines).

Subactivity 8.2 included two sets of reservoir simulation cases for the 7-well DSU: (1) propane injection and (2) rich gas injection with a tracer. These sets were used to evaluate gas-breakthrough from the gas-injection well (MB2) to the offset production wells (MB1, MB3, and TF1-4) under different operating conditions. The minimum production BHP (100 psi), injection time (30 days), soaking time (7 days), and production time (60 days) [cycle time of 97 days] were held constant across eight cycles over a two-year EOR period. Figure 2 shows an example of the injection, soaking, and production cycles in the huff-n-puff EOR process for one of the simulated cases using a gas-injection rate of 0.5 MMscfd, offset wells closed, and maximum injection well BHP of 1500 psi.

Figure 2. Time series of oil production at well MB2.

This dashboard provides an interactive platform for the users to select customized scenarios to visualize the EOR well performance based on different EOR operating parameters.

Figure 134. General layout of the UI showing the Welcome page.

Tracer Injection Page

The Tracer Injection page shows the results of the EOR well performance with rich gas injection with tracers. The four controllers on top of this page allow the users to customize visualizations of the simulation results for all combinations of the simulation case matrix. The four controllers are:

1. **Injection Rate:** The injection rate controller is a radio button controller where the users can select one of the seven values (0.5, 1.5, 3.0, 6.0, 8.0, 10, or 18 MMscfd). The default value is set at 0.5 MMscfd.

2. **Injection Well BHP:** The injection well BHP controller is a radio button controller where the users can select one value from the four pressure levels (1500, 3000, 5500, or 7500 psi). The default value is set at 1500 psi.

3. **Offset:** The offset controller is a checkbox controller where the user can select one or two of the values (open or closed), which selects whether the status of the external offset wells (MB1, MB3, TF1, and TF4) is either open or closed. The default value is set as closed. However, if the users uncheck both values, then the value will still be set as closed to avoid generating an empty data set.

4. **Select Wells:** The select wells controller is a checkbox controller where the user can select one or multiple wells. The default value is set as "MB2" (the injection well). However, if the user unchecks all wells, then the value will set as the default well of "MB2" to avoid generating an empty data set.

In the upper right-hand corner of the page is a button labeled “Submit.” After the user has made the controller selections, the user must click the Submit button for the visualization tool to launch a new set of plots.

Figure 135 shows the default rich gas (Tracer) page for a gas injection rate of 0.5 MMscfd, closed offset production wells, and 1500-psi injection well BHP.

EERC NA61335.AI

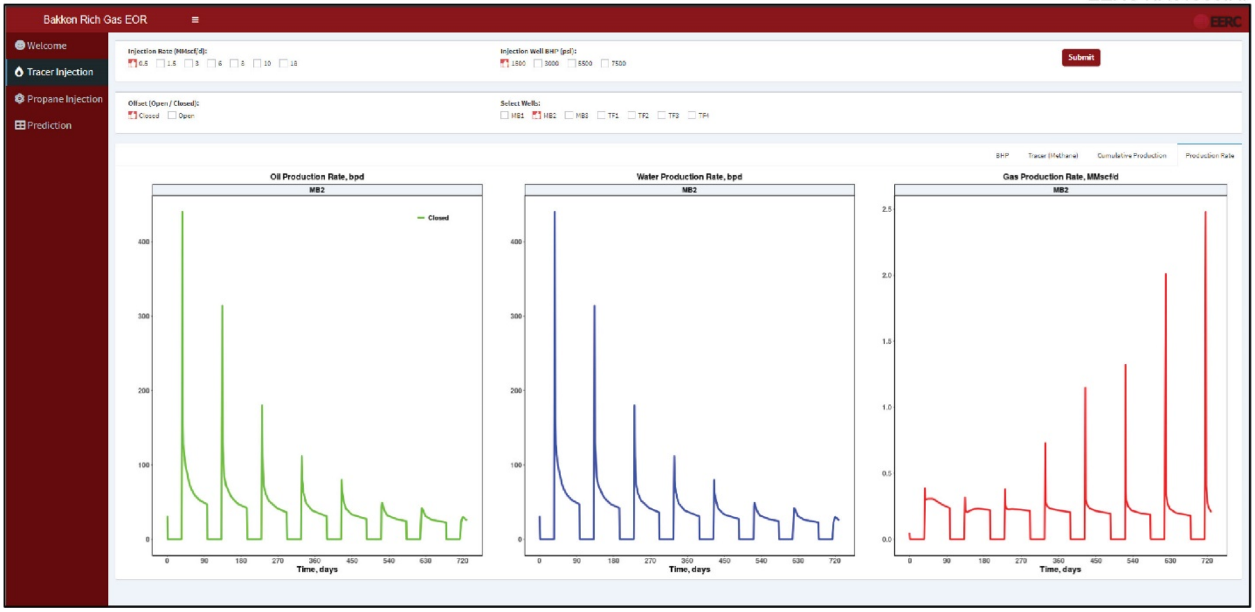

Injection Rate (MMscf/d): ☒ 0.5 ☐ 1.5 ☐ 3 ☐ 6 ☐ 8 ☐ 10 ☐ 18

Injection Well BHP (psi): ☒ 1500 ☐ 3000 ☐ 5500 ☐ 7500

Offset (Open / Closed): ☒ Closed ☐ Open

Select Wells: ☐ MB1 ☒ MB2 ☐ MB3 ☐ TF1 ☐ TF2 ☐ TF3 ☐ TF4

Figure 135. Tracer Injection page of the UI showing the rich gas EOR reservoir simulation results for injection Well MB2 and the oil, water, and gas production rates.

Below the controllers, four tabs navigate the user to one of four pages showing different plots for the four target variables: BHP, tracer (methane), cumulative production, and production rate. The default tab is “Production Rate.” On each tab, the four controllers allow the user to modify the injection rate, injection pressure, offset, and select wells to create customized plots.

1. **BHP:** The BHP tab contains plots of the simulated well BHPs in psi.

2. **Tracer (methane):** The Tracer (methane) tab produces two columns of plots: one for the simulated methane tracer molar rate (K gmol/day) and one for simulated cumulative methane tracer production (K gmol). As previously described, two sets of reservoir simulations were run, one using propane (C3) and one using rich gas with a tracer (tracer injection). The term “tracer” in this context refers to the “TRC-C1” tracer attached to methane, as described in Table 26.

3. **Cumulative Production:** The Cumulative Production tab shows the simulated cumulative production for oil, water, and gas during the rich gas EOR process. The plots

are separated into three columns for oil (left column), water (middle column), and gas (right column).

4. **Production Rate:** The Production Rate tab shows three columns of plots presenting the oil, water, and gas production rates. Users can use the radius controllers (injection rate and injection pressure) to switch to different levels of injection rate and pressure. Users can use the checkbox controllers to visualize different scenarios of production rates. If the users check the "Open" box in the offset controller, a dashed black line representing the "Open" offset scenario will be shown in the plots. Users can use the "Select Wells" controller to add more wells to the three column plots. Plots within the same column share the same scales in both axes.

Example plots for the BHP, Tracer (methane), Cumulative Production, and Production Rate are shown in Figures 136 through 139, respectively, for a gas injection rate of 18 MMscfd, closed offset production wells, and 7500-psi injection well BHP, for Wells MB2 (injection well), TF2, and TF3.

EERC NA61336.AI

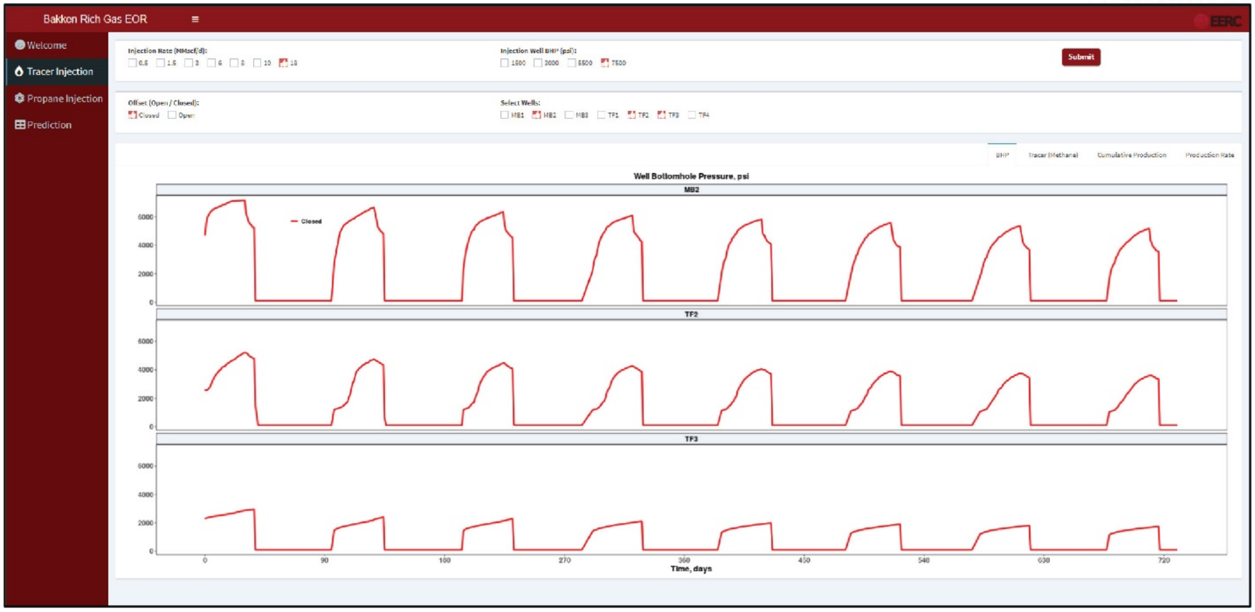

Injection Rate (MMscf/d): ☐ 0.5 ☐ 1.5 ☐ 3 ☐ 6 ☐ 8 ☐ 10 ☒ 18

Injection Well BHP (psi): ☐ 1500 ☐ 3000 ☐ 5500 ☒ 7500

Offset (Open / Closed): ☒ Closed ☐ Open

Select Wells: ☐ MB1 ☒ MB2 ☐ MB3 ☐ TF1 ☒ TF2 ☒ TF3 ☐ TF4

Figure 136. Tracer Injection page of the UI showing the BHP tab for Wells MB2, TF2, and TF3 for the given conditions of gas injection rate of 18 MMscfd, closed external offset production wells (MB1, MB3, TF1, and TF4), and 7500-psi injection well BHP.

EERC NA61337.AI

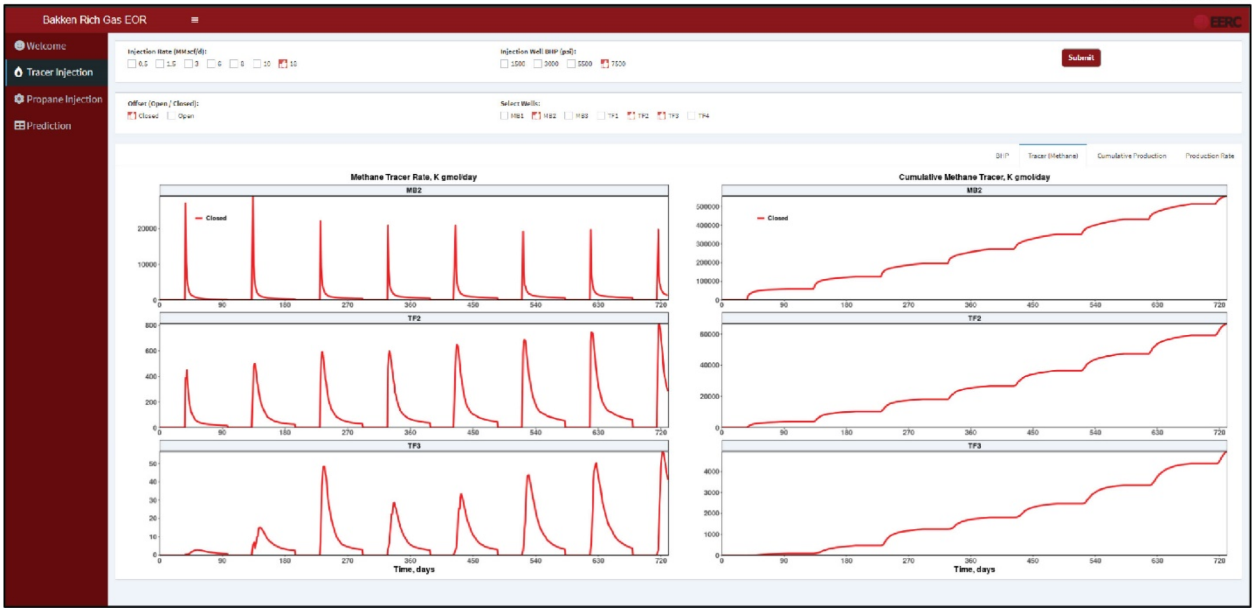

Injection Rate (MMscf/d): ☐ 0.5 ☐ 1.5 ☐ 3 ☐ 6 ☐ 8 ☐ 10 ☒ 18

Injection Well BHP (psi): ☐ 1500 ☐ 3000 ☐ 5500 ☒ 7500

Offset (Open / Closed): ☒ Closed ☐ Open

Select Wells: ☐ MB1 ☒ MB2 ☐ MB3 ☐ TF1 ☒ TF2 ☒ TF3 ☐ TF4

Figure 137. Tracer Injection page of the UI showing the Tracer (methane) tab for Wells MB2, TF2, and TF3 for the given conditions of gas injection rate of 18 MMscfd, closed external offset production wells (MB1, MB3, TF1, and TF4), and 7500-psi injection well BHP.

EERC NA61338.AI

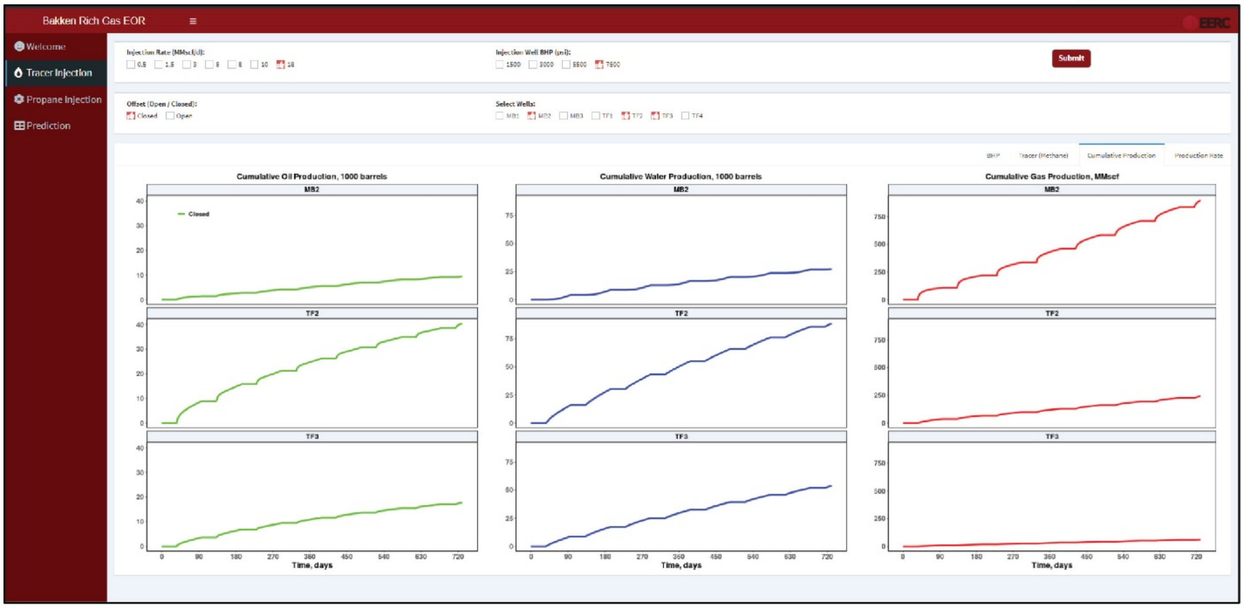

Injection Rate (MMscf/d): ☐ 0.5 ☐ 1.5 ☐ 3 ☐ 6 ☐ 8 ☐ 10 ☒ 18

Injection Well BHP (psi): ☐ 1500 ☐ 3000 ☐ 5500 ☒ 7500

Offset (Open / Closed): ☒ Closed ☐ Open

Select Wells: ☐ MB1 ☒ MB2 ☐ MB3 ☐ TF1 ☒ TF2 ☒ TF3 ☐ TF4

Figure 138. Tracer Injection page of the UI showing the Cumulative Production tab for Wells MB2, TF2, and TF3 for the given conditions of gas injection rate of 18 MMscfd, closed external offset production wells (MB1, MB3, TF1, and TF4), and 7500-psi injection well BHP.

Injection Rate (MMscf/d): ☐ 0.5 ☐ 1.5 ☐ 3 ☐ 6 ☐ 8 ☐ 10 ☑ 18

Injection Well BHP (psi): ☐ 1500 ☐ 3000 ☐ 5500 ☑ 7500

Offset (Open / Closed): ☑ Closed ☐ Open

Select Wells: ☐ MB1 ☑ MB2 ☐ MB3 ☐ TF1 ☑ TF2 ☑ TF3 ☐ TF4

Figure 139. Tracer Injection page of the UI showing the Production Rate tab for Wells MB2, TF2, and TF3 for the given conditions of gas injection rate of 18 MMscfd, closed external offset production wells (MB1, MB3, TF1, and TF4), and 7500-psi injection well BHP.

Propane Injection Page

The Propane Injection page is identical to the Tracer Injection page but instead shows the results of the well EOR performance with propane injection. Instead of a Tracer (methane) tab, there is a Tracer (propane) tab to reflect propane injection. The term "tracer" in this context refers to the propane (C3) component of the produced gas. Instead of plotting the molar concentration of the tracer, the Tracer (propane) page shows the gas mole fraction of propane, defined as (propane/[methane + ethane + propane]), which is, therefore, a fraction bound between 0 and 1.

Figure 140 shows an example of the Tracer (propane) tab for a gas injection rate of 18 MMscfd; external offset production wells (MB1, MB3, TF1, and TF4); and 7500-psi injection well BHP for Wells MB2 (injection well), TF2, and TF3. The figure illustrates gas breakthrough from the injection well (MB2) to the Offset Wells TF2 and TF3, where it grows progressively larger with each successive HnP cycle.

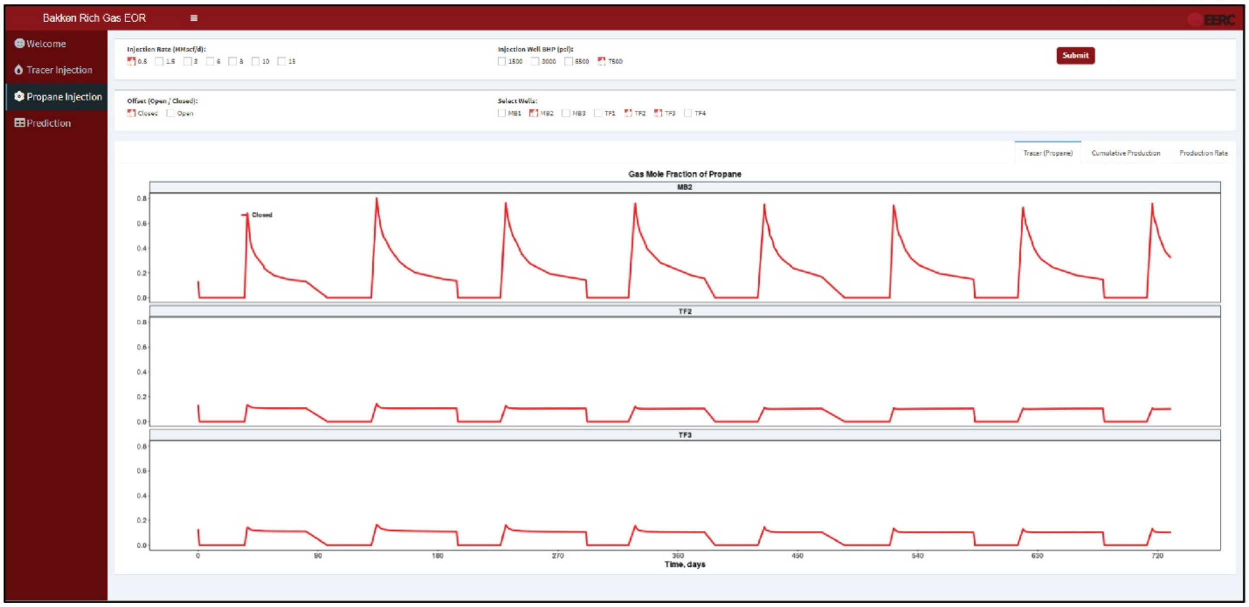

Injection Rate (MMscf/d): ☑ 0.5 ☐ 1.5 ☐ 3 ☐ 6 ☐ 8 ☐ 10 ☐ 18

Injection Well BHP (psi): ☐ 1500 ☐ 3000 ☐ 5500 ☑ 7500

Offset (Open / Closed): ☑ Closed ☐ Open

Select Wells: ☐ MB1 ☑ MB2 ☐ MB3 ☐ TF1 ☑ TF2 ☑ TF3 ☐ TF4

Figure 140. Propane Injection page of the UI showing the Tracer (propane) tab for Wells MB2, TF2, and TF3 for the given conditions of gas injection rate of 18 MMscfd, closed external offset production wells (MB1, MB3, TF1, and TF4), and 7500-psi injection well BHP.

Prediction Page

As discussed earlier, the term "forecasting" in "RTVFC" refers to predictive modeling – the rapid generation of a prediction about future performance that the EOR site operator can compare against the observed performance. The Prediction page shows visualization of forecasted results from ML-based predictive models that were trained on the reservoir simulations. The created ML models were uploaded to the R-Shiny server and deployed to make predictions of different rich gas EOR scenarios.

ML Model Development

For this proof of concept, XGBoost was used as the algorithm for predictive modeling; however, this could be replaced with a variety of other ML algorithms (e.g., RF, SVM, or NN). XGBoost is a boosting ensemble learning algorithm that integrates predictions of "weak" tree models to achieve a strong tree model via a sequential process (Chen and Guestrin, 2016). The simplified XGBoost algorithm works by building a sequential list of decision trees, and in each successive round, the decision tree uses the residuals from the prior decision tree as the target variable. The loss function, or the errors between the predicted and actual values, are minimized using a gradient descent approach to estimate the coefficients within the XGBoost model. There are seven hyperparameters to tune, and the optimal values were tuned by *k*-fold cross validation (Table 31).

Table 31. Hyperparameters of the XGBoost Algorithm

Parameter	Description
nrounds	Maximum number of iterations
max_depth	Maximum depth of the tree
gamma	Regularization coefficient
min_child_weight	Minimum number of instances required in a child node
eta	Learning rate
subsample	Number of samples supplied to a tree
colsample_bytree	Number of features (variables) supplied to a tree

The predictor variables were identical to the controllers used in the visualizations: 1) injection rate (0.5, 1.5, 3.0, 6.0, 8.0, 10, or 18 MMscfd), 2) injection well BHP (1500, 3000, 5500, or 7500 psi), and 3) offset well status (open or closed). In addition to these three EOR parameters, the timestamp was also used as an input variable since time is highly correlated with the EOR performance.

The target variables were oil, water, and gas production rates and cumulative production for the seven wells and two different injectates (rich gas with tracer or propane). Therefore, the total number of target variables was 3 (oil, water, and gas) × 1 (production rate) × 7 (seven wells) × 2 (two injectates) = 42. The cumulative production data were calculated from the production rate data, which will lead to the final number of target variables as 84.

The input data and the 42 target variables (production rate variables) were compiled and used as the data to develop the ML models. The compiled data were randomly divided into training and testing sets by the ratio of 0.8:0.2 (i.e., 80% of the compiled data were randomly placed into the training set and the remaining 20% were placed into the test set). The training set was used to train the XGBoost model, and the testing set was used to evaluate the performance of the model. The modeling performance was evaluated using r^2 and relative root mean square error (RRMSE), where a model with high r^2 and low RRMSE values was considered as a good performing model. The RRMSE is defined as the value of the root mean square error divided by the mean value of that variable.

Corresponding to the target variables, 84 XGBoost models were developed. The average (± standard deviation) values of R^2 values for both training and test sets for models with rich gas injection were 0.996 (±0.008) and 0.984 (±0.025), respectively, and for models with propane injection were 0.997 (±0.004) and 0.985 (±0.02), respectively. The average (± standard deviation) values of RRMSE values for both training and test sets for models with rich gas injection were 0.04 (±0.08) and 0.08 (±0.16), respectively, and for models with propane injection were 0.03 (±0.04) and 0.05 (±0.07), respectively.

Figure 141 shows the r^2 and RRMSE performance results for all of the 42 models in the training and test sets for the models with EOR injection by rich gas or propane. Approximately 60% of the models had r^2 values greater than 0.9, and roughly 85% of the models had RRMSE values less than 0.1 for both training and test sets. These performance indicators showed that most of the models performed well for both the training and test sets. Therefore, for the current study, all the models were accepted for predictive modeling purposes.

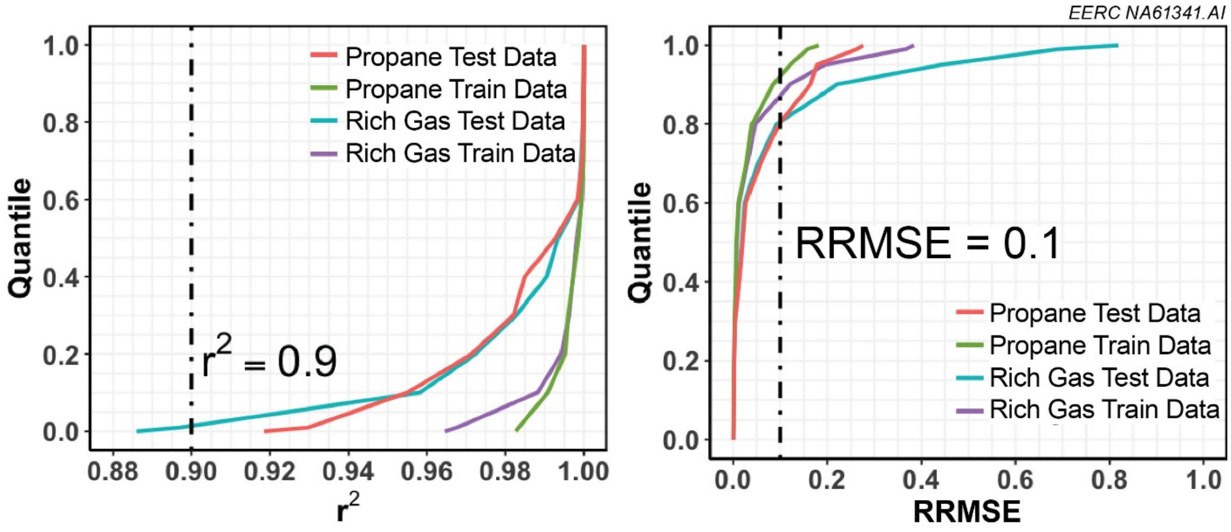

Figure 141. Quantile plots of the modeling performance evaluated by r^2 and RRMSE values for the training and test sets of EOR rich gas or propane injection.

In this proof of concept, the training and testing data for the predictive modeling were the same data as the simulations used for the real-time visualizations. However, this need not be the case. The real-time visualizations are designed to display data acquired in the field and saved to the R-Shiny server—these data can be any data type acquired at various frequencies (e.g., hourly, daily, weekly, etc.). The simulations were used as an example. In contrast, the workflow for developing the predictive models requires reservoir simulations that explore the parameter space of the EOR operating controls. Therefore, prior to initiating the rich gas EOR, a set of reservoir simulations would be required that identifies the EOR operating controls and their expected ranges, generates the reservoir simulation outputs, and then trains and tests ML-based models using the model development strategy summarized here.

ML Model Deployment

Once the XGBoost models were developed, they were saved to a local drive and deployed to the R-Shiny server. The fitted XGBoost models allow the user to create forecasts of the target variables based on their user-defined selections of the predictor variables (injection rate, injection well BHP, and offset well status). These forecasts allow the operator to compare the observed data (visualization) against the forecasted data (prediction) to evaluate whether to continue operating the EOR project as is or to make one or more adjustments.

The controllers in the Prediction page allow the user to customize the EOR scenario. Once the EOR scenario is selected, the set of input variables will be created, and then the XGBoost model will be used to create the forecast. For this proof of concept, the predictions show the full 2-year EOR period (January 1, 2021 – December 31, 2022). The input data set, therefore, contains 731 rows of time (ranging from Day 1 to Day 731) and repeating data of the EOR operational variables (injection rate, injection well BHP, and offset well status). The user selections of the input data are then entered into the developed 42 XGBoost models to make time-series predictions of the 84 target variables (42 production rate variables and 42 derived cumulative production variables).

Like the Submit button on the Tracer Injection and Propane Injection pages, in the upper right-hand corner of the Prediction page is a button labeled “Prediction.” After the user has made the controller selections, the user must click the Prediction button for the tool to deploy the ML models and create predictions.

Figure 142 shows two examples of the Prediction page for cumulative oil, water, and gas production for Wells TF2 and TF3 with tracer injection, open and closed offset wells, and two different sets of user inputs: (top) 18-MMscfd injection rate and 7500-psi injection well maximum BHP and (bottom) 9.1-MMscfd injection rate and 3750-psi injection well maximum BHP. In the first scenario with greater injection rate and BHP, the prediction for Well TF2 estimates ~45 Mbbl in cumulative oil production, ~100 Mbbl in cumulative water production, and ~250 MMscf (closed) or ~350 MMscf (open) in cumulative gas production. However, in the second scenario with half the injection rate and BHP, the prediction for Well TF2 estimates ~40 Mbbl in cumulative oil production, ~100 Mbbl in cumulative water production, and ~175 MMscf in cumulative gas production. This rapid prediction informs the operator that the marginal gain in oil production from the higher injection rate and BHP scenario (roughly 5 Mbbl greater cumulative oil production over the 2-year EOR period) is associated with significantly greater gas production (roughly 75- to 175-MMscf greater cumulative gas production for the closed and open scenarios, respectively). Consequently, the operator may decide to reduce the injection rate if the EOR operation does not want excess gas production. In addition, plotting the open and closed offset scenarios shows that oil and water production are largely invariant to external offset well status, whereas gas production is more sensitive and Well TF2 produces more gas when the Offset Wells MB1, MB3, TF1, and TF4 are open.

The Prediction page allows the operator to explore many combinations of injection rate, offset well status, and injection well maximum BHP and to compare those outcomes against the observed data to determine when and if EOR operational changes are required.

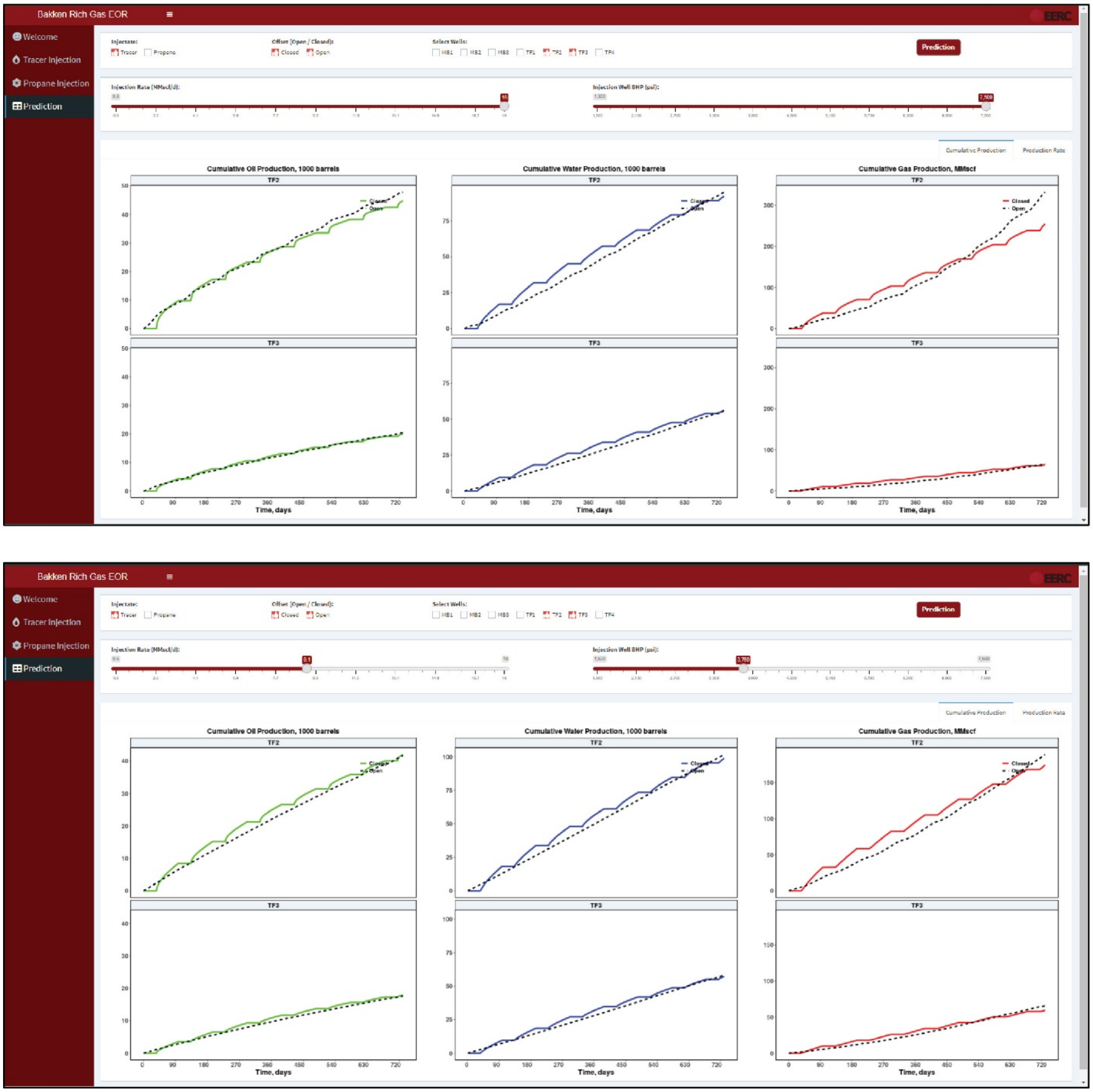

Injectate: ☒ Tracer ☐ Propane

Offset (Open / Closed): ☒ Closed ☒ Open

Select Wells: ☐ MB1 ☐ MB2 ☐ MB3 ☐ TF1 ☒ TF2 ☒ TF3 ☐ TF4

Injection Rate (MMscf/d): 18

Injection Well BHP (psi): 7,500

Injectate: ☒ Tracer ☐ Propane

Offset (Open / Closed): ☒ Closed ☒ Open

Select Wells: ☐ MB1 ☐ MB2 ☐ MB3 ☐ TF1 ☒ TF2 ☒ TF3 ☐ TF4

Injection Rate (MMscf/d): 9.1

Injection Well BHP (psi): 3,750

Figure 142. Prediction page of the UI showing results of the XGBoost predictions of cumulative oil, water, and gas production for Wells TF2 and TF3 for rich gas injection with tracer, open and closed offset wells, and two different sets of user inputs: (top) 18-MMscfd injection rate and 7500-psi injection well maximum BHP and (bottom) 9.1-MMscfd injection rate and 3750-psi injection well maximum BHP.

Real-Time Control

As previously discussed, Control methods in RTVFC refer to operational changes that the EOR site operator can enact (e.g., changing gas injection rates) to affect the observed performance and potentially improve the EOR outcome. The integration of visualizing reservoir surveillance data in real-time, rapidly forecasting reservoir performance, and deploying operational changes to affect EOR performance constitute RTVFC. The real-time visualizations are designed to show field data for well BHP, tracer or propane breakthrough, production rate, and cumulative production. The real-time forecasting is designed to predict future well performance based on EOR operational controls. In this proof-of-concept study, the EOR operational controls include injection rate, injection well BHP, and offset status (open or closed), as these factors are significantly related to rich gas EOR performance. Comparative assessments between the real-time visualization (what is occurring in the field) and forecasting (what is predicted to occur given a set of EOR operational controls) provide a means for real-time control.

Summary and Conclusions

The goal of Subactivity 8.2.1 was to explore RTVFC for improved reservoir surveillance during rich gas EOR. A large set of synthetic reservoir simulations were created to generate well responses (oil, gas, and water production, well BHP, and tracer or propane breakthrough) for a set of EOR operating parameters that included offset well status (open or closed), injectate (rich gas or propane), injection rate (0.5, 1.5, 3.0, 6.0, 8.0, 10, or 18 MMscfd), and injection well BHP (1500, 3000, 5500, or 7500 psi). A UI was developed to provide real-time visualization designed to be consistent with similar processes that the EERC has used on other gas injection projects. ML-based models using the XGBoost algorithm were developed to provide rapid forecasting of well performance given a set of user-defined EOR operating parameters. These predictive models allow the user to modify the offset well status, injection rate, injection well BHP, and rapidly forecast future production performance. The combination of real-time visualization tools with real-time forecasting tools provides a framework for real-time control—operational changes that the EOR site operator can enact (e.g., changing gas injection rates) to affect the observed performance and potentially improve the EOR outcome.

Subactivity 8.2.2 – Embedded Discrete Fracture Modeling–Artificial Intelligence–Automatic History Matching (EDFM–AI–AHM) Testing

Introduction

The modeling and simulation efforts in Activities 7 and 8 showed that history matching was one of the most time-consuming tasks because of the uncertainties in fracture parameters. Recently, an innovative method and software named EDFM–AI–AHM was developed to assist the history-matching process by tuning fracture and matrix parameters automatically based on a set of input ranges provided by the reservoir engineer (Sim Tech, LLC, 2021). The method utilizes NN-based proxy models by sampling stochastic reservoir model realizations and updating the proxy models using Markov Chain Monte Carlo (MCMC) methods (Carpenter, 2018; Dachanuwattana and others, 2018a, b; Eltahan and others, 2019, 2020; Tripoppoom and others, 2019). The approach has been applied to several field cases (Du and others, 2017; Liu and others, 2020b; Tripoppoom and others, 2020a, b).

The EDFM–AI–AHM software was tested in Activity 8 to compare two reservoir simulation models and their forecasted EOR performance: one using manually tuned fracture parameters and one using EDFM–AI–AHM-tuned fracture parameters. The results from this proof-of-concept evaluation of EDFM–AI–AHM will inform future work for reservoir simulation of EOR performance in the BPS and the integration of physics-based reservoir simulations with AI and ML.

Methods

AHM Workflow

Figure 143 illustrates the general workflow employed in the AHM process (Tripoppoom and others, 2019). The first step was to screen and identify uncertain parameters to include in the AHM. For this proof-of-concept, EDFM–AI–AHM was used to estimate four uncertain fracture parameters: height (ft), half-length (ft), conductivity (mD-ft), and initial water saturation (Sw), which have been shown to significantly affect the history matching for unconventional reservoirs. Initial cases that covered the input ranges of the uncertain parameters were generated by Latin hypercube sampling (LHS) and simulated via the reservoir simulator and EDFM. In the first iteration, the inputs and results of the initial simulation cases were extracted to train an initial set of NNs. Next, the NN-MCMC algorithm was run to perform history matching automatically and select acceptable history-matching solutions. The simulation inputs and results obtained were then used to retrain the NN in the second iteration. The workflow would stop if no significant improvement were detected in the latest iteration (Stopping Criteria); otherwise, the workflow would continue until the maximum number of iterations were reached.

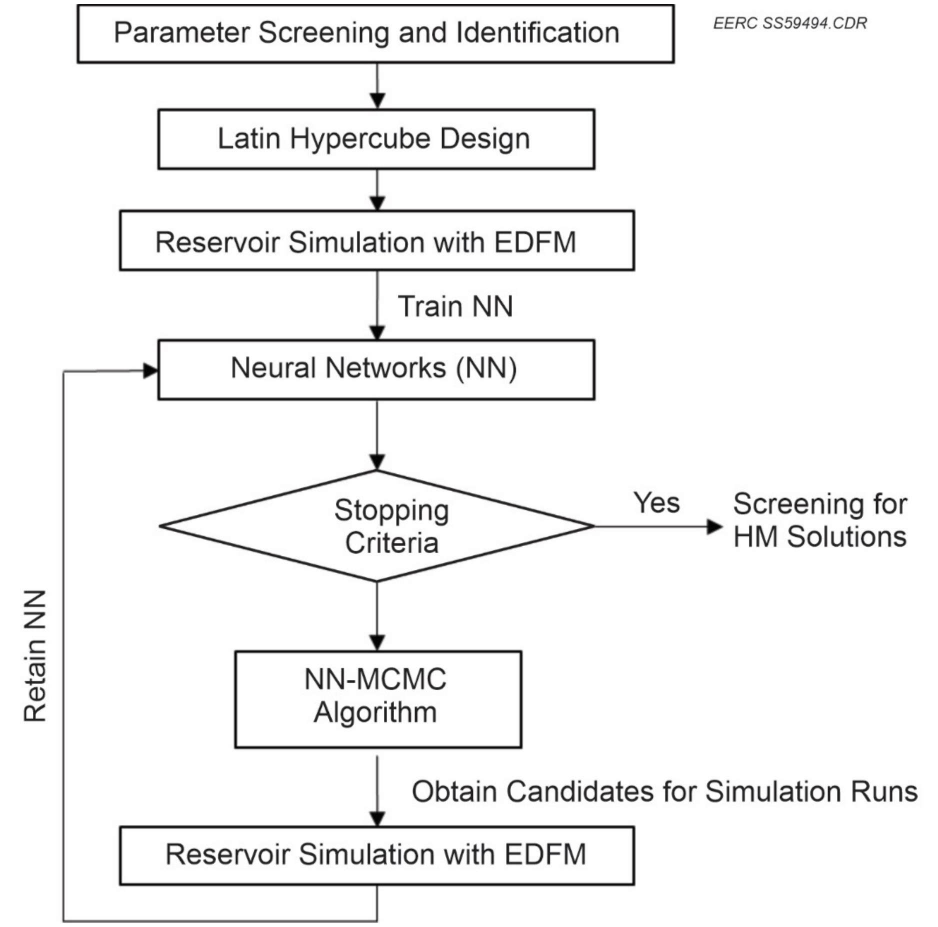

Figure 143. AHM workflow (modified from Tripoppoom and others, 2019).

EDFM–AI–AHM Implementation

Fracture Parameter Ranges

EDFM–AI–AHM was used to tune the fracture parameters of four wells (MB2, MB3, TF2, and TF3) in the seven-well DSU model that was previously described in Subactivity 8.2 (Figure 144). The other three wells were omitted from the reservoir simulations to reduce the computational burden for this proof-of-concept testing of EDFM–AI–AHM. Table 32 shows the initial ranges (minimum and maximum values) for each of the four uncertain fracture parameters, which were input into EDFM–AI–AHM by the reservoir engineer.

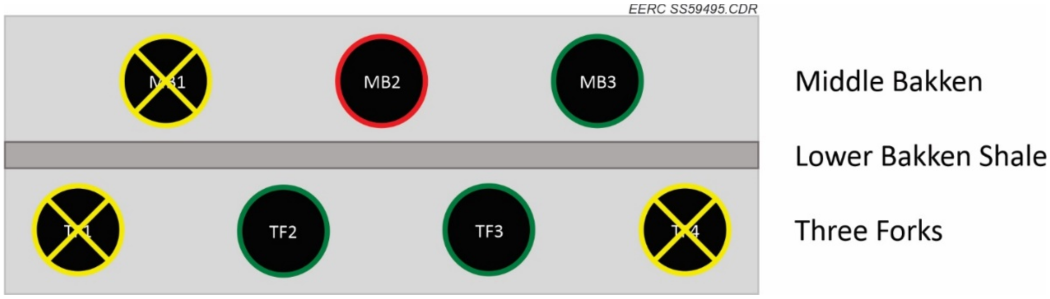

Figure 144. Illustration of the seven-well DSU model identifying the MB and TF wellbores and the well that was used for rich gas injection (MB2 – red outline) or production (green outlines), as described in the text. For this application, Wells MB1, TF1, and TF4 were removed from the seven-well DSU model to reduce the computational burden for this proof-of-concept testing of EDFM–AI–AHM (yellow Xs).

Table 32. Uncertain Fracture Parameters and Initial Ranges (minimum and maximum) Used for the EDFM–AI–AHM Simulations for Wells MB2, MB3, TF2, and TF3

Uncertain Parameters	Unit	Min. Value	Max. Value
Fracture Height	ft	100	150
Fracture Half-Length	ft	300	420
Fracture Conductivity	mD-ft	10	30
Initial Fracture Water Saturation	Fraction	0.3	0.7

Global Objective Function

The response variables (parameters) were historical oil, water, and gas production data, which were used to define a global objective function (GOF) as:

$$\text{GOF} = \frac{\sum_{j=1}^{m}\sum_{i=1}^{n}\left[NL_{ij} \times 100\right]^2 \times w_{ij}}{\sum_{j=1}^{m}\sum_{i=1}^{n} w_{ij}} \qquad \text{[Eq. 9]}$$

Where NL_{ij} is the normalized local error, defined as:

$$NL_{ij} = \frac{X_{ij,model} - X_{ij,history}}{X_{j,max} - X_{j,min}} \qquad \text{[Eq. 10]}$$

Where *i* and *j* are the indices for data points and response parameters, respectively; *m* and *n* are the indices for the number of responsive parameters and data points, respectively; and $X_{ij,model}$, $X_{ij,history}$, and w_{ij} are the modeling data, historical data, and weight of data at index *i* of response parameter *j*, respectively.

The Equation 10 definition of GOF allows one global value to represent multiple local errors (Tripoppoom and others, 2019).

Neural Networks

NNs were employed to train proxy models to predict response parameters. In general, NNs consist of input, hidden, and output layers, as shown in Figure 145. The input layer consists of all the original input parameters (e.g., x_1, x_2, x_3, and x_4 in Figure 145). The four uncertain parameters listed in Table 32 (fracture height, fracture half-length, fracture conductivity, and fracture water saturation) were used as input layers of the NN to predict the response parameters at different dates for the four selected wells (MB2, MB3, TF2, and TF3); thus the total number of input layers was 16 (i.e., four uncertain parameters × four wells). The output layer includes the final predictions from the NN model. There were three response parameters (oil, water, and gas production) for each of the four wells (MB2, MB3, TF2, and TF3); thus the total number of output layers was 12 (i.e., three responses × four wells). The "learning" of the NN occurs in the hidden layer (or layers), which captures the relationships between inputs and outputs.

The NN-MCMC is a multiple-proxy-based algorithm for AHM. While the conventional MCMC algorithm can quantify uncertainty and obtain multiple history-matching solutions, the algorithm is time-consuming when performed together with a reservoir simulator. The proxy-based MCMC algorithm improves the efficiency of MCMC by replacing a simulation run with a single proxy model. The multiple proxy-based MCMC further accelerates the proxy-based MCMC by using multiple proxy models to mitigate the nonlinearity in the history matching. NNs were utilized to generate proxy models for the multiple-proxy-based MCMC algorithm to perform the AHM (Tripoppoom and others, 2020a, b).

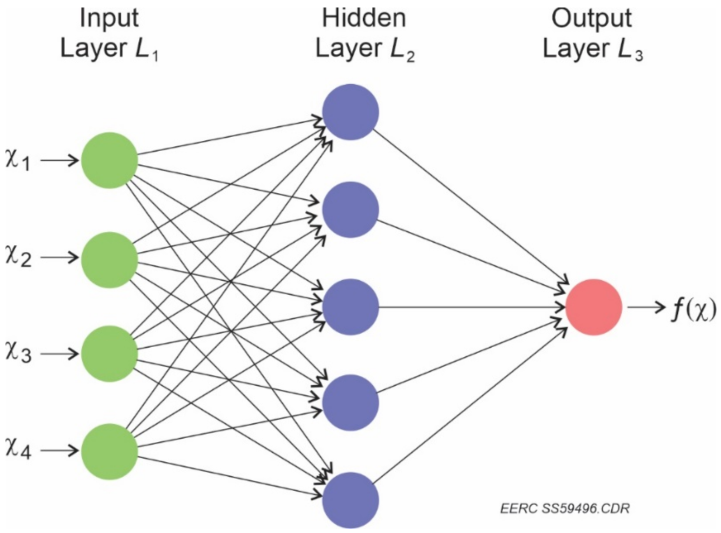

Figure 145. Representation of a simple feedforward NN showing input, hidden, and output layers (Boehmke and Greenwell, 2020).

Results

Initial Simulation Cases

Forty initial simulation cases were generated via LHS. Figure 146 shows the simulation results for the 40 initial simulation cases for Well TF3 oil, gas, and water rates. In each panel, the colored lines show the simulation results, and the hollow circles show the historical production data (History). As shown in the figures, the simulation results provided coverage of the production history for oil, water, and gas rates. While a few cases had similar production trends compared to the historical data, most of the cases presented significant deviation from the production history. The inputs and results of these 40 cases for all the match points were used to train the initial NN, then the NN-MCMC algorithm was used to perform the AHM.

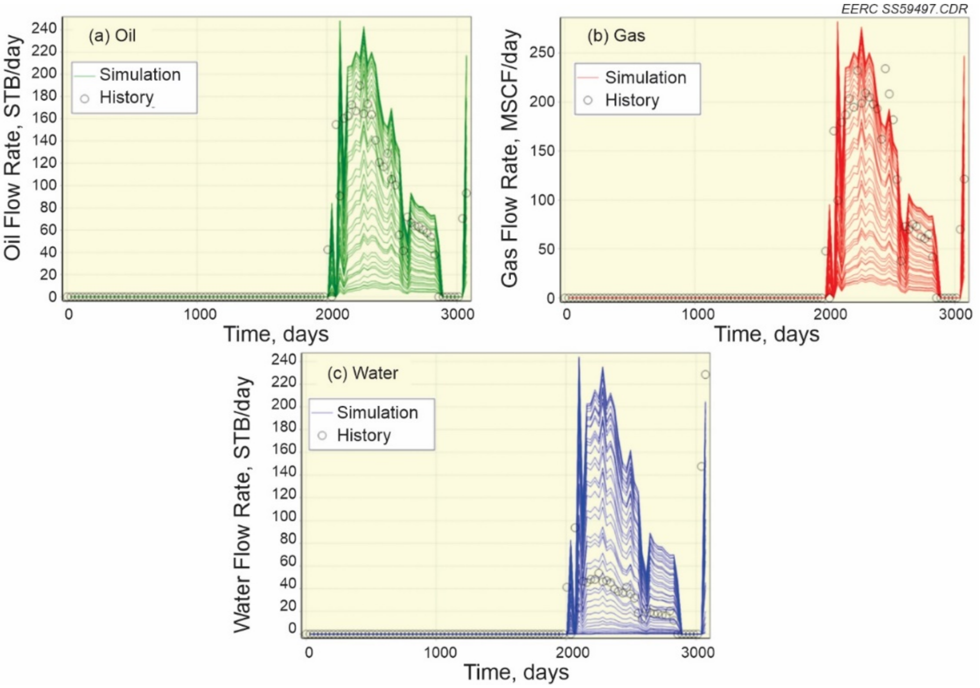

Figure 146. Simulation results for the 40 initial simulation cases for Well TF3 a) oil rate, b) gas rate, and c) water rate. The colored lines in each panel show the simulation results, and the hollow circles show the historical production data (History).

NN-MCMC and AHM

Twenty solutions were generated by the NN-MCMC algorithm during each iteration and were verified via the reservoir simulation with EDFM. The maximum number of iterations was set to six to provide a reasonable balance between computational burden and reservoir simulation solutions. The AHM workflow ran through all six iterations (i.e., did not achieve the stopping criteria) and generated an additional 120 cases. Therefore, with the 40 initial simulation cases, the AHM workflow generated 160 cases in total for the history-matching process. After screening the solutions by setting error constraints for the response parameters for each well, 120 solutions with global errors smaller than the error constraints were selected to compare with the historical data. The solutions that met the error constraints are presented in Figure 147 and show that the history-matching quality (agreement between the historical and simulated production data) was significantly improved as compared to the results of the initial 40 simulation cases. The best solution was defined as the case with the lowest GOF. Plots in Figure 148a–c show the history-matching results of the best solution for oil, gas, and water production rates, respectively.

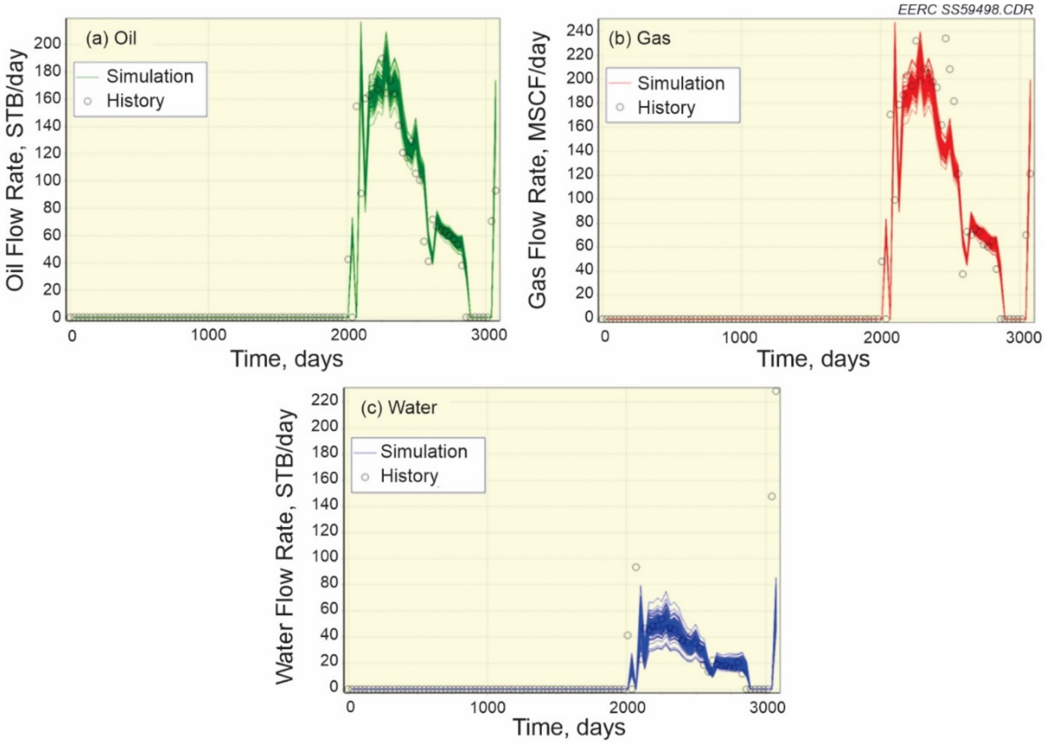

Figure 147. Simulation results of the 120 history-matching solutions with global errors smaller than the error constraints for Well TF3 a) oil rate, b) gas rate, and c) water rate.

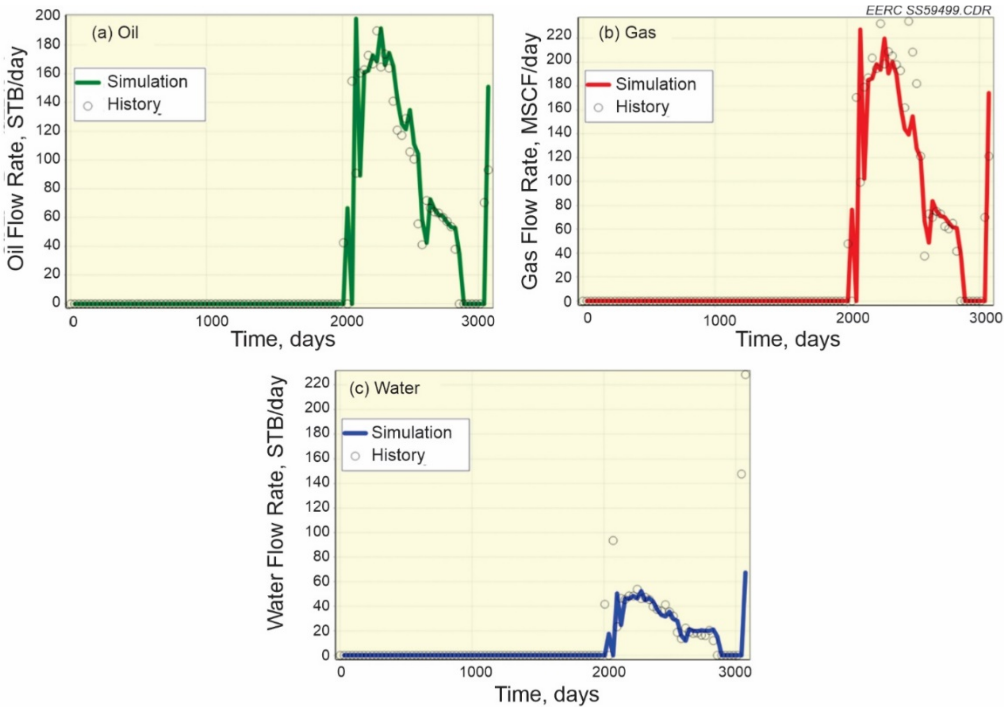

Figure 148. Simulation results of the best solution for Well TF3 a) oil rate, b) gas rate, and c) water rate.

Fracture Parameter Distributions

The prior and posterior distribution of uncertain parameters for the 120 solutions with global errors smaller than the error constraints for Well TF3 are shown in Figure 149. The prior distributions are assumed to be a uniform distribution (informationless) between the minimum and maximum value (gray bars in Figure 149). The posterior distributions suggest that fracture height, fracture half-length, and fracture conductivity could vary greatly and indicate that there are many combinations of these three fracture parameters within the specified ranges that yield similar history-matching results (Figure 149a–c). In contrast, the posterior distribution shows a narrow range of the fracture initial water saturation that provided acceptable history-matching solutions (approximately 0.40 to 0.45) (Figure 149d). This means that the change of initial fracture water saturation caused a larger impact on the history-matching results than other three fracture parameters. The red vertical line in Figure 149 shows the best result across all four fracture parameters, or the final history-matching result.

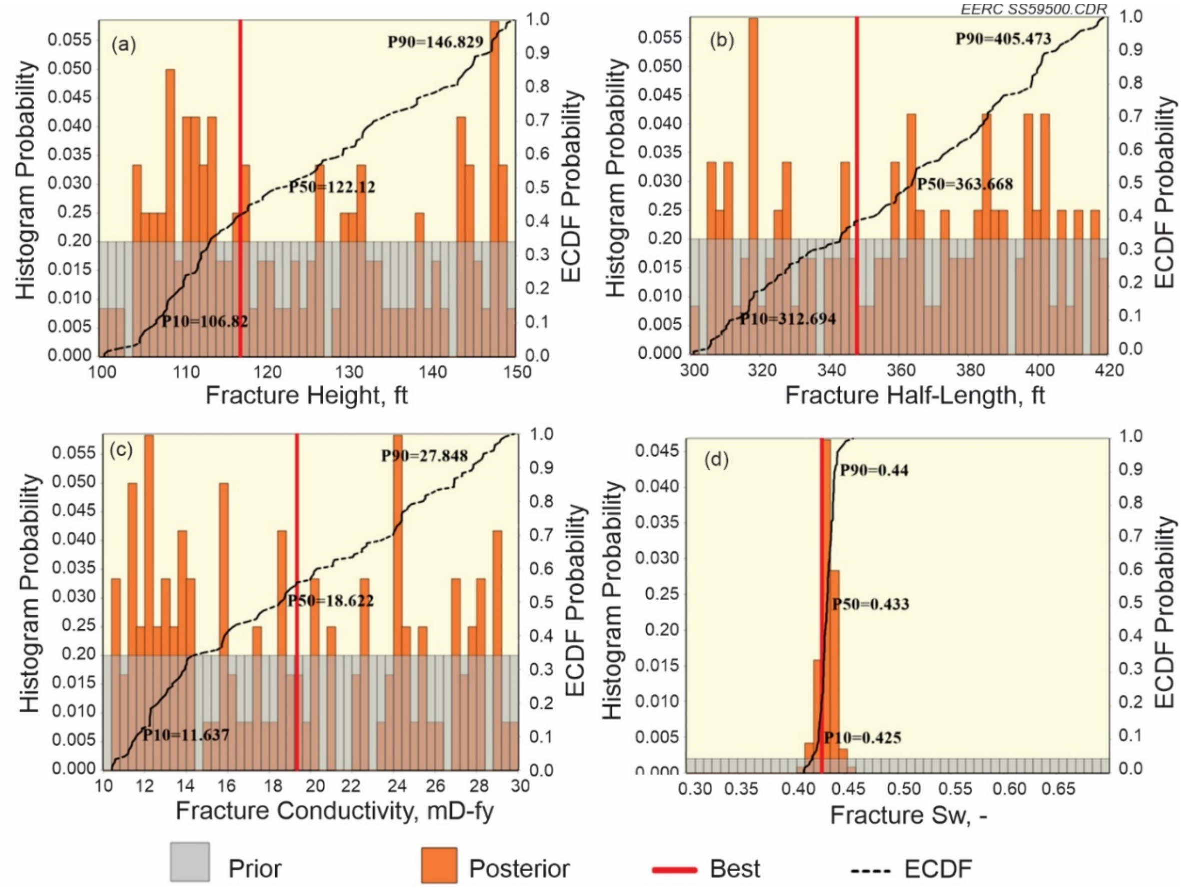

Figure 149. Prior and posterior distribution of the four uncertain fracture parameters from the 120 solutions with global errors smaller than the error constraints for Well TF3: a) fracture height, b) fracture half-length, c) fracture conductivity, and d) fracture initial water saturation. The ECDF (empirical cumulative distribution function) shows the cumulative probability and identifies the 10th percentile (P10); 50th percentile (P50), or median; and 90th percentile (P90) estimates.

Figure 150 shows a parallel coordinate plot of the four uncertain fraction parameters for all 160 simulation cases of Well TF3, showing the 40 non-history-matching solutions (Non-HM Sol), 120 history-matching solutions (HM Sol), and the best solution (Best). This figure again shows the nonunique nature of the inverse solutions for fracture height, fracture half-length, and fracture conductivity (i.e., many combinations of these three parameters within the specified ranges yield similar history-matching results) and that only a small range of initial fracture water saturations could generate acceptable history-matching solutions.

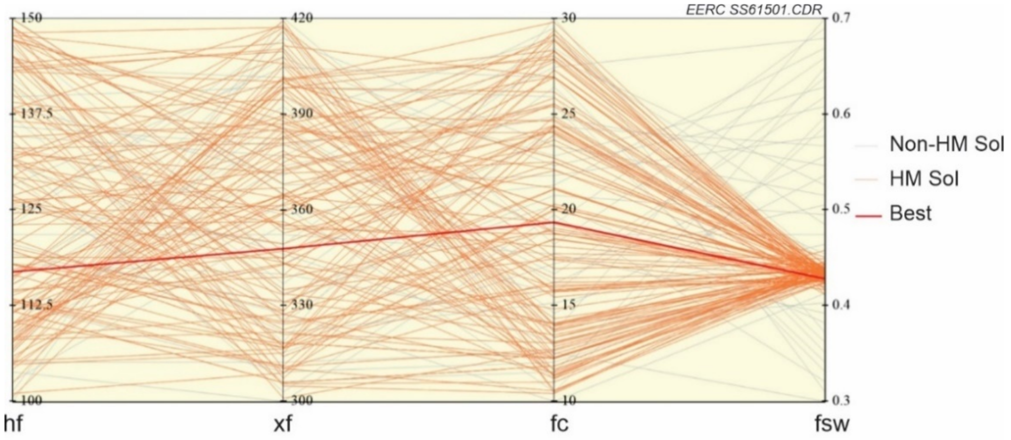

Figure 150. Parallel coordinate plot of the four uncertain fraction parameters (hf = fracture height, xf = fracture half-length, fc = fracture conductivity, and fsw = fracture initial water saturation) for all 160 simulation cases of well TF3, showing the 40 non-history-matching solutions (Non-HM Sol), 120 history-matching solutions (HM Sol), and the best solution (Best).

Comparing EOR Performance

Figure 151 compares the manual and automatic history-matching results for the cumulative oil production of the well group including Wells MB2, MB3, TF2, and TF3. The model tuned by EDFM–AI–AHM provided a more accurate oil production result: a closer simulated result to the historical production data.

To test the sensitivity of the simulated EOR performance to the fracture parameters, a simulation matrix with ten cases (as shown in Table 33 was designed to vary the gas injection rate, injection time, soaking time, production time, and injectate, and these were used to generate simulations using the manually tuned and EDFM–AI–AHM-tuned simulation models. The simulation results in Figure 152 show that the EOR performance could be quite different between the two models even though the same HnP operational parameters were used. Stated differently, the interactions between the four fracture parameters and the EOR operational parameters can yield a pronounced difference in the simulated EOR performance. A more detailed comparison in Figure 153 shows that the percentage difference between the manually tuned and EDFM–AI–AHM-tuned simulation models could vary between 7% and 21%, depending on the injectate and operational settings for EOR.

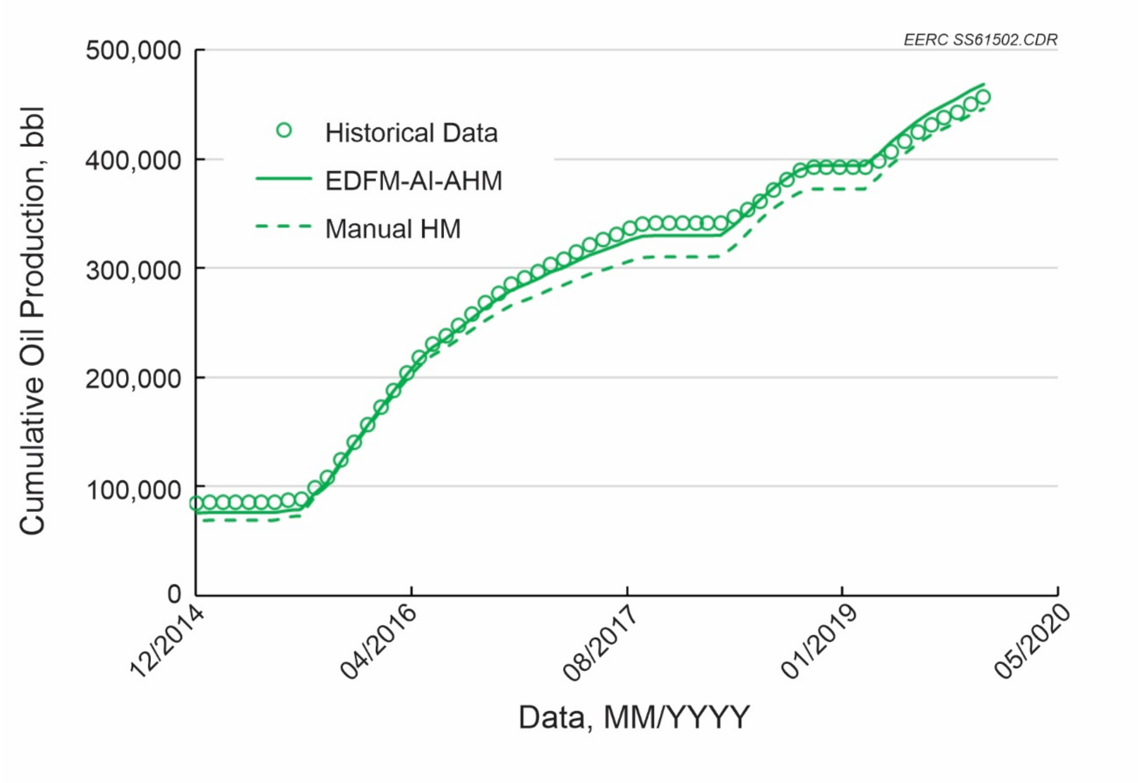

Figure 151. Comparison of manually tuned and EDFM–AI–AHM-tuned history-matching results for the cumulative oil production of the well group of Wells MB2, MB3, TF2, and TF3.

Table 33. Simulation Case Matrix Used for EOR Predictive Results Comparison

Case No.	Injectate	Inj. Rate, MMscf/d	Inj. Time, day	Soaking Time, day	Prod. Time, day
1	Rich gas	3	30	7	60
2	Rich gas	6	30	7	60
3	Rich gas	4	60	7	60
4	Rich gas	6	20	0	60
5	Rich gas	6	30	0	60
6	Rich gas	6	20	7	60
7	Rich gas	6	20	0	90
8	Rich gas	6	20	0	30
9	Propane	3	30	7	60
10	Propane	6	30	7	60

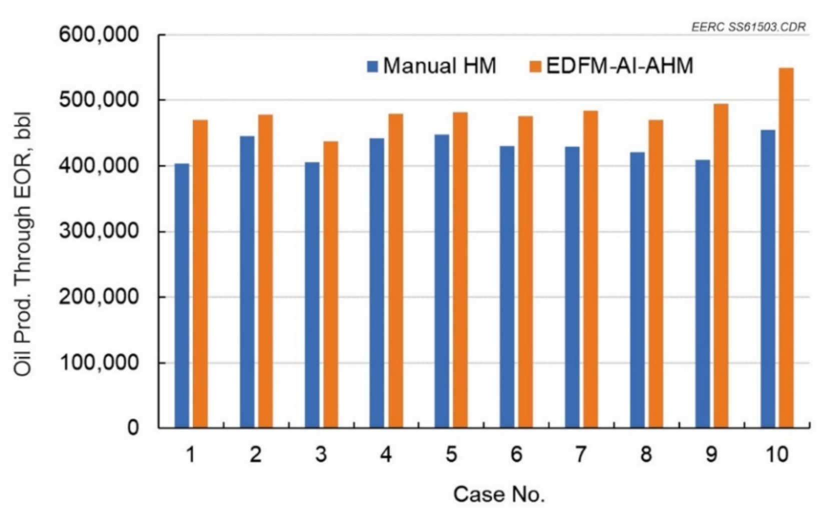

Figure 152. Comparison of EOR predictive results for the well group (MB2, MB3, TF2, and TF3) using the manually tuned and EDFM–AI–AHM-tuned reservoir simulation models.

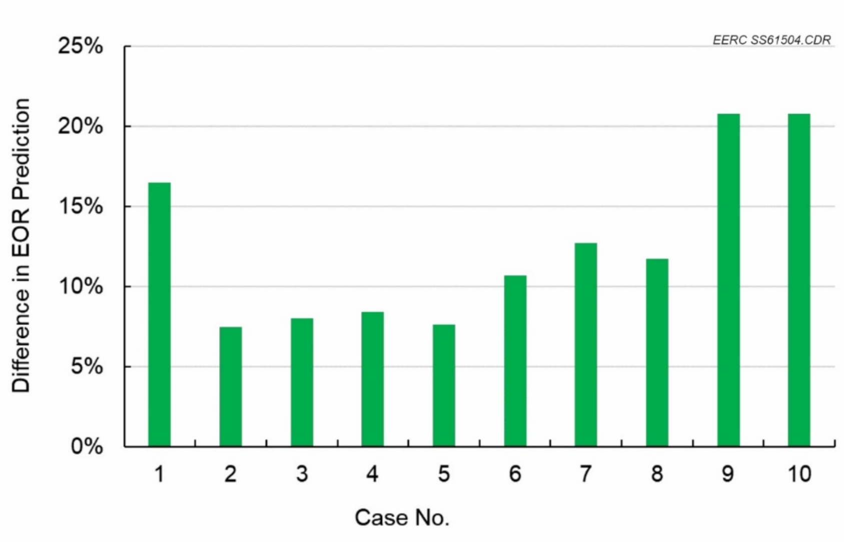

Figure 153. Percentage difference between EOR predictive results for the well group (MB2, MB3, TF2, and TF3) using the manually tuned and EDFM–AI–AHM-tuned reservoir simulation models.

Subtask 8.2 Summary

This work provided a proof-of-concept testing of the EDFM–AI–AHM software to compare two reservoir simulation models and their forecasted EOR performance: one using manually tuned fracture parameters and one using EDFM–AI–AHM-tuned fracture parameters. Four uncertain fracture parameters: height (ft), half-length (ft), conductivity (mD-ft), and initial water saturation (Sw), which have been shown to significantly affect the history matching for unconventional reservoirs, were the focus of the history matching.

The results showed that the EDFM–AI–AHM solution provided more accurate results than the manually tuned solution. In addition, the AHM workflow and automated NN routines in the EDFM–AI–AHM software greatly accelerated the history-matching process over the more labor- and time-intensive manual history-matching process. Lastly, the AHM workflow included with EDFM–AI–AHM provided deeper insights about the fracture parameter distributions and the potential interactions between the fracture parameters and the EOR operational parameters of injection rate, injection time, soak time, and production time.

The modeling and simulation efforts in Activities 7 and 8 showed that history matching was one of the most time-consuming tasks because of the uncertainties in fracture parameters. The results from this proof-of-concept evaluation show that using EDFM–AI–AHM will significantly improve future work for reservoir simulation of EOR performance in the BPS by accelerating the history-matching process and providing more accurate solutions and, therefore, more accurate production forecasts.

SUBTASK 3.1 – BAKKEN RICH GAS EOR RESEARCH EFFORTS: OVERALL OBSERVATIONS AND CONCLUSIONS

OBSERVATIONS

The laboratory-, modeling-, and field-based activities conducted by the EERC over the course of Subtask 3.1 yielded valuable insight regarding the potential for using rich gas injection as a means of EOR in the BPS. Key observations from the project include the following:

- MMP was not achieved in the reservoir during the pilot test. Achieving MMP in a reservoir at an advanced state of depletion requires considerable quantities of injection gas or, perhaps, the use of water injection as a means of pressurization prior to gas injection.

- Reservoir surveillance and monitoring data demonstrate the injected gas can be controlled and contained within the DSU.

- Injection fluid composition has a large impact on reservoir oil MMP and enriching produced gas with additional ethane and/or propane before injection will favorably alter reservoir response. The lower MMP achievable with enriched gas would also allow for using less injection gas for initial repressuring of the reservoir and continuation of injection operations at lower pressure.

- Injection of rich gas (ca. 70/20/10 methane/ethane/propane) produced from the BPS can achieve MMP at pressures that are similar to the pressures required by CO_2, approximately 2420 psi. Methane requires very high pressures to achieve MMP: 4200 psi. Ethane requires approximately 1350 psi to reach MMP and propane about 550 psi to achieve MMP.

- Adding NGLs like ethane and propane to produced gas is an efficient way to lower MMP if excess NGLs are available.

- At pressures above MMP, phase partitioning occurs between the thousands of complex HC components in crude oil and the injected gas. The HC composition of both the injectant-dominated phase and the bulk crude oil phase is continually changing with pressure and temperature. The oil-rich phase has higher molecular weights, viscosities, and densities (lower API gravities) after exposure to all tested injection fluids, but propane shows the least negative changes, since it vaporizes the broadest spectrum of liquid HC components.

- Results of HC extraction experiments from core specimens are consistent with the miscible-phase sampling experiments, as would be expected based on the concentration gradient/diffusion extraction mechanism that appears to be a major factor controlling rock extractions.

- At 5000 psi, produced gas does nearly as well as propane at extracting the bulk of HCs from core samples. However, even at 5000 psi, methane can only slowly extract heavier HCs.

- The traditional fracture system model used for simulation can replicate the depletion and evaluate the EOR mechanisms using a small-scale model, but it encounters numerical challenges in the gas injection simulation at larger scale and has difficulties handling strong interference effects between wells.

CONCLUSIONS

The results and lessons learned from the Stomping Horse rich gas EOR pilot activities indicate that developing an effective, economical EOR approach for the Bakken will require more field tests. Robust reservoir characterization and understanding of the behavior of the injected fluid in the reservoir are necessary to create realistic geomodels and conduct valid dynamic simulations of potential EOR scenarios. This knowledge is essential to designing the operational parameters of injectivity tests and interpreting the results.

There is great reason to be optimistic about the future of EOR in tight oil formations such as the Bakken. The results of EERC laboratory studies suggest significant potential for high rates of oil mobilization using both CO_2 and produced field gas injection under the right conditions. The results of the lab studies, combined with rigorous statistical analysis of well production data and associated modeling efforts, confirm the notion that fluid mobility within the reservoir is controlled by fractures. As more knowledge is gained about the nature and distribution of fracture networks in the Bakken, the industry will be in a better position to predict and, ultimately, influence fluid mobility. New field tests are necessary to develop a more complete understanding of those conditions. Improvements in modeling software specifically designed to address challenges inherent in unconventional tight reservoirs, combined with the application of machine learning and artificial intelligence to reservoir surveillance data processing and interpretation, will streamline the design and execution of future EOR pilots. Thoughtful and creatively engineered field tests within a well-characterized geologic setting will yield the fundamental knowledge needed to take Bakken oil production to the next level.

MILESTONES

The completed milestone table can be found in Table 34.

Table 34. Milestones

Milestone Title/ Description	Planned Completion Date	Actual Completion Date	Verification Methods	Comments
M1 – Conduct Project Kickoff Meeting with DOE Personnel to Review Project Priorities and Directions	1/31/2018	12/14/2017	An initial list of key priorities will be generated.	
M2 – Complete Initial Assessment of Test Site Rich Gas Quality and Quantity	10/31/2017	10/15/2017	A summary of rich gas quality and quantity from the LR facility will be included in the quarterly report.	
M3 – Finalize Fluids Sampling Collection and Analysis Plan	10/31/2017	10/15/2017	The plan will be included in the quarterly report.	
M4 – Complete Initial Reservoir Geocellular Model	11/30/2017	10/31/2017	A summary of initial geocellular modeling of the reservoir will be included in the quarterly report.	
M5 – Complete Rich Gas in Shale Permeability Studies	5/31/2020	5/31/2020	A summary of the studies will be included in the quarterly report.	
M6 – Complete Minimum Miscibility Pressure and Rock Extraction Studies	4/30/2019	4/30/2019	Reported in the quarterly report.	
M7 – Complete Temporal Changes in Gas and Fluid Composition Studies	7/31/2019	7/30/2019	Reported in the quarterly report.	
M8 – Samples for Wettability and Relative Permeability Testing Collected	12/31/2019	12/15/2019	Reported in the quarterly report.	
M9 – Samples for Brittleness Testing Collected	12/31/2019	12/15/2019	Reported in the quarterly report.	
M10 – Initial EDFM Model Complete	3/31/2020	3/31/2020	Reported in the quarterly report.	

Continued . . .

Table 34. Milestones (continued)

Milestone Title/ Description	Planned Completion Date	Actual Completion Date	Verification Methods	Comments
M11 – Reservoir Characterization and Performance Database Complete	3/31/2020	3/31/2020	Reported in the quarterly report.	
M12 – Pilot Test Database Complete	3/31/2020	3/31/2020	Reported in the quarterly report.	
M13 – Initial Large-Scale Model Complete	6/30/2020	6/30/2020	Reported in the quarterly report.	
M14 – XRD–XRF Calibration Complete	9/30/2020	9/30/2020	Reporting in the quarterly report.	
M15 – Initiate Virtual Learning-Based Modeling	9/30/2020	9/30/2020	Reported in the quarterly report.	
M16 –Wettability and Relative Permeability Studies Complete	8/31/2021	8/31/2021	Reported in the quarterly report.	
M17 – Brittleness Studies Complete	8/31/2021	8/31/2021	Reported in the quarterly report.	
M18 – Conformance Treatment Modeling Studies Complete	10/31/2021		Reported in the quarterly report.	
M19 – Large-Scale EOR Modeling Studies Complete	10/31/2021		Reported in the quarterly report.	
M20 – Virtual Learning Method Development Studies Complete	11/30/2021	6/21/2021	Reported in the quarterly report.	
M21 – RTVFC Method Development Studies Complete	11/30/2021	6/21/2021	Reported in the quarterly report.	

REFERENCES

Ahmad, W., Vakili-Nezhaad, G., Al-Bemani, A.S., and Al-Wahaibi, Y., 2016, Uniqueness, repeatability analysis and comparative evaluation of experimentally determined MMPs: J. Pet. Sci. Eng., v. 147, p. 218–227.

Akaike, H., 1973, Information theory and an extension of the maximum likelihood principle, *in* Petrov, B.N., and Csáki, F., eds., 2nd International Symposium on Information Theory, Tsahkadsor, Armenia, USSR, September 2–8, 1971, Budapest: Akadémiai Kiadó, p. 267–281. Republished in Kotz, S., and Johnson, N. L., eds., 1992, Breakthroughs in statistics, I: Springer-Verlag, p. 610–624.

Al Abbad, M.A., Sanni, M.L., Kokal, S., Krivokapic, A., Dye, C., Dugstad, Ø., Hartvig, S.K., and Huseby, O.K., 2019, A step change for single-well chemical-tracer tests: field pilot testing of new sets of novel tracers: SPE Reservoir Evaluation & Engineering, 2019, v. 22, no. 1, p. 253–265.

Al-Qasim, A., Kokal, S., Hartvig, S., and Huseby O., 2020, Subsurface monitoring and surveillance using inter-well gas tracers: Upstream Oil and Gas Technology, v. 3. 100006.

Al-Qasim, A., Kokal, S., Hartvig, S., and Huseby, O., 2019, Reservoir description insights from inter-well gas tracer test: Presented at the Abu Dhabi International Petroleum Exhibition & Conference, November 11.

Alfi, M., Hosseini, S.A., Alfi, M., and Shakiba, M., 2015, Effectiveness of 4D seismic data to monitor CO_2 plume in Cranfield CO_2-EOR project: Presented at the Carbon Management Technology Conference, November 17.

Alvarez, J.O., Saputra, I.W., and Schechter, D.S., 2017, Potential of improving oil recovery with surfactant additives to completion fluids for the Bakken: Energy & Fuels, v. 31, no. 6, p. 5982–5994.

American Petroleum Institute, 1998, Recommended practices for core analysis—Section 5.3.2.1.1—Boyle's law double-cell (matrix cup) method for grain volume, 2nd Ed.: Exploration and Production Department, American Petroleum Institute, February.

Ayirala, S.C., and Rao, D.N., 2011, Comparative evaluation of a new gas/oil miscibility-determination technique: J. Can. Pet. Technol., v. 50, p. 71–81. DOI: 10.2118/99606-PA.

Boehmke, B., and Greenwell, B., 2020, Hands-on machine learning with R: CRC Press.

Bommer, P.A., and Bayne, M.A., 2018, Active well defense in the Bakken—case study of a ten-well frac defense project, McKenzie County, North Dakota: Presented at the SPE Hydraulic Fracturing Technology Conference and Exhibition, The Woodlands, Texas.

Bommer, P., Bayne, M., Mayerhofer, M., Machovoe, M., and Staron, M., 2017, Redesigning from scratch and defending offset wells—case study of a six-well Bakken Zipper Project, McKenzie County, ND: SPE 184851.

Cai, L., Ding, D.Y., Wang, C., and Wu, Y.S., 2015, Accurate and efficient simulation of fracture matrix interaction in shale gas reservoirs: Transport in Porous Media, v. 107, no. 2, p. 305–20.

Cao, R., Li, R., Girardi, A., Chowdhury, N., and Chen, C., 2017, Well interference and optimum well spacing for Wolfcamp development at Permian Basin: Presented at the Unconventional Resources Technology Conference, Austin, Texas.

Carpenter, C., 2018, Embedded discrete fracture modeling with artificial intelligence in Permian Basin: Journal of Petroleum Technology, v. 70, no. 05, p. 63–64.

Chambers, J., Cleveland, W., Kleiner, B., and Tukey, P., 1983, Graphical methods for data analysis: New York, Chapman and Hall, 395 p.

Chang, W., Cheng, J., Allaire, J.J., Sievert, C., Schloerke, B., Xie, Y., Allen, J., McPherson, J., Dipert, A., and Borges, B., 2021, Shiny: Web Application Framework for R. R package version 1.6.0. https://CRAN.R-project.org/package=shiny (accessed 2021).

Chen, H., Chang, S., Thomas, G., Wang, W., Mashat, A., and Shateeb, H., 2021, Comparison of water and gas tracers field breakthrough: Presented at the SPE Annual Technical Conference and Exhibition, September 15.

Chen, T., and Guestrin, C., 2016, XGBoost—a scalable tree boosting system, *in* Proceedings of the 22nd ACM SIGKDD International Conference on Knowledge Discovery and Data Mining: New York, New York, p. 785–794.

Choi, E.S., Cheema, T., and Islam, M.R., 1997, A new dual-porosity/dual-permeability model with non-Darcian flow through fractures: Journal of Petroleum Science and Engineering, v. 17, nos. 3–4, p. 331–344.

Choudhury, M.D., Dutta, T., and Tarafdar, S., 2015, Growth kinetics of NaCl crystals in a drying drop of gelatin—transition from faceted to dendritic growth: June 2015.

Conlin, J.M., Hale, J.L., Sabathier, J.C., Faure, F., and Mas, D., 1990, Multiple-fracture horizontal wells—performance and numerical simulation: Presented at the European Petroleum Conference, the Hague, Netherlands.

Dachanuwattana, S., Jin, J., Zuloaga-Molero, P., Li, X., Xu, Y., Sepehrnoori, K., Yu, W., and Miao, J., 2018a, Application of proxy-based MCMC and EDFM to history match a Vaca Muerta shale oil well: Fuel, v. 220, p. 490–502.

Dachanuwattana, S., Xia, Z., Yu, W., Qu, L., Wang, P., Liu, W., Miao, J., and Sepehrnoori, K., 2018b, Application of proxy-based MCMC and EDFM to history match a shale gas condensate well: Journal of Petroleum Science and Engineering, v. 167, p. 486–497.

Donnelly, J., 2014, Comments—global shale prospects: Journal of Petroleum Technology, v. 66, p. 18.

Du, S., Liang, B., and Yuanbo, L., 2017, Field study—embedded discrete fracture modeling with artificial intelligence in Permian Basin for shale formation: Presented at the SPE Annual Technical Conference and Exhibition, October.

DW Energy Group, 2016, Whiting petroleum's Mark Williams looks at Bakken history: www.dwenergygroup.com/whiting-petroleums-mark-williams-looks-bakken-history-and08242016/ (accessed November 2021).

Eltahan, E., Ganjdanesh, R., Yu, W., Sepehrnoori, K., Drozd, H., and Ambrose, R., 2020, Assisted history matching using Bayesian inference—application to multi-well simulation of a huff-n-puff pilot test in the Permian Basin: Presented at the Unconventional Resources Technology Conference, 20–22 July 2020, p. 278–294.

Eltahan, E., Yu, W., Sepehrnoori, K., Kerr, E., Miao, J., and Ambrose, R., 2019, Modeling naturally and hydraulically fractured reservoirs with artificial intelligence and assisted history matching methods using physics-based simulators: Presented at the SPE Western Regional Meeting, April.

Esquivel, R., and Blasingame, T.A., 2017, Optimizing the development of the Haynesville shale—lessons learned from well-to-well hydraulic fracture interference: Presented at the SPE/AAPG/SEG Unconventional Resources Technology Conference, Austin, Texas.

Feng, R., Zhang, Y., Rezagholilou, A., Roshan, H., and Sarmadivaleh, M., 2020, Brittleness index—from conventional to hydraulic fracturing energy model: Rock Mechanics and Rock Engineering, v. 53, p. 739–753.

Fiallos Torres, M.X., Yu, W., Ganjdanesh, R., Kerr, E., Sepehrnoori, K., Miao, J., and Ambrose, R., 2019, Modeling interwell fracture interference and huff-n-puff pressure containment in Eagle Ford using EDFM: Presented at the SPE Oklahoma City Oil and Gas Symposium, Oklahoma City, Oklahoma.

Fleury, M., and Romero-Sarmiento, M., 2016, Characterization of shales using T1–T2 NMR maps: Journal of Petroleum Science and Engineering, v. 137, p. 55–62.

Gelman, A., and Hill, J. 2007, Data analysis using regression and multilevel/hierarchical models: New York, Cambridge University Press, 648 p.

Ghorbani, M., Momeni, A., Safavi, S., and Gandomkar, A., 2014, Modified vanishing interfacial tension (VIT) test for CO_2–oil minimum miscibility pressure (MMP) measurement: J. Natural Gas Sci. Eng., v. 20, p. 92–98.

Glazewski, K.A., Taunton, M.A., Wilson, W.I., Kurz, B.A., Kovacevich, J., Azzolina, N.A., Hamling, J.A., Sorensen, J.A., Steadman, E.N., Harju, J.A., and Gorecki, C.D., 2020, Produced water management and recycling options in North Dakota – 2020: Final report for North Dakota Legislative Management Energy Development and Transmission Committee and North Dakota Industrial Commission Oil & Gas Research Council, Grand Forks, North Dakota, Energy & Environmental Research Center, September.

Gold, R., 2014, The boom—how fracking ignited the American energy revolution and changed the world: New York, New York, Simon & Schuster.

Grieser, W.V., and Bray, J.M., 2007, Identification of production potential in unconventional reservoirs: Paper presented at the Production and Operations Symposium, Society of Petroleum Engineers, Oklahoma City, Oklahoma, March 2007.

Harris, N.B., Miskimins, J.L., and Mnich, C.A., 2011, Mechanical anisotropy in the Woodford Shale, Permian Basin—origin, magnitude, and scale: The Leading Edge, v. 30, no. 3, p. 284–291.

Haghshenas, B., and Qanbari, F., 2020, Applications of rate and pressure transient analysis in huff-n-puff gas EOR for unconventional reservoirs: Presented at the SPE Improved Oil Recovery Conference, virtual.

Hawthorne, S.B., and Miller, D.J., 2019, A comparison of crude oil hydrocarbon mobilization by vaporization gas drive into methane, ethane, and carbon dioxide at 15.6 MPa and 42°C: Fuel, v. 249, p. 392–399.

Hawthorne, S.B., Sorensen, J.A., Miller, D.J., Gorecki, C.D., Harju, J.A., and Pospisil, G., 2019, Laboratory studies of rich gas interactions with Bakken crude oil to support enhanced oil recovery: Presented at the Unconventional Resources Technology Conference (URTeC), Denver, Colorado, July 22–24, 2019, URTeC: 961, 8 p.

Hawthorne, S.B., and Miller, D.J., 2018, Determining minimum miscibility pressure of an oil composition with a fluid: U.S. Patent 9 879 522, 2018.

Hawthorne, S.B., Jin, L., Kurz, B.A., Miller, D.J., Grabanski, C.B., Sorensen, J.A., Pekot, L.J., Bosshart, N.W., Smith, S.A., Burton-Kelly, M.E., Heebink, L.V., Gorecki, C.D., Steadman, E.N., and Harju, J.A., 2017, Integrating petrographic and petrophysical analyses with CO_2 permeation and oil extraction and recovery in the Bakken tight oil formation: Paper presented at SPE Canada Unconventional Resources Conference, Calgary, Alberta, Canada, February 15–16, 2017, SPE-185081-MS.

Hawthorne, S.B., Miller, D.J., Jin, L., and Gorecki, C.D., 2016, Rapid and simple capillary-rise/vanishing interfacial tension method to determine crude oil minimum miscibility pressure: pure and mixed CO_2, methane, and ethane: Energy & Fuels, v. 30, p. 6365–6372.

Hawthorne, S.B., Gorecki, C.D., Sorensen, J.A., Steadman, E.N., Harju, J.A., and Melzer, S., 2013, Hydrocarbon mobilization mechanisms from Upper, Middle, and Lower Bakken reservoir rocks exposed to CO_2: Paper presented at the SPE Unconventional Resources Conference–Canada, Calgary, Alberta, November 5–7, 2013, SPE 167200.

Helsel, D.R., Hirsch, R.M., Ryberg, K.R., Archfield, S.A., and Gilroy, E.J., 2020, Statistical methods in water resources: U.S. Geological Survey Techniques and Methods, book 4, chapter A3, 458 p. DOI: https://doi.org/10.3133/tm4a3. [Supersedes USGS Techniques of Water-Resources Investigations, book 4, chapter A3, version 1.1.]

Herman, J., and Usher, W., 2017, SALib—an open-source Python library for sensitivity analysis: Journal of Open Source Software, v. 2, no. 9. DOI:10.21105/joss.00097.

Herwanger, J.V., Bottrill, A.D., and Mildren, S.D., 2015, Uses and abuses of the brittleness index with applications to hydraulic stimulation: Paper presented at the Unconventional Resources Technology Conference, San Antonio, Texas, July 20–22, 2015. Society of Exploration Geophysicists, American Association of Petroleum, p. 1215–1223.

Hoffman, T.B., and Evans, J.G., 2016, Improved oil recovery IOR pilot projects in the Bakken Formation: Presented at the SPE Low Perm Symposium, Denver, Colorado.

Hughes, J.D., 2013, A reality check on the shale revolution: Nature, v. 494, p. 307–308.

Hu, H., 2014, Methane adsorption comparison of different thermal maturity kerogens in shale gas system: Chin. Journal of Geochemical, v. 33, p. 425–430.

Huseby, O., Sagen, J., Wangen, M., and Viig, S.O., 2010, Planning and interpretation of offshore-field tracer tests using accurate and refined tracer simulations: Presented at the SPE Latin American and Caribbean Petroleum Engineering Conference, December 1.

Jarvie, D.M., Hill, R.J., Ruble, T.E., and Pollastro, R.M., 2007, Unconventional shale-gas systems—the Mississippian Barnett Shale of north-central Texas as one model for thermogenic shale-gas assessment: American Association of Petroleum Geologists Bulletin, v. 91, p. 475–499.

Jervis, M., Bakulin, A., and Smith, R., 2018, Making time-lapse seismic work in a complex desert environment for CO_2 EOR monitoring—design and acquisition: The Leading Edge, v. 37, no. 8, p. 598–606.

Jin, L., Barajas-Olalde, C., Bosshart, N., He, J., Adams, D., Kalenze, N., Hamling, J., and Gorecki, C., 2021, Application of CO_2 injection monitoring techniques for CO_2 EOR and associated geologic storage: Available at SSRN 3812730, March 25.

Jin, L., Jiang, T., Dotzenrod, N.W., Patil, S.B., Klenner, R.C.L., Sorensen, J.A., and Bosshart, N.W., 2019, Modeling study of the unconventional Bakken Formation for gas injection EOR: Presented at the 4th EAGE Conference on Petroleum Geostatistics, Florence, Italy, September 2–6, 2019.

Jin, L., Hawthorne, S., Sorensen, J., Pekot, L., Bosshart, N., Gorecki, C., Steadman, E., and Harju, J., 2017a, Utilization of produced gas for improved oil recovery and reduced emissions from the Bakken Formation: Presented at the 2017 SPE Health, Safety, Security, Environment & Social Responsibility Conference – North America, New Orleans, Louisiana, April 18–20, 2017, SPE-184414-MS.

Jin, L., Hawthorne, S., Sorensen, J., Pekot, L., Kurz, B., Smith, S., Heebink, L., Herdegen, V., Bosshart, N., Torres, J., Dalkhaa, C., Peterson, K., Gorecki, C.D., Steadman, E.N., and Harju, J.A., 2017b, Advancing CO_2 enhanced oil recovery and storage in unconventional oil play—experimental studies on Bakken shales: Applied Energy, v. 208, p. 171–183.

Jin, L., Sorensen, J.A., Hawthorne, S.B., Smith, S.A., Pekot, L.J., Bosshart, N.W., Burton-Kelly, M.E., Miller, D.J., Grabanski, C.B., Gorecki, C.D., Steadman, E.N., and Harju, J.A., 2017c, Improving oil recovery by use of carbon dioxide in the Bakken unconventional system—a laboratory investigation: SPE Reservoir Evaluation & Engineering, v. 20, no. 03, p. 602–612.

Jin, L., Hawthorne, S., Sorensen, J., Kurz, B., Pekot, L., Smith, S., Bosshart, N., Azenkeng, A., Gorecki, C., and Harju, J., 2016, A systematic investigation of gas-based improved oil recovery technologies for the Bakken tight oil formation, *in* Proceedings of the 4th Unconventional Resources Technology Conference: Paper presented at the American Association of Petroleum Geologists Unconventional Resources Technology Conference, San Antonio, Texas, USA. doi: https://doi.org/10.15530/urtec-2016-2433692.

Jin, X., Shah, S.N., Truax, J.A., and Roegiers, J.-C., 2014, A practical petrophysical approach for brittleness prediction from porosity and sonic logging in shale reservoirs: Paper presented at the Society of Petroleum Engineers Annual Technical Conference and Exhibition, Amsterdam, the Netherlands, October 2014.

Johnson, J.E., Webb, S.M., Ma, C., and Fischer, W.W., 2016, Manganese mineralogy and diagenesis in the sedimentary rock record: Geochimica et Cosmochimica Acta, v. 173, p. 210–231.

Kackstaetter, U., 2014, SEDMIN—Microsoft Excel™ spreadsheet for calculating fine-grained sedimentary rock mineralogy from bulk geochemical analysis: Open Geosciences, v. 6, p. 170–181. doi: https://doi.org/10.2478/s13533-012-0170-3.

Kang, Y., Shang, C., Zhou, H., Huang, Y., Zhao, Q., Deng, Z., Wang, H., and Ma, Y.Z., 2020, Mineralogical brittleness index as a function of weighting brittle minerals—from laboratory tests to case study: Journal of Natural Gas Science and Engineering, v. 77, 103278.

Katiyar, A., Patil, P.D., Rohilla, N., Crosley, M., Miller, T., Rozowski, P., Evans, J., Bozeman, T., and Nguyen, Q.P., 2021, Unconventional reservoir hydrocarbon-gas foam enhanced-oil-recovery pilot—design, implementation, and performance analysis: SPE Reservoir Evaluation & Engineering, v. 24, no. 1, p. 194–204.

Kazempour, M., Kiani, M., Nguyen, D., Salehi, M., Bidhendi, M.M., and Lantz, M., 2018, Boosting oil recovery in unconventional resources utilizing wettability altering agents—successful translation from laboratory to field: Presented at the SPE Improved Oil Recovery Conference, Tulsa, Oklahoma.

Kias, E., Maharidge, R., and Hurt, R., 2015, Mechanical versus mineralogical brittleness indicesacross various shale plays: Society of Petroleum Engineers SPE-174781-MS, SPE Annual Technical Conference and Exhibition, September 28–30, Houston, Texas, 15 p.

Krishnamurthy, J., Srinivasan, K., Layton, N., and Drouillard, M., 2019, Frac hits—good or bad? a comprehensive study in the Bakken: Presented at the SPE Annual Technical Conference and Exhibition, Calgary, Alberta, Canada: SPE-195927-MS.

Kumar, A., and Sharma, M.M., 2018, Diagnosing fracture-wellbore connectivity using chemical tracer flowback data: Presented at the SPE/AAPG/SEG Unconventional Resources Technology Conference, July 23.

Kurtoglu, B., Sorensen, J.A., Braunberger, J., Smith, S., and Kazemi, H., 2013, Geologic characterization of a Bakken reservoir for potential CO_2 EOR: Paper presented at Society of Exploration Geophysicists, American Association of Petroleum Geologists, Society of Petroleum Engineers Unconventional Resources Technology Conference, Denver, Colorado, 12–14 August, 2013, p. 1834–1844. doi: https://doi.org/10.1190/urtec2013-186.

LeFever, J.A., and Helms, L.D., 2006, Bakken Formation reserve estimates: North Dakota Geological Survey, Bismarck, North Dakota.

LeFever, J.A., 2007, Bakken Middle Member lithofacies 3: NDGS Geologic Investigations, No. 45, six maps in series.

Li, X., Chen, G., Chen, Z., Wang, L., Wang, Y., Dong, D., Lu, Z., Wang, S., Huang, J., and Zhang, C., 2016, An insight into the mechanism and evolution of shale reservoir characteristics with over-high maturity: Journal of Natural Gas Geoscience, v. 1, no. 5, p. 373–382.

Li, H., He, J., and Misra, S., 2018, Data-driven in situ geomechanical characterization in shale reservoirs: Paper presented at the Society of Petroleum Engineers Annual Technical Conference and Exhibition, Dallas, Texas, 24–26 September.

Lindsay, G., Miller, G., Xu, T., Shan, D., and Baihly, J., 2018, Production performance of infill horizontal wells vs. pre-existing wells in the major United States unconventional basins: Presented at the SPE Hydraulic Fracturing Technology Conference and Exhibition, The Woodlands, Texas: SPE-189875-MS.

Lindsay, G.J., White, D.J., Miller, G.A., Baihly, J.D., and Sinosic, B., 2016, Understanding the applicability and economic viability of refracturing horizontal wells in unconventional plays: Presented at the SPE Hydraulic Fracturing Technology Conference, The Woodlands, Texas: SPE-179113-MS.

Litvak, M.L., Nagarajan, N.R., Prasad, R.S., and Shaarawim K., 2020, Successful field test of enhancing Bakken oil recovery with propane injection Part II. development and application of innovative simulation technology: Presented at the Unconventional Resources Technology Conference, virtual: URTEC-2020-2775-MS.

Liu, C., Yu, W., Chang, C., Li, Q., and Sepehrnoori, K., 2020, Proxy based assisted history matching and well spacing optimization in shale gas development of a real field case: Presented at the SPE Improved Oil Recovery Conference, August.

Liu, Z., and Sun, Z., 2015, New brittleness indexes and their application in shale/clay gas reservoir prediction: Petroleum Exploration and Development, v. 42, p. 129–137.

Liu, Z.X., Liang, Y., Wang, Q., Guo, Y.J., Gao, M., Wang, Z.B., and Liu, W.L., 2020, Status and progress of worldwide EOR field applications: Journal of Petroleum Science and Engineering, v. 193, no. 107449.

Lolon, E., Hamidieh, K., Weijers, L., Mayerhofer, M., Melcher, H., and Oduba, O., 2016, Evaluating the relationship between well parameters and production using multivariate statistical models—a Middle Bakken and Three Forks case history: SPE 179171.

Mahmud, H.M., Arumugam, S., and Mahmud, W., 2019, Potential of low-salinity waterflooding technology to improve oil recovery: Enhanced Oil Recovery Processes – New Technologies, IntechOpen Book Series. DOI: 10.5772/intechopen.88082.

Marongiu-Porcu, M., Lee, D., Shan, D., and Morales, A., 2015, Advanced modeling of interwell-fracturing interference—an Eagle Ford shale oil study: Presented at the SPE Annual Technical Conference and Exhibition, Houston, Texas: SPE-174902-PA.

McElreath, R., 2016, Statistical rethinking—a Bayesian course with examples in R and Stan: Florida, Chapman and Hall, 487 p.

Michael, K., Golab, A., Shulakova, V., Ennis-King, J., Allinson, G., Sharma, S., and Aiken, T., 2010, Geological storage of CO_2 in saline aquifers—a review of the experience from existing storage operations: International Journal of Greenhouse Gas Control, v. 4, no. 4, p. 659–67.

Milliken, K.L., Zhang, T., Chen, J., and Ni, Y., 2021, Mineral diagenetic control of expulsion efficiency in organic-rich mudrocks, Bakken Formation (Devonian-Mississippian), Williston Basin, North Dakota, USA: Marine and Petroleum Geology, v. 127, 104869.

Minitab 19 Statistical Software, 2020, Computer software: State College, PA, Minitab, Inc. www.minitab.com.

Mirzaei, M., and Cipolla, C.L., 2012, A workflow for modeling and simulation of hydraulic fractures in unconventional gas reservoirs: Presented at the SPE Middle East Unconventional Gas Conference and C-4TFibition, UAE, Abu Dhabi: SPE-153022-MS.

Mlella, M., Ma, M., Zhang, R., and Mokhtari, M., 2020, Machine learning for geophysical characterization of brittleness—Tuscaloosa Marine Shale case study: Paper presented at the Society of Exploration Geophysicists International Exposition and Annual Meeting, Virtual, October.

Moghadam, A.M., and Salehi, M.B., 2019, Enhancing hydrocarbon productivity via wettability alteration—a review on the application of nanoparticles: Reviews in Chemical Engineering, v. 35, no. 4, p. 531–563.

Mohaghegh, S., 1995. Neural network—what it can do for petroleum engineers: Journal of Petroleum Technology, v. 47, p. 42.

Moinfar, A., Varavei, A., Sepehrnoori, K., and Johns, R.T., 2014, Development of an efficient embedded discrete fracture model for 3D compositional reservoir simulation in fractured reservoirs: Society of Petroleum Engineers, v. 19, no. 2, p. 289–303. DOI:10.2118/154246-PA

Moore, D.M., and Reynolds, R.C., 1997, X-ray diffraction and the identification and analysis of clay minerals (2d ed.): New York, Oxford, Oxford University Press, Oxford.

Morad, S., Ketzer, J., and De Ros, L.F., 2000, Spatial and temporal distribution of diagenetic alterations in siliciclastic rocks—implications for mass transfer in sedimentary basins: Sedimentology, v. 47, p. 95–120.

Mur, A., Barajas-Olalde, C., Adams, D.C., Jin, L., He, J., Hamling, J.A., and Gorecki, C.D., 2020, Integrated simulation to seismic and seismic reservoir characterization in a CO_2 EOR monitoring application: The Leading Edge, v. 39, no. 9, p. 668–78.

Mustafa, A., Abdulraheem, A., Abouelresh, M.I., and Sahin, A., 2019, Lithofacies controls on mechanical properties and brittleness in Qusaiba Shale, Rub'Al-Khali Basin, Saudi Arabia: Paper presented at the International Petroleum Technology Conference, Beijing, China, March 2019.

Nagarajan, N.R., Stoll, D., Litvak, M.L., Prasad, R.S., and Shaarawi, K., 2020, Successful field test of enhancing Bakken oil recovery by propane injection Part I. field test planning, operations, surveillance, and results: Presented at the SPE/AAPG/SEG Unconventional Resources Technology Conference, virtual: URTEC-2020-2768-MS.

Nesheim, T.O., 2019, Examination of downward hydrocarbon charge within the Bakken—Three Forks petroleum system—Williston Basin, North America: Marine and Petroleum Geology, v. 104, p. 346–360.

Nicksiar, M., and Martin, C.D., 2013, Crack initiation stress in low porosity crystalline and sedimentary rocks: Engineering Geology, v. 154, p. 64–76.

Nordeng, S.H., and Helms, L.D., 2010, Bakken source system – Three Forks Formation assessment: North Dakota Department of Mineral Resources, 22 p., April.

Nordeng, S.H., and LeFever, J.A., 2009, Organic geochemical patterns in the Bakken Source System: North Dakota Geological Survey, Geologic Investigations No. 79.

North Dakota Geological Survey, 2020, Core analysis: https://www.dmr.nd.gov/ndgs/core_analysis/ (accessed 2020).

Novak, A., and Egenhoff, S., 2019, Soft-sediment deformation structures as a tool to recognize synsedimentary tectonic activity in the middle member of the Bakken Formation, Williston Basin, North Dakota: Marine and Petroleum Geology, v. 105, p. 124–140.

Ojha, S.P., Misra, S., Sinha, A., Dang, S., Sondergeld, C., and Rai, C., 2017, Estimation of pore network characteristics and saturation-dependent relative permeability in organic-rich shale samples obtained from Bakken, Wolfcamp, and Woodford Shale Formations: Society of Petrophysicists and Well Log Analysts, SPWLA-2017-F, SPWLA 58th Annual Logging Symposium, June 17–21, Oklahoma City, Oklahoma.

Pappenberger, F., Beven, K.J., Ratto, M., and Matgen, P., 2008, Multi-method global sensitivity analysis of flood inundation models: Advances in Water Resources, v. 31, no. 1, p. 1–14.

Paris, A.G., and Stewart, R.R., 2020, Predicting reservoir quality in the Bakken Formation, North Dakota, using petrophysics and 3C seismic data: Interpretation, v. 8, p. T851–T868.

Pearson, C.M., Griffin, L., Wright, C., and Weijers, L., 2013, Breaking up is hard to do—creating hydraulic fracture complexity in the Bakken central basin: SPE 163827.

Pei, P., He, J., and Ling, K., 2014, Correlating geomechanical properties of the Bakken Formation rocks with lithofacies and sequence: Paper presented at the 48th U.S. Rock Mechanics/Geomechanics Symposium, Minneapolis, Minnesota, June 2014.

Perez Altamar, R., and Marfurt, K., 2014, Mineralogy-based brittleness prediction from surface seismic data—application to the Barnett Shale: Interpretation, v. 2, p. T1–T17.

Pospisil, G., Weddle, P., Strickland, S., McChesney, J., Tompkins, K., Neuroth, T., Pearson, C.M., Griffin, L., Kaier, T., Sorensen, J., and Jin, L., 2020, Report on the first rich gas EOR cyclic multiwell huff 'n' puff pilot in the Bakken tight oil play: Presented at the 2020 Society of Petroleum Engineers (SPE) Annual Technical Conference and Exhibition, Denver, Colorado, October 5–7, 2020. SPE-201471-MS.

Psarras, P., Holmes, R., Vishal, V., and Wilcox, J., 2017, Methane and CO_2 adsorption capacities of kerogen in the Eagle Ford shale from molecular simulation: Accounts of Chemical Research, v. 50, no. 8, p. 1818–1828.

Pruess, K., 1992, Brief guide to the MINC-method for modeling flow and transport in fractured media: Lawrence Berkeley Laboratory, California, May 1.

Pruess, K., and Narasimhan, T.N., 1985, A practical method for modelling fluid and heat flow in fractured porous media: SPE Journal, v. 25, p. 14–26.

Rahmanifard, H., and Plaksina, T., 2019, Application of artificial intelligence techniques in the petroleum industry—a review: Artificial Intelligence Review, v. 52, p. 2295–2318.

R Core Team (2021). R: A language and environment for statistical computing. R Foundation for Statistical Computing, Vienna, Austria. URL www.R-project.org/.

Rao, D.N., and Lee, J.I., 2003, Determination of gas–oil miscibility conditions by interfacial tension measurements: J. Colloid Interface Sci., v. 262, no. 2, p. 474–482.

Rickman, R., Mullen, M.J., Petre, J.E., Grieser, W.V., and Kundert, D., 2008, A practical use of shale petrophysics for stimulation design optimization—all shale plays are not clones of the Barnett Shale: Paper presented at the Society of Petroleum Engineers Annual Technical Conference and Exhibition, Denver, Colorado, September.

Salciccioli, J.D., Crutain, Y., Komorowski, M., and Marshall, D.C., 2016, Sensitivity analysis and model validation: Secondary Analysis of Electronic Health Records, p. 263–271.

Sani, A.M., Podhoretz, S.B., and Chambers, B.D., 2015, The use of completion diagnostics in Haynesville shale horizontal wells to monitor fracture propagation, well communication, and production impact: Presented at the SPE/CSUR Unconventional Resources Conference, Calgary, Alberta, Canada. SPE-175917-MS.

Sanni, M., Abbad, M., Kokal, S., Ali, R., Zefzafy, I., Hartvig, S., and Huseby, O., 2017, A field case study of an interwell gas tracer test for gas-EOR monitoring: Presented at the Abu Dhabi International Petroleum Exhibition & Conference, November 13.

Scherz, R.Y., Rainbolt, M.F., Pradhan, Y., and Tian, W., 2019, Evaluating the impact of frac communication between parent, child, and vertical wells in the Midland Basin, Lower Spraberry, and Wolfcamp reservoirs: Presented at the SPE Hydraulic Fracturing Technology Conference and Exhibition, The Woodlands, Texas: SPE-194349-MS.

Schwarz, G.E., 1978, Estimating the dimension of a model: Annals of Statistics, v. 6, no. 2, p. 461–464. DOI:10.1214/aos/1176344136.

Sharma, A., Shook, G.M, and Pope, G.A., 2014, Rapid analysis of tracers for use in EOR flood optimization: Presented at the SPE Improved Oil Recovery Symposium, April 12.

Sharma, M.M., and Manchanda, R., 2015, The role of induced un-propped (IU) fractures in unconventional oil and gas wells: Presented at the SPE Annual Technical Conference and Exhibition, Houston, Texas, SPE-174946-MS.

SimTech, LLC, 2021, EDFM-AI automatic history matching (AHM): www.simtechnologyus.com/ahm.html (accessed November 2021).

Sobol, I.M., 2001, Global sensitivity indices for nonlinear mathematical models and their Monte Carlo estimates: Mathematics and Computers in Simulation, v. 55, no. 1–3, p. 271–280.

Sobol, I.M., 1993, Sensitivity estimates for nonlinear mathematical models: Mathematical Modeling and Computational Experiments, v. 1, no. 4, p. 407–414.

Sonnenberg, S.A., 2020, The Bakken–Three Forks super giant play, Williston Basin: American Association of Petroleum Geologists Bulletin, v. 104, p. 2557–2601.

Sorensen, J.A., Pekot, L.J., Torres, J.A., Jin, L., Hawthorne, S.B., Smith, S.A., Jacobson, L.L., and Doll, T.E., 2018, Field test of CO_2 injection in a vertical Middle Bakken well to evaluate the potential for enhanced oil recovery and CO_2 storage: Paper presented at the Unconventional Resources Technology Conference, Houston, Texas, July 23–25, 2018, URTeC Paper No. 2902813.

Sorensen, J.A., and Hamling, J.A., 2016, Enhanced oil recovery—historical Bakken test data provide critical insights on EOR in tight oil plays: American Oil & Gas Reporter, v. 59, no. 2, p. 55–61.

Sorensen, J.A., Hawthorne, S.B., Smith, S.A., Braunberger, J.R., Liu, G., Klenner, R., Botnen, L.S., Steadman, E.N., Harju, J.A., and Doll, T.E., 2014, Subtask 1.10 – CO_2 storage and enhanced Bakken recovery research program: Final report (May 1, 2013 – May 31, 2013) for U.S. Department of Energy National Energy Technology Laboratory Cooperative Agreement No. DE-FC26-08NT43201, EERC Publication 2014-EERC-06-13, Grand Forks, North Dakota, Energy & Environmental Research Center, June.

Tayyib, D., Al-Qasim, A., Kokal, S., and Huseby, O., 2019, Overview of tracer applications in oil and gas industry: Paper presented at the SPE Kuwait Oil & Gas Show and Conference, Mishref, Kuwait, October.

Thakur, G., 2019, Enhanced recovery technologies for unconventional oil reservoirs: Journal of Petroleum Technology, v. 71, no. 9, p. 66–69.

Thomas, F.B., Holowach, N., Zhou, X., Bennion, D.B., and Bennion, D.W., 1994, In miscible or near-miscible gas injection, which is better?: SPE/DOE Improved Oil Recovery Symposium, Tulsa, Oklahoma, April 17–20, 1994, SPE/DOE 27811, 14 p.

Tran, T., Sinurat, P., and Wattenbarger, R., 2011, Production characteristics of the Bakken shale oil: Paper presented at the Society of Petroleum Engineers Annual Technical Conference and Exhibition, Denver, Colorado, October 2011.

Tripoppoom, S., Wang, X., Liu, Z., Yu, W., Xie, H., Sepehrnoori, K., and Miao, J., 2020a, Characterizing hydraulic and natural fractures properties in shale oil well in Permian Basin using assisted history matching: Fuel, v. 275, p. 117950.

Tripoppoom, S., Xie, J., Yong, R., Wu, J., Yu, W., Sepehrnoori, K., Miao, J., Chang, C., and Li, N., 2020b, Investigation of different production performances in shale gas wells using assisted history matching—hydraulic fractures and reservoir characterization from production data: Fuel, v. 267, p. 117097.

Tripoppoom, S., Yu, W., Huang, H., Sepehrnoori, K., Song, W., and Dachanuwattana, S., 2019, A practical and efficient iterative history matching workflow for shale gas well coupling multiple objective functions, multiple proxy-based MCMC and EDFM: Journal of Petroleum Science and Engineering, v. 176, p. 594–611.

Tucker, M.E., 2001, Sedimentary petrology—an introduction to the origin of sedimentary rocks: John Wiley & Sons.

Vidma, K., Abivin, P., Fox, D., Reid, M., Ajisafe, F., Marquez, A., Yip, W., and Still, J., 2019, Fracture geometry control technology prevents well interference in the Bakken: Presented at the SPE Hydraulic Fracturing Technology Conference and Exhibition, The Woodlands, Texas: SPE-194333-MS.

Wang, F.P., and Gale, J.F., 2009, Screening criteria for shale-gas systems: Gulf Coast Association of Geological Societies Transactions, v. 59, p. 779–793.

Warren, J.E., and Root, P.J., 1963, The behavior of naturally fractured reservoirs: Society of Petroleum Engineers Journal, v. 3, no. 3, p. 245–255.

Weddle, P., Griffin, L., and Pearson, C.M., 2017, Mining the Bakken—driving cluster efficiency higher using particulate diverters: Paper presented at the SPE Hydraulic Fracturing Technology Conference and Exhibition, The Woodlands, Texas, USA, January 2017. doi: https://doi.org/10.2118/184828-MS.

Weniger, P., Kalkreuth, W., Busch, A., and Kross, B.M., 2010, High-pressure methane and carbon dioxide sorption on coal and shale samples from the Paraná Basin, Brazil: International Journal of Coal Geology, v. 84, p. 190–205.

Wickham, H., 2016, ggplot2: Elegant Graphics for Data Analysis. Springer-Verlag New York, 2016.

Wocken, C.W., Stevens, B.G., Almlie, J.C., and Schlasner, S.M., 2012, End-use technology study – an assessment of alternative uses for associated gas; Topical Report for North Dakota

Industrial Commission Contract No. G024-052, Grand Forks, North Dakota, Energy & Environmental Research Center, September.

Wood, D.A., 2020, Brittleness index predictions from Lower Barnett Shale well log data applying an optimized data matching algorithm at various sampling densities: Geoscience Frontiers 101087.

Xu, Y., Cavalcante Filho, J.S.A., Yu, W., and Sepehrnoori, K., 2017, Discrete-fracture modeling of complex hydraulic-fracture geometries in reservoir simulators: SPE Reservoir Evaluation Engineering, v. 20, no. 2, p. 403–422.

Xu, J., and Sonnenberg, S., 2016, Brittleness and rock strength of the Bakken Formation, Williston Basin, North Dakota: Paper presented at the Society of Petroleum Engineers, Society of Exploration Geophysicists, American Association of Petroleum Unconventional Resources Technology Conference, San Antonio, Texas, 1–3 August 2016, p. 2237–2254.

Xu, Y., 2015, Implementation and application of the embedded discrete fracture model (EDFM) for reservoir simulation in fractured reservoirs [Master Thesis]: The University of Texas at Austin, Austin, Texas.

Yan, X, Huang, Z., Yao, J., Li, Y., and Fan, D., 2016, An efficient embedded discrete fracture model based on mimetic finite difference method: Journal of Petroleum Science and Engineering, v. 145, p. 11–21.

Yang, Y., Sone, H., Hows, A., and Zoback, M., 2013, Comparison of brittleness indices in organic-rich shale formations: Paper presented at the 47th U.S. Rock Mechanics/Geomechanics Symposium, San Francisco, California, June 2013.

Yarbrough, L.D., Carr, R., and Lentz, N., 2019, X-ray fluorescence analysis of the Bakken and Three Forks Formations and logging applications: Journal of Petroleum Science and Engineering, v. 172, p. 764–775. DOI: https://doi.org/10.1016/j.petrol.2018.08.070.

Yoon, H., 2020, Integrated geomechanics and geophysics in induced seismicity—experiments of geo-architected rocks and machine learning applications: Sandia National Laboratories, Albuquerque, New Mexico.

Yu, W., Fiallos Torres, M.X., Liu, C., Miao, J., and Sepehrnoori, K., 2020, Complex fracture hits modeling and analysis for parent-child wells in Eagle Ford: Presented at the SPE Annual Technical Conference and Exhibition, virtual: SPE-201455-MS.

Yu, W., Javadpour, F., Varavei, A., and Sepehrnoori, K., 2014, Sensitivity analysis of hydraulic fracture geometry in shale gas reservoirs: Journal of Petroleum Science and Engineering, v. 113, p. 1–7.

Yuncong, G.A., Mifu, Z.H., Jianbo, W.A., and Chang, Z.O., 2014, Performance and gas breakthrough during CO_2 immiscible flooding in ultra-low permeability reservoirs: Petroleum Exploration and Development, v. 41, p. 88–95.

Zaluski, W., El-Kaseeh, G., Lee, S.Y., Piercey, M., and Duguid, A., 2016, Monitoring technology ranking methodology for CO_2-EOR sites using the Weyburn-Midale Field as a case study: International Journal of Greenhouse Gas Control, v. 54, p. 466–478.

Zeng, Z., and Jiang, A., 2009, Geomechanical study of Bakken Formation for improved oil recovery: Paper presented at the International Society for Rock Mechanics International Symposium on Rock Mechanics—SINOROCK 2009, the University of Hong Kong, China, May 2009.

Zhang, D., Ranjith, P., and Perera, M., 2016, The brittleness indices used in rock mechanics and their application in shale hydraulic fracturing—a review: Journal of Petroleum Science and Engineering, v. 143, p. 158–170.

Zhang, L., Huang, H., Wang, Y., Ren, B., Ren, S., Chen, G., and Zhang, H., 2014, CO_2 storage safety and leakage monitoring in the CCS demonstration project of Jilin oilfield, China: Greenhouse Gases: Science and Technology, v. 4, p. 425–439.

Zhang, P., 2012, On the distributional properties of model selection criteria: Journal of the American Statistical Association, v. 87, p. 732–737.

Zoback, M.D., 2010, Reservoir geomechanics: California, Cambridge University Press.

APPENDIX A

DIAGNOSTIC PLOTS FOR LINEAR REGRESSION MODELS

DIAGNOSTIC PLOTS FOR LINEAR REGRESSION MODELS

Appendix A provides diagnostic plots for the fitted Set 1 and Set 2 linear regression models. Each figure has the same four-panel layout.

The upper left-hand panel provides a normal probability plot (Chambers and others, 1983), which is a graphical technique for assessing whether the residuals from the fitted regression model are approximately normally distributed. The residuals are plotted against a theoretical normal distribution such that the points should form an approximate straight line (red diagonal line in each panel). Departures from this straight line indicate departures from normality.

The lower left-hand panel provides a histogram of the residuals from the fitted regression model. Like the normal probability plot, the histogram should reflect an approximately normal distribution, with greater frequency at zero and symmetrical bars to the left and right of zero.

The upper right-hand panel shows the residuals from the fitted regression model versus the fitted (predicted) value of the response variable. Plots of the residuals versus predicted values will allow for visual inspection of homoscedasticity (the variability in the residuals does not vary over the range of predicted values) and bias (the residual values generally plot equally above and below zero). For ideal regression model behavior, this plot should show a horizontal cloud of data rather than a pattern that has curvature, and the variability of that cloud of data should not substantially change as one scans from left to right across the graph (Helsel and others, 2020).

Finally, the lower right-hand panel shows the residuals from the fitted regression model versus the order of the observations. Like the preceding plot, for ideal regression model behavior, this plot should show a horizontal cloud of data rather than a pattern that has curvature, and the variability of that cloud of data should not substantially change as one scans from left to right across the graph (Helsel and others, 2020).

The remainder of this appendix provides subsections for each regression model and the four-panel regression diagnostic plot.

A.1 ET 1 LINEAR REGRESSION MODELS

A.1.1 DSU Incremental Oil Production

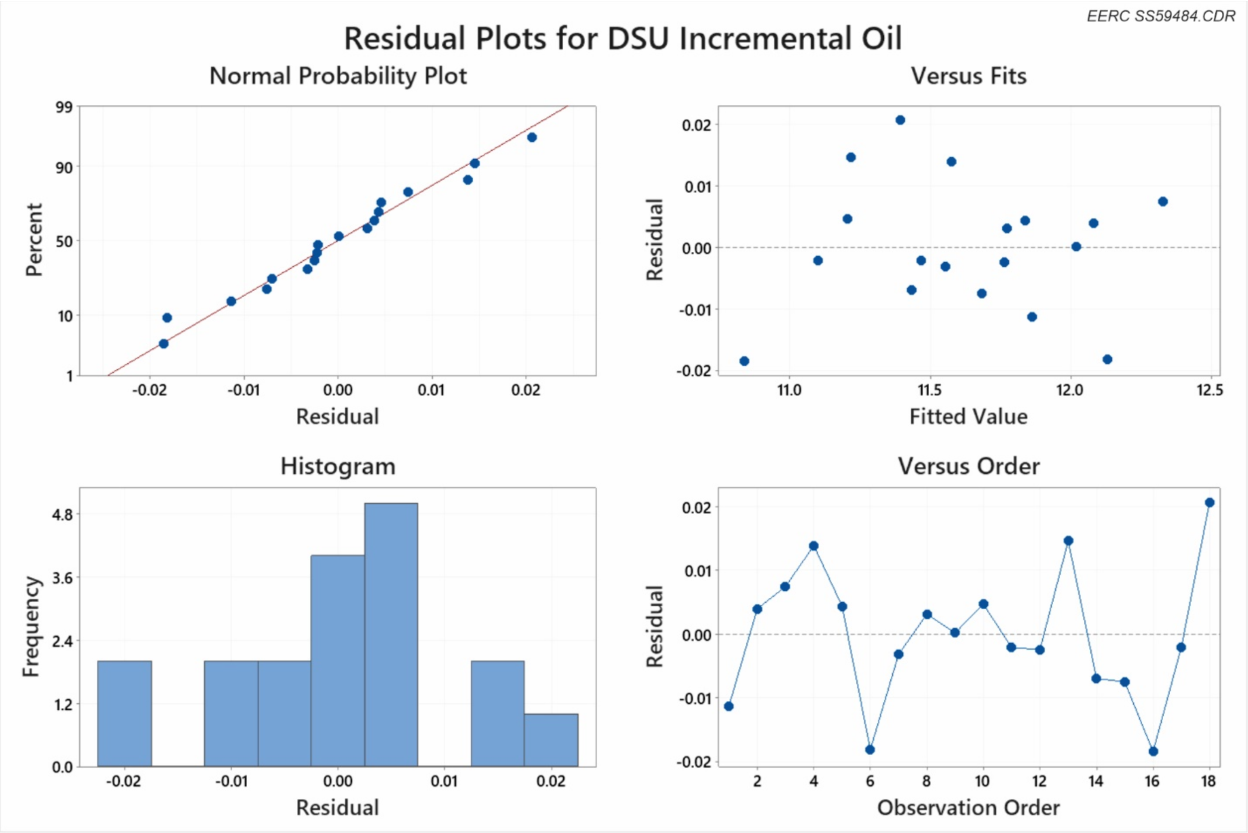

Figure A-1. Diagnostic plots for the Set 1 fitted linear regression model for DSU incremental oil production.

A.1.2 DSU Incremental Water Production

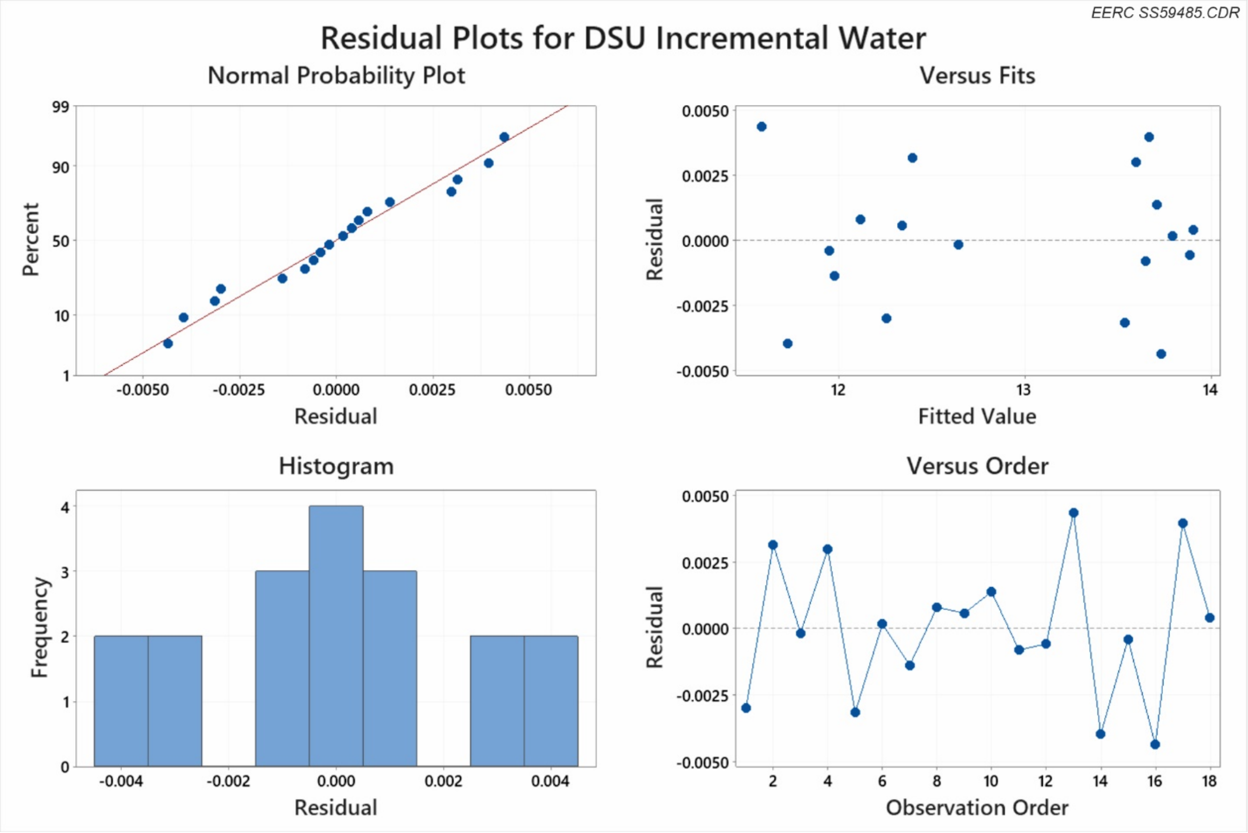

Figure A-2. Diagnostic plots for the Set 1 fitted linear regression model for DSU incremental water production.

A.1.3 DSU Incremental Gas Production

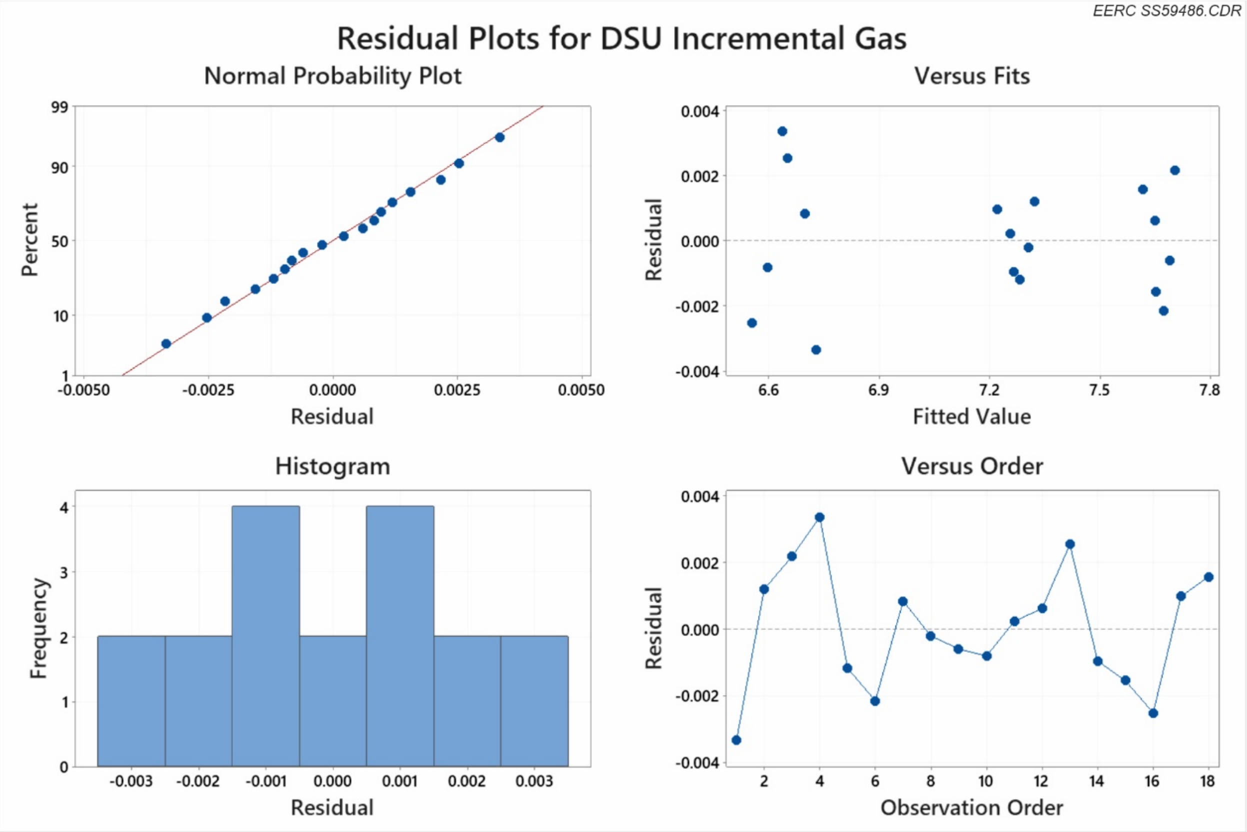

Figure A-3. Diagnostic plots for the Set 1 fitted linear regression model for DSU incremental gas production.

A.1.4 DSU Incremental Net Revenue – $60/stb Oil and $3/bbl Water

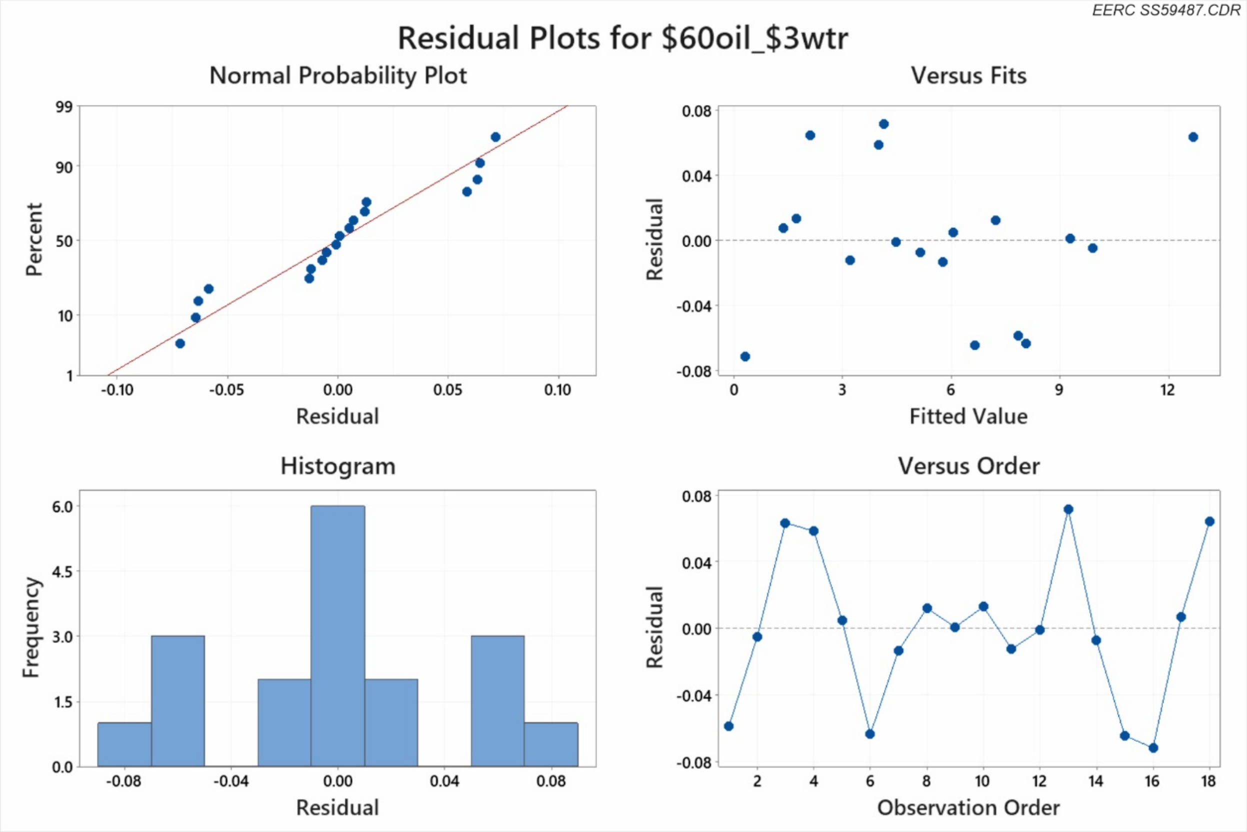

Figure A-4. Diagnostic plots for the Set 1 fitted linear regression model for DSU incremental net revenue assuming $60/stb oil price and $3/bbl water cost.

A.1.5 DSU Incremental Net Revenue – $50/stb Oil and $4/bbl Water

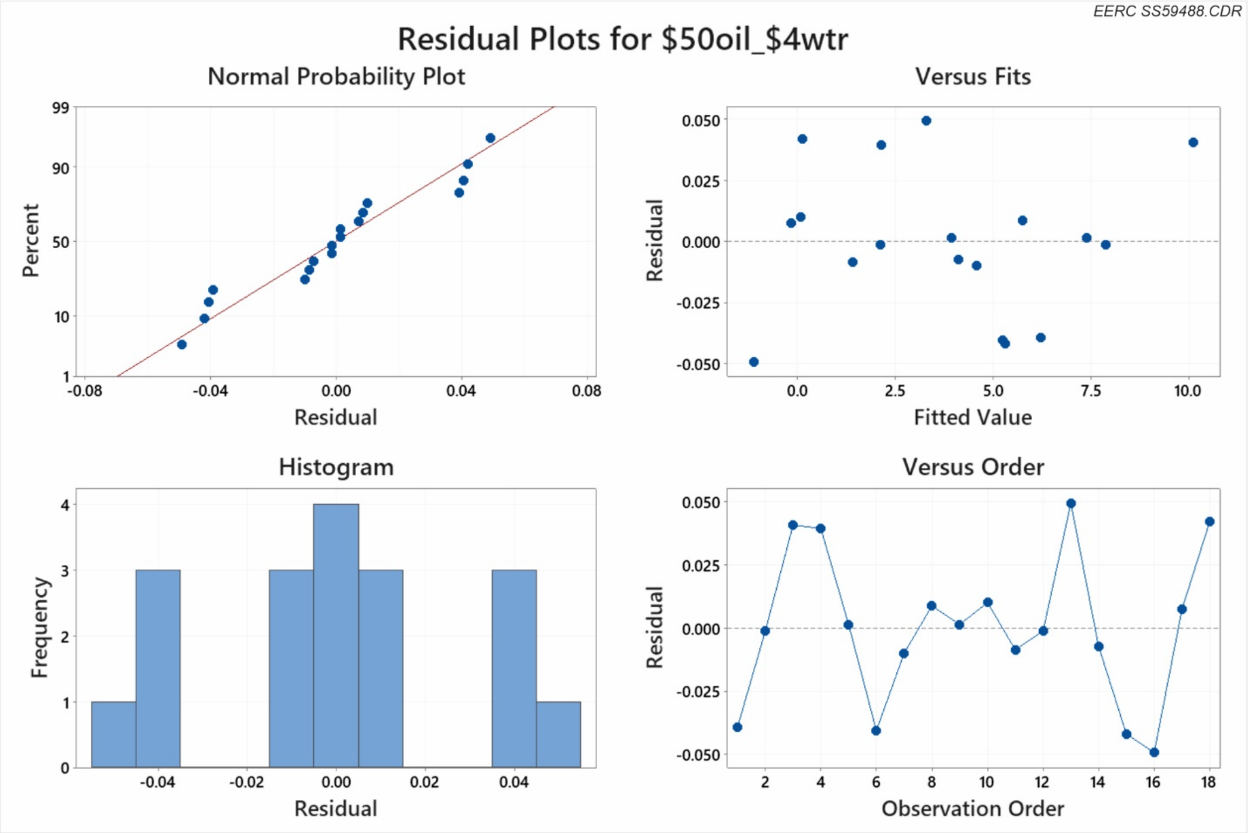

Figure A-5. Diagnostic plots for the Set 1 fitted linear regression model for DSU incremental net revenue assuming $50/stb oil price and $4/bbl water cost.

A.2 SET 2 LINEAR REGRESSION MODELS

A.2.1 DSU Incremental Oil Production

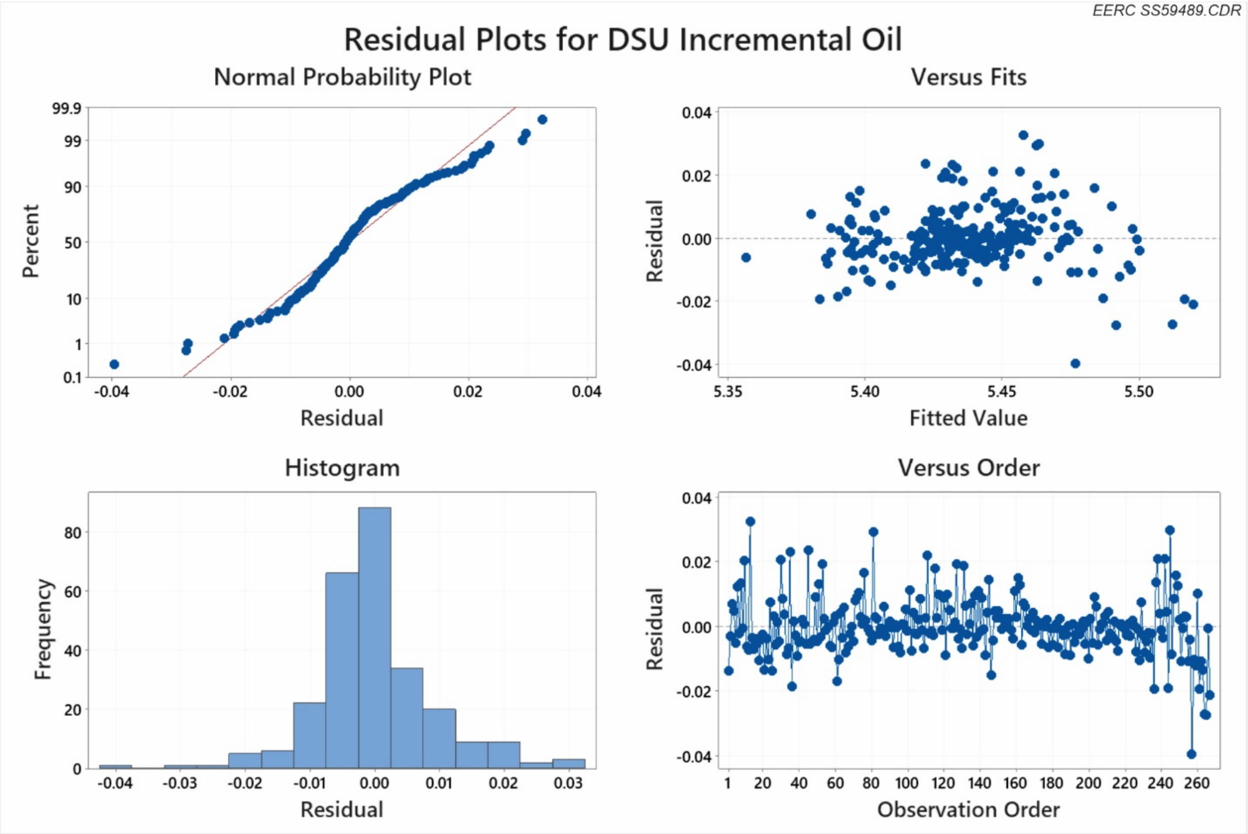

Figure A-6. Diagnostic plots for the Set 2 fitted linear regression model for DSU incremental oil production.

A.2.2 DSU Incremental Water Production

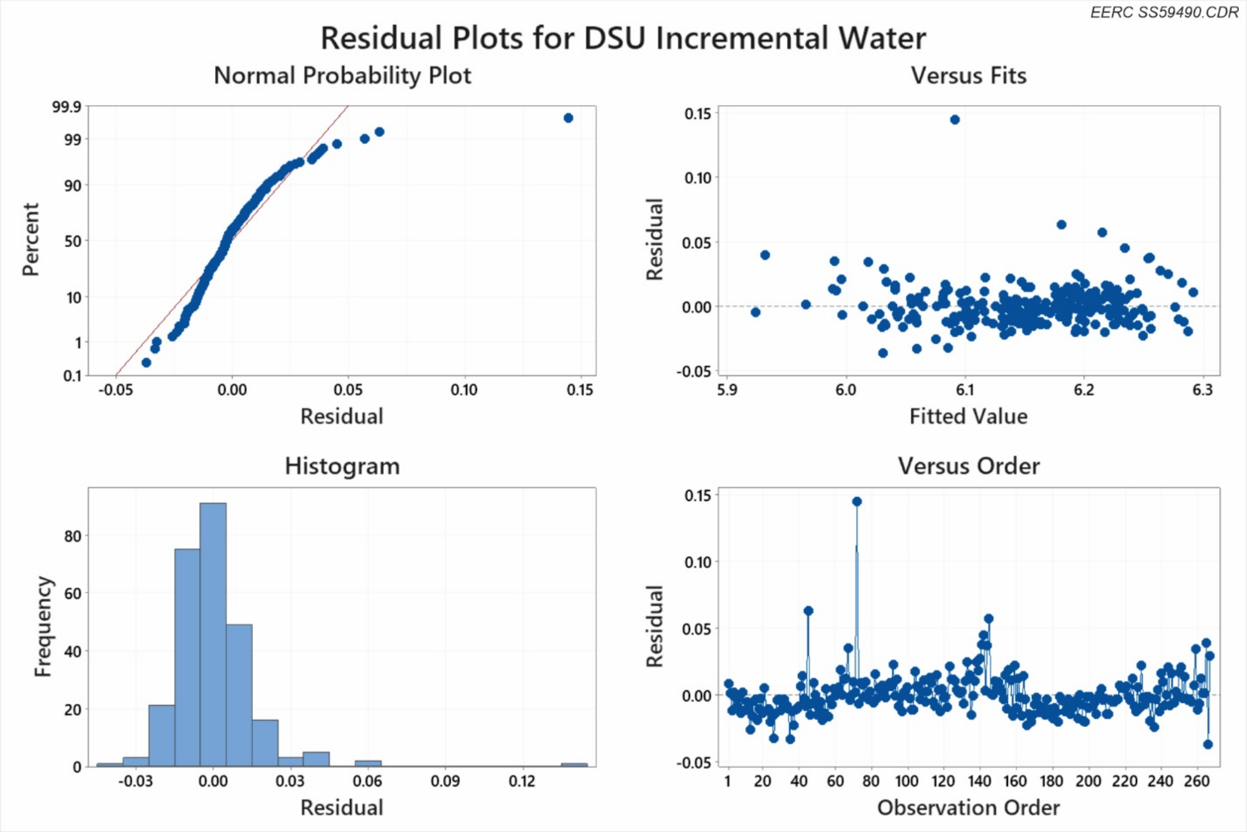

Figure A-7. Diagnostic plots for the Set 2 fitted linear regression model for DSU incremental water production.

A.2.3 DSU Incremental Gas Production

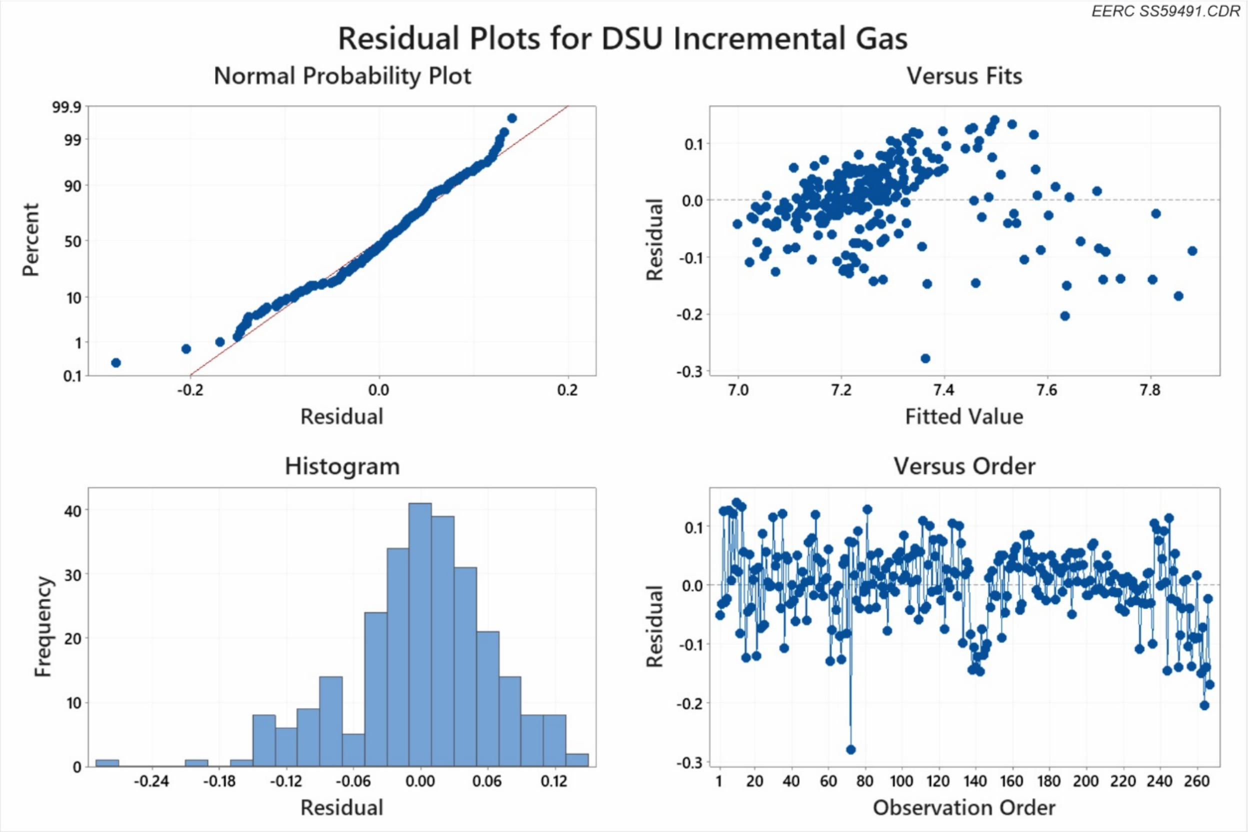

Figure A-8. Diagnostic plots for the Set 2 fitted linear regression model for DSU incremental gas production.

A.2.4 DSU Incremental Net Revenue – $60/stb Oil and $3/bbl Water

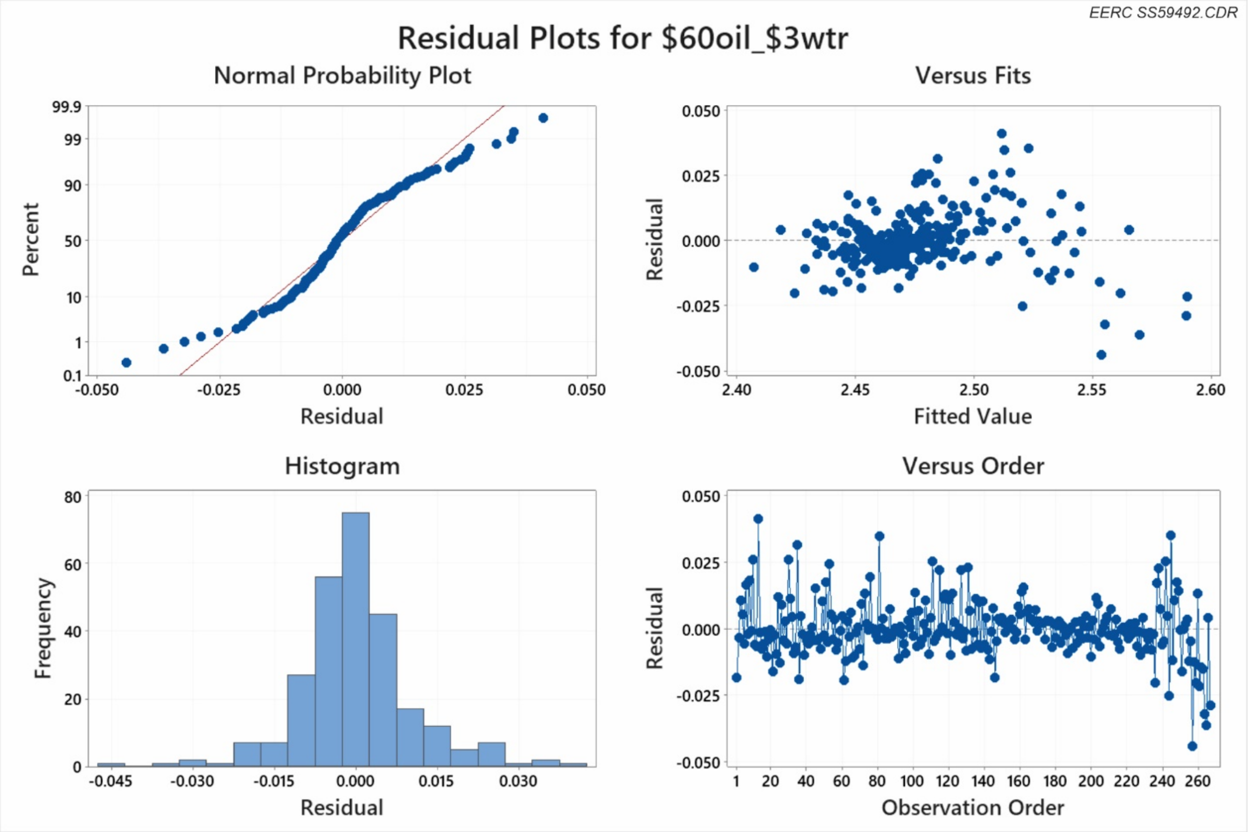

Figure A-9. Diagnostic plots for the Set 2 fitted linear regression model for DSU incremental net revenue assuming $60/stb oil price and $3/bbl water cost.

A.2.5 DSU Incremental Net Revenue – $50/stb Oil and $4/bbl Water

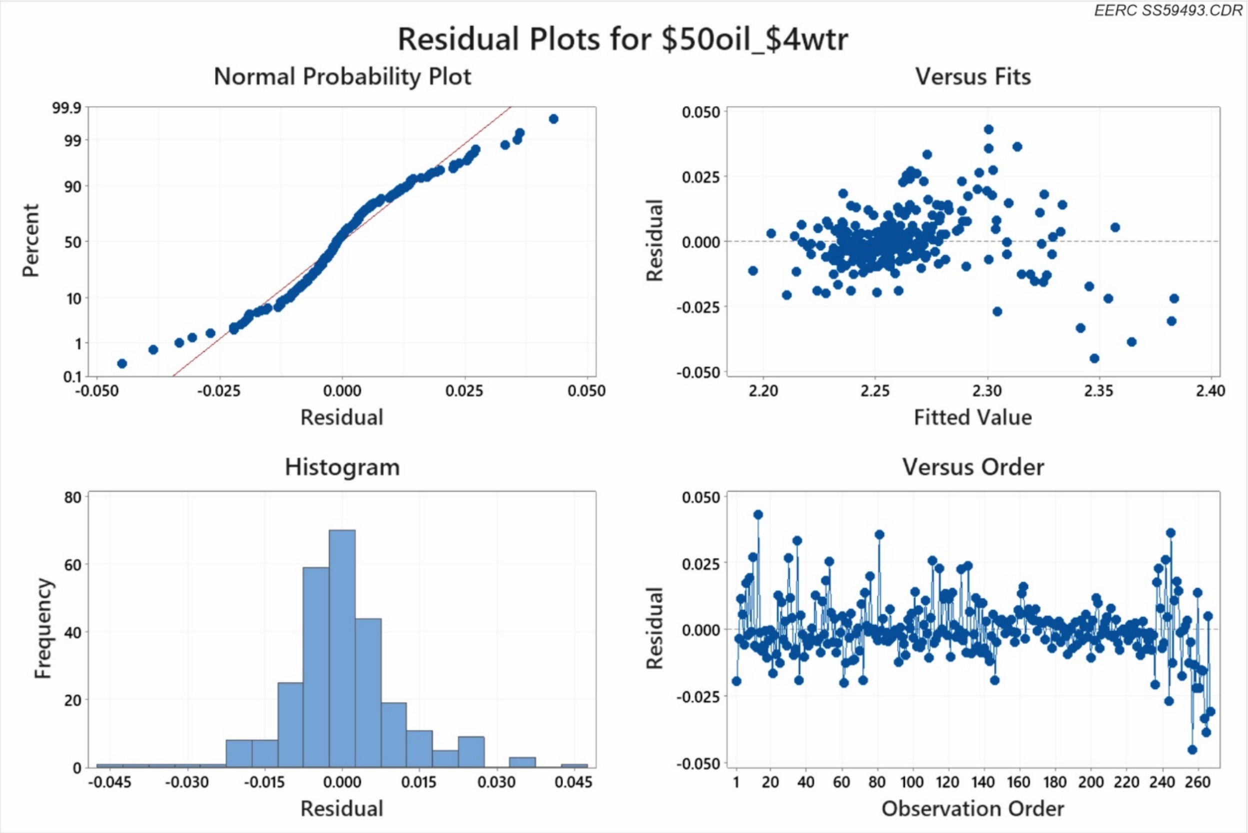

Figure A-10. Diagnostic plots for the Set 2 fitted linear regression model for DSU incremental net revenue assuming $50/stb oil price and $4/bbl water cost.